Title

Production of 117mSn and 119mTe via Proton Bombardment on Natural Antimony: Applications for Charged Particle Reaction Modeling and Theranostics

Author

Apgar, Catherine

Publication Date

2024

Peer reviewed|Thesis/dissertation

Production of ^{117m}Sn and ^{119m}Te via Proton Bombardment on Natural Antimony: Applications for Charged Particle Reaction Modeling and Theranostics

By

Catherine Apgar

A dissertation submitted in partial satisfaction of the

requirements for the degree of

Doctor of Philosophy

in

Engineering – Nuclear Engineering

in the

Graduate Division

of the

University of California, Berkeley

Committee in charge:

Professor Lee Allen Bernstein, Chair
Professor Karl Van Bibber
Professor Rebecca Abergel
Professor Lee Fleming

Summer 2024

Production of ^{117m}Sn and ^{119m}Te via Proton Bombardment on Natural Antimony: Applications for Charged Particle Reaction Modeling and Theranostics

Abstract

Production of ^{117m}Sn and ^{119m}Te via Proton Bombardment on Natural Antimony: Applications for Charged Particle Reaction Modeling and Theranostics

By

Catherine Apgar

Doctor of Philosophy in Engineering – Nuclear Engineering

University of California, Berkeley

Professor Lee Allen Bernstein, Chair

The Auger-emitting radionuclides ^{117m}Sn and ^{119}Sb are promising candidates for a number of both combined therapeutic and diagnostic treatments. Pre-clinical and clinical trials have demonstrated success in treating small mass tumors, osteoarthritis, and palliative care in treating bone metastases. However, limited reaction measurements exist for their production. To address this, a Tri-Laboratory Effort in Nuclear Data collaboration between Brookhaven National Laboratory, Los Alamos National Laboratory, and Lawrence Berkeley National Laboratory (TREND) measured production cross sections for these isotopes via proton-induced reactions on ^{nat}Sb. This experimental data provides cross section measurements for for ^{117m}Sn and ^{119m}Te, the latter of which is a generator for ^{119}Sb. This data can inform production of these radionuclides for medical applications.

This dissertation offers 24 supplementary experimental ^{nat}Sb(p,x) reaction channels for incident proton energies up to 200 MeV as well as 54 measurements on monitor foils – ^{nat}Nb, ^{nat}Cu, and ^{nat}Ti. Large experimental datasets like this provide an opportunity to explore the theory and existing capabilities to model charged particle nuclear reactions. Using TALYS 1.95, 40 base parameters were explored and adjusted to match experimental data, with over 12,000 calculations performed.

Comparative results favor a phenomenological model for nuclear level density. Data also suggests that a reduction in the width of the angular momentum distribution is necessary. as measured in the isomer-to-ground-state ratio for neighboring Odd-A Te isotopes, ^{119}Te and ^{121}Te. Adjustments to the pre-equilibrium model for residual nucleon-nucleon interactions and modifications to the imaginary volume potential well in the optical model improved fit for the largest reaction channels – specifically for ^{nat}Sb(p,xn) channels. In addition to providing data for proton-induced reactions, this dissertation provides indications of secondary neutron-induced reactions produced by high-energy proton reactions across stacked target

measurements. This underscores the complexities and highlights the need for further research on the impact of neutron flux in stacked target experiments.

In addition to the fundamental science component of this thesis, a brief overview of the feasibility of commercial production of these radionuclides is discussed. This section highlights economic considerations for commercialization by reviewing case studies and the main requirements for setting up a cyclotron radiopharmacy.

For Stanley, Stella, and Thomas.
And to my cats – Stanley, Stella, and Thomas, who weren't particularly helpful.

Contents

List of Figures

List of Tables

Acknowledgments

I've been gifted throughout my life with the privilege of sound guidance, advice, and opportunities. Thanking every individual and moment that has influenced me would likely fill more pages than this dissertation.

Lee, thank you for being an ally and an inspiration. Thank you for your patience and for encouraging me to persist. I looked forward to and feared our meetings, especially mid-analysis, when I struggled through data inconsistencies. You took the time to help me when needed, even if it took several hours of discussion. Thank you for guiding me in my research and analysis rather than simply directing me. You are a fantastic advisor. I want to extend my gratitude to Alicia for guidance at a critical juncture.

Andrew V., thank you for your unwavering interest in my work and for keeping me on task through the lockdown and beyond to help me reach this endpoint. Please take care of "teh" pothos and Thai Constellation – they have much history.

To the members of my dissertation committee, thank you not only for your time and assistance in completing this document but also for your personal contributions to my education. Rebecca, thank you for the opportunity to instruct your lab class in Lewis Hall. It was an exciting part of my academic career, and I am grateful for the experience I gained and your support throughout the semester. That historical lab space is invaluable to the department. Karl, I still recall the day we talked on the phone prior to my acceptance to the MEng program and reflect on how the opportunity impacted my career path. I appreciate your confidence in me despite my unconventional background and your guidance both in the MEng program and as a committee member. Lee Fleming, the MEng program, and your courses specifically, taught me a valuable lesson about not becoming complacent. My previous work experience convinced me that I understood business, but I learned more in the first two weeks of your classes than I did in six years in industry. The MEng program corrected many tactics I had learned or adopted from business culture and I look forward to carrying these skills into my next career.

Jon and Morgan, although events prevented in-person collaboration for a significant portion of our studies, I learned so much from each of you. Jon – you developed the backbone for my analysis with Curie. You taught me the basics from day one with my capstone group. Morgan – you developed the backbone for my analysis with your work in TALYS. You taught me the basics from day one as my GSI for NE 101.

As a member of the isotope production group at UCB and LBNL, I am so thankful to have worked with such diverse and talented individuals. Batch, thank you for helping me through this journey. I would not have passed my qualifying exam without your help. Shamsu, although our interactions were infrequent, your advice at a pivotal moment inspired me to put foils back on detectors over a year after an experiment to get one last cross section measurement. I am glad I did that to confirm my analysis; there will always be more to explore. Abby, with many things on your plate, you always volunteered for experimental work no matter how strenuous or time-consuming. Your attention to detail facilitated analysis and I am so excited for your future in the group. I will miss having you as a cubicle partner!

To Ellen, Etienne, and Meiring, thank you for hosting me at LANL when in-person collaboration was limited and for not mentioning my sunburn when we first met. It was quite an adventure and an exciting experiment. Ellen, I still haven't mentally processed the drive-thru event. Dmitri and Michael, thank you for the opportunity to conduct experiments at BNL. Learning about the facility and assisting in experiments there was an incredible experience. Your personalities reminded me so much of my East Coast roots. Michael, "We can just go." Dmitri, when we sat at the airport gate observing a truly bizarre scene, your humor was the highlight of months of travel across the US and abroad.

Thank you to the staff of the 88" Cyclotron — You were always informative, helpful, understanding, and, most importantly, kind. A friendly smile, much like a rising tide, lifts all ships. Thank you for lifting my spirits every day!

To Andrew B., you were a remarkable professor and positively influenced me to speak my truth. Our discussion and the book you lent me influenced me at the time, and I often think back on it when I have similar experiences. It is still an uphill battle, but your recognition and actions are a reminder that things can change.

To Mary, Mike, Tom, John, and many others, thank you for being leaders, not bosses. You helped me grow. Andy S., I certainly did have my head in the clouds; that eclipse was no exception. I am proud to have worked with all of you.

Kelsey, Lance, and James – Thank you for your support, friendship, and instruction during and after our time in the MEng program. For Jeremy and Aaron, your resolute and unwavering friendship, time, understanding, direction, and tolerance of my protracted phone calls have inspired me through this process.

To my family, words cannot express my gratitude for your help and comfort despite being 2927.8 miles away. Mom, thank you for joining me in traversing my move to California. With a dog. And a cat. All in the cab of a U-Haul truck. I miss you. Thank you for taking care of Parker. Thank you for taking care of Thomas while I was traveling for work. Thank you for answering the phone at all hours of the day and night. You helped me in celebrating my accomplishments and advising me through conflicts. I could never have done this without you.

Chapter 1

Introduction

1.1 Research Motivation

Isotope Production

The data presented in this dissertation seeks to inform production of high-yield, radiopure theranostic isotopes ^{117m}Sn and the generator for ^{119}Sb – ^{119m}Te, via proton bombardment on ^{nat}Sb and to investigate existing reaction models in comparison to experimental work. Although "theranostic" did not enter the lexicon until the early 21st century, radionuclides have been used for medical applications since the early 20th century [1]. Theranostics, a portmanteau of "therapy" and "diagnostic", are pharmaceuticals that use one or more radionuclides introduced *in vivo* for the diagnosis and treatment of various diseases, ranging from arthritis to late-stage metastatic cancer.

Theranostics are administered via injection or brachytherapy. The former introduces these radionuclides labeled with ligands or nanoparticles that selectively target and bind to treatment areas. In contrast, brachytherapy sources are directly placed in the body in the treatment area. Brachytherapy sources are removed after treatment or left in place if the isotope half-life ($t_{1/2}$) is short enough to decay to a stable state with no side effects from the implant.

Therapeutic radionuclides used in vivo undergo α emission, β^- emission, or Auger emission. Their use in therapy is dependent on the desired treatment. Preferential characteristics for a radionuclide for therapeutic use include a reasonable $t_{1/2}$ for administration, high radiotoxicity within target sites with minimal damage to nearby healthy tissue, and the ease of radiolabeling to a targeting vector.

Diagnostic radionuclides are frequently used in combination with therapeutic radionuclides to monitor the drug post-administration and distribution to the target location [2]. The properties of diagnostic radionuclides enable their use in Single Photon Emission Computed Tomography (SPECT) or Positron Emission Tomography (PET). Numerous radionuclides have demonstrated promise across a spectrum of theranostic applications, each with advantages based on specific characteristics. Among the list of candidates, ^{117m}Sn, an Auger-emitter,

is of particular interest due to its emission of both low-energy conversion electrons (CE) from 126.82(3) keV to 155.88(3) keV leading to an Auger electron cascade, as well as its characteristic decay gamma at 158.56 (2) keV [3].

The emitted CE and Auger electrons have a sub-mm range in tissue [4], resulting in a locacalized dose to affected tissue. In addition, the 158.56 (2) keV characteristic decay gamma from ^{117m}Sn is comparable to the 140.511(1) keV decay gamma from ^{99m}Tc, a standard for medical imaging [5, 6, 7] as seen in a study by Krishnamurthy *et al.*[8].

These unique characteristics make ^{117m}Sn an appealing radionuclide for simultaneous therapeutic and diagnostic use. Similarly, ^{119}Sb produces CE and Auger electrons in the range of 19.405(8) keV to 22.986(8) keV [9], providing even higher precision dose deposition with a range of less than 10 µm.

However, due to the short half life of ^{119}Sb, practical clinical applications require an isotope generator — in this case, ^{119m}Te. ^{119}Sb is the progeny isotope of ^{119m}Te; as is the case with ^{99}Mo and ^{99m}Tc, the progeny isotope can be chemically separated from its longer-lived parent isotope on site. Therefore, commercial use of ^{119}Sb can be facilitated with a ^{119m}Te generator. This work seeks to demonstrate a production pathway for these isotopes for pre-clinical and clinical trials with the goal of informing radiopharmaceutical treatments and large-scale commercial production.

Charged Particle Reaction Modeling

Experimental cross sections were measured for ^{nat}Sb (p,x) ^{117m}Sn and ^{nat}Sb (p,x) ^{119m}Te, along with 24 additional cross section measurements (14 independent and 10 cumulative) for ^{nat}Sb (p,x) reactions. In addition to expanding the experimental dataset for these Auger-emitting radionuclides, the additional ^{nat}Sb(p,x) channels present an opportunity to better understand charged particle reaction modeling. Expanding the database of charged particle reactions and improving reaction models facilitates advancements for medical radionuclide production and the broader nuclear data community.

Aside from radionuclide production, data accuracy and comprehensive theoretical reaction models extend to other applications of nuclear data, including astrophysics, next-generation reactor design, nuclear structure, and nonproliferation. There is a wealth of data from prior experiments. However, the nuclear data evaluation process from experimental results through evaluation and validation is complex as illustrated by the nuclear data pipeline [10] in Figure 1.1.

Data accuracy depends on experimental techniques and the nuclear data available at the time. The lack of accurate evaluated data affects nuclear reaction models, which can cause a chain reaction that results in a lack of confidence in these models. The further cascade can result in both personal and financial risks. For this reason, this research provides the nuclear data, including reaction thresholds, $t_{1/2}$, and decay gammas available at present that were used for analysis.

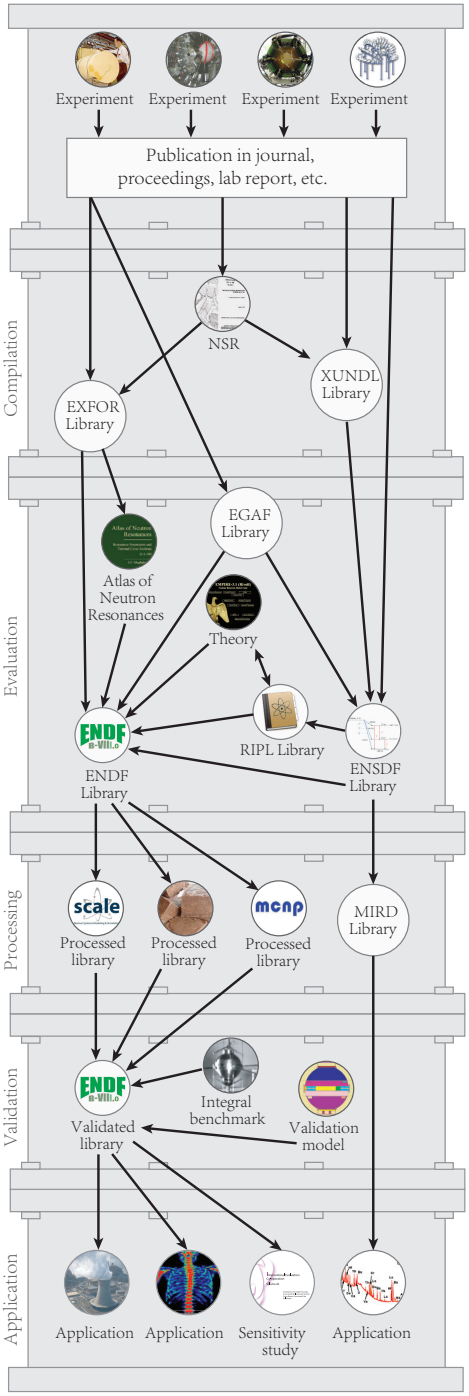

Figure 1.1: The Nuclear Data Pipeline [10], illustrating the steps from experimental results, compilation, evaluation, processing, validation, and finally to application.

1.2 Results

Stacked target measurements were performed at Lawrence Berkeley National Laboratory (LBNL), Los Alamos National Laboratory (LANL), and Brookhaven National Laboratory (BNL), covering an incident proton energy range up to 200 MeV. In addition to the two isotopes of interest, 24 cross sections for ^{nat}Sb(p,x) reactions are presented. Experimental cross section measurements for ^{nat}Nb(p,x) reactions are also provided. The inclusion of ^{nat}Nb foils was motivated by the need for experimental data for the ^{nat}Nb(p,4n)^{90}Mo reaction, a proposed proton-induced monitor standard [11]. The appendices of this document provide an additional 25 cross section measurements for proton-induced reactions on ^{nat}Nb (6 independent and 19 cumulative), 20 cross section measurements for ^{nat}Cu(p,x) reactions (6 independent and 14 cumulative), and 8 cross section measurements for ^{nat}Ti(p,x) reactions (2 independent and 6 cumulative).

A comprehensive dataset covering energies up to 200 MeV and up to 43 data points per reaction channel provided a valuable opportunity to compare experimental results to theoretical reaction models. Building on the work of Fox *et al.* [12, 13], a systematic adjustment to level density, pre-equilibrium, and neutron optical potential parameters in TALYS 1.95 was performed. The phenomenological Back-shifted Fermi Gas level density model provided the best fit for experimental data. Adjustments to the spin cut-off parameter improved the isomer to ground state production ratio in neighboring odd-A isotopes – ^{119}Te and ^{121}Te, with ^{123m}Te used for validation. These isotopes are of interest due to their long-lived, low excitation, high-spin isomers ($J^\pi = 11/2^-$) compared to their low-spin ($J^\pi = 1/2^+$) ground states. A significant truncation in angular distribution was required for population of these levels as observed by Rodrigo *et al.* [14].

Pre-equilibrium transition rates in the two-component exciton model were both globally adjusted as well as multiplicative factors for residual nucleon-nucleon interactions. Further adjustments to the imaginary volume term of the neutron optical potential model also improved fit. A final set of parameter inputs for TALYS 1.95 is provided based on qualitative and quantitative analysis, carefully considering the underlying physical implications associated with adjusting each parameter.

1.3 Scope of Dissertation

This dissertation focuses on the five experimental results from LBNL, LANL, and BNL for the production of the medical radioisotope ^{117m}Sn and the isotope generator for ^{119}Sb, ^{119m}Te via proton bombardment on ^{nat}Sb targets.

Chapter 2 provides an overview on the stacked target experiments at each location as well as detector setup. Full details are listed in Appendix A.

Chapter 3 discusses the methodology for analyzing stacked target experiments including variance minimization through monitor reactions at each location to determine cross section measurements.

Chapter 4 leverages this experimental dataset in comparison to theoretical predictions from TALYS 1.95, a nuclear reaction modeling program. This section discusses various parameters and optimal adjustments. Full details are listed in Appendices E, F, and G.

Chapter 5 discusses the ideal production energy via ^{nat}Sb(p,x) to maximize yield with minimal contaminants. Beyond the basic science, a crucial component is a feasible production pathway, both economically and logistically, for the radionuclides [15]. This section reviews the considerations in establishing a facility for radionuclide production and the regulatory requirements in brief.

Chapter 2

Experimental Method

The experiments detailed in this work were conducted at the Lawrence Berkeley National Laboratory (LBNL) 88-Inch Cyclotron (88") [16] for $E_p < 55\,MeV$, the Los Alamos National Laboratory (LANL) Isotope Production Facility (IPF) for $E_p < 100\,MeV$ and the Brookhaven National Laboratory (BNL) Brookhaven Linac Isotope Producer (BLIP) for $E_p < 200\,MeV$.

2.1 Stacked Target Design:

Experiments at each facility utilized a stacked target measurement design [17, 11, 18, 19, 12, 13]. Stacked target experiments offer the advantage of measuring multiple cross section data points across a range of energies with a single irradiation. The thickness of the target stack leads to uncertainty due to range straggling and existing limitations in stopping power calculations. This is mitigated through the use of monitor foils throughout the stack and nominally varying the density of target materials to reproduce monitor reaction cross sections. ^{nat}Sb target foils were used along with ^{nat}Cu and ^{nat}Ti monitor foils for proton-induced reactions as recognized by the IAEA [20]. This procedure of calculating and minimizing uncertainty is discussed in section 3.3. Several sets of target and monitor foils were stacked for each measurement, separated by thicker degrader foils to reduce the beam energy for each subsequent target foil. The following sections describe the setup at each experimental facility. Target stack details are in Tables A.1-A.5.

In addition to calculations for radionuclide production via ^{nat}Sb(p,x), ^{nat}Nb foils were included in several measurements as a contribution to previous work by the TREND group. This research is motivated by the characterization of the ^{nat}Nb(p,4n)^{90}Mo reaction channel. ^{nat}Nb(p,4n)^{90}Mo is a clean reaction, as it can only be produced via an independent (p,4n) reaction. It has a significant $t_{1/2}$ ($5.67\,(5)\,h$[21]) for post-irradiation measurements. A basic pictogram of this setup is shown in Figure 2.1 The detailed characterization of this potential monitor reaction requires an extensive dataset. Results for ^{nat}Nb(p,4n)^{90}Mo, as well as other ^{nat}Nb(p,x) reactions from this work, is detailed in Appendix J.

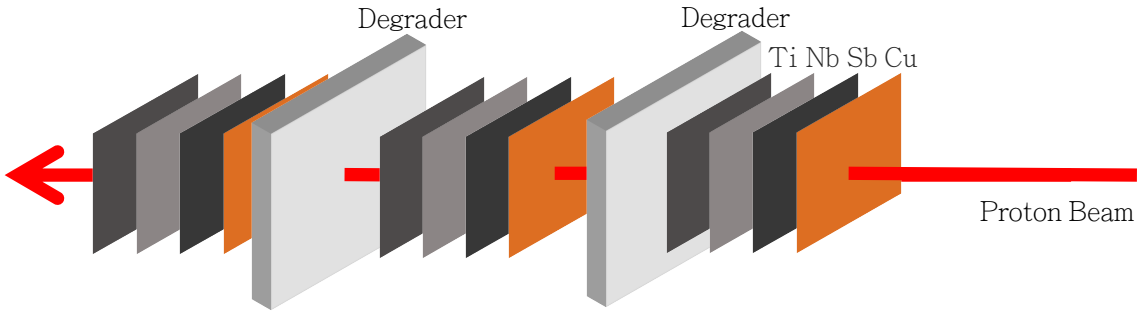

Figure 2.1: Stacked target foil packs with degraders between each compartment

Irradiation at Lawrence Berkeley National Laboratory (2020):

Two measurements were conducted in 2020 at LBNL. The first experiment utilized a 55 MeV incident proton beam, and the second experiment used a 35 MeV incident proton beam. The capability to fine-tune incident particle energy at LBNL's 88" Cyclotron is in contrast to the experiments conducted at LANL's IPF and BNL's BLIP. This flexibility reduces uncertainties that arise from range straggling and secondary neutron production associated with thick degraders at other facilities. However, the downside is that a single experiment cannot cover as broad of an energy range as other facilities. The LBNL irradiations covered an energy range from threshold production of the radionuclides of interest through the co-production of potential contaminant isotopes.

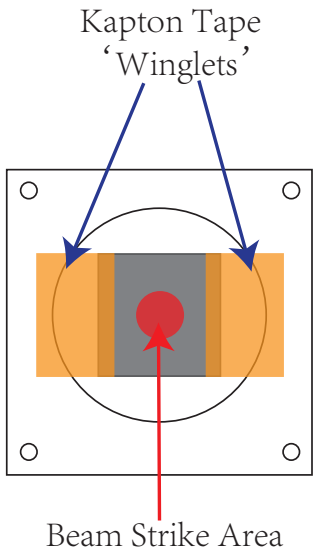

Figure 2.2: A representative diagram of Kapton 'winglet' placement and beam strike area on a foil.

Each stack was comprised of 10 of each: 25 µm ^{nat}Cu (99.95%, Lot #300711914 from Goodfellow Cambridge Ltd., Huntingdon PE29 6WR United Kingdom), 25 µm ^{nat}Ti (99.6+%, Lot #300711931 from Goodfellow Cambridge Ltd.), 25 µm ^{nat}Nb foils (99.8%, Lot # T23A035 from Alfa Aesar, Ward Hill, MA 01835 USA) and 25 µm ^{nat}Sb on a 25 µm Permanent Polyester backing with 25 µm Bostick 1430 adhesive layer (95+%, Lot #300858965, from Goodfellow Cambridge Ltd.). The adopted value of 95% ^{nat}Sb purity was based on Goodfellow XRF results, utilizing a Fischerscope X-RAY XDV-SDD spectrometer. Target foils were cut to 2.5 cm x 2.5 cm in size and sanitized with isopropyl alcohol. Foils were characterized by taking four measurements each of length and width with digital calipers (Mitutoyo America Corp.). Foil thickness was gauged using a digital

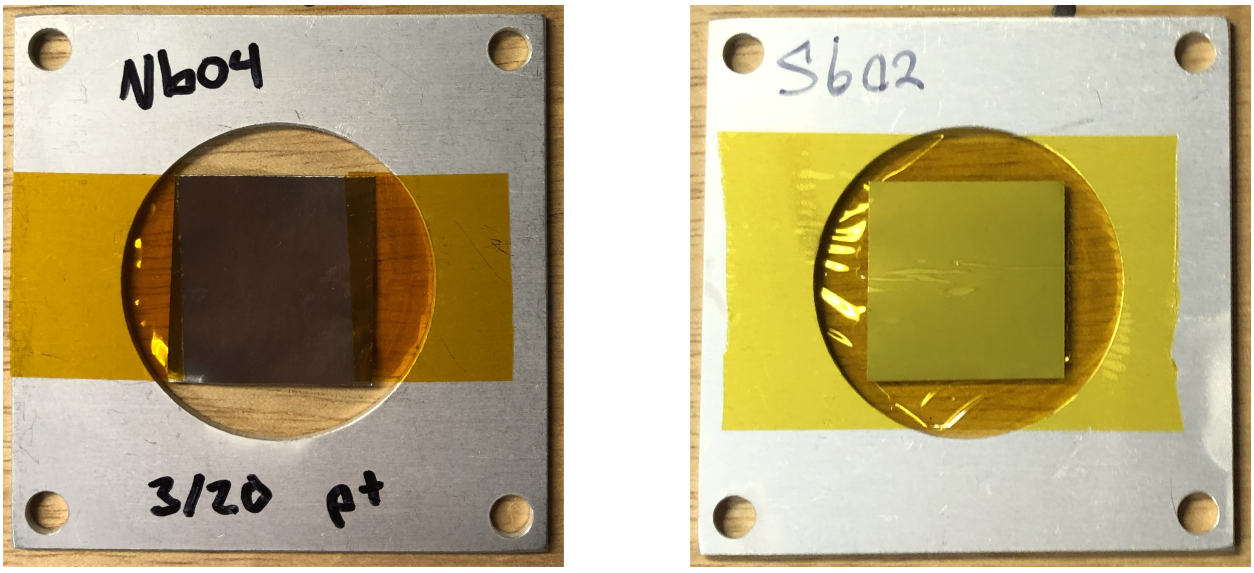

Figure 2.3: Representative ^{nat}Nb and ^{nat}Sb foils mounted prior to irradiation.

micrometer (Mitutoyo America Corp.). The mass of the foils was measured with a 0.1 mg precision Mettler Toledo AL204 analytical balance.

^{nat}Ti, ^{nat}Cu, and ^{nat}Nb foils were mounted on frames using Kapton polyimide tape with 12 µm silicone adhesive on 13 µm polyimide backing. The Kapton tape "winglets" were placed outside the incident beam area, as illustrated in Figure 2.2.

^{nat}Sb foils were encased in Kapton to prevent loss of target material and dispersible contamination. An example of the different foil mounts is shown in Figure 2.3.

Each irradiation stack included ten compartments, separated by ^{nat}Al degraders. Each compartment included a target ^{nat}Sb foil along with ^{nat}Cu and ^{nat}Ti monitor foils. The 55 MeV run included ^{nat}Nb foils as well. ^{nat}Al degraders decreased proton energy between each compartment, providing ^{nat}Sb(p,x) cross section measurements across an energy range with a single irradiation. Stainless steel plates were placed in the front and back of each stack to assess the beam profile.

The LBNL stacks were loaded into the beam box seen in Figure 2.4, machined from 6061 aluminum alloy. The beam box was mounted onto the electrically-isolated Cave 0 beamline[16] and included a clamp-on water plate cooling line. Further details on the design and construction of the beam box are discussed in Voyles *et al.*[19].

The first irradiation at LBNL was scheduled to be a 1–hour irradiation with 200 nA nominal current. Shortly into the run, the beam current was inconsistent. The foils were irradiated intermittently for 8961 s, with 4670 s of beam on target. The second irradiation at 35 MeV had an average current of 150 nA, with the beam remaining consistent for the duration of the 3595 s run. Full details of the stack designs for these irradiations can be found in Table A.1 and Table A.2 of Appendix A.

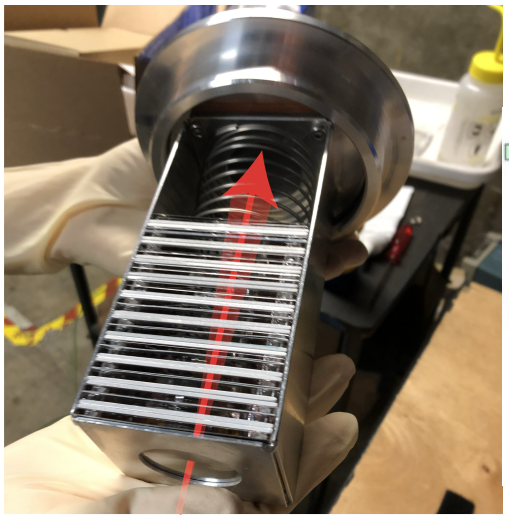

Figure 2.4: The target box used for LBNL irradiations, with the red arrow indicating the beam direction.

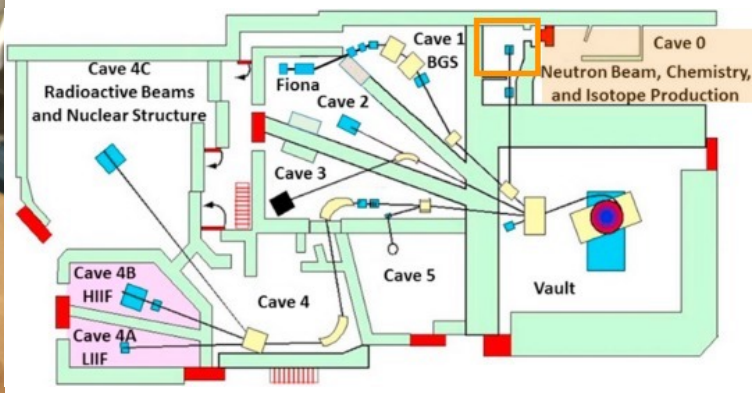

Figure 2.5: Diagram of the 88" cyclotron [16].

Post-irradiation, the stainless steel plates at the front and rear of the stack were exposed with radiochromic film (Gafchromic EBT3). Based on analysis of the films, the beam was within the boundaries of the foils for both irradiations. A sample analysis of the profile is visualized in Figure 2.6.

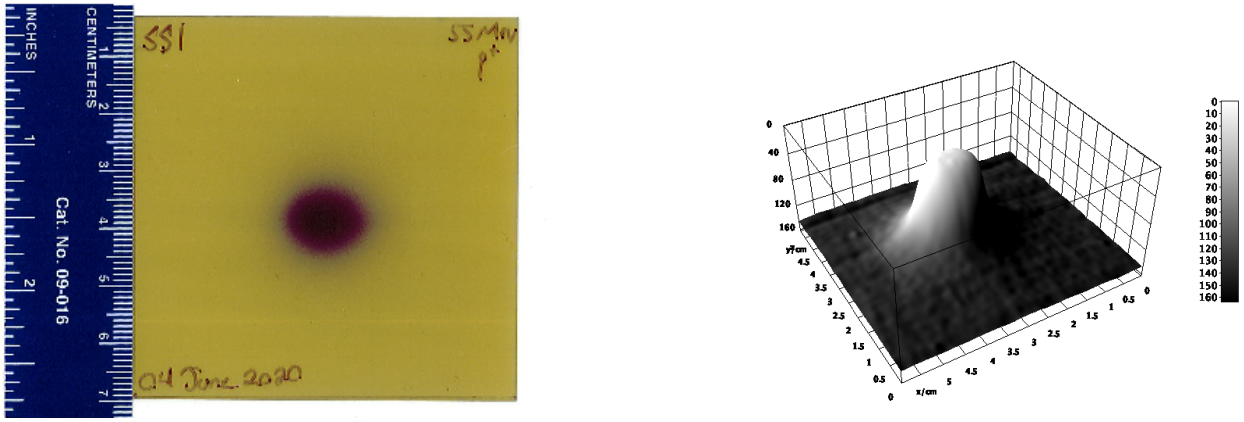

Figure 2.6: Gafchromic film exposed to Stainless Steel plate and beam profile assessment.

Irradiation at Los Alamos National Laboratory

The LANL stack consisted of 10 of each: 25 µm ^{nat}Cu, 25 µm ^{nat}Ti, 25 µm ^{nat}Nb foils and 25 µm ^{nat}Sb targets on polyester backings, all from the same batches and prepared as described in section 2.1. The stack included 9 ^{nat}Al degraders and utilized stainless steel plates at the front and back of the stack to monitor the beam profile as described above in section 2.1. Detailed characterization of degraders, schematics of the beam box, and upstream beamline components is available for reference [22][12].

Foils were mounted on 1 mm acrylic frames. Each set of frames in an energy compartment was held together with baling wire for removal via remote manipulators in the IPF hot cell post-irradiation. The box with foil packs in place can be seen in Figure 2.7. The energy loss

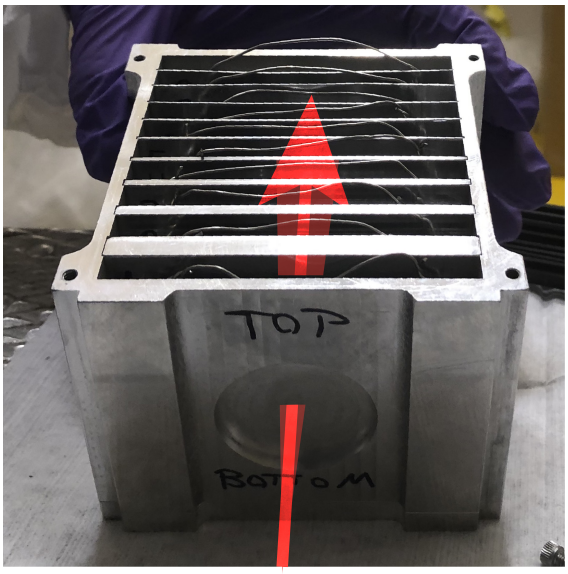

Figure 2.7: The target box used for LANL irradiations. The red arrow shows the beam direction as it enters through a 0.411 mm thick, 4.58 cm diameter circular aluminum window.

in the upstream materials from the beam box, as well as the window, were taken into account in calculating the incident proton energy [22, 12]. The stack was irradiated for 3594 s with a proton beam of 200 nA nominal current. The beam current, measured using an inductive pickup, was stable for the duration of the irradiation. Full details of the stack design are provided in Table A.4 of Appendix A.

Irradiation at Brookhaven National Laboratory

The BNL stack consisted of 7 of each: 25 µm ^{nat}Cu and 25 µm ^{nat}Nb foils, and 25 µm ^{nat}Sb targets on polyester backings from the batches described in section 2.1. The stack included 6 ^{nat}Cu degraders and utilized stainless steel plates at the front and back of the stack to map

out a beam profile. The foils, degraders, and stainless steel plates were characterized in the same manner as outlined in section 2.1.

Foils were mounted on 0.5mm thickness acrylic frames. ^{nat}Ti was excluded from this irradiation as IAEA monitor reactions lack evaluated data for ^{nat}Ti above 100 MeV [20]. As with the LANL irradiation, each set of frames in an energy compartment was held together with baling wire to facilitate the removal after irradiation. The target box with foil packs in place can be seen in Figure 2.8. The stack was irradiated for 7362 s with an incident 200 MeV

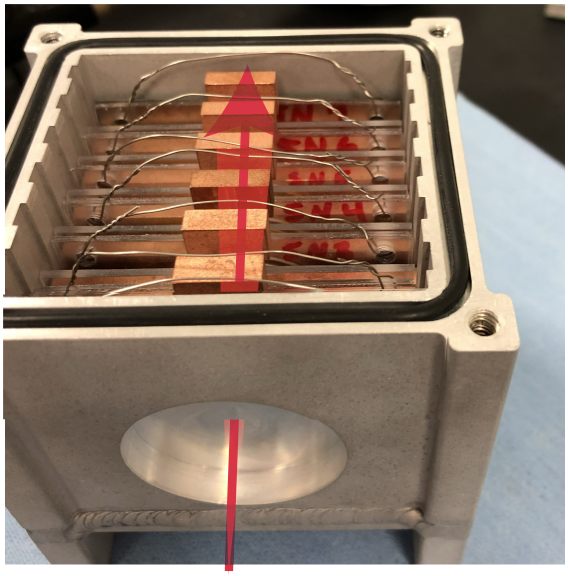

Figure 2.8: The target box used for BNL irradiations. The red arrow shows the trajectory of the beam as it enters the front of the beam box through the 0.908 mm aluminum window, as illustrated.

proton beam at 150 nA nominal current. The beam current, measured using toroidal beam transformers, was stable for the duration of the irradiation. Full details of the stack design are provided in Table A.5 of Appendix A.

Irradiation at Lawrence Berkeley National Laboratory (2022):

Due to the number of activation products with characteristic decay gammas near the 158.6 keV decay gamma energy of ^{117m}Sn [3], an additional irradiation was performed, in which reaction products were assayed using a Low-Energy Photon Spectrometer (LEPS) High-Purity Germanium (HPGe) detector. The isotopes with decay gammas in this energy region can be seen in Table 3.2. This subsequent run was performed to further quantify radiopurity of ^{117m}Sn for medical applications. The 55 MeV energy region includes the threshold for production of ^{113}Sn, a long-lived ($t_{1/2}$=115.09±0.03 days) contaminant (Table C.1).

The 2022 LBNL irradiation consisted of 6 of each: 25 µm ^{nat}Cu (99.95%, Lot #300958705 from Goodfellow Cambridge Ltd.), 25 µm ^{nat}Ti (99.6+%, Lot #300942464 from Goodfellow

Cambridge Ltd.), and 25 µm ^{nat}Sb targets on polyester backings, all from the same batches and prepared as described in section 2.1. The stack utilized ^{nat}Al degraders and stainless steel plates at the front and back of the stack to map out a beam profile as described above. The foils and stainless steel plates were characterized and mounted to frames in the same manner as outlined in section 2.1. The stack was irradiated for 3511 s with an incident 55 MeV proton beam of 150 nA nominal current. The beam current was stable for the duration of the irradiation. Full details of the stack design are provided in Table A.3 of Appendix A.

2.2 Gamma Decay Spectroscopy:

The activated foils were counted post-irradiation at each laboratory. Below is a description of the detectors, distances, locations, and time frames for each of these assays.

Counting at Lawrence Berkeley National Lab (2020):

Four ORTEC IDM-200-V HPGe detectors and one ORTEC GMX series (model GMX-50220-S) HPGe detector were set up for counting. After the 55 MeV irradiation, counting began within roughly 25 min., following the end-of-bombardment (EoB). Initial counting focused on measuring the short-lived ^{nat}Cu (p,x) ^{63}Zn monitor reaction ($t_{1/2} = 38.47 \pm 0.05$ m [23]), as well as several short-lived products on the ^{nat}Sb foils. The 35 MeV irradiation took place approximately 24 hours after the 55 MeV irradiation, with assay starting within approximately 25 minutes of EoB. Foils were counted over 40 days to allow for complete quantification of long-lived reaction products.

Counting at Los Alamos National Lab:

Foils were removed and placed on detectors within 3 hours following EoB in the IPF high bay using one ORTEC IDM-200-V HPGe detector and one ORTEC GEM p-type coaxial HPGe detector (model GEM20P-PLUS). Due to the time required to remove foils, limited data was acquired for the short-lived ^{nat}Cu(p,x)^{63}Zn monitor reaction. However, several other monitor reactions were measured, providing a robust dataset for monitor reactions. Foils were counted at IPF for 3 days before being relocated to the LANL TA-48 Countroom, where counting continued for 14 days. The samples were then shipped to LBNL to continue data collection on the detectors discussed in 2.2. This facilitated the assay of isotopes with $t_{1/2}$ exceeding 1-2 weeks. Counting continued at LBNL for approximately 3 more weeks, with additional data taken roughly 10 months later to better characterize the long-lived ^{nat}Cu (p,x) ^{56}Co and ^{nat}Cu (p,x) ^{58}Co monitor reactions.

Counting at Brookhaven National Laboratory:

Foils were removed and placed on detectors within 2 hours following EoB. Initial measurements took place at BLIP for 2 hours in order to obtain at least one spectrum for each foil. Detector setup consisted of an ORTEC GEM p-type coaxial HPGe detector (model GEM25P4-70) as well as one ORTEC IDM-200-V HPGe detector The foils and the IDM were then moved to Building 801, where an ORTEC POPTOP detector and an ORTEC tran-SPEC detector were used. Foils were counted at this facility for approximately 4 weeks, at which time the foils were shipped to LBNL to continue data collection on the detectors discussed in section 2.2.

Counting at Lawrence Berkeley National Laboratory (2022):

One ORTEC IDM-200-V HPGe detector, one ORTEC GMX series (model GMX-50220-S) HPGe detector, one ORTEC GLP-36360/13-P-S LEPS HPGe detector, and one ORTEC GLP-32340/13P4-SMN LEPS HPGe detector were set up for counting.

Foils were removed in less than 15 minutes after EoB to begin counting. Initial counting was based on capturing the short-lived ^{nat}Cu(p,x)^{63}Zn monitor reaction, as well as several short-lived residual products from ^{nat}Sb(p,x) reactions. The foils were assayed for approximately 2 months, with additional measurements taken 1 year later to measure the ^{123}Te isomer.

Chapter 3

Data Analysis

3.1 Detector Calibrations

Gamma spectroscopy requires calibration from well-characterized sources for both energy and detector efficiency as a function of incident photon energy. This is vital to calculating residual product activity and, ultimately, the cross section and yield of the observed residual nuclides. The calibrations performed for each experiment are detailed below. Each detector was calibrated at a range of distances to reduce dead time during experimental measurements on activated foils— preferably below 10% when possible.

LBNL 2020 Detector Calibration

Detectors were calibrated with ^{137}Cs, ^{133}Ba, and ^{152}Eu sources (Eckert & Ziegler, Valencia, CA 91355 USA) at distances ranging from 15–80 cm from the detector face. A sample calibration spectrum is shown in Figure 3.1

LANL Detector Calibration:

Detectors at IPF were calibrated with ^{137}Cs, ^{60}Co, ^{133}Ba, ^{152}Eu, ^{226}Ra, ^{210}Po, ^{22}Na, and ^{241}Am sources (Eckert & Ziegler) at distances ranging from 25–65 cm. LANL staff provided calibrations for measurements in the Countroom.

BNL Detector Calibration:

Detectors at both BLIP and the Bldg. 801 were calibrated with ^{152}Eu, ^{137}Cs, ^{133}Ba, ^{60}Co, ^{226}Ra, ^{210}Pb, ^{22}Na, and ^{241}Am sources (Eckert & Ziegler) at distances ranging from 15–65 cm from the detector face.

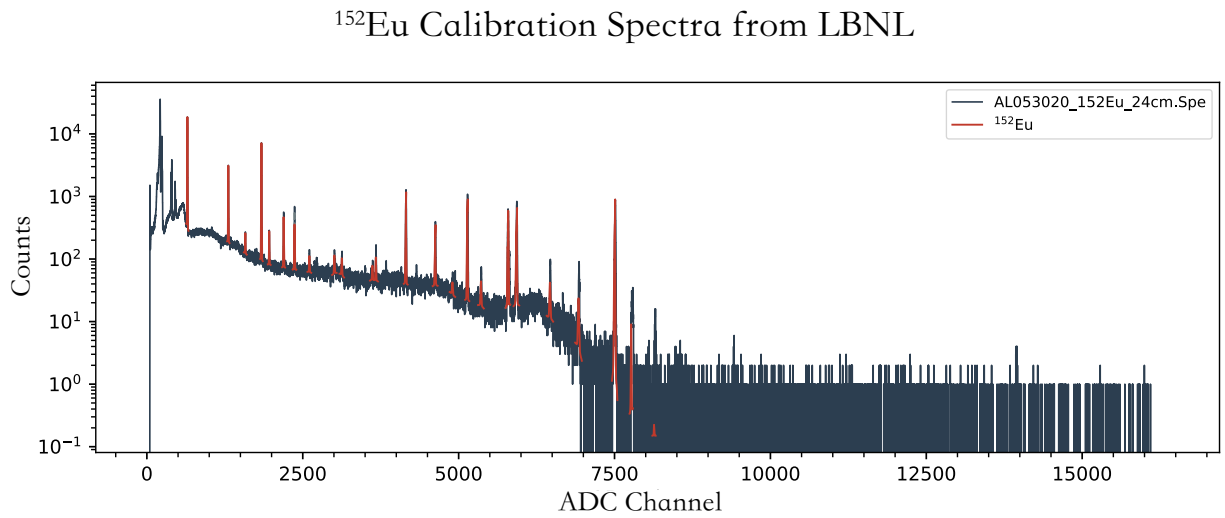

Figure 3.1: ^{152}Eu calibration spectrum.

LBNL 2022 Detector Calibration:

Detectors were calibrated with ^{137}Cs, ^{133}Ba, ^{152}Eu, ^{60}Co, ^{109}Cd, ^{57}Co, and ^{241}Am sources (Eckert & Ziegler) at distances ranging from 15–80 cm from the detector face. The additional sources used in this experiment reduced uncertainty for measurements in the sub-300 keV energy region of the LEPS detector.

3.2 Foil Activation Analysis:

Curie [24], a Python toolkit for experimental nuclear data analysis, was used for peak fitting, calibration for energy, efficiency, and resolution. Curie uses a quadratic fit for energy calibration, an automatic peak-fitting routine, and a semi-empirical formula for efficiency calibration [25]. A list of expected residual products and decay data was used to fit the gamma spectra. The characteristic decay gammas used to measure residual products from ^{nat}Sb(p,x) reactions are listed in Appendix D. Decay gammas for residual products for proton-induced reactions on ^{nat}Ti, ^{nat}Cu, and ^{nat}Nb are provided in Appendix H. A sample gamma spectrum of an ^{nat}Sb foil is shown in Figure 3.2. Activity $A(t)$ for each observed product was obtained using the net counts in a spectrum by fitting the specific energy peak or peaks, factoring in decay gamma intensity, the residual product decay constant, detector efficiency, measurement time, and attenuation within the foil .

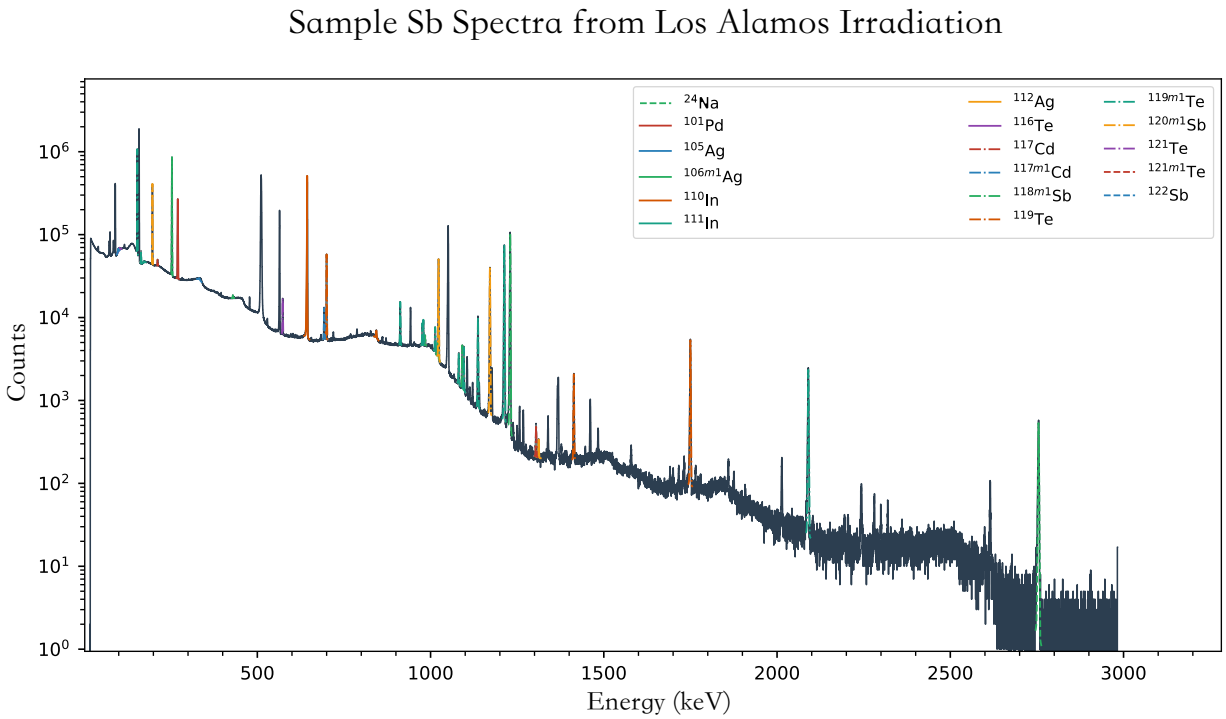

Figure 3.2: Sb spectrum taken on an ORTEC GEM20P-PLUS HPGe detector at LANL. While more products were fit here than are provided in the results, insufficient data existed to confidently publish their cross sections.

"Independent" $A(t)$ values, for channels where the residual product had no parent products feeding it, could be calculated using Equation 3.1.

$$A(t) = \frac{N_t \lambda F_{att}}{(1 - e^{-\lambda t_R}) I_\gamma \epsilon_D (t_L / t_R)} \tag{3.1}$$

$A(t)$ is the activity of the product at time t, N_t represents the net counts in a given peak in the spectra, λ is the decay constant for the product, F_{att} is a correction factor for photon attenuation, the $(1 - e^{-\lambda t_R})$ term accounts for decay over the count time, (t_R) is the count time, I_γ is gamma intensity, ϵ_D is detector efficiency as a function of energy and distance, and t_L/t_R is the ratio of the live time (t_L) to the count time (t_R) to account for detector dead time. Photon attenuation was based on data from the XCOM-Photon Cross Section Database [26]. Activities for independently produced residual products at EoB (A_0) were calculated with a fit of observable measurements of $A(t)$ using the first order Bateman equation (Equation 3.2):

$$A(t) = A_0 e^{-\lambda t} \tag{3.2}$$

If a residual product was fed by the decay of other residual nuclides, the calculated activity utilized a higher-order Bateman equation:

$$A_i(t) = \lambda_i \sum_{j=1}^{i} N_j(0) \left(\prod_{k=j}^{i-1} \frac{\lambda_k}{\lambda_k - \lambda_i} \right) e^{-\lambda_j t} \tag{3.3}$$

where i is the progeny isotope and j are parent isotopes. When possible, an independent A_0 was calculated; for complex decay chains or isotopes with a lack of measurable gammas in the decay chain, a "cumulative" value was calculated.

3.3 Characterizing Beam Current and Incident Particle Energy

Stacked target measurements inherently introduce uncertainty between calculated and actual current or energy within each compartment due to limitations in stopping power calculations and range straggling. To reduce systematic uncertainty, a technique of *variance minimization* can be applied. This established procedure can be used to determine current and energy in each bin, as described in Graves *et al.*[17], Voyles *et al.*[11, 19], Morrell *et al.*[18], and Fox *et al.*[12, 13]. The technique is designed to address uncertainty and inconsistency by treating the density of the materials in the stack as a free parameter to minimize variance between calculated current in each energy bin based on accepted IAEA monitor reaction cross section values.

The monitor reactions of interest utilized at each site are as follows:

- LBNL:
  ^{nat}Cu(p,x)^{62}Zn,^{63}Zn,^{65}Zn,^{56}Co,^{58}Co
  ^{nat}Ti(p,x)^{46}Sc, ^{48}V
- LANL:
  ^{nat}Cu(p,x)^{62}Zn,^{65}Zn,^{56}Co,^{58}Co
  ^{nat}Ti(p,x)^{46}Sc,^{48}V
- BNL:
  ^{nat}Cu(p,x)^{58}Co

^{46}Sc experimental measurements deviated from IAEA evaluated values for energies approaching 100 MeV as seen in Appendix I.5d. This was attributed to limited experimental data for evaluation at these higher energies.

The proton beam current ($I_{p,i}$) for the production of the i^{th} activity in a given monitor reaction was calculated using Equation 3.4.

$$I_{p,i} = \frac{R_i}{(\rho_N \Delta r)\tilde{\sigma}_i} \tag{3.4}$$

Here, R_i is the calculated reaction rate during the irradiation, $\tilde{\sigma_i}$ is the flux-averaged monitor cross section, and $\rho_N \Delta r$ is the areal density of the foil.

The flux-weighted average cross section ($\tilde{\sigma_i}$) for monitor reaction products depends on the broadening of the proton energy distribution. It is calculated using Equation 3.5

$$\tilde{\sigma_i} = \frac{\int \sigma_i(E)\phi(E)dE}{\int \phi(E)dE} \tag{3.5}$$

where $\sigma_i(E)$ is the IAEA recommended cross section and $\phi(E)$ is the proton energy distribution in a given foil, calculated in Curie for all stack elements using the Anderson and Ziegler methodology [27, 24].

In contrast to previous work, this analysis utilized the nominal reaction rate R in lieu of A_0 to address fluctuations in incident beam current experienced most significantly during the LBNL 55 MeV irradiation in 2020 (section 2.1). Calculated activities at EoB for shorter-lived isotopes were greatly impacted by the loss of beam as seen in the plot of $^{\text{nat}}$Cu (p,x) ^{63}Zn production during the 55 MeV run at LBNL in Figure 3.3. Here, t=0 is EoB.

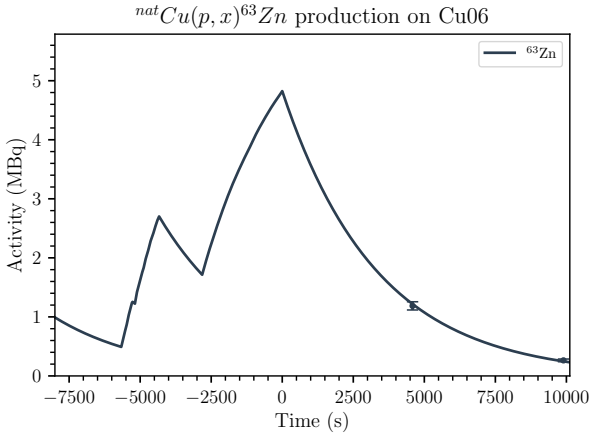

Figure 3.3: ^{63}Zn production and decay based on measured decay gammas.

The optimal value of this global multiplicative factor is calculated using a χ^2 goodness of fit test. This approach provides a more accurate quantification of particle current in each energy bin across the stack. This parameter can then be optimized with a goodness of fit test χ^2 to determine a local minimum for all monitor foils.

A further evaluation of correlated uncertainties in measurement followed the methodology of Huber *et al.*[28]. Uncertainties for monitor reactions, both within a single foil and during a single irradiation, are correlated to a certain degree. This includes the beam current measurement, foil characterization, and detector setup. Each correlated factor can be assigned a weighting factor. This introduces a covariance matrix $\mathbf{V}_{ij}$ between one monitor

reaction current calculation I_j, and the correlated uncertainty to all other monitor reactions i within an energy bin as seen in Equation 3.6.

$$\langle I \rangle = \frac{\sum_{i,j} I_j \left(\mathbf{V}_{ij}^{-1}\right)}{\sum_{i,j} \left(\mathbf{V}_{ij}^{-1}\right)} \tag{3.6}$$

The elements of the covariance matrix between different monitor reactions are calculated using Equation 3.7.

$$\mathbf{V}_{ij} = \mathrm{Cov}\left[I_i, I_j\right] = \sum_{\beta} \frac{\partial I}{\partial \beta_i} \delta_{\beta_i} \mathrm{Corr}\left[\beta_i, \beta_j\right] \delta_{\beta_j} \frac{\partial I}{\partial \beta_j} \tag{3.7}$$

Where i and j are distinct monitor reactions in an energy bin. β_i and β_j represent the correlation between the monitor reactions i and j with regards to initial activity A_0, areal density $\rho_N \Delta r$, irradiation time Δt_{irr}, decay constant λ, and the flux-weighted energy dependent cross section $\int \sigma(E) \frac{d\phi}{dE} dE$.

This work followed the assumptions of Voyles *et al.*[19] for the assumed correlation between different variables. Δt_{irr} is 100% correlated for all monitor reactions. $\rho \Delta r$ is 100% correlated for reactions in the same monitor foil and uncorrelated for reactions in different foils. λ is uncorrelated for all reactions. A_0 is mildly correlated between monitor reactions because of consistent detector setup within an individual experiment. A 30% value for mild correlation was proposed by the work of Huber *et al.*[28]. Similarly, $\int \sigma(E) \frac{d\phi}{dE} dE$ was considered mildly correlated for reactions within the same foil and uncorrelated for reactions in different foils. The correlation matrices for the various monitor reactions are in Appendix B.

Uncertainty in current $\delta_{\langle I \rangle}$ was calculated by error propagation across the individual monitor reaction measurements for each energy bin as seen in Equation 3.8.

$$\delta_{\langle I \rangle} = \sqrt{\frac{1}{\sum_{i,j} \left(\mathbf{V}_{ij}^{-1}\right)}} \tag{3.8}$$

The optimal adjustments in areal density for each experiment is shown in Figure 3.4.

IAEA monitor reactions for incident proton energies above 100 MeV is limited to a single reaction, $^{\mathrm{nat}}\mathrm{Cu}\,(\mathrm{p,x})\,^{58}\mathrm{Co}$, which resulted in a comparatively shallow minimum in reduced χ^2 for the experiment at BNL. Existing experimental data for $^{\mathrm{nat}}\mathrm{Cu}\,(\mathrm{p,x})\,^{56}\mathrm{Co}$ was leveraged as a validation check for BNL results but was not incorporated into final calculations.

A visualization of the improvement in current among the monitor reactions through adjusting the areal density in the stack is shown in Figures 3.5a, 3.5b. The application of this variance minimization technique provides the energy and flux within each compartment for $^{\mathrm{nat}}\mathrm{Sb}$ and $^{\mathrm{nat}}\mathrm{Nb}$ foils, with the LANL $^{\mathrm{nat}}\mathrm{Sb}$ energies and flux plotted in Figure 3.6. These are used to calculate the cross sections for proton-induced reactions on $^{\mathrm{nat}}\mathrm{Sb}$ foils in section 3.4.

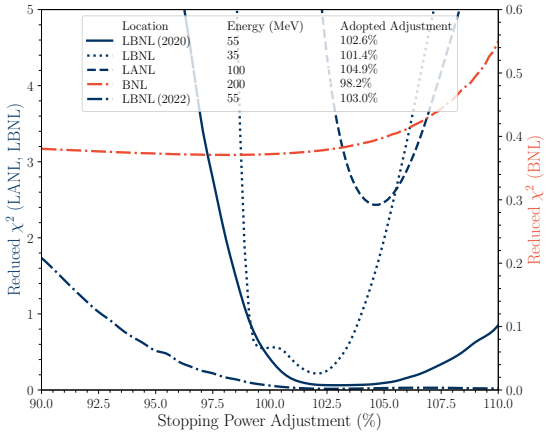

Figure 3.4: Local minima for the various experiments after exploring a ±10% change in density.

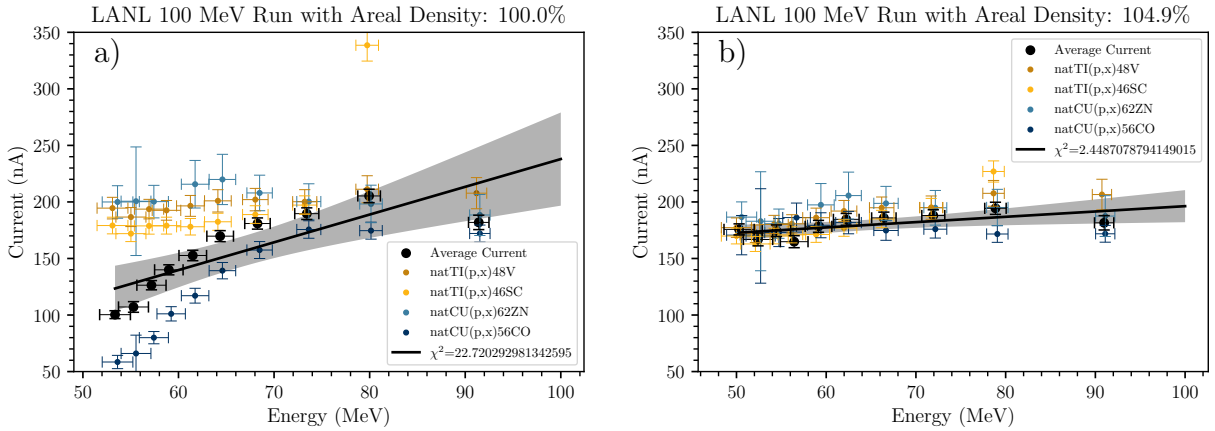

Figure 3.5: LANL calculated beam currents across all monitor reactions, a) prior to variance minimization and b) following a variance minimization areal density enhancement of 4.9%.

3.4 Cross Section Calculation:

With an optimized calculation of current and energy within each compartment, the residual product cross sections were calculated using Equation 3.9.

$$\sigma = \frac{A_0}{I(\rho\Delta r)(1 - e^{-\lambda t_{irr}})} \tag{3.9}$$

Results presented in this paper are classified as either independent *(i)*, having been directly populated through the proton-induced reaction on ^{nat}Sb, or cumulative *(c)*, where the total

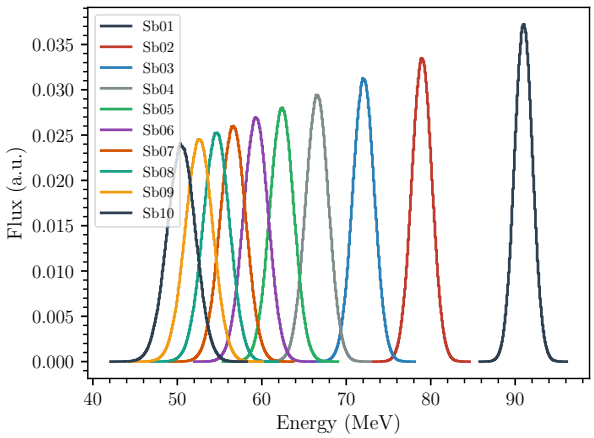

Figure 3.6: Energy and current distribution across the stack for ^{nat}Sb foils at LANL.

cross section includes direct production and contributions from the decay of co-produced isotopes.

A stacked target measurement will provide a number of cross section data points across a broad energy range. This comes with the drawback of missing short-lived isotopes and metastable states.

This is of import for this work as the isotopes of interest are both long-lived isomers. For this research, a measured isotope with direct IT decay with a half life of less than 5 minutes will be reported as *(m+g)*, or a delineation will not be made, with analysis using the total cross section for the isotope. If a metastable isomer is directly measured through a (p,x) reaction, it is marked as such *(m)*. If the ground state cross section measurement is separable from metastable isomer decay – for example if the isomer goes through EC β^+ decay, or if the ground state is separable from the isomer or any co-produced parent product, the ground state is reported individually *(g)*. In the case of an isotope with well established metastable isomers that both feed the ground state and cannot be deconvoluted through these measurement techniques, results are reported as *(m+g)*. The decay data at time of analysis is presented in Appendices D and H.

For isotopes with long-lived metastable isomeric states, as it pertains to this measurement technique, the naming convention, based on current nuclear data, specifies whether the measurement pertains to the ground state (g), the isomeric state (m), or both states (m+g) A residual product labeled as both an independent channel and as an (m+g) channel indicates that an isomeric state is present in the referenced nuclear structure data with a $t_{1/2} \leq 1s$. The independent and cumulative cross section data for the ^{nat}Sb(p,x) residual products measured in these experiments is provided in Table 3.1. Additional cross section data for residual products via proton-induced reactions on ^{nat}Nb, ^{nat}Ti, and ^{nat}Cu are available in Appendix J.

This experimental method inherently limits the number of measurements of independent

and cumulative cross sections. As incident proton energies approach 200 MeV, roughly 200 potential residual nuclei can be produced. The potential products are colorized in this section of the chart of nuclides, with the initial isotopes highlighted in green in Figure 3.7. Stacked

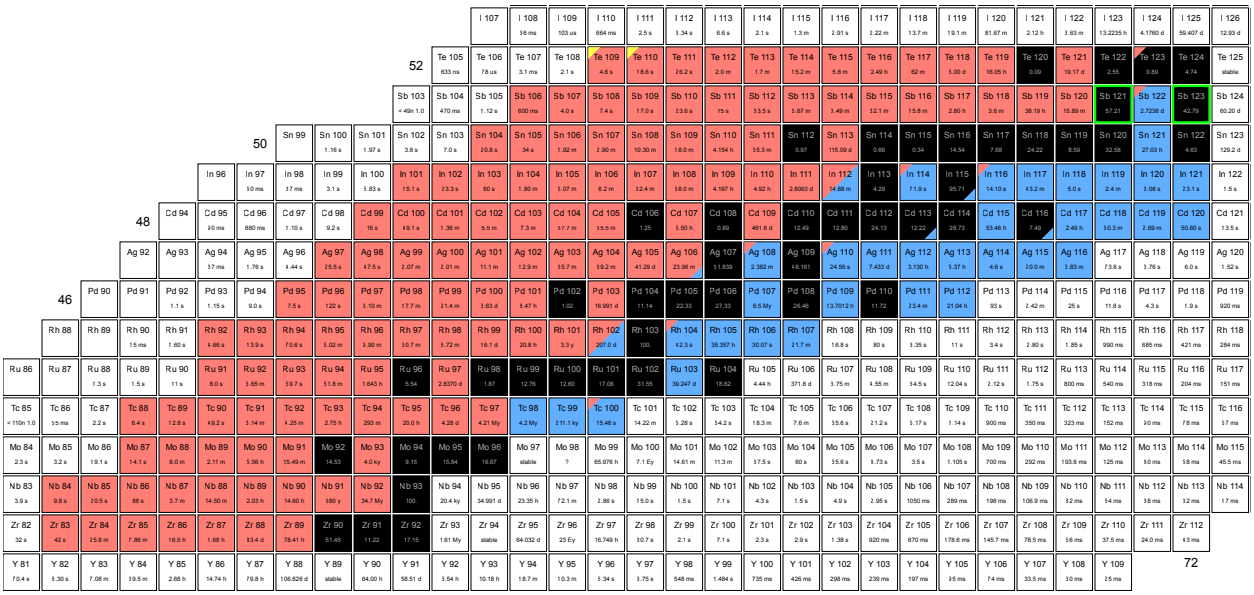

Figure 3.7: Subsection of the Chart of Nuclides, highlighting the potential residual products produced via incident protons at 200 MeV.

target measurements provide the benefit of many data points for cross sections over a wide energy range in a single irradiation, but they are limited in measuring isotopes that are either short-lived, near-stable, or lack characteristic decay gammas. Future work within the group will explore experiments via prompt, in-beam measurements to expand the database of measurements for proton-induced reactions.

3.5 Cross Section Measurements

The following section includes a short description of the 16 independent and 10 cumulative residual product cross section measurements for ^{nat}Sb(p,x) reactions. Further details on decay data and reaction thresholds are provided in Appendices D and C. The full details for measured cross sections are provided in Table 3.1. Monitor foil reaction data is available in Appendices H, J, and I.

^{89m}Nb$_{(i)}$

The independent cross section for ^{89m}Nb was measured via its 588 keV decay gamma (Figure 3.8). Measurements were limited by the high reaction threshold of 118.7 MeV and

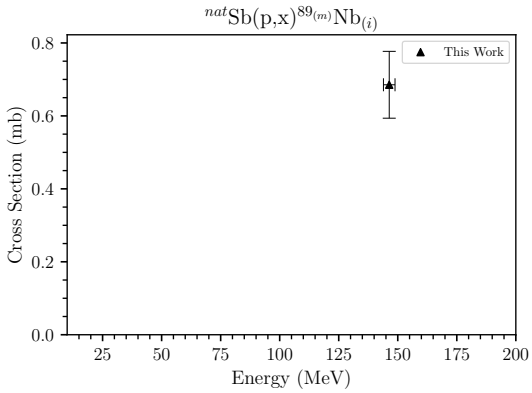

Figure 3.8: Experimental cross section measurements for ^{89m}Nb production.

small reaction cross section, compounded by a relatively short half-life ($t_{1/2} = 1.100\,(33)$ h).

^{91m}Nb$_{(c)}$

The cumulative cross section for ^{91m}Nb was measured via the 603.5 keV, 1082.6 keV, 1204.67 keV, 1790.6 keV, and 1984.6 keV decay gammas at BNL (Figure 3.9). Despite the long $t_{1/2} = 60.86\,(22)$ d, limited counting statistics introduced significant uncertainty.

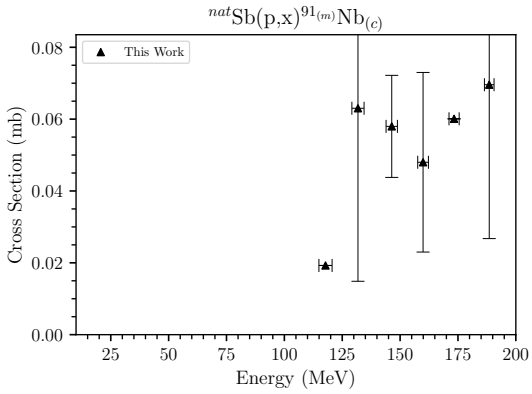

Figure 3.9: Experimental cross section measurements for ^{91m}Nb production.

^{106m}Ag$_{(i)}$

The independent cross section for ^{106m}Ag was measured via several characteristic gammas, specifically the 1527.65 keV decay gamma. This residual product has a minimum reaction

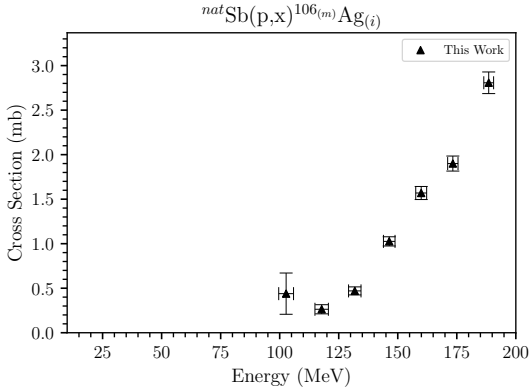

Figure 3.10: Experimental cross section measurements for ^{106m}Ag production.

threshold of 64.625 MeV (Figure 3.10).

$^{109m+g}$In$_{(c)}$

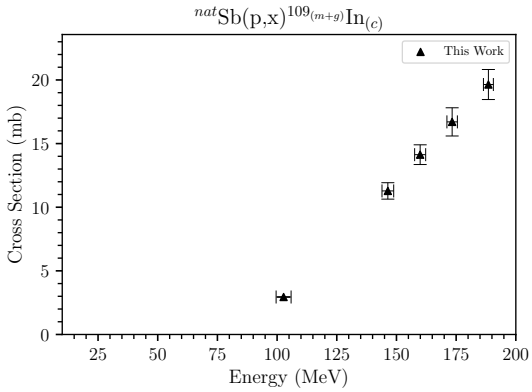

Figure 3.11: Experimental cross section measurements for $^{109m+g}$In production

The cumulative cross section for $^{109m+g}$In was measured via the 288.1 keV, 426.3 keV, 623.8 keV, 1148.5 keV, 1419 keV, and 1622.3 keV decay gammas at BNL (Figure 3.11).

$^{111m+g}$In$_{(c)}$

The cumulative cross section for $^{111m+g}$In was determined via the 171.28 keV, and 245.35 keV decay gammas at BNL and LANL. The product was not observed at LBNL (Figure 3.12).

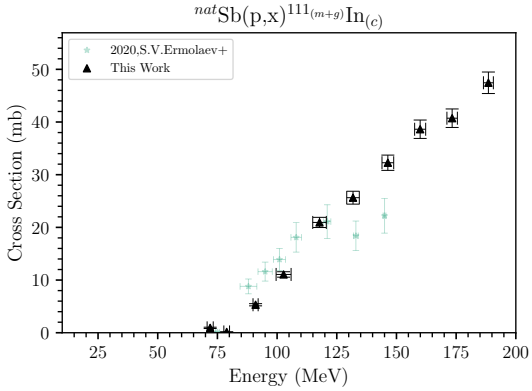

Figure 3.12: Experimental cross section measurements for^{111m+g}In production [29].

^{114m}In$_{(i)}$

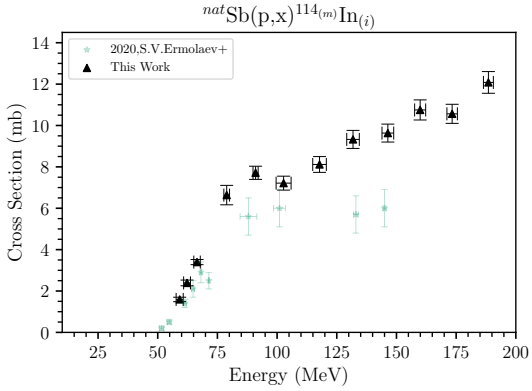

Figure 3.13: Experimental cross section measurements for ^{114m}In production [29].

^{114m}In is independently produced since both neighboring isobars, ^{114}Cd and ^{114}Sn, are stable (Figure 3.13). Production via ^{nat}Sb(p,x) reactions is influenced by competing reaction channels, including via α-breakup reactions. The reaction threshold is 28.089 MeV. Two decay gammas at 190.27 keV and 558.43 keV were employed to determine the production of ^{114m}In. The 190.27 keV decay gamma overlaps significantly with ^{97}Rh, so this decay gamma was not used for high-energy foils where the threshold energy for ^{97}Rh production is possible. Similarly, the 558.43 keV decay gamma is close to a ^{104}Cd decay gamma, so it was excluded for the first 10 hours of measurement for foils above the threshold of co-production of ^{104}Cd, allowing for ^{104}Cd to decay to background levels.

^{109g}Sn$_{(c)}$

The cumulative cross section for ^{109g}Sn was observed via the 1026.4 keV and 1464.2 keV decay gammas (Figure 3.14).

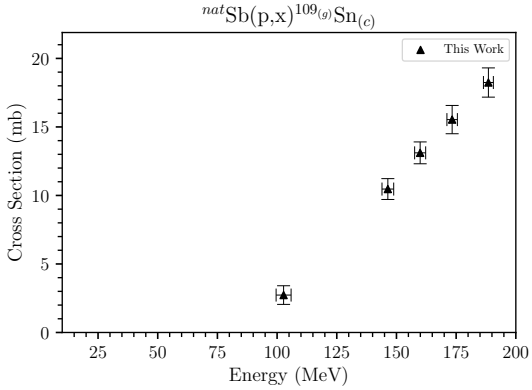

Figure 3.14: Experimental cross section measurements for ^{109g}Sn production.

^{110g}Sn$_{(c)}$

The cumulative cross section for ^{110g}Sn was measured via observation of the 280.5 keV decay gamma (Figure 3.15).

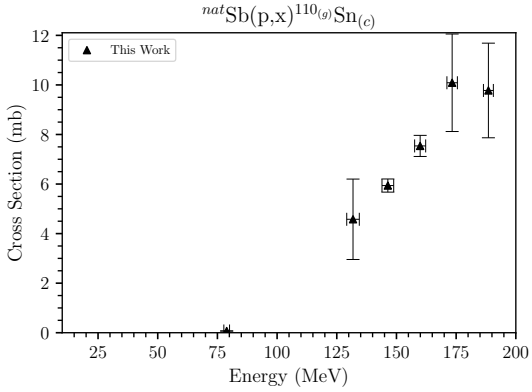

Figure 3.15: Experimental cross section measurements for ^{110g}Sn production.

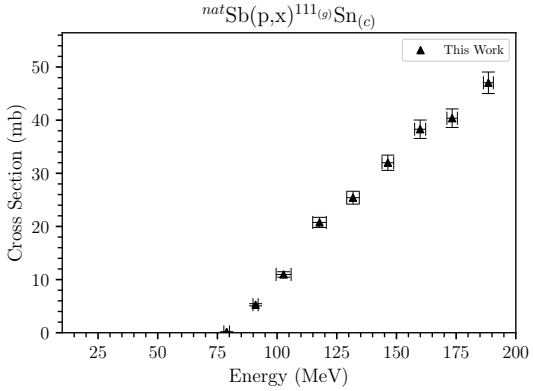

Figure 3.16: Experimental cross section measurements for ^{111g}Sn production.

^{111g}Sn$_{(c)}$

The cumulative cross section for the production of ^{111g}Sn was determined via observation of the 1610.47 keV and 1914.7 keV at LANL and BNL (Figure 3.16).

^{113m}Sn$_{(i)}$

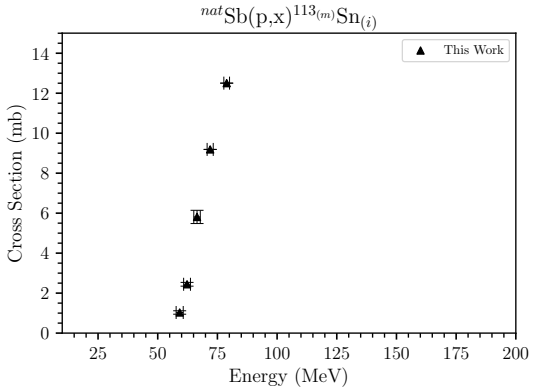

Figure 3.17: Experimental cross section measurements for ^{113m}Sn production.

^{113m}Sn was observed for foils irradiated at LANL (Figure 3.17). With a minimum reaction threshold of 37.145 MeV, a short $t_{1/2} = 21.4\,(4)$ m, and a single low energy, low-intensity gamma, it was not observed reliably at all locations or on all detectors.

$^{113m+g}Sn_{(c)}$

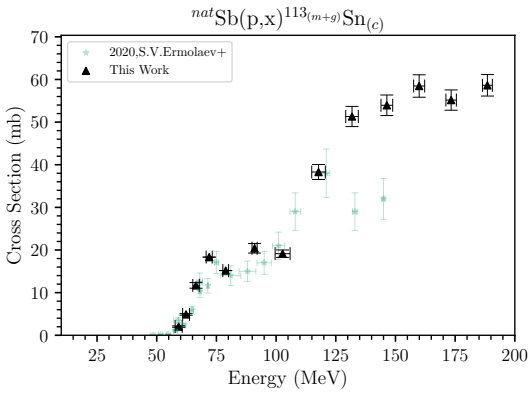

Figure 3.18: Experimental cross section measurements for $^{113m+g}$Sn production [29].

The cumulative cross section for $^{113m+g}$Sn was calculated using the 255.134 keV and 391.698 keV decay gammas at LANL and BNL (Figure 3.18). Production was not seen at LBNL energies. This is of great importance as this is a main contaminant in the production of ^{117m}Sn for theranostic use. Although the minimum reaction threshold for production is 37.145 MeV, production below 55 MeV appears to be minimal.

$^{117m}Sn_{(c)}$

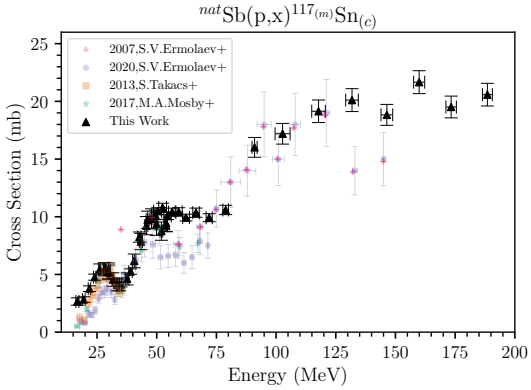

Figure 3.19: Experimental cross section measurements for ^{117m}Sn production.

The ^{117m}Sn reaction product was measured via its 158.6 keV and less intense 156.02 keV decay gammas (Figure 3.19). However, as discussed in section 3.6, it is noteworthy that there

are a significant number of potential residual products with decay gammas in this energy region. This merited the second LBNL activation measurement using a higher-resolution LEPS.

^{119m}Sn$_{(c)}$

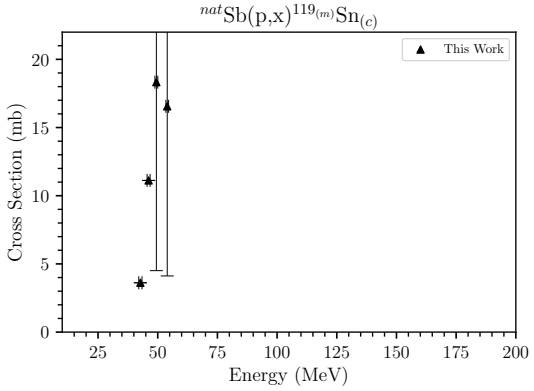

Figure 3.20: Experimental cross section measurements for ^{119m}Sn production.

The cumulative cross section for ^{119m}Sn was measured with the 23.875 keV decay gamma as seen in Figure 3.20. There are few measurements due to the low energy of this gamma – as such, it was only observed at LBNL on the LEPS detector.

^{115g}Sb$_{(c)}$

The cumulative cross section for ^{115g}Sb was measured via observation of the 489.3 keV and 497.31 keV decay gammas, seen in Figure 3.21. With $t_{1/2} = 32.1\,(3)$ m for both this isotope and the only potential progeny, ^{115}Sn being stable, only two data points were calculable.

^{116m}Sb$_{(i)}$

The isomer of ^{116}Sb, with a minimum reaction threshold of 43.876 MeV, was measured independently via the decay of ^{116}Te directly to the ground state of ^{116}Sb (Figure 3.22). Measurements for this isomer mainly utilized the 844.0 keV, 972.6 keV, and 1072.4 keV decay gammas.

^{118m}Sb$_{(i)}$

Similar to ^{116m}Sb, ^{118m}Sb was measured independently due to the decay of ^{118}Te proceeding directly to the ground state (Figure 3.23). The minimum reaction threshold for

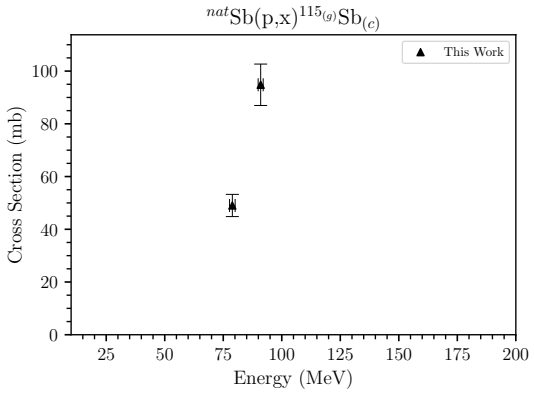

Figure 3.21: Experimental cross section measurements for ^{115g}Sb production.

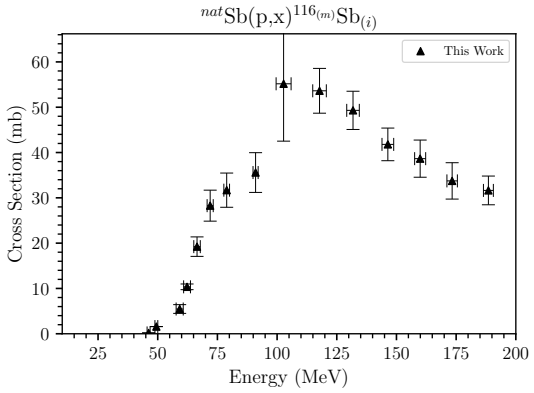

Figure 3.22: Experimental cross section measurements for ^{116m}Sb production.

production is 26.282 MeV. ^{118m}Sb shares a 1229.7 keV decay gamma with ^{118g}Sb, and due to the comparatively longer half-life of ^{118}Te ($t_{1/2}$=6.00 d), this gamma was not used. Instead, the 1050.7 keV decay transition via EC $\beta+$ to ^{118}Sn was employed. This is close in energy to ^{117m}Cd, with $t_{1/2} = 3.36\,(5)$ h, which has a 1051.7 keV gamma, but ^{117m}Cd's shorter $t_{1/2}$ and lower decay intensity facilitated measurement approximately 30 hours following EoB, as seen in Figure 3.23.

^{120m}Sb$_{(i)}$

^{120m}Sb was measured independently, with a minimum reaction threshold of 9.33 MeV, seen in Figure 3.24. It decays via EC to stable ^{120}Sn. Although the isomer shares 1171.7 keV, 1023.3 keV, and 197.3 keV decay gammas with the ground state, its $t_{1/2} = 5.76\,(2)$ d compared

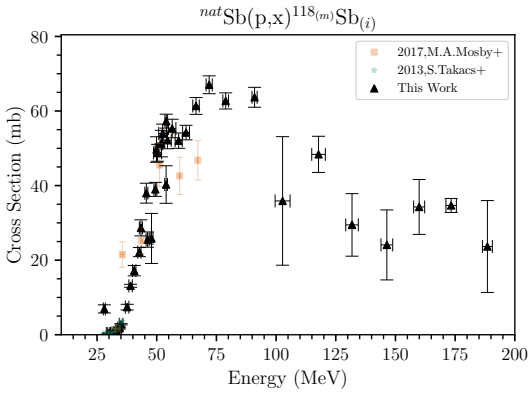

Figure 3.23: Experimental cross section measurements for ^{118m}Sb production[30, 31].

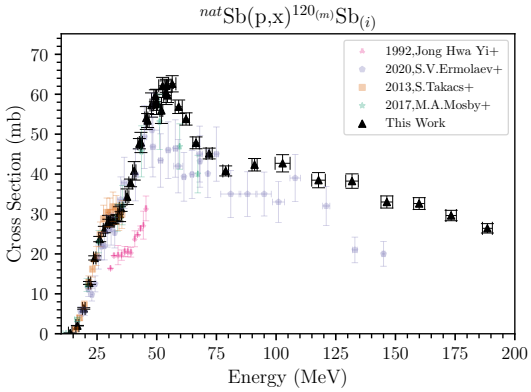

Figure 3.24: Experimental cross section measurements for ^{120m}Sb production[32, 29, 31, 30].

to the ground state ($t_{1/2} = 15.89\,(4)$ m) facilitated its measurement. This isomer was measured one day after EoB, where contributions from the ground state would be negligible. It is important to note that the higher energy points for the cross section observed at BNL have a noticeable offset in magnitude. Secondary neutron production within the stacked target materials has been posited as a contributing factor as discussed in section 3.7.

$^{122(m+g)}$Sb$_{(c)}$

The cross section for $^{122(m+g)}$Sb was observed via the 1140.7 keV decay gamma from ^{122}Sb, seen in Figure 3.25. The ^{122m}Sb isomer ($t_{1/2} = 4.191\,(3)$ m) decays entirely to the $t_{1/2} = 2.7238\,(2)$ d ground state and was not independently observed. The higher energy points for the cross section, observed in the 100 MeV and above range, demonstrate the

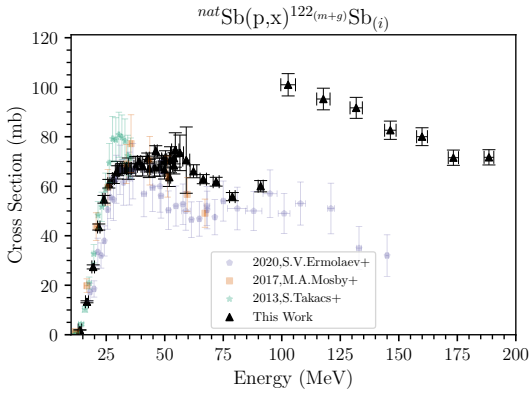

Figure 3.25: Experimental cross section measurements for $^{122(m+g)}$Sb production[29, 30, 31].

similar offset observed in ^{120m}Sb, seen in Figure 3.24 described above. This is also likely due to secondary neutron production in the stacked targets measured at BNL's BLIP via (n,γ) on ^{121}Sb or via fast neutrons on ^{123}Sb undergoing an (n,2n) reaction. This is further discussed in section 3.7.

^{116g}Te$_{(i)}$

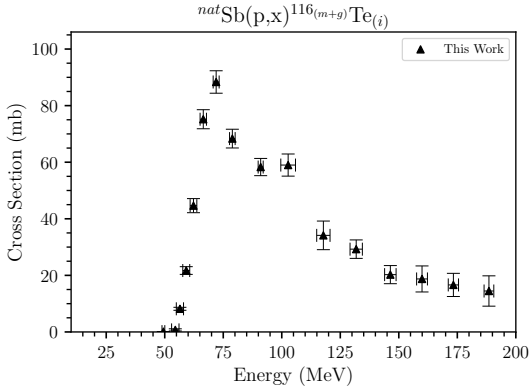

Figure 3.26: Experimental cross section measurements for ^{116g}Te production.

^{116g}Te was measured independently with characteristic gammas at 628.7 keV at lower incident proton energies. This decay gamma was excluded at higher incident proton energies due to its proximity to the 628.1 keV decay gamma of ^{102}Rh and its isomer. In certain cases, it was possible to use the 93.7 keV decay gamma along with the decay gammas of the shorter-lived progeny, ^{116}Sb at 931.8 keV and 2225 keV gamma as well. The 1293.6 keV

gamma was excluded as it is shared with the longer-lived isomeric state of ^{116}Sb, which decays solely by EC β^+. (Figure 3.26). The reaction threshold for this channel is 45.85 MeV.

^{117g}Te$_{(i)}$

The independent cross section for ^{117g}Te, with a reaction threshold of 37.882 MeV, was measured directly via the decay gammas at 719.7 keV, 886.7 keV, 923.9 keV, 1716.4 keV, and 2300 keV (Figure 3.27).

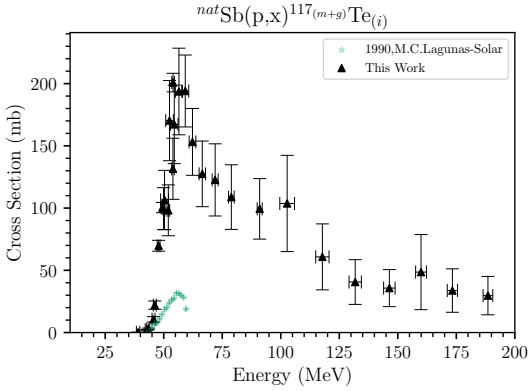

Figure 3.27: Experimental cross section measurements for ^{117g}Te production[33].

^{118g}Te$_{(i)}$

^{118g}Te could not be directly measured due to a lack of characteristic gammas, but an independent cross section was measured via the decay gamma of its progeny (Figure 3.28). ^{118g}Te decays directly to the ground state of ^{118}Sb which, with a $t_{1/2}$ =3.6 (1) m, will quickly reach secular equilibrium with ^{118g}Te. Both the isomer and ground state of ^{118}Sb share a characteristic 1229.33 (3) keV decay gamma. ^{118m}Sb decays solely through EC β^+; therefore, the 1229.33 (3) keV decay gamma can be used as a proxy for ^{118g}Te after several days, when contributions from ^{118m}Sb ($t_{1/2}$ =5.00 (2) h) were negligible This calculation method follows the work of Lagunas-Solar *et al.*[33], Yi *et al.*[32], and Miller *et al.*[34]. ^{118g}Te can serve as a generator for ^{118}Sb, a radionuclide that has been explored for Positron Emission Tomography (PET) imaging. With a minimum reaction threshold of 27.127 MeV, and a large production cross section, it is a candidate for co-production at higher incident proton energies to minimize contaminant production.

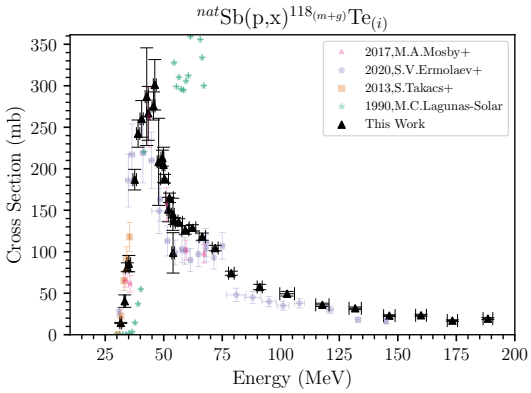

Figure 3.28: Experimental cross section measurements for ^{118g}Te production[30, 29, 31, 33].

^{119g}Te$_{(i)}$

^{119g}Te is not directly fed by its isomer. An independent cross section for the ground state, with a minimum reaction threshold of 19.501 MeV was calculated with characteristic decay gammas at 644.01 (4) keV and 699.85 (6) keV. (Figure 3.29).

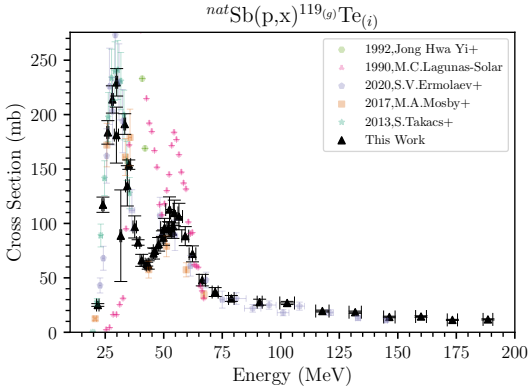

Figure 3.29: Experimental cross section measurements for ^{119g}Te production[32, 29, 31, 33].

^{119m}Te$_{(i)}$

The independent cross section for ^{119m}Te (Figure 3.30), with a minimum reaction threshold of 19.764 MeV was measured using several decay gammas. The 1048.44 (6) keV gamma was excluded from calculations for the first several days due to proximity to the 1050.69 (3) keV

decay from ^{118m}Sb. ^{119m}Te is one of the critical radionuclides of interest for this experiment as a generator for ^{119g}Sb.

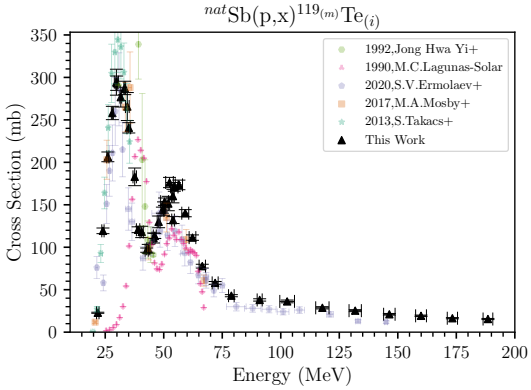

Figure 3.30: Experimental cross section measurements for ^{119m}Te production[32, 29, 31, 33, 30].

^{121g}Te$_{(i)}$

The isomer of ^{121}Te undergoes IT and populates the ground state. However, an independent cross section with a minimum reaction threshold of 1.857 MeV for the ground state ^{121g}Te (Figure 3.31) ($t_{1/2} = 19.17\,(4)$ d) was derived using the characteristic 470.472 keV and 573.139 keV decay gammas from the first few days following irradiation. ^{121g}Te does not share characteristic gammas with its isomer. Further, the much longer half-life of the isomer ($t_{1/2} = 164.2\,(8)$ d) compared to the ground state allowed for a correction for isomer feeding using measurements from the first few days following EoB.

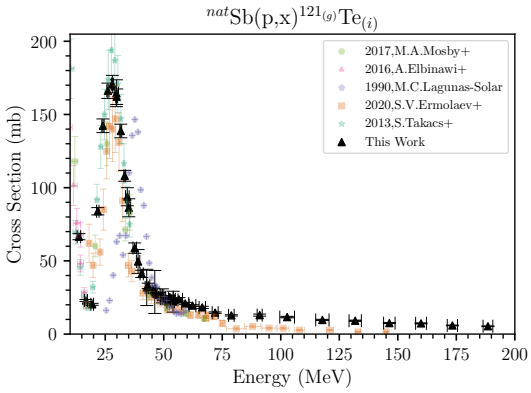

Figure 3.31: Experimental cross section measurements for ^{121g}Te production[35, 29, 31, 33].

^{121m}Te$_{(i)}$

The independent cross section measurement of ^{121m}Te, with a minimum reaction threshold energy 2.149 MeV was measured via characteristic decay gammas at 212.189 (30) keV and 1102.149 (18) keV (Figure 3.32). This product is not directly fed by any other products in this reaction, and with $t_{1/2}$=164.2 (8) d, measurement of this cross section was straightforward.

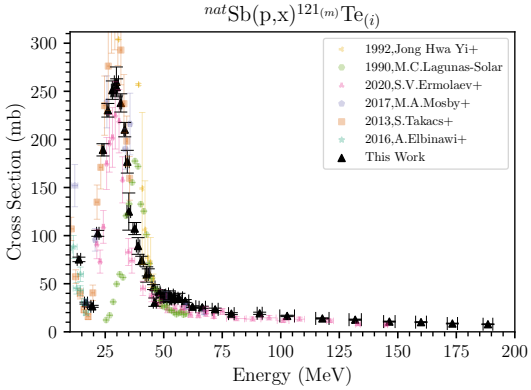

Figure 3.32: Experimental cross section measurements for ^{121m}Te production [32, 33, 29, 30, 31, 35].

^{123m}Te$_{(i)}$

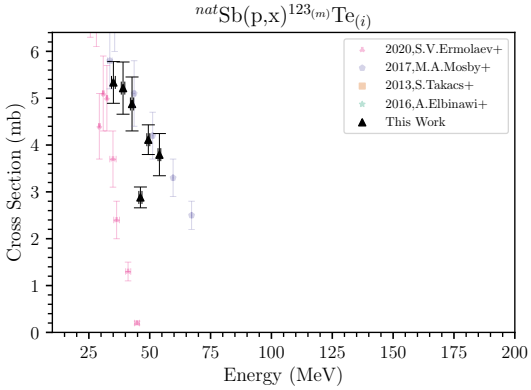

Figure 3.33: Experimental cross section measurements for ^{123m}Te production[29, 30, 31, 35].

The independent measurement of ^{123m}Te (Figure 3.33), with a minimum reaction threshold of 1.091 MeV, was measured using its characteristic 158.97 (5) keV decay gamma. This

measurement was taken approximately a year after EoB. Despite a $t_{1/2}$ of 119.7 (3) d, each foil was measured for several days. This measurement was delayed, allowing remaining potential products within the 150-160 keV range to decay. This cross section was of specific interest as a validation check for reaction modeling discussed in Section 4.4.

Compiled Sb(p,x) Cross Section Measurements

Table 3.1: Independent and cumulative cross sections measured on Sb foils

E_p (MeV)	188.511 (2077)	173.324 (2192)	159.924 (2311)	146.390 (2451)	131.800 (2633)	117.773 (2848)	102.724 (3138)
Location	BNL	BNL	BNL	BNL	BNL	BNL	BNL
$^{89m}Nb_{(i)}$				0.685 (92)			
$^{91m}Nb_{(c)}$	0.070 (43)	0.060 (64)	0.048 (25)	0.058 (14)	0.063 (48)	0.019 (39)	
$^{106m}Ag_{(i)}$	2.807 (121)	1.900 (84)	1.569 (73)	1.026 (52)	0.470 (45)	0.264 (51)	0.439 (232)
$^{109(m+g)}In_{(c)}$	19.641 (1180)	16.705 (1108)	14.129 (775)	11.280 (645)			2.945 (2984)
$^{111(m+g)}In_{(c)}$	47.448 (2042)	40.723 (1757)	38.629 (1746)	32.270 (1450)	25.635 (1223)	20.939 (966)	11.065 (517)
$^{114m}In_{(i)}$	12.082 (525)	10.564 (461)	10.752 (486)	9.633 (433)	9.327 (436)	8.116 (382)	7.214 (336)
$^{109}Sn_{(c)}$	18.242 (1067)	15.536 (1032)	13.109 (797)	10.467 (761)			2.730 (680)
$^{110}Sn_{(c)}$	9.776 (1909)	10.087 (1967)	7.538 (426)	5.939 (265)	4.578 (1623)		
$^{111}Sn_{(c)}$	47.033 (2024)	40.367 (1742)	38.292 (1731)	31.988 (1437)	25.411 (1212)	20.756 (958)	10.968 (512)
$^{113(m+g)}Sn_{(c)}$	58.630 (2519)	55.167 (2380)	58.467 (2634)	53.945 (2410)	51.318 (2371)	38.293 (1757)	19.139 (867)
$^{117m}Sn_{(c)}$	20.581 (982)	19.513 (944)	21.662 (993)	18.829 (907)	20.108 (992)	19.141 (978)	17.192 (896)
$^{116m}Sb_{(i)}$	31.637 (3170)	33.739 (4014)	38.649 (4102)	41.795 (3602)	49.308 (4219)	53.624 (4943)	55.169 (12658)
$^{118m}Sb_{(i)}$	23.660 (12320)	34.677 (1877)	34.271 (7363)	24.090 (9385)	29.455 (8387)	48.374 (4851)	35.887 (17240)
$^{120m}Sb_{(i)}$	26.412 (1179)	29.618 (1300)	32.618 (1481)	33.008 (1523)	38.246 (1810)	38.471 (1901)	42.700 (2162)
$^{122(m+g)}Sb_{(c)}$	71.681 (3082)	71.528 (3086)	80.018 (3607)	82.625 (3693)	91.663 (4240)	95.240 (4370)	100.991 (4505)
$^{116}Te_{(i)}$	14.475 (5361)	16.622 (4094)	18.735 (4602)	20.259 (3204)	29.267 (3263)	34.140 (5059)	58.992 (3912)
$^{117}Te_{(i)}$	29.676 (15427)	33.733 (17450)	48.562 (30173)	35.708 (14897)	40.584 (17985)	60.794 (26501)	103.701 (38653)
$^{118}Te_{(i)}$	19.411 (1227)	17.053 (969)	23.432 (1220)	22.995 (1098)	31.849 (1605)	36.036 (2001)	49.406 (2808)
$^{119g}Te_{(i)}$	11.820 (551)	11.376 (509)	14.477 (703)	14.059 (735)	18.450 (1038)	19.506 (910)	26.928 (1454)
$^{119m}Te_{(i)}$	15.473 (677)	16.396 (716)	19.248 (869)	21.059 (950)	25.317 (1175)	28.680 (1324)	36.185 (1629)
$^{121g}Te_{(i)}$	5.349 (232)	5.898 (259)	7.313 (331)	7.507 (337)	9.114 (425)	9.650 (444)	11.599 (526)
$^{121m}Te_{(i)}$	7.902 (341)	8.639 (385)	10.063 (454)	10.649 (476)	12.636 (584)	13.917 (640)	16.538 (738)
E_p (MeV)	90.987 (1073)	78.886 (1194)	71.967 (1280)	66.464 (1359)	62.279 (1429)	59.192 (1486)	56.485 (1540)
Location	LANL	LANL	LANL	LANL	LANL	LANL	LANL
$^{111(m+g)}In_{(c)}$	5.312 (208)	0.151 (6)	0.926 (124)				
$^{114m}In_{(i)}$	7.713 (318)	6.636 (469)		3.398 (124)	2.391 (137)	1.593 (107)	
$^{110}Sn_{(c)}$		0.070 (560)					
$^{111}Sn_{(c)}$	5.262 (204)	0.150 (8)					
$^{113m}Sn_{(i)}$		12.503 (29170)	9.188 (25320)	5.811 (331)	2.442 (94)	1.031 (86)	
$^{113(m+g)}Sn_{(c)}$	20.403 (1120)	15.174 (35345)	18.329 (50505)	11.700 (665)	4.889 (188)	2.036 (169)	
$^{117m}Sn_{(c)}$	16.014 (858)	10.590 (404)	9.918 (349)	10.351 (401)	9.926 (292)	10.420 (365)	10.406 (338)
$^{115}Sb_{(c)}$	94.809 (7855)	49.030 (4212)					
$^{116m}Sb_{(i)}$	35.581 (4386)	31.693 (3777)	28.274 (3420)	19.228 (2151)	10.359 (627)	5.463 (965)	
$^{118m}Sb_{(i)}$	63.682 (2668)	62.703 (2163)	67.037 (2395)	61.357 (2256)	54.218 (1951)	52.050 (2054)	55.312 (2488)
$^{120m}Sb_{(i)}$	42.340 (1563)	40.794 (1256)	45.152 (1352)	47.827 (1486)	53.805 (1535)	56.864 (1694)	62.615 (2032)
$^{122(m+g)}Sb_{(c)}$	60.009 (2278)	55.807 (1652)	61.826 (1780)	62.861 (1839)	66.050 (2630)	70.551 (13393)	73.493 (7186)
$^{116}Te_{(i)}$	58.289 (3043)	68.343 (3312)	88.355 (3969)	75.190 (3368)	44.644 (2494)	21.712 (1365)	8.181 (527)
$^{117}Te_{(i)}$	99.375 (24307)	108.829 (25958)	122.640 (28989)	127.485 (26371)	153.164 (26831)	194.074 (28883)	193.666 (34794)

Table 3.1 Continued from previous page

$^{118}Te_{(i)}$	57.549 (3192)	74.145 (2464)	104.430 (3269)	118.169 (4351)	128.810 (3747)	126.392 (5327)	135.419 (4400)
$^{119g}Te_{(i)}$	27.660 (2722)	31.077 (2717)	36.974 (4084)	47.915 (5288)	72.040 (7342)	88.352 (8728)	106.314 (12182)
$^{119m}Te_{(i)}$	37.945 (1366)	42.930 (1237)	58.010 (1629)	77.726 (2229)	111.336 (3200)	140.109 (4201)	173.405 (5665)
$^{121g}Te_{(i)}$	12.938 (702)	12.773 (461)	14.624 (506)	18.211 (783)	19.460 (610)	20.865 (778)	23.729 (1156)
$^{121m}Te_{(i)}$	19.283 (1139)	18.920 (1012)	23.399 (1224)	25.536 (1097)	26.140 (909)	32.054 (1494)	35.333 (4699)
E_p (MeV)	54.511 (1583)	53.981 (564)	53.929 (562)	52.463 (1630)	51.952 (579)	50.354 (1679)	49.912 (594)
Location	LANL	LBNL2022	LBNL	LANL	LBNL	LANL	LBNL
$^{117m}Sn_{(c)}$	10.061 (302)	9.233 (537)	9.462 (727)	10.803 (369)	8.753 (791)	10.487 (297)	9.375 (989)
$^{119m}Sn_{(c)}$		16.558 (12439)					
$^{118m}Sb_{(i)}$	52.142 (2259)	57.279 (1871)	40.287 (5036)	53.959 (2527)	51.264 (3557)	48.799 (2271)	49.674 (3424)
$^{120m}Sb_{(i)}$	59.709 (1789)	62.116 (1634)	60.380 (2963)	62.105 (2115)	55.934 (3253)	57.582 (1622)	58.082 (3162)
$^{122(m+g)}Sb_{(c)}$	74.654 (6949)	71.279 (2249)	68.386 (3428)	70.695 (5260)	63.653 (3762)	71.073 (3260)	66.565 (3652)
$^{116}Te_{(i)}$	0.727 (379)						
$^{117}Te_{(i)}$	167.233 (31521)	200.822 (7471)	131.571 (24550)	170.285 (32224)	98.193 (20443)	106.532 (23779)	99.516 (16912)
$^{118}Te_{(i)}$	137.188 (4124)	98.650 (24325)	145.136 (19335)	165.027 (5627)	150.859 (14756)	187.918 (5334)	204.754 (21198)
$^{119g}Te_{(i)}$	109.643 (11749)	97.513 (2910)	92.343 (6095)	112.793 (11583)	94.819 (6789)	96.071 (8584)	86.971 (7035)
$^{119m}Te_{(i)}$	171.084 (5165)	132.001 (4100)	160.232 (7962)	176.227 (6043)	151.474 (8472)	153.629 (4370)	145.499 (7917)
$^{121g}Te_{(i)}$	23.319 (1050)	22.118 (7132)	22.823 (1265)	25.145 (1157)	21.868 (1384)	24.257 (1040)	24.615 (1412)
$^{121m}Te_{(i)}$	34.920 (4195)	34.124 (3656)	34.866 (2185)	38.147 (4393)	34.389 (2404)	39.389 (2981)	37.652 (2105)
$^{123m}Te_{(i)}$		3.795 (450)					
E_p (MeV)	49.426 (601)	47.815 (613)	46.176 (633)	45.640 (636)	43.380 (661)	42.733 (672)	40.580 (696)
Location	LBNL2022	LBNL	LBNL2022	LBNL	LBNL	LBNL2022	LBNL
$^{117m}Sn_{(c)}$	10.163 (404)	9.820 (866)	9.738 (749)	9.227 (791)	7.850 (702)	8.240 (441)	6.173 (594)
$^{119m}Sn_{(c)}$	18.329 (13823)		11.123 (11366)			3.617 (6562)	
$^{116m}Sb_{(i)}$	1.583 (2140)		0.181 (192)				
$^{118m}Sb_{(i)}$	38.987 (1877)	25.829 (6710)	25.520 (2041)	37.968 (2667)	28.664 (2155)	22.166 (1225)	17.186 (1384)
$^{120m}Sb_{(i)}$	59.615 (1503)	57.298 (3036)	53.413 (1748)	54.043 (2858)	47.915 (2536)	47.615 (1284)	40.809 (2312)
$^{122(m+g)}Sb_{(c)}$	70.553 (1913)	67.757 (3680)	74.269 (2101)	67.689 (3657)	67.171 (3673)	71.342 (2079)	68.064 (3946)
$^{116}Te_{(i)}$	0.111 (484)						
$^{117}Te_{(i)}$	100.404 (4113)	69.734 (4349)	22.015 (3348)	10.633 (2148)	2.968 (611)	2.177 (314)	
$^{118}Te_{(i)}$	212.783 (9601)	208.343 (52479)	301.186 (30369)	275.624 (16943)	266.755 (32453)	286.854 (58850)	260.083 (22081)
$^{119g}Te_{(i)}$	90.635 (2535)	80.840 (6259)	74.867 (2232)	72.384 (5111)	61.830 (3851)	62.586 (1758)	66.077 (5510)
$^{119m}Te_{(i)}$	143.665 (3574)	129.880 (6886)	113.351 (3044)	110.871 (5860)	98.169 (5186)	96.577 (2507)	118.022 (6676)
$^{121g}Te_{(i)}$	26.123 (4771)	26.843 (1512)	28.778 (14686)	29.717 (1703)	32.913 (1859)	31.873 (12382)	41.127 (2489)
$^{121m}Te_{(i)}$	35.657 (5328)	41.397 (2279)	30.820 (4352)	46.501 (2557)	61.779 (3709)	59.606 (7942)	74.208 (4331)
$^{123m}Te_{(i)}$	4.114 (317)		2.882 (222)			4.877 (576)	
E_p (MeV)	39.040 (721)	37.596 (738)	35.074 (784)	34.439 (791)	33.339 (376)	31.651 (392)	29.891 (409)
Location	LBNL2022	LBNL	LBNL2022	LBNL	LBNL	LBNL	LBNL
$^{117m}Sn_{(c)}$	5.248 (237)	4.613 (526)	4.118 (196)	4.146 (564)	4.095 (510)	4.558 (588)	5.180 (636)
$^{118m}Sb_{(i)}$	13.125 (397)	7.405 (760)	2.811 (171)	1.792 (259)	0.924 (202)	0.518 (82)	0.289 (115)
$^{120m}Sb_{(i)}$	37.790 (959)	34.325 (1957)	31.454 (798)	29.957 (1861)	29.013 (813)	28.362 (830)	27.859 (816)
$^{122(m+g)}Sb_{(c)}$	69.974 (2127)	68.056 (3956)	67.192 (1925)	67.109 (4301)	67.282 (2002)	67.138 (2009)	66.271 (2002)

Table 3.1 Continued from previous page

$^{117}Te_{(i)}$	0.223 (97)						
$^{118}Te_{(i)}$	242.352 (16407)	186.874 (12416)	85.685 (9823)	81.330 (5335)	40.485 (7522)	14.262 (634)	
$^{119g}Te_{(i)}$	82.496 (2522)	96.779 (10155)	154.026 (4331)	134.527 (18513)	191.319 (9476)	88.707 (42075)	229.652 (12616)
$^{119m}Te_{(i)}$	120.620 (3425)	182.905 (10400)	240.656 (6095)	265.688 (16484)	287.612 (7889)	276.767 (11663)	293.183 (8442)
$^{121g}Te_{(i)}$	49.582 (8150)	58.729 (3537)	86.272 (6144)	93.812 (6176)	108.094 (3690)	138.731 (4643)	162.141 (5299)
$^{121m}Te_{(i)}$	89.247 (8665)	107.337 (6280)	125.010 (19320)	176.836 (11830)	210.174 (7499)	237.932 (9478)	254.492 (8472)
$^{123m}Te_{(i)}$	5.215 (557)		5.336 (445)				
E_p (MeV)	29.778 (886)	28.051 (430)	26.122 (455)	24.025 (484)	21.826 (522)	19.431 (571)	16.774 (641)
Location	LBNL	LBNL	LBNL	LBNL	LBNL	LBNL	LBNL
$^{117m}Sn_{(c)}$	5.311 (683)	5.449 (574)	5.430 (481)	4.764 (265)	3.767 (247)	2.824 (241)	2.654 (320)
$^{118m}Sb_{(i)}$	0.334 (78)	6.931 (1095)					
$^{120m}Sb_{(i)}$	28.192 (1462)	26.108 (796)	23.722 (662)	18.998 (527)	12.725 (362)	6.334 (191)	2.023 (62)
$^{122(m+g)}Sb_{(c)}$	66.486 (3576)	63.099 (2000)	61.020 (1739)	54.722 (1556)	43.520 (1225)	27.404 (822)	13.313 (400)
$^{119g}Te_{(i)}$	181.150 (25703)	213.914 (12542)	183.634 (10801)	117.192 (7014)	25.062 (1253)		
$^{119m}Te_{(i)}$	294.371 (15277)	258.096 (7846)	206.451 (5731)	119.333 (3318)	22.829 (651)		
$^{121g}Te_{(i)}$	164.524 (9174)	170.735 (5971)	166.193 (5234)	142.284 (4667)	83.895 (2492)	20.347 (671)	22.937 (709)
$^{121m}Te_{(i)}$	259.812 (15502)	251.210 (9562)	230.288 (7066)	189.155 (6357)	102.364 (3086)	26.502 (1039)	29.834 (1007)
E_p (MeV)	13.762 (745)						
Location	LBNL						
$^{120m}Sb_{(i)}$	0.155 (5)						
$^{122(m+g)}Sb_{(c)}$	1.932 (68)						
$^{121g}Te_{(i)}$	66.544 (2094)						
$^{121m}Te_{(i)}$	75.288 (2342)						

3.6 Channels with decay γ-rays from 153-159 keV

The analysis of ^{117m}Sn was complicated by several competing channels, including many A=117 products undergoing a 158.6 keV decay to stability. Other potential reaction products share decay gammas within this energy region as seen in Table 3.2. While the lifetimes of the different products allowed them to be uniquely determined, the proximity of their decay energies made it particularly challenging without the use of a high-energy resolution LEPS detector. The A=117 potential products and their decay via a 158.6 keV gamma is shown in Figure 3.34.

Table 3.2: Isotopes With Direct γ Decays Around 158.6 keV.

Parent	$t_{1/2}$e	Decay mode	E_γ (keV)	I_γ (%)
^{119m}Te[9]	4.70 (4) d	EC+β^+	153.59 (3)	66 (3)%
^{117m}Sn[3]	13.60 (4) d	IT	156.02 (3)	2.113 (6)%
^{116}Te[36]	2.49 (4) h	EC+β^+	157.14 (9)	0.435 (21)%
^{117m}In[3]	116.2 (3) m	IT+β^-	158.562 (12)	15.9 (16)%
^{117}Sb[37]	2.80 (1) h	EC+β^+	158.562 (12)	85.9 (4)%
^{117m}Sn[3]	13.60 (4) d	IT	158.562 (12)	86.4 (4)%
^{117}In[3]	43.2 (3) m	β^-	158.562 (12)	87 (9)%
^{123m}Te[38]	119.7 (1) d	IT	158.97 (5)	84.3 (3)%

3.7 Evidence of Secondary Neutron Production

The combination of a high-energy incident proton beam and thick degraders used in the target stacks opens the possibility of significant secondary particle production. While the majority of secondary charged particles are stopped by degraders, the secondary neutron flux increases with target thickness, leading to significant co-production of nuclides via (n,x) reactions. This was observed in ^{122}Sb and ^{120m}Sb in the experiment conducted at BNL, where thick copper degraders and a large moderating water layer influenced the stack. This was compounded by the high incident proton energy. ^{122}Sb, seen in Figure 3.35, can be produced by the (p,pn) reaction on ^{123}Sb, but also via ^{121}Sb(n,γ) or ^{123}Sb(n,2n).

Similarly, the cross section for ^{120m}Sb production, seen in Figure 3.36, can be produced through (p,x) reactions or (n,xn) reactions on ^{121}Sb and ^{123}Sb for x=2 or x=4 respectively. Further evidence for the contribution of secondary neutron flux is observed in the measurement of ^{124}Sb, a product that is only produced in this material via (n,γ) on ^{123}Sb (Figure 3.37). The previous work of Fox *et al.* [13, 39] also observed an elevated cross section in ^{74}As, the production of which could be from either (p,pn) or (n,2n) on ^{75}As (Figure 3.38).

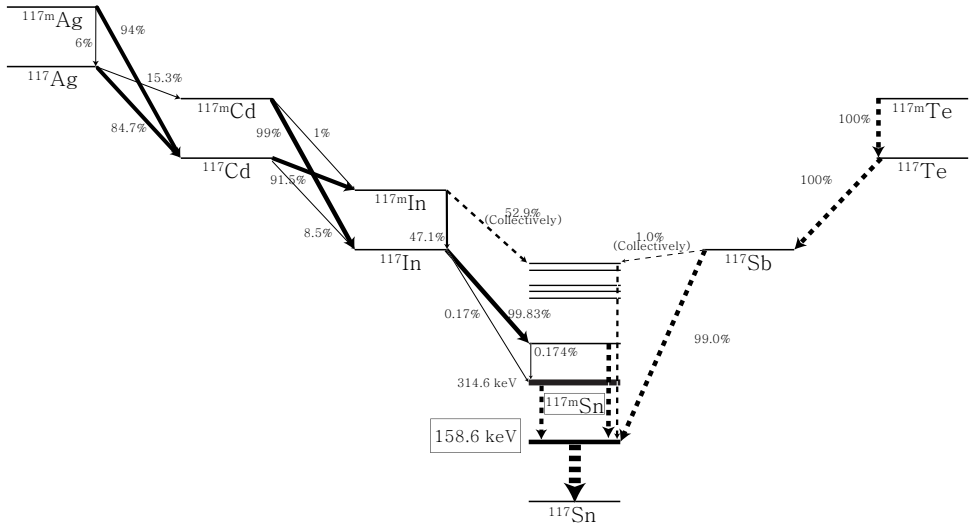

Figure 3.34: A=117 Decay scheme.

A strong indication of the production of further neutron-deficient ^{nat}Sb isotopes via (n,xn) reactions from energetic secondary neutrons is seen in ^{118m}Sb and ^{116}Sb. The significant jump near 100 MeV, which is the transition between the lowest energy data points at BNL and the highest data points at LANL. Similar discontinuities are seen in ^{nat}Sb products measured by these experiments, but not in (p,xn) products. Even among monitor foils, the production of ^{64}Cu has a marked increase in the transition between low-energy BNL and high-energy LANL measurements seen in Figure 3.38. This could be produced via ^{63}Cu(n,γ)^{64}Cu or ^{65}Cu(n,2n)^{64}Cu. Finally, ^{92m}Nb shows a similar discontinuity, which could be the result of ^{93}Nb(n,2n)^{92m}Nb Figure 3.39. These results are also in agreement with earlier work using the GEANIE spectrometer at LANL by Bernstein *et al.*[40] involving (n,xn) reactions for incident neutron energies up to 200 MeV. The results of the GEANIE experiment showed significant yields with up to 15 outgoing neutrons. This result suggests the need for caution in interpreting stacked target measurements and the need to characterize the neutron flux produced throughout the stack.

Further evidence that these jumps can be attributed to secondary neutrons will be shown in the TALYS modeling chapter later in this dissertation.

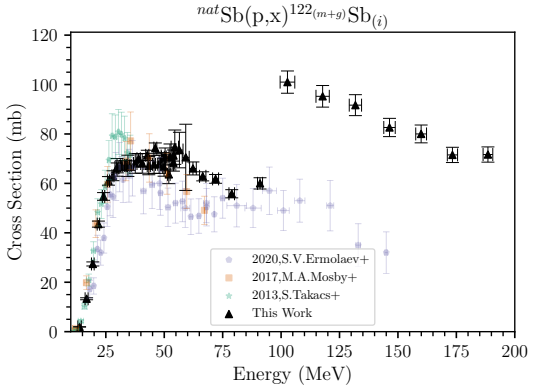

Figure 3.35: ^{122}Sb Cross Section [29, 30, 31].

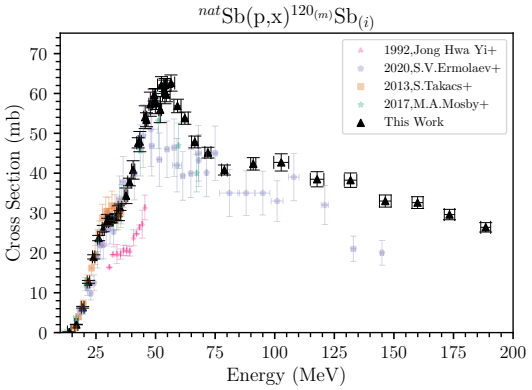

Figure 3.36: ^{120m}Sb Cross Section [29, 30, 31, 32].

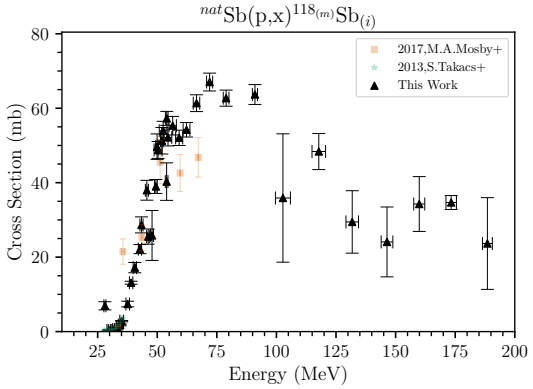

Figure 3.36: ^{118m}Sb Cross Section [30, 31].

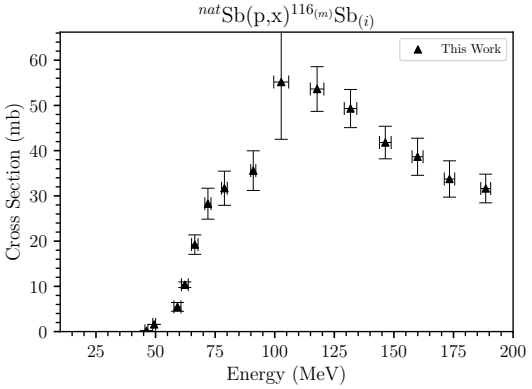

Figure 3.37: ^{116m}Sb Cross Section.

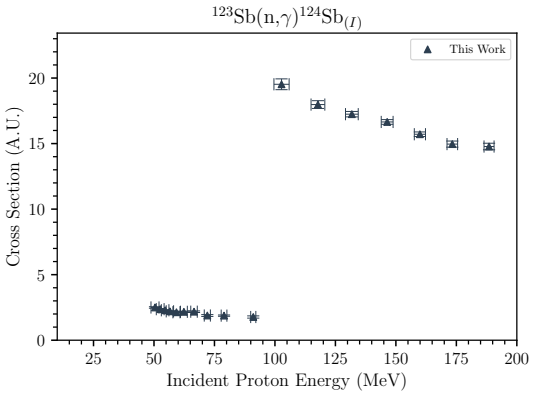

Figure 3.37: ^{124}Sb, measured via the 1691 keV decay gamma.

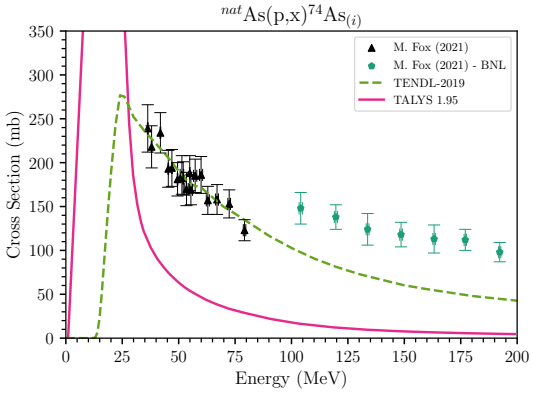

Figure 3.38: ^{74}As measurement from a prior experiment, demonstrating a similar offset for measurements at BNL [13].

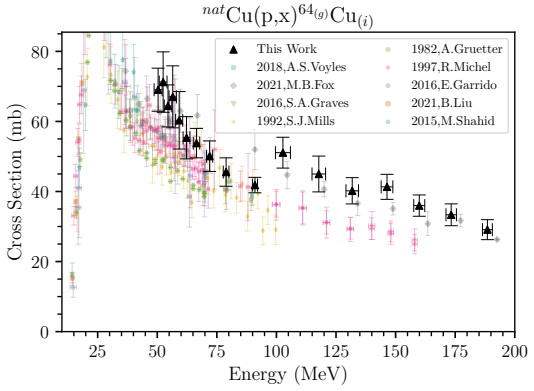

Figure 3.38: ^{64}Cu Cross Section.

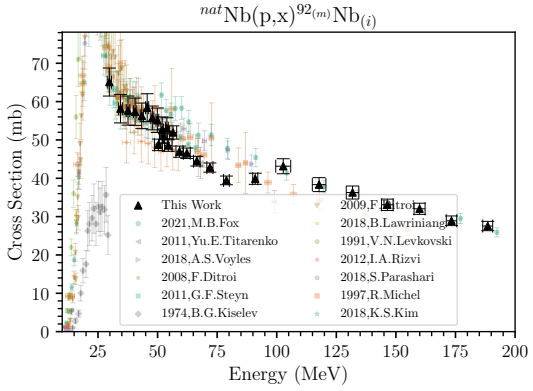

Figure 3.39: ^{92m}Nb Cross Section.

Chapter 4

Reaction Modeling with Experimental Data

The experimental results presented in this work stand alone to inform production pathways for medical radionuclides. Additionally, as part of the TREND collaboration, this work provides an opportunity to explore the underlying physics for high-energy charged particle-induced reactions. Experimental data was compared to four nuclear reaction modeling codes – EMPIRE 3.2.3 [41], CoH 3.5.3 [42], ALICE-20 [43], and TALYS 1.95 [44]. A comparison among these codes is shown in Figure 4.1. ^{118}Te – a high energy (p,xn) channel, and ^{117m}Sn

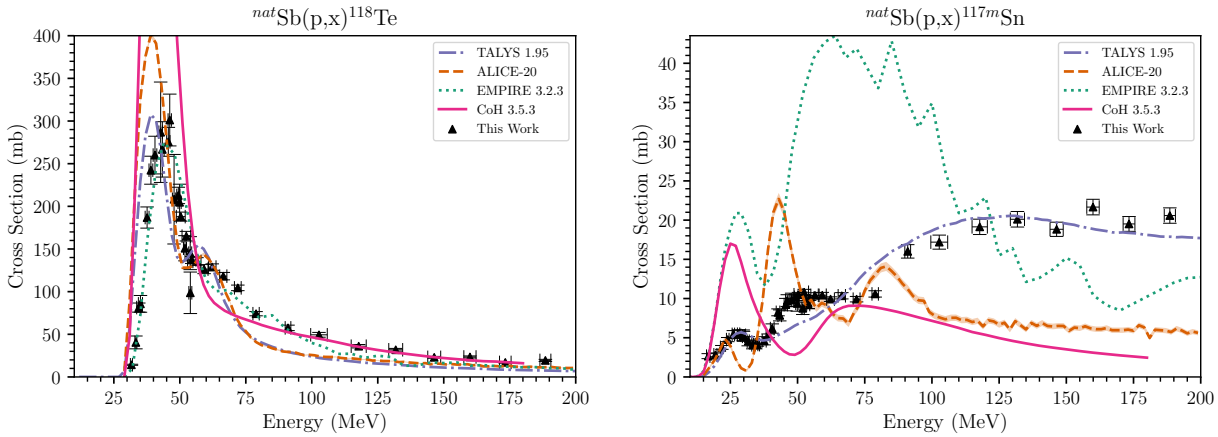

Figure 4.1: Comparison of EMPIRE 3.2.3 [41], CoH 3.5.3 [42], ALICE-20 [43], and TALYS 1.95 [44] for ^{118}Te and ^{117m}Sn.

– a channel with competing (p,xp,xn) and (p,$x\alpha$) emissions illustrates the contrasting results among reaction modeling codes. TALYS 1.95 was selected for analysis since its deterministic model enabled faster computational speed and the opportunity to review and fine-tune 40 base parameters, amassing a dataset of over 12,000 calculations. Parameter adjustments in

TALYS 1.95 were done so in a physically defensible manner. The following section outlines the formalism behind established proton-induced nuclear reactions in the energy range covered by these experiments.

4.1 Nuclear Reaction Theory

Basic physics dictates that energy, momentum, and charge are conserved in a nuclear reaction. The total nuclear reaction cross section (σ_{tot}) is dominated by elastic scattering (σ_{el}), where the incident particle and target nucleus retain their initial states after reaction. The cross section for elastic scattering decreases as incident particle energy increases and other reaction channels are opened. These other reaction channels are collectively referred to as non-elastic scattering channels (σ_{non}). The total nuclear cross section is the sum of elastic scattering and all non-elastic scattering channels, as seen in Equation 4.1.

$$\sigma_{tot} = \sigma_{el} + \sigma_{non} \tag{4.1}$$

The energy and angular momentum introduced by a projectile incident on a target nucleus influence the statistical probability for a specific nuclear reaction to occur. These nuclear reactions are diagrammed in Figure 4.2.

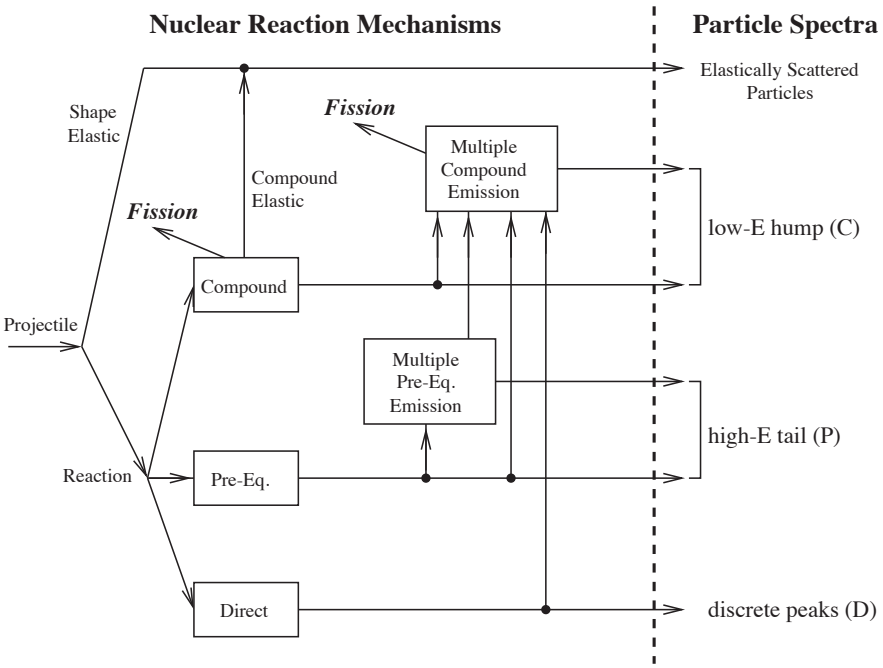

Figure 4.2: Nuclear reaction mechanisms [44].

For incident particle energies covered by this work, the total reaction cross section contribution, aside from elastic scattering, includes compound and pre-equilibrium reactions, with negligible influence from direct reactions. *Compound* reactions are dominant at lower projectile energies; energy and angular momentum are statistically distributed throughout the nucleons in the target nucleus. The resulting compound nucleus is in a highly excited state and will decay to stability. The decay of the compound nucleus is irrespective of its formation, known as the Bohr independence hypothesis or the "amnesia assumption." [45] This return to stability can include either particle emission or prompt gamma emission, relaxing the residual product to a metastable or ground state.

At higher incident energies, the projectile is more likely to interact with individual nucleons in the target nucleus. This interaction can result in the ejection of nucleons via *pre-equilibrium* or *multiple pre-equilibrium* emission[44]. This interaction occurs following the formation of a compound nucleus, but prior to equilibration of energy and angular momentum distribution. Following pre-equilibrium emission, an excited nucleus can transition to a lower-energy excited state, at which point compound emission of particles will dominate as described above.

At still higher incident particle energies, the nucleus will undergo a *direct* reaction, where the projectile will interact with individual nucleons prior to the formation of a compound nucleus, again leading to particle or energy emission. Direct reactions have a negligible contribution to experimental results from this work.

These reaction mechanisms can be seen physically in Figure 4.3 – the experimental cross section measurement for ^{nat}Sb in which the compound peaks in the low-energy region and the high-energy pre-equilibrium region tail are indicated.(p,xn)^{119g}Te. The dual peaks in the compound region are a result of the natural isotopic abundance of ^{nat}Sb, with 57.213 (32)% ^{121}Sb and 42.787 (32)% ^{123}Sb [46]. The threshold energy for ^{121}Sb(p,3n)^{119}Te is lower than that of ^{123}Sb(p,5n)^{119}Te.

While this serves as a basic illustration of the compound and pre-equilibrium regions, it is important to note that the sole ejectiles in this case are neutrons. The visual interpretation for cross sections involving competing ejectile mechanisms (e.g. (p,2xp,2xn) and (p,$x\alpha$)) becomes increasingly complex. The threshold energy for these competing reactions for ^{nat}Sb(p,x) are provided in Appendix C. These serve to illustrate the complexity of modeling residual product cross sections.

Total Cross Section Derivation

The geometric cross section σ_{geo} assumes a spherical nucleus and is the surface area of the nucleus and projectile $\sigma_{geo} = \pi R_0 (A^{1/3})^2$[47] where the Fermi radius $R_0 = 1.2 \times 10^{-15} m$ and A is the atomic number. This is restricted to values in a range from 0.1 -2.7 barns, where a barn $b = 10^{-28}\, m^2$. While the geometric cross section is a straightforward calculation, it is not representative of the total reaction cross section, as seen in experimental work due to the non-zero range of the nuclear force. The reaction of an incident particle on a target nucleus can transfer energy and momentum between the nucleons. The resulting system of interactions satisfies the time-independent radial Schrödinger Equation, seen in 4.2 [48]

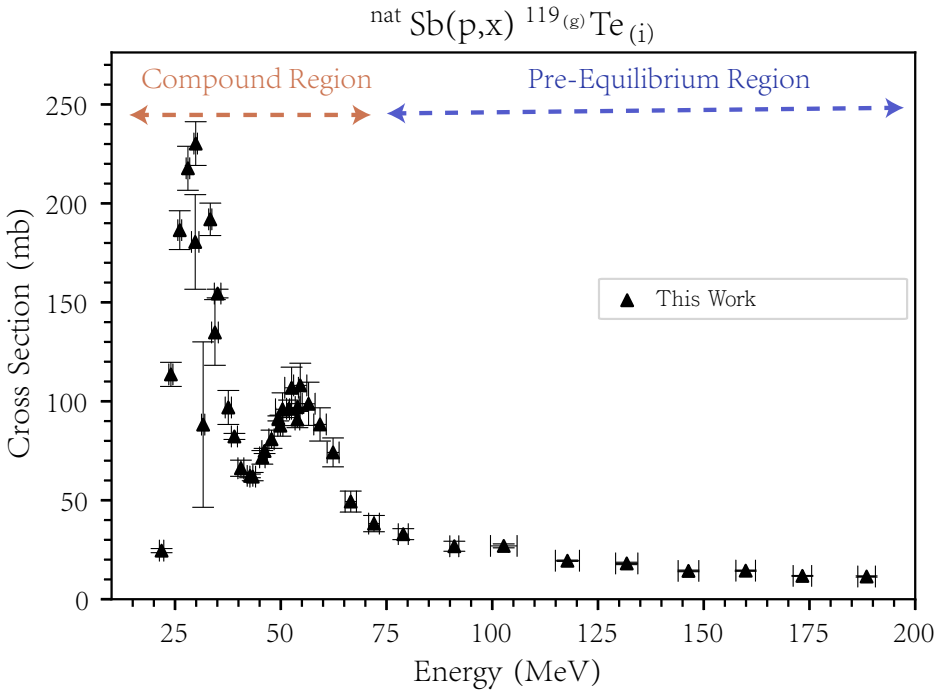

Figure 4.3: ^{119}Te Experimental data, identifying compound and pre-equilibrium regions.

$$-\frac{\hbar^2}{2m}\left(\frac{d^2R(r)}{dr^2}+\frac{2}{r}\frac{dR(r)}{dr}\right)+\left[V(r)+\frac{\ell(\ell+1)\hbar^2}{2mr^2}\right]R(r)=ER(r) \tag{4.2}$$

where m is the incident particle mass, r is the nuclear radius, $R(r)$ is the radial part of the wave function, E is the energy eigenvalue, and $V(r)$ is the potential energy well. For short distances, the strong nuclear force is dominant over the Coulomb force. The former work by Yukawa *et al.*[49] discusses the quantum mechanics of the strong nuclear force and its range.

The particle collision can be non-central, with an impact parameter D. An incident particle with mass m and velocity v will have a classical orbital angular momentum mvD. In observation of quantum mechanics, this value will be an integer multiple of the Planck constant $\hbar$ as seen in Equation 4.3[47]

$$mvD=\ell\hbar D=\ell\frac{\hbar}{mv}\equiv\ell\lambda\!\!\!^{-} \tag{4.3}$$

where ℓ is the incident particle angular momentum prior to collision and $\lambda\!\!\!^{-}$ is the *reduced* de Broglie wavelength where $\lambda\!\!\!^{-}=\dfrac{\lambda}{2\pi}$. The cross section for a particle in the area between $\ell\lambda\!\!\!^{-}$ and $(\ell+1)\lambda\!\!\!^{-}$ can then be defined by Equation 4.4.

$$\sigma_\ell=\pi(\ell+1)^2\lambda\!\!\!^{-2}-\pi\ell^2\lambda\!\!\!^{-2}=(2\ell+1)\pi\lambda\!\!\!^{-2} \tag{4.4}$$

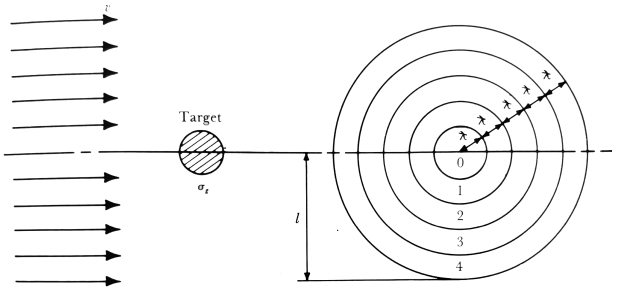

Figure 4.4: Visual representation of the orbital momenta of the incident particle [47].

The total scattering cross section is then the sum of σ_ℓ, or the maximum impact parameter R[48], where R is the sum of the radii for the incident particle and target nucleus. Therefore, the maximum ℓ is approximated as R/λ as seen in Equation 4.5.

$$\sigma_{sc} = \sum_{\ell=0}^{R/\lambda} (2\ell + 1)\pi\lambda^2 \tag{4.5}$$

Note that this approximation neglects the quantum-theoretical expression of orbital angular momentum, where $\ell\hbar$ is expressed as $[\ell(\ell+1)]^{1/2}\hbar$. This incident particle interaction is visualized in Figure 4.4.

At higher energies, residual product channels are opened. Collectively, these can be referred to as the non-elastic cross section. Incident particle energy and angular momentum dictate whether an individual non-elastic reaction channel is open. This is the reaction threshold energy, which incorporates the reaction's Q-value and the energy from the center-of-mass system. Reaction thresholds for this experimental data are provided in Appendix C.

Similar to the derivation of the total scattering cross section, the total non-elastic cross section is provided in Equation 4.6. The derivation introduces the complex coefficient variable corresponding to the outgoing particles' orbital angular momentum the variable η_ℓ

$$\sigma_{\mathrm{r}} = \sum_{\ell=0}^{\infty} \pi\lambda^2(2\ell + 1)\left(1 - |\eta_\ell|^2\right) \tag{4.6}$$

vis.

$$\sigma_{tot} = \sum_{\ell=0}^{\infty} (2\ell + 1)\pi\lambda^2 + \pi\lambda^2(2\ell + 1)\left(1 - |\eta_\ell|^2\right) \tag{4.7}$$

This explains significantly larger cross sections from experimental results compared to the calculated geometric cross section. For example, a particle with low energy can have a high λ, and therefore a high interaction probability. The total nuclear cross section can be approximated on the order of 5 b, as seen in Equation 4.8. This is corroborated by experimental data.

$$\sigma_{tot} = \pi((R_0(1 + A^{1/3})) + 5)^2 \approx 5 - 6\,b \tag{4.8}$$

The Optical Model

The solutions to Schrödinger's Equation have a wavelike form. Therefore, nuclear scattering, both elastic and non-elastic, can be described using the same formalism applied to optics. The nuclear optical model provides a theoretical framework to describe the interaction between nucleons in the target nucleus. The optical model potential $\mathcal{U}(r)$ is comprised of both a real $\mathcal{V}(r)$ and imaginary $\mathcal{W}(r)$ component, described in Equation 4.9 [50].

$$\mathcal{U}(r) = \mathcal{V}(r) + i\mathcal{W}(r) \tag{4.9}$$

$\mathcal{V}(r)$ and $\mathcal{W}(r)$ contain a form factor with a Woods-Saxon shape, seen in Equation 4.10, with a derivative form factor used for the imaginary volume term [51]

$$f\left(r, R_i, a_i\right) = \left(1 + \exp\left[\left(r - R_i\right)/a_i\right]\right)^{-1} \tag{4.10}$$

where r is the radius, R_i is the nuclear radius $R_i = r_i A^{1/3}$, and a_i is the "diffuseness" parameter, which represents the breadth of the fall-off region of the potential from 90% of the maximum well depth to 10%. The formal details of the analysis are provided in section 4.6.

Building on the understanding of interactions with the incorporation of orbital angular momentum and the strong nuclear force, the optical model provides an average distribution for the elastic and non-elastic cross sections for incident particles on a target nucleus and, crucially, the orbital angular momentum dependent transmission coefficients T_l.

$$\left\langle \sigma_l(E) \right\rangle_{\text{optical}} = \pi \lambda\!\!\!^{-2} (2l + 1) T_l \tag{4.11}$$

These transmission coefficients quantify the probability of a particle tunneling through a potential well [47]

$$T = \frac{\mathbf{j}_{emergent}}{\mathbf{j}_{incident}} \tag{4.12}$$

where $\mathbf{j}$ is the current density – the magnitude of the wave vector in Equation 4.13

$$\mathbf{j} = \frac{\hbar}{2im}(\psi * \nabla\psi - \psi\nabla\psi*) \tag{4.13}$$

These transmission coefficients play a significant role in modeling residual product cross sections.

Residual Product Cross Section Calculations

Residual product cross sections in this work undergo multiple emissions through compound and pre-equilibrium decay. A residual product with atomic number Z, neutron number N, and isomeric states i is summarized in Equation 4.14[52].

$$\sigma_{\text{non}}(Z,N) = \sum_{i=0,\text{ isomers}} \sigma_{\text{prod },i}(Z,N) \tag{4.14}$$

where the residual product channel $\sigma_{\text{non}}(Z,N)$ is a summation of all potential outgoing particles and isomeric states

$$\sigma_{prod,i}(Z,N) = \sum_{i_n=0}^{\infty}\sum_{i_p=0}^{\infty}\sum_{i_d=0}^{\infty}\sum_{i_t=0}^{\infty}\sum_{i_h=0}^{\infty}\sum_{i_\alpha=0}^{\infty} \sigma_i^{ex}\left(i_n,i_p,i_d,i_t,i_h,i_\alpha\right)\delta_N\delta_Z \tag{4.15}$$

Compound decay is based on Hauser-Feshbach (HF) formalism [53], a well-established theory for calculating residual product channels. In contrast to the Weisskopf-Ewing theory, The HF theory incorporates the conservation of angular momentum and angular distribution of incident projectiles and ejectiles. This theory is applicable in the region that does not include overlapping resonances and assumes an energy-averaged level density spacing over Breit-Wigner resonances, i.e. $D \gg \Gamma$[54], where Γ is the total width for resonances with spin J and D is the average spacing.

In low-energy regions, the compound nucleus and ejected particles are described as a summation over Breit-Wigner resonances Γ as shown in Equation 4.16

$$\sigma_{ab}^J(E) = \pi\lambda\!\!\!^{-2}\omega_a^J \sum_\lambda \frac{\Gamma_{\lambda a}\Gamma_{\lambda b}}{\left(E-E_\lambda\right)^2 + \frac{1}{4}\Gamma_\lambda^2} \tag{4.16}$$

where a is the initial target nucleus and b is the product, E is the incident particle energy E_λ is the resonance energy, $\lambda\!\!\!^{-}$ is the reduced de Broglie wavelength, $\Gamma_{\lambda a}$ and $\Gamma_{\lambda b}$ are the partial de Broglie resonance wavelength widths for initial and final products, Γ_λ is the total resonance wavelength, and ω_a^J, is defined in Equation 4.17

$$\omega_a^J = \frac{2J+1}{\left(2i_a+1\right)\left(2I_a+1\right)} \tag{4.17}$$

where i_a is the projectile spin and I_a is the target spin. Using HF formalism, where an energy interval Δ contains significant resonances such that $D/\Delta \ll 1$, the energy-averaged cross section integral yields Equation 4.18

$$\left\langle \sigma_{ab}^J(E)\right\rangle = \pi\lambda\!\!\!^{-2}\omega_a^J\frac{2\pi}{D}\left\langle\frac{\Gamma_a\Gamma_b}{\Gamma}\right\rangle \tag{4.18}$$

Individual width fluctuations are accounted for via a width fluctuation factor W_{ab}

$$\left\langle \sigma_{ab}^J(E)\right\rangle = \pi\lambda\!\!\!^{-2}\omega_a^J\frac{2\pi}{D}\frac{\left\langle\Gamma_a\right\rangle\left\langle\Gamma_b\right\rangle}{\left\langle\Gamma\right\rangle}W_{ab} \tag{4.19}$$

Simplifying over all resonances, the average cross section is calculated via Equation 4.20.

$$\left\langle \sigma_a^J(E)\right\rangle = \pi\lambda\!\!\!^{-2}\omega_a^J 2\pi\frac{\left\langle\Gamma_a\right\rangle}{D} \tag{4.20}$$

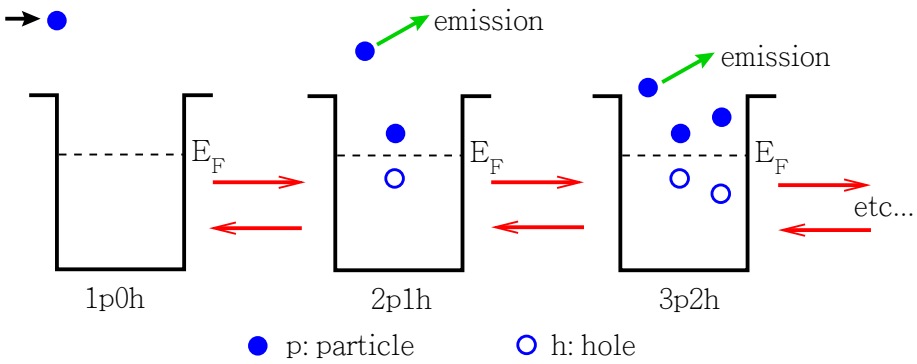

Figure 4.5: Visualization of reaction flow in the exciton model [44].

This is equivalent to Equation 4.11, and therefore we can use the transmission coefficient T from optical model calculations, arriving at Equation 4.21

$$T_c = 2\pi \frac{\langle \Gamma_c \rangle}{D} \tag{4.21}$$

Substituting in the transmission coefficient, and with assumptions regarding angular momentum coupling and conservation of parity, Equation 4.22 provides results based on HF for a compound system

$$\frac{d\sigma_{ab}^{\mathrm{HF}}}{dE_b} = \pi\lambda^2 \sum_{J\Pi} \omega_a^J \frac{\sum_{\{j_a\}} T_a}{\sum_c \sum_{\{n_c\}} \sum_{\{j_c\}} T_c} \sum_{I_b \Pi_b} \sum_{\{j_b\}} T_b \rho\left(E_b, I_b, \Pi_b\right) \tag{4.22}$$

where Π is the parity, $\sum_{\{j_i\}}$ is the sum of orbital angular momenta of either the incident particle, initial nucleus, or final product, $\sum_{\{n_i\}}$ is the sum of states in the incident particle, initial nucleus, or final product, and $\rho\left(E_b, I_b, \Pi_b\right)$ level density in the final product. For the reaction modeling presented in this paper, the width fluctuation is negligible.

In pre-equilibrium reactions, nuclear interactions are governed by the exciton model. This model is based on the concept of nucleon-hole pairs referred to as excitons. Each exciton can scatter off of other nucleons, causing a decrease in the average energy of individual nucleons in the nucleus, as visualized in Figure 4.5. The exciton scattering probabilities can be adjusted to best represent measured data.

The exciton model characterizes the nuclear state based on the total energy E_{tot} of the system and the particles (p) above the Fermi surface and holes (h) below for protons (π) and neutrons(ν) in the reaction. The potential configurations of the shared excitation energy between these pairs are equally probabilistic and are expressed by an exciton number $n = p_\pi + h_\pi + p_\nu + n_\nu$ as seen in Figure 4.6[44]. The exciton scattering probabilities can be adjusted to best represent measured data. ***

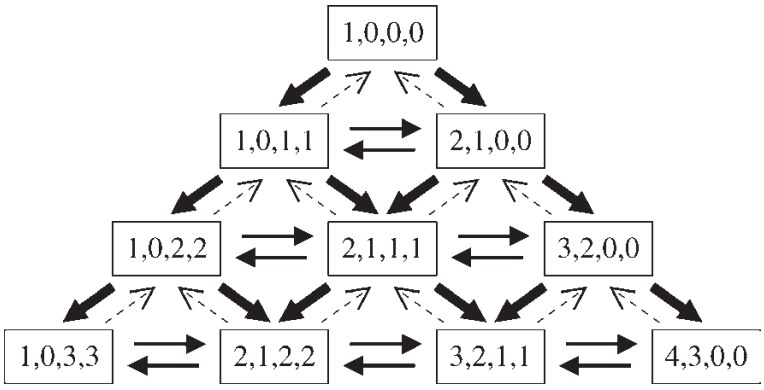

Figure 4.6: Potential reaction pathways [55].

This applies to incident particles with energies above the neutron separation energy. This is delineated into multiple compound decay, modeled by HF formalism and multiple pre-equilibrium decay 4.23

$$\frac{d\sigma_k^{\mathrm{PE}}}{dE_k} = \sigma^{\mathrm{CF}} \sum_{p_\pi=p_\pi^0}^{p_\pi^{\max}} \sum_{p_\nu=p_\nu^0}^{p_\nu^{\max}} W_k\left(p_\pi, h_\pi, p_\nu, h_\nu, E_k\right) \tau\left(p_\pi, h_\pi, p_\nu, h_\nu\right) P\left(p_\pi, h_\pi, p_\nu, h_\nu\right) \tag{4.23}$$

where variables are defined as follows:

- σ^{CF} is the compound nucleus cross section.
- $W_k\left(p_\pi, h_\pi, p_\nu, h_\nu, E_k\right)$ is the emission rate, derived by Cline and Blann 4.24[56],

$$W_k\left(p_\pi, h_\pi, p_\nu, h_\nu, E_k\right) = \frac{2s_k+1}{\pi^2\hbar^3}\mu_k E_k \sigma_{k,\mathrm{inv}}\left(E_k\right) \frac{\omega\left(p_\pi - Z_k, h_\pi, p_\nu - N_k, h_\nu, E^{\mathrm{tot}} - E_k\right)}{\omega\left(p_\pi, h_\pi, p_\nu, h_\nu, E^{\mathrm{tot}}\right)} \tag{4.24}$$

  where the ejectile k has a mass μ_k and spin s_k and $\sigma_{k,inv}(E_k)$ is the surrogate reaction provided by the optical model.

- $\tau\left(p_\pi, h_\pi, p_\nu, h_\nu\right)$ is the lifetime of the exciton.
- $P\left(p_\pi, h_\pi, p_\nu, h_\nu\right)$ is the average pre-equilibrium population of residual nucleons that are configured as particles or holes.

Formal derivation of these components is detailed in the TALYS 1.95 manual [44].

Multiple pre-equilibrium emission transition rates are calculated with an effective square matrix with respect to collision probability:

$$\begin{aligned}
\lambda^{1p}_{\pi\pi}(u) &= \frac{2\pi}{\hbar} M^2_{\pi\pi}\omega(2,1,0,0,u) \\
\lambda^{1h}_{\pi\pi}(u) &= \frac{2\pi}{\hbar} M^2_{\pi\pi}\omega(1,2,0,0,u) \\
\lambda^{1p}_{\nu\pi}(u) &= \frac{2\pi}{\hbar} M^2_{\nu\pi}\omega(1,1,1,0,u) \\
\lambda^{1h}_{\nu\pi}(u) &= \frac{2\pi}{\hbar} M^2_{\nu\pi}\omega(1,1,0,1,u), \\
\lambda^{1p1h}_{\pi\nu}(u) &= \frac{2\pi}{\hbar} M^2_{\pi\nu}\omega(0,0,1,1,u)
\end{aligned} \tag{4.25}$$

The corresponding reaction probability for $\lambda^{1p}_{\nu\nu}$, $\lambda^{1h}_{\nu\nu}$, $\lambda^{1p}_{\pi\nu}$, $\lambda^{1h}_{\pi\nu}$, and $\lambda^{1p1h}_{\nu\pi}$ can be calculated by swapping π and ν . This ultimately depends on the average squared matrix element M^2 and adjustments to nucleon-nucleon parameters, discussed in section 4.5.

4.2 Theoretical Reaction Modeling with Experimental Data

Analysis with TALYS 1.95 explored 40 base parameters, several of which were adjusted 2-dimensionally for outgoing particles. Details are provided in Appendices E, F, and G. This analysis iteratively adjusted level density, optical model, and pre-equilibrium parameters as shown in Figure 4.7.

TALYS parameters were explored and optimized using two approaches for goodness of fit (χ^2). For a single residual product channel c, a goodness of fit is determined as follows:

$$\chi^2_c = \frac{1}{N_p}\sum_{i=1}^{N_p}\left(\frac{\sigma^i_T - \sigma^i_E}{\Delta\sigma^i_E}\right)^2 \tag{4.26}$$

Where N_p is the number of measured data points for a reaction channel, σ_T is the calculated cross section from TALYS at a given energy, σ_E is the experimentally measured cross section, and $\Delta\sigma^i_E$ is the experimental data uncertainty. The contribution to the overall goodness of fit χ^2_{tot} by a channel was calculated using Equation 4.27

$$\chi^2_{\text{tot}} = \frac{1}{N_c}\sum_{c=1}^{N_c}\chi^2_c w_c \tag{4.27}$$

Here, N_c is the number of residual product channels used in the analysis, χ^2 is the goodness of fit for the channel, and w_c is the weighting factor for that channel.

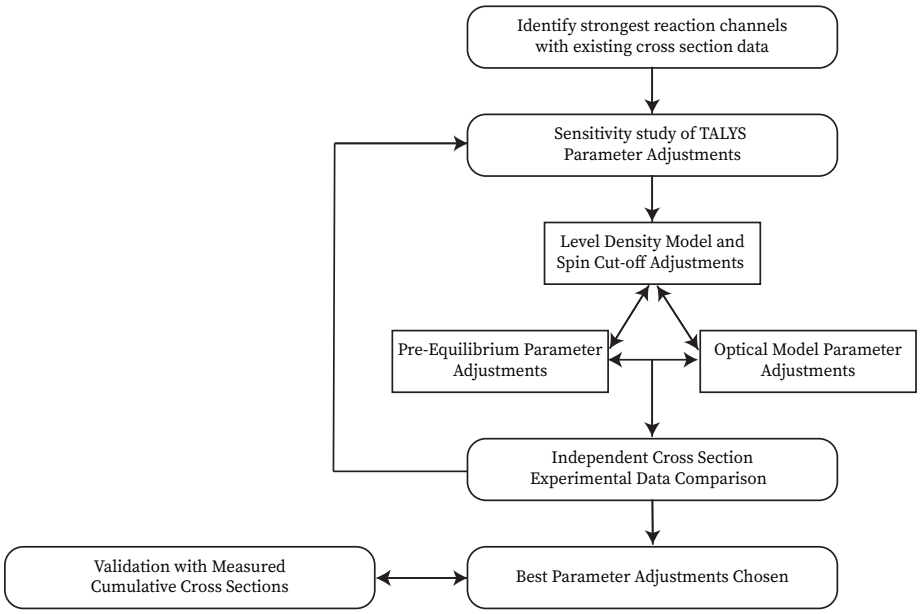

Figure 4.7: Flow chart of the iterative modeling process.

This does not address the surplus of measurement points below 55 MeV and the lack of data for measurements above 200 MeV. Fitting of the pre-equilibrium region for larger magnitude reactions was de-prioritized, as well as residual products with a reaction threshold near and above 100 MeV. Alternate weighting within a channel, however, would restrict the statistical impact of data points in the region of interest for isotope production below 55 MeV.

The weighting factor was considered from two approaches. The first weighting factor is based on the summation of the channel cross section across the energy region and is referred to here as "Cumulative $\sigma\chi^2$"(Equation 4.28):

$$w_c = \frac{\sum_{i=1}^{N_p} \sigma_T^{ci}(E)}{\sum_{c=1}^{N_c} \sum_{i=1}^{N_p} \sigma_T^{ci}(E)} \tag{4.28}$$

The second approach is based on the maximum cross section value relative to other channels, here referred to as "Maximum $\sigma\chi^2$ " (Equation 4.29)

$$w_c = \frac{\sigma_{T,\,\max}^{c}}{\sum_{c=1}^{N_c} \sigma_{T,\,\max}^{c}} \tag{4.29}$$

These approaches have a trade-off for reaction modeling by prioritizing the majority of data points – 26 of 43 measurements are below 55 MeV. This region is valuable for the production of isotopes of interest, but this weighting factor neglects higher incident-energy

protons, where data is sparse. This has a significant impact on the fit for pre-equilibrium parameters.

4.3 Selected Independent Cross Sections:

Analysis was based on seven (p,xn) channels for production of Te isotopes and specific long-lived isomers – $^{116(m+g)}$Te, $^{117(m+g)}$Te, $^{118(m+g)}$Te, ^{119g}Te, ^{119m}Te, ^{121g}Te, and ^{121m}Te. Additional validation used experimental data from ^{116m}Sb, ^{118m}Sb, ^{120m}Sb, $^{122(m+g)}$Sb, and ^{114m}In.

Data points above 100 MeV for Sb products, obtained at BNL, were excluded from analysis due to the potential significant contribution of (n,xn) contamination from secondary neutron production. These 12 large-magnitude independent cross sections formed a comparative set that was used to guide reaction modeling parameter adjustments. Nine cumulative channels and an additional three weaker independent channels were used for validation.

4.4 Level Density Adjustments

Level Density Models:

TALYS includes both phenomenological and microscopic level density models. Calculations for the residual reaction channels were performed using these level density models, with LDM 2, the phenomenological Back-Shifted Fermi Gas Model outperforming others. The BFG model shifts the baseline energy level for calculating excitation energy. This updated model addresses nuclear pairing and nuclear structure, which the CT+FGM does not adequately explain. Sample results can be seen in Figure 4.8,Figure 4.9. Table 4.1 shows the reduced χ^2 values for the selected independent cross sections.

Table 4.1: Available level density models in TALYS 1.95

`ldmodel`	**Reduced χ^2**
1	6.5135
2	5.7367
3	79.7651
4	7.5453
5	10.7160
6	13.5216

Adjustments to the Spin Cut-Off Parameter σ^2

The observation of two adjacent Odd-A Te isotopes (^{119}Te and ^{121}Te) from these experiments offered an opportunity to optimize reaction models for spin distribution values in unresolved multi-MeV nuclear states near Z=50. since production cross section for with J^π =1/2+ ground states and J^π =11/2- isomers were measured. The simplified decay schema for these isotopes is shown in Figure 4.12. Another neighboring isomer, ^{123m}Te, was used as validation as it also displays a significant change in spin and parity for a long-lived,

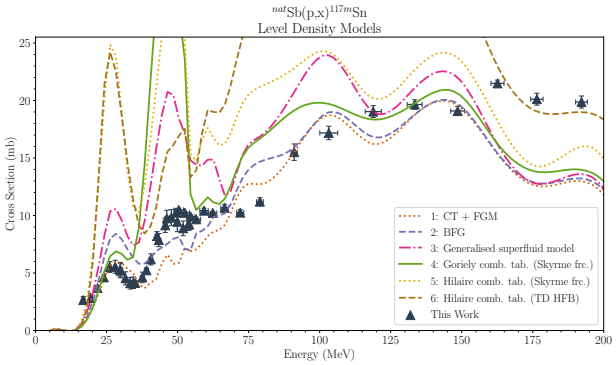

Figure 4.8: Experimental data for ^{117m}Sn with comparative level density models.

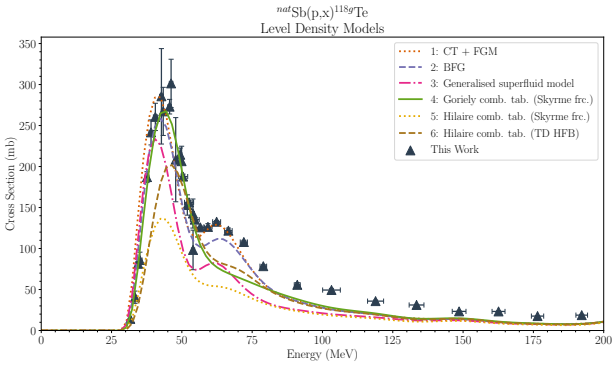

Figure 4.9: Experimental data for ^{118}Te with comparative level density models.

low-energy isomer. Its simplified decay schema is shown in Figure 4.15. Unfortunately, measuring its ground state is outside of the scope of this work due to time constraints as it has a $t_{1/2}$ exceeding 10^{16}y. The application of the `rspincut` adjustment improves the fit for the measurable isomer of ^{123m}Te.

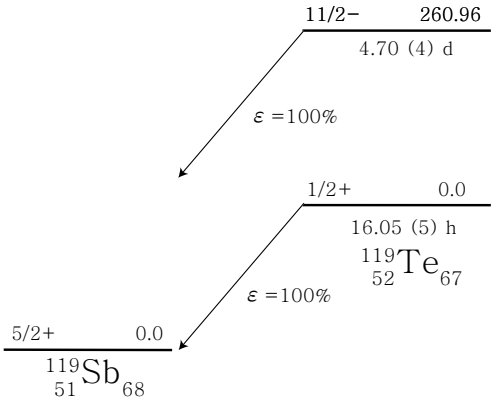

Figure 4.10: ^{119}Te Decay

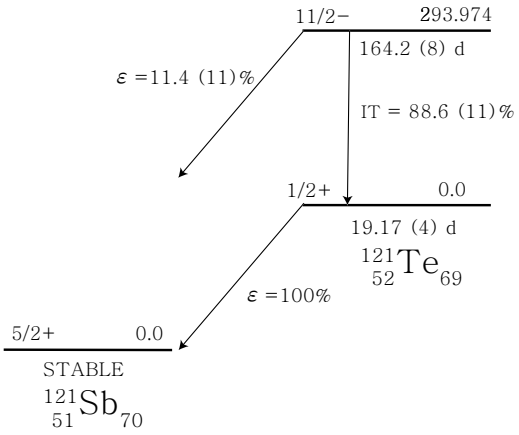

Figure 4.11: ^{121}Te Decay

Figure 4.12: Decay Schema for ^{119}Te and ^{121}Te.

TALYS systematically over-predicted the population of the high-spin isomeric state and under-predicted the population of the low-spin ground state for both isotopes from these experimental results seen in Fig 4.14. The phenomenological level density models used in TALYS 1.95 assume an energy-dependent Gaussian distribution in nuclear spin, with the

$\sigma^2(E_x)$ referred to as the spin cutoff parameter. The spin cut-off parameter, introduced in Equation 4.30 has both spin and energy-dependent contributions.

$$\rho\left(p,h,J,E_x\right) = (2J+1)R_n(J)\omega\left(p,h,E_x\right) \tag{4.30}$$

Where $R_n(J)$ provides the spin distribution for quasi-continuum states, provided in Equation 4.31.

$$R_n(J) = \frac{2J+1}{\pi^{1/2}n^{3/2}\sigma^3}\exp\left[-\frac{\left(J+\frac{1}{2}\right)^2}{n\sigma^2}\right] \tag{4.31}$$

where, utilizing the two-component exciton model[53], for a given exciton number n this is satisfied by Equation 4.32

$$\sum_J (2J+1)R_n(J) = 1 \tag{4.32}$$

with the spin cut-off parameter σ^2 defined in Equation 4.33

$$\sigma^2 = 0.24nA^{2/3} \tag{4.33}$$

Combined with the two-component exciton model described in Equation 4.23, this provides a function for particle-hole level density in Equation 4.34.

$$\rho\left(p_\pi,h_\pi,p_\nu,h_\nu,J,E_x\right) = (2J+1)R_n(J)\omega\left(p_\pi,h_\pi,p_\nu,h_\nu,E_x\right) \tag{4.34}$$

Because of this, an adjustment to the spin cut-off parameter ($\sigma^2(E_x)$) was investigated. The `rspincut` variable acts as a global multiplier to $\sigma^2(E_x)$ which determines the width of angular momentum of level densities, essentially increasing or decreasing the chance for a reaction to populate a certain level in the residual nucleus (Equation 4.35).

$$\begin{aligned}
\sigma^2\left(E_x\right) &= \sigma_d^2 && \text{for } 0 \le E_x \le E_d \\
&= \sigma_d^2 + \frac{E_x - E_d}{S_n - E_d}\left(\sigma_F^2\left(E_x\right) - \sigma_d^2\right) && \text{for } E_d \le E_x \le S_n \\
&= \sigma_F^2\left(E_x\right) && \text{for } E_x \ge S_n.
\end{aligned} \tag{4.35}$$

with E_x being the excitation energy, E_d the continuum energy, S_n the neutron separation energy. As such, σ_d^2 is the level density for low-lying discrete levels and σ_F^2 represents level density in the continuum (Equation 4.36):

$$\begin{aligned}
\sigma_F^2 = (E_x) &= 0.01389A^{5/3}\sqrt{U/a} \\
\sigma_d^2 &= \frac{1}{3\sum_{i=N_L}^{N_U}(2J_i+1)}\sum_{i=N_L}^{N_U} J_i\left(J_i+1\right)\left(2J_i+1\right)
\end{aligned} \tag{4.36}$$

where A is the atomic mass, U is the effective excitation energy accounting for pairing shift, J_i is the level spin, and N_L and N_U represent the lower and upper discrete levels, respectively. These levels can be modified in TALYS based on the known discrete levels.

Values for `rspincut` range from 0.0-10.0 with a default value of 1. The full range was explored, with a local minimum at 0.4, as seen in Figure 4.13. This is in agreement with published results by Rodrigo *et al.* [14]. In the interest of completeness, all phenomenological level density models were investigated. While all three models displayed a minimum at or around 0.4, the BFG model had the best fit, as seen in Table 4.2.

An additional variable, `spincutmodel` (Equation 4.37), can be used to modify the formula in regions with large shell effects.

$$\begin{aligned} \texttt{spincutmodel 1} : \sigma^2 &= c\frac{a}{\tilde{a}}\sqrt{\frac{U}{a}} \\ \texttt{spincutmodel 2} : \sigma^2 &= c\sqrt{\frac{U}{a}} \end{aligned} \tag{4.37}$$

Where U is the effective excitation energy in the BFG accounting for pairing shift, a is the level density parameter, and $\tilde{a}$ is the asymptotic level density parameter. The m/g ratios for the neighboring Te isotopes were improved with `spincutmodel`=2.

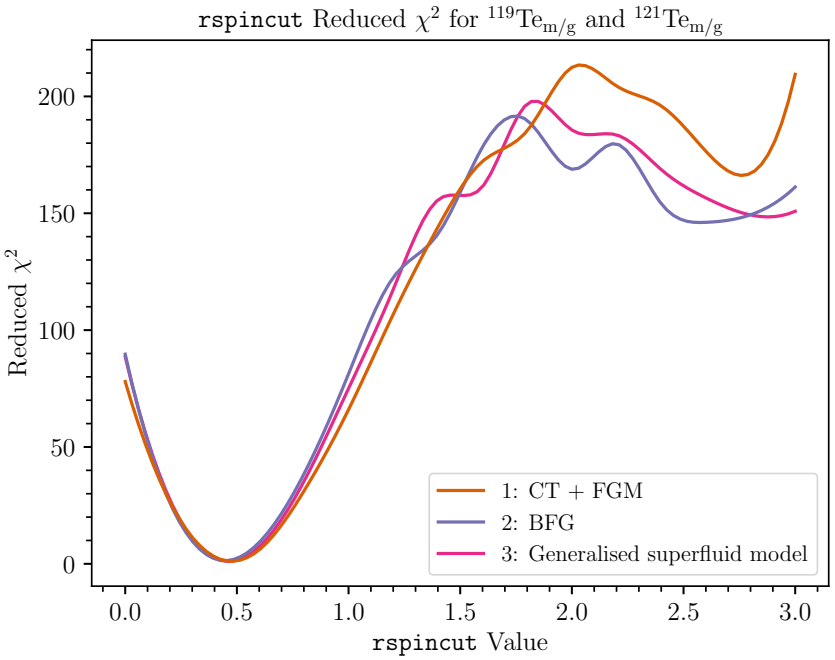

Figure 4.13: Reduced χ^2 minimization around the local minima.

Table 4.2: Phenomenological model reduced χ^2 at `rspincut` = 0.4 vs Default `rspincut` = 1.0

`ldmodel`	`rspincut` = 0.4	`rspincut` = 1.0
1	2.528029	45.0339
2	1.407499	58.32051
3	2.079992	51.68439

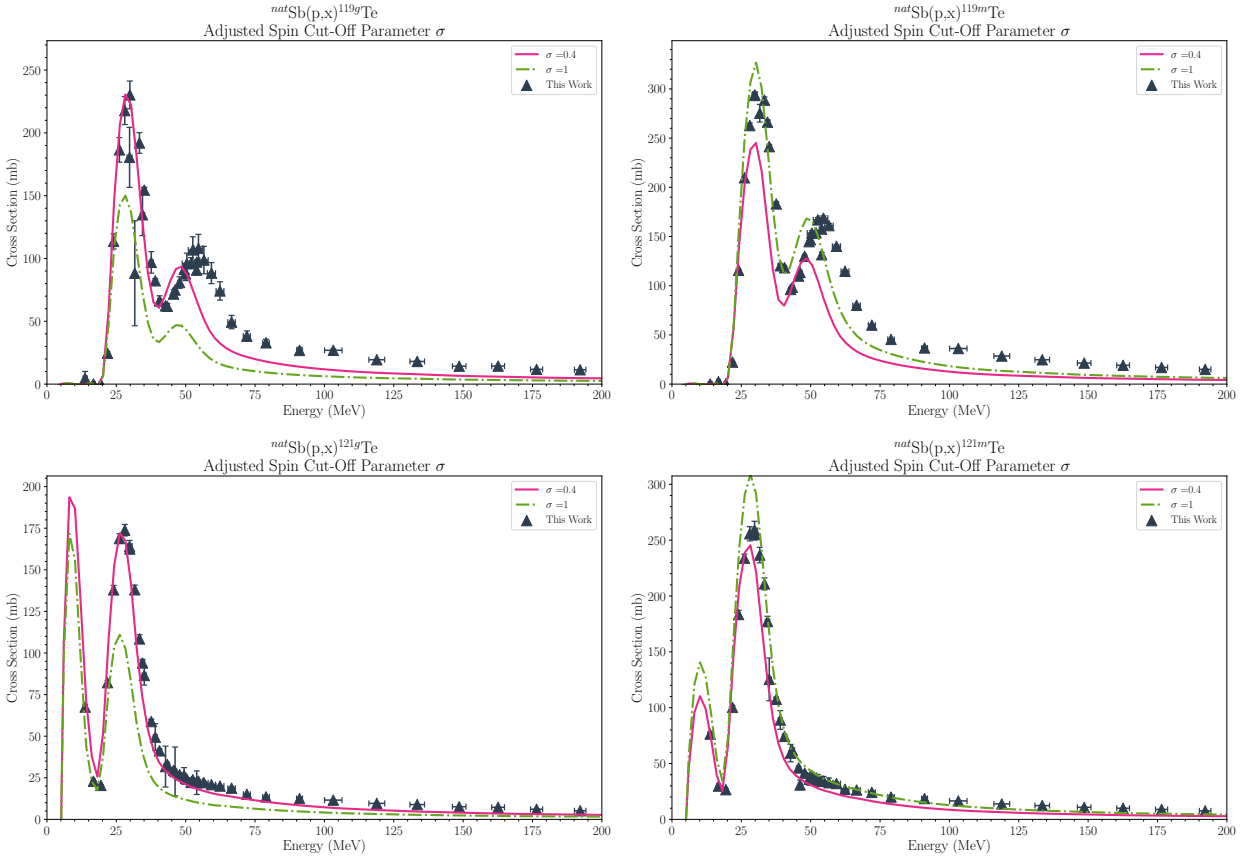

Figure 4.14: Default (1.0 - green-dashed curves) vs adjusted (0.4 - solid red line) TALYS value for `rspincut`

.

Additional validation of this reduction in spin is provided by the high-spin isomer in ^{123}Te, whose decay schema is shown in Figure 4.15.

While the ground state was not observed due to its long lifetime ($t_{1/2} > 10^{16}$ y), the `rspincut` and `spincutmodel` adjustments improved the fit for the observed isomer as seen in Figure 4.16.

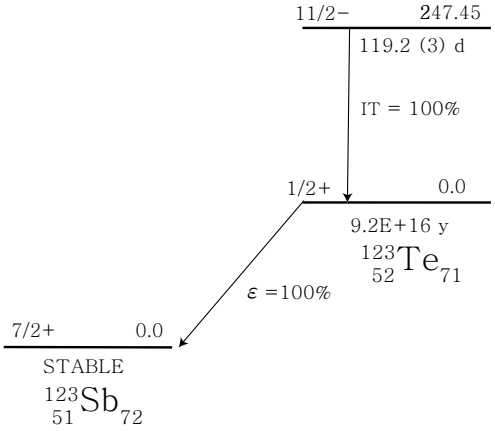

Figure 4.15: ^{123}Te Decay

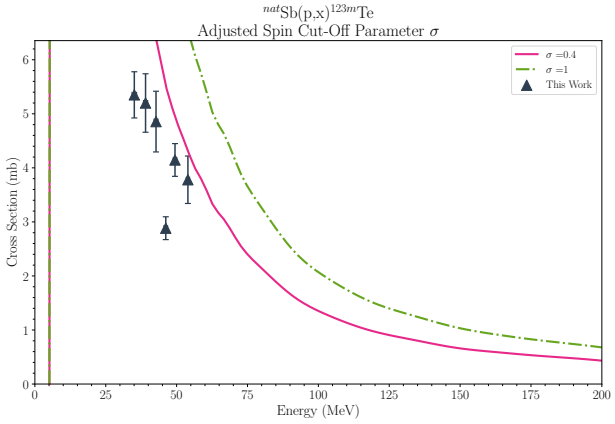

Figure 4.16: Default vs adjusted TALYS value for `rspincut` for ^{123m}Te

Figure 4.17: Decay Schema and experimental data for ^{123m}Te.

4.5 Adjustments to Pre-equilibrium Parameters

Following the work of Fox *et al.* [12], the `M2Constant` ($\mathbf{C_1}$), `M2Limit`($\mathbf{C_2}$), and `M2Shift` ($\mathbf{C_3}$) pre-equilibrium parameters were adjusted. These function as global adjustments to an energy-dependent semi-empirical equation for the square matrix element in the 2-component exciton model, seen in Equation 4.38.

$$M^2 = \frac{\mathbf{C_1} A_p}{A^3}\left[7.48\mathbf{C_2} + \frac{4.62\times10^5}{\left(\frac{E^{\mathrm{tot}}}{n.A_p} + 10.7\mathbf{C_3}\right)^3}\right] \tag{4.38}$$

In Equation 4.38, A_p is the atomic mass of the projectile, A is the atomic mass of the target nucleus, E^{tot} is the energy of the composite nucleus.

While this improved the fit by both shifting the reaction threshold to align with experimental data and a better fit in the compound peak, the model still underestimated the higher energy pre-equilibrium region in (p,xn) reactions. M^2 is a global constant that does not account for differences between protons and neutrons in residual nucleon-nucleon interactions. These can be separately adjusted in TALYS with the multiplying parameters `rpipi`, `rnunu`, `rpinu`, and `rnupi`, seen in Equation 4.39, where $R_{\pi\pi}$ is `rpipi`, $R_{\nu\nu}$ is `rnunu`, $R_{\pi\nu}$ is `rpinu`, and $R_{\nu\pi}$ is `rnupi` which represent exciton scattering probabilities for neutrons (ν) and protons (π) respectively .

$$\begin{aligned} M^2_{\pi\pi} &= R_{\pi\pi} M^2 \\ M^2_{\nu\nu} &= R_{\nu\nu} M^2 \\ M^2_{\pi\nu} &= R_{\pi\nu} M^2 \\ M^2_{\nu\pi} &= R_{\nu\pi} M^2 \end{aligned} \tag{4.39}$$

TALYS also offers the option to modify energy binning for generating the particle spectra and transmission coefficients via the `equidistant` keyword. The default mode in TALYS 1.95 is to use logarithmic energy binning, which facilitates faster and more precise calculation of the evaporation peak in the neutron spectrum, i.e. `equidistant n`. However, given that the results of these experiments extend to 200 MeV incident proton energy, logarithmic energy bin spacing is not ideal. TALYS allows for the use of equally spaced energy bins by setting `equidistant` to `y`. The effect of this adjustment on the threshold energy for the reaction is dramatic. An example is shown in Figure 4.18 for ^{116}Te, which has a high energy threshold for production. This setting was used for all reaction modeling in this analysis.

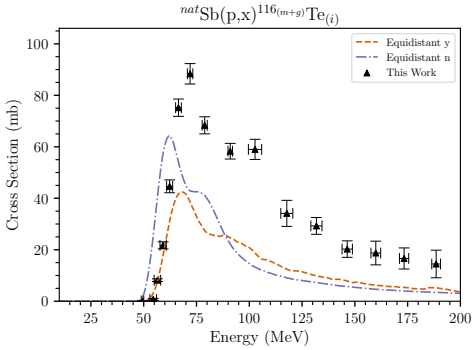

Figure 4.18: Experimental results and theoretical models for `equidistant` adjustment.

4.6 Adjustments to Optical Model Parameters

The default optical model potential in TALYS is based on the parameterization of Koning and Delaroche [50]. Further detail is provided in the TALYS 1.95 manual. The phenomenological optical model potential describes the interaction between the incident particle and the nucleons within the target nucleus, described in Equation 4.40.

$$\begin{aligned} \mathcal{U}(r,E) = &- \mathcal{V}_V(r,E) - i\mathcal{W}_V(r,E) - i\mathcal{W}_D(r,E) \\ &+ \mathcal{V}_{SO}(r,E)\cdot \mathrm{l}\cdot\sigma + i\mathcal{W}_{SO}(r,E)\cdot \mathrm{l}\cdot\sigma + \mathcal{V}_C(r), \end{aligned} \tag{4.40}$$

The optical model is comprised of real $\mathcal{V}$ and imaginary $\mathcal{W}$ components of the volume (V), surface (D), spin-orbit (SO) potentials seen in Equation 4.41

$$
\begin{aligned}
\mathcal{V}_V(r,E) &= V_V(E) f\left(r, R_V, a_V\right) \\
\mathcal{W}_V(r,E) &= W_V(E) f\left(r, R_V, a_V\right) \\
\mathcal{W}_D(r,E) &= -4 a_D W_D(E) \frac{d}{dr} f\left(r, R_D, a_D\right) \\
\mathcal{V}_{SO}(r,E) &= V_{SO}(E) \left(\frac{\hbar}{m_\pi c}\right)^2 \frac{1}{r}\frac{d}{dr} f\left(r, R_{SO}, a_{SO}\right) \\
\mathcal{W}_{SO}(r,E) &= W_{SO}(E) \left(\frac{\hbar}{m_\pi c}\right)^2 \frac{1}{r}\frac{d}{dr} f\left(r, R_{SO}, a_{SO}\right)
\end{aligned}
\tag{4.41}
$$

where $V_V(E)$, $W_V(E)$, $W_D(E)$, $V_{SO}(E)$, and $W_{SO}(E)$ are energy-dependent potential well depths and $f(r, R_i, a_i)$ is the Woods-Saxon form factor. These variables have adjustable parameters detailed in Equation 4.43. The Coulomb potential energy component for charged particles is given by Equation 4.42

$$
\begin{aligned}
\mathcal{V}_C(r) &= \frac{Z(z)e^2}{2R_C}\left(3 - \frac{r^2}{R_C^2}\right), \quad \text{for } r \le R_C \\
&= \frac{Z(z)e^2}{r}, \quad \text{for } r \ge R_C,
\end{aligned}
\tag{4.42}
$$

where R_C is the Coulomb radius, r is the radius, and $Z(z)$ is the charge of the projectile.

The formulae for the energy-dependent component of the optical model parameters for protons or neutrons are provided in Equation 4.43, with the TALYS-adjustable parameters denoted in **bold**:

$$
\begin{aligned}
V_V(E) &= \mathbf{v_1}\left[1 - \mathbf{v_2}\left(E - E_f\right) + \mathbf{v_3}\left(E - E_f\right)^2 - \mathbf{v_4}\left(E - E_f\right)^3\right] \\
W_V(E) &= \mathbf{w_1}\frac{\left(E - E_f\right)^2}{\left(E - E_f\right)^2 + \left(\mathbf{w_2}\right)^2} \\
\mathbf{R_V} &= \text{ constant} \\
\mathbf{a_V} &= \text{ constant} \\
W_D(E) &= \mathbf{d_1}\frac{\left(E - E_f\right)^2}{\left(E - E_f\right)^2 + \left(\mathbf{d_3}\right)^2}\exp\left[-\mathbf{d_2}\left(E - E_f\right)\right] \\
\mathbf{R_D} &= \text{ constant} \\
\mathbf{a_D} &= \text{ constant} \\
V_{SO}(E) &= \mathbf{v_{so1}}\exp\left[-\mathbf{v_{so2}}\left(E - E_f\right)\right] \\
W_{SO}(E) &= \mathbf{w_{so1}}\frac{\left(E - E_f\right)^2}{\left(E - E_f\right)^2 + \left(\mathbf{w_{so2}}\right)^2} \\
\mathbf{R_{SO}} &= \text{ constant} \\
\mathbf{a_{SO}} &= \text{ constant} \\
\mathbf{R_C} &= \text{ constant},
\end{aligned}
\tag{4.43}
$$

where $\mathbf{R_i}$ and $\mathbf{a_i}$ are constants describing the geometry of the Woods-Saxon shape form factors for the $V_i(E)$ and $W_i(E)$ potential wells.

While several variables were analyzed to adjust the model's fit to experimental results, many were difficult to justify from a physical perspective. Both the proton and neutron potentials were investigated. $\mathbf{R_i}$ and $\mathbf{a_i}$ values, including `rvadjust`, `avadjust`, etc. were initially adjusted, with further details in Appendix G. These values affect form factors $f(r, R_i, a_i)$, therefore impacting **both** the real and imaginary components of the V, D, SO, and C potentials. Although adjusting values improved fit to a certain extent, modifying the real Volume potential, for example, is difficult to justify given the assumption of fixed nuclear radius. They were, therefore, left at default values. However, the imaginary potentials, adjustable through variables in the $W_i(E)$ formulas in Equation 4.43, were modified, specifically $W_V(E)$ variables $\mathbf{w_1}$ and $\mathbf{w_2}$, `w1adjust` and `w2adjust` respectively, for the volume term of the imaginary neutron potential well. `w1adjust` was increased to 2.5, while `w2adjust` was decreased to 0.6. This is visualized in Figure 4.19, with `w1adjust` effectively deepening the well and `w2adjust` narrowing the well, affecting the absorption and emission of neutrons in a nuclear reaction.

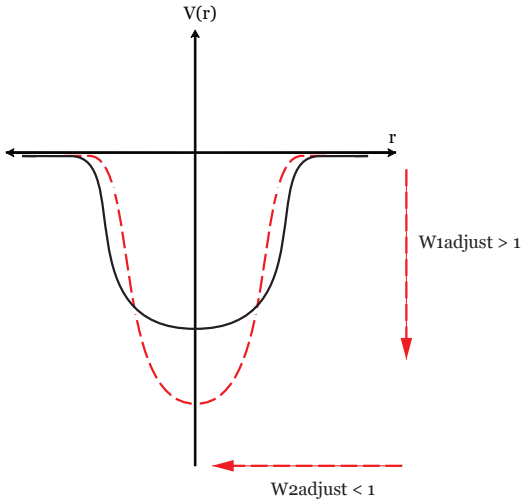

Figure 4.19: TALYS adjustments to the imaginary part of neutron optical model potential

.

Lastly, for incident particle energies approaching 200 MeV, further adjustments to the real and imaginary volume potentials may have been needed. However, modifying these parameters did not yield significant changes to the model.

4.7 Comparison of modeled and measured independent channels

The vast majority of the independent channels, including all of the (p,xn) reactions that result in the formation of Te residual products were used for optimization. These showed an overall improvement in goodness of fit using the χ^2 calculations referenced in Equations 4.26, 4.27, 4.28, and 4.29. Tabulated results can be seen in Table 4.3

Table 4.3: Optimized χ^2 for Independent Cross Sections and Adjusted TALYS Parameters

	TALYS 1.95 Default	Optimized Parameters	Improvement Ratio
Cumulative χ^2	27.54	4.42	6.23
Maximum χ^2	31.43	4.15	7.58

Twelve of the largest measured reaction channels were used to optimize TALYS parameters. The plotted results are shown in Figures 4.20, 4.21, 4.21, 4.22, 4.22, 4.23, 4.23, 4.24, 4.24, 4.25, 4.25, and 4.26 with tabulated results by isotope in Table 4.5.

^{nat}Sb(p,xn)Te channels had the highest magnitude cross sections and, therefore, had the largest influence on the overall χ^2 minimization procedure. In contrast, the smaller channels that resulted in the formation of Sb residual products showed mixed results. Some channels show a poorer overall fit between the measured and modeled residual product cross sections. This systematic disagreement between optimized modeling for Sb(p,x)Sb channels, which could also be formed via ^{nat}Sb(n,xn)Sb reactions, further supports the idea that there is significant co-production of neutron-deficient Sb nuclei via secondary neutrons produced in the target stacks. Neutron-deficient products with the same Z as the target foil in high-energy stacked target activation experiments may be misinterpreted, and further studies of secondary neutron production should be performed to explore the role of the particles in isotope production.

In order to further explore the potential contributions of (n,xn) reactions from secondary neutrons on the production of neutron-deficient Sb nuclei a further review of these channels alone and a holistic check on all previous TALYS adjustments was performed. Nevertheless, this does not wholly explain why the reaction model adjustments do not improve the Sb and In residual channels used. The best reaction model parameters from this second optimization were all generally in agreement *except* for adjustments to the pre-equilibrium residual nucleon-nucleon interactions `rpipi`, `rpinu`, `rnupi`, and `rnunu`, shown in Table 4.4. The significant deviation in the magnitude of the parameters required to fit the Sb and In excitation functions,

Table 4.4: Adjustments to pre-equilibrium to improve fit for Sb and In products.

TALYS Parameter	Best Fit (Te)	Best Fit (Sb, In)
`rpipi`	1	0.25
`rpinu`	1.5	4
`rnupi`	1.5	0.75
`rnunu`	1.5	0.25

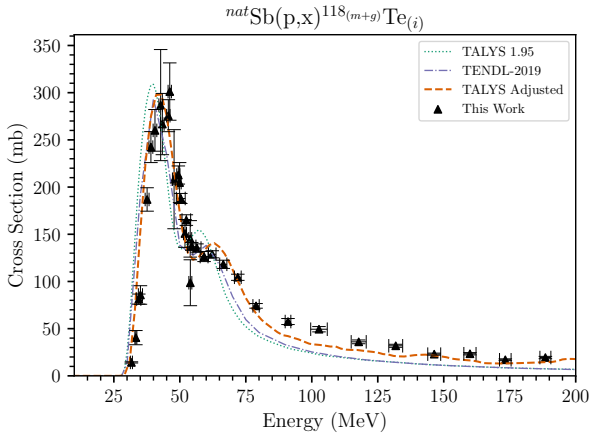

Figure 4.20: Experimental and theoretical measurements for ^{118}Te.

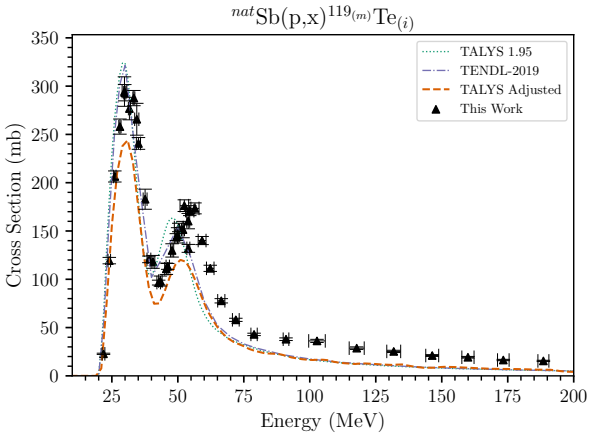

Figure 4.21: Experimental and theoretical measurements for ^{119m}Te.

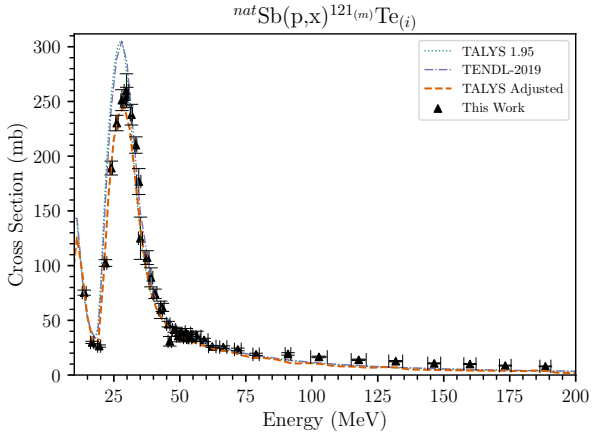

Figure 4.21: Experimental and theoretical measurements for ^{123m}Te.

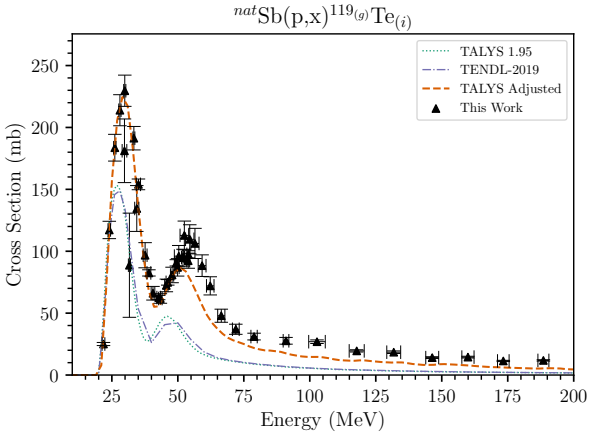

Figure 4.22: Experimental and theoretical measurements for ^{119g}Te.

including, most notably, a large increase in `rpinu` and decrease in `rnunu`. These adjustments would enhance proton emission while decreasing neutron emission, but significantly dampened the compound peaks of residual Te products.

Lastly, among the parameters explored but **not** ultimately adjusted, improvements were seen when optical model parameters for the real part of the potential well were adjusted. However, as discussed in section 4.6, it is difficult to justify changing these variables.

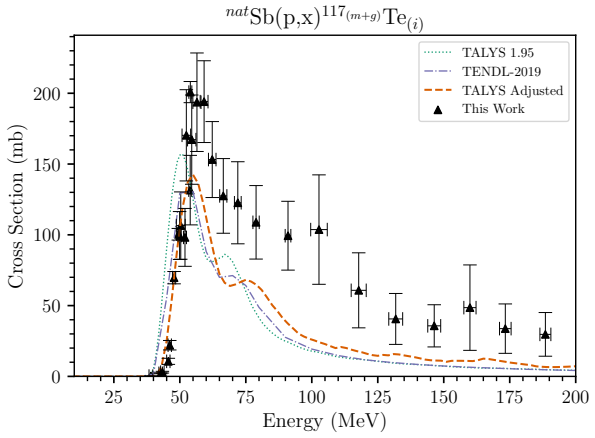

Figure 4.22: Experimental and theoretical measurements for ^{117}Te.

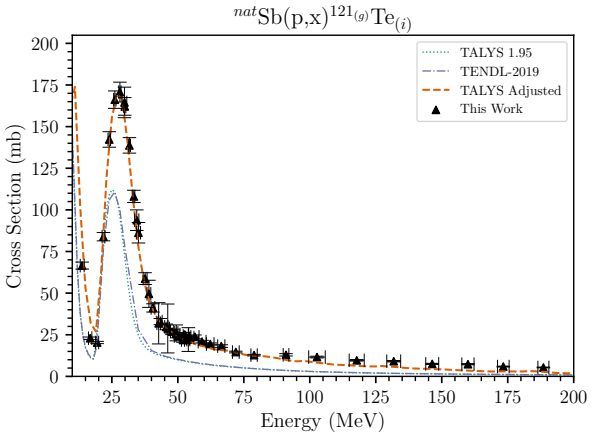

Figure 4.23: Experimental and theoretical measurements for ^{121g}Te.

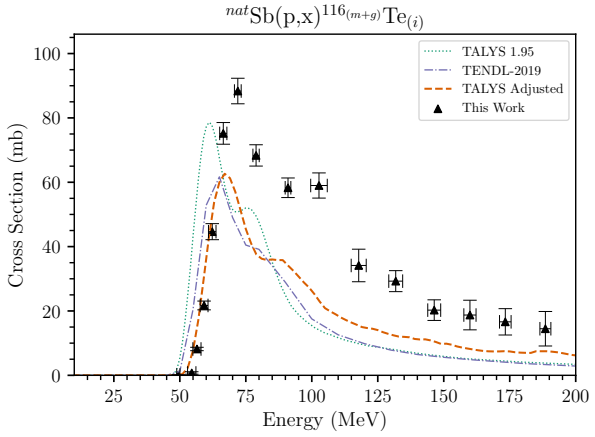

Figure 4.23: Experimental and theoretical measurements for ^{116}Te.

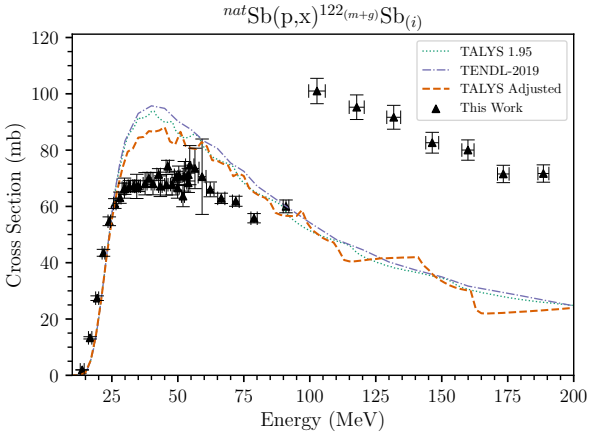

Figure 4.24: Experimental and theoretical measurements for ^{122}Sb.

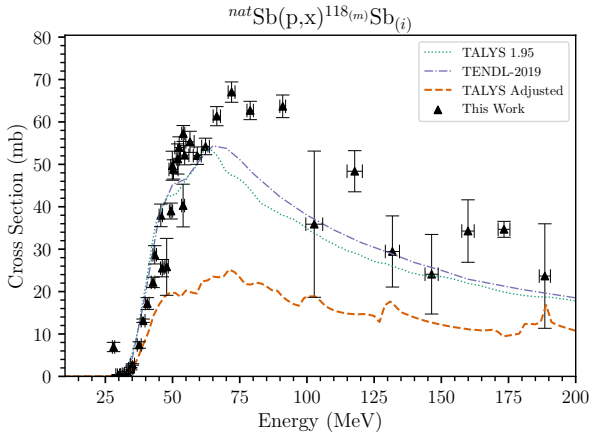

Figure 4.24: Experimental and theoretical measurements for ^{118m}Sb.

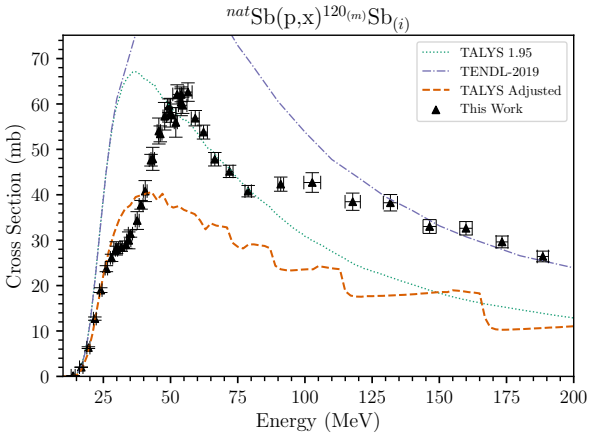

Figure 4.25: Experimental and theoretical measurements for ^{120m}Sb.

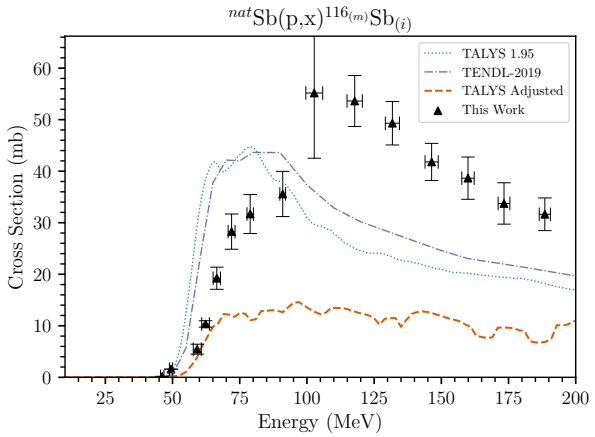

Figure 4.25: Experimental and theoretical measurements for ^{116m}Sb

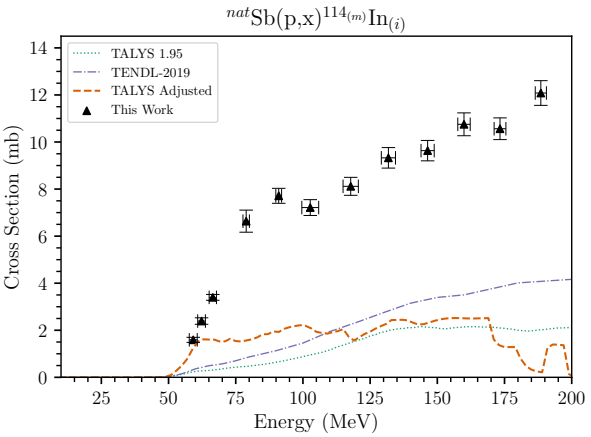

Figure 4.26: Experimental and theoretical measurements for ^{114m}In

Table 4.5: Tabulated Chi Square improvements by isotope

Isotope	Sum of Measurements (mb)	Maximum Cross Sectio (mb)	χ^2 (Default)	χ^2 (Optimized)	Improvement Ratio
^{118}Te	4497.24	301.19	457.22	41.36	11.06
^{119m}Te	5273.01	294.37	211.14	97.58	2.16
^{121m}Te	3229.94	259.81	68.35	30.44	2.25
^{119}Te	3424.78	229.65	148.76	22.78	6.53
^{117}Te	2534.30	200.82	1148.87	20.24	56.78
^{121}Te	2095.37	170.73	190.68	35.33	5.40
^{116}Te	558.04	88.36	1293.79	50.70	25.52
^{122}Sb	2228.27	74.65	71.19	54.11	1.32
^{118m}Sb	1000.21	67.04	42.66	122.45	0.35
^{120m}Sb	1463.03	62.62	381.31	74.97	5.09
^{116m}Sb	132.36	35.58	345.40	15.75	21.93
^{114m}In	89.42	12.08	328.37	246.69	1.33

4.8 Validation with Cumulative Cross Sections and Smaller Independent Channels

Isotopes produced both directly and indirectly via the decay of other reaction products are referred to as cumulative channels. It is particularly challenging, or not possible to deconvolute these cumulative channels into their independent counterparts. In lieu of this, the cumulative results add in the parent product cross sections and corresponding branching ratio along the drip line for the isotope. Because several products comprise these cross sections, the physics behind their modeling is significantly more complex. Using these products to guide reaction modeling is, therefore, not appropriate. However, these channels provide an opportunity to validate the adjustments made to improve the fit to the independent channels.

Nine cumulative channels were used for validation: ^{109g}In, ^{109g}Sn, ^{110g}Sn, ^{111g}In, ^{111g}Sn, ^{113g}Sn, ^{115g}Sb, ^{117m}Sn, and ^{119m}Sn. ^{91m}Nb was excluded because the `equidistant y` command in TALYS 1.95 does not provide results for this residual product, despite the reaction threshold being within the incident proton energy from these experiments.

Validation also includes 3 independent channels: ^{106m}Ag, ^{113m}Sn and ^{123m}Te. These were either weakly fed channels or had few experimental measurements and were, therefore, used for validation instead of sensitivity analysis. Much like ^{91m}Nb, ^{89m}Nb was excluded since `equidistant y` in TALYS 1.95 does not provide results for this residual product.

These validation cross sections are illustrated in Figures 4.27, 4.28, 4.28, 4.29, 4.29, 4.30, 4.30, 4.31, 4.31, 4.32, 4.32, and 4.33, with default and optimized input parameters.

The improvement in the goodness of fit to parameter adjustments cumulative channels due to the parameter optimization is shown in Table 4.6.

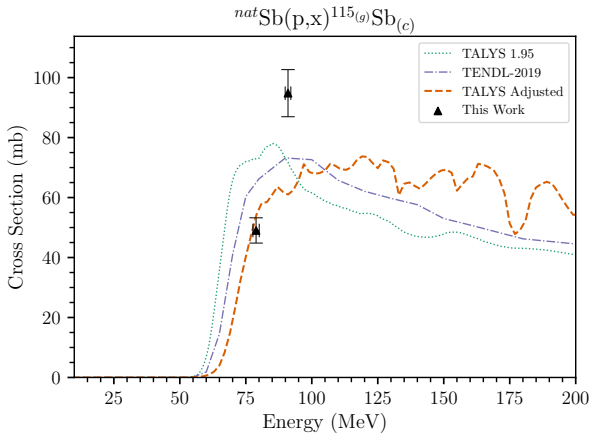

Figure 4.27: Experimental and theoretical measurements for ^{115}Sb.

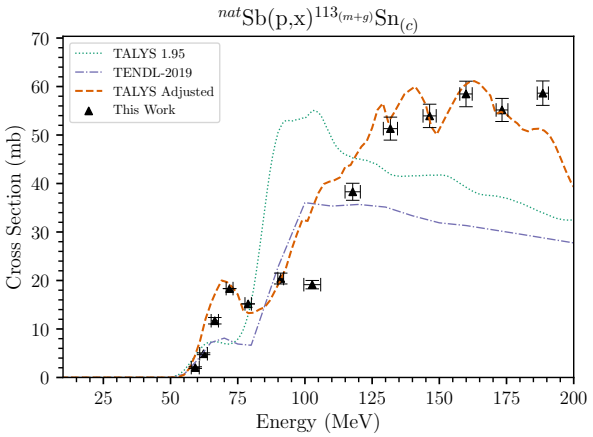

Figure 4.28: Experimental and theoretical measurements for ^{113}Sn.

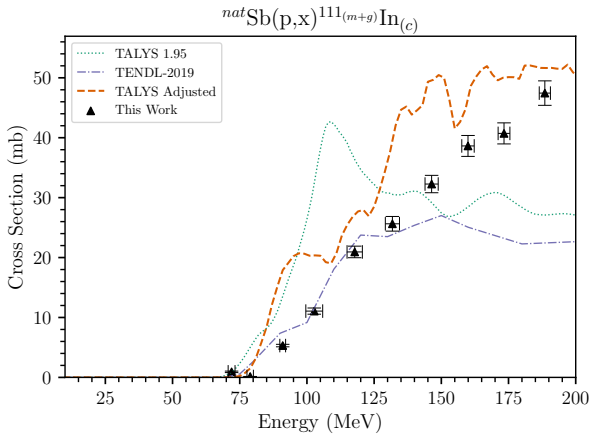

Figure 4.28: Experimental and theoretical measurements for ^{111}In.

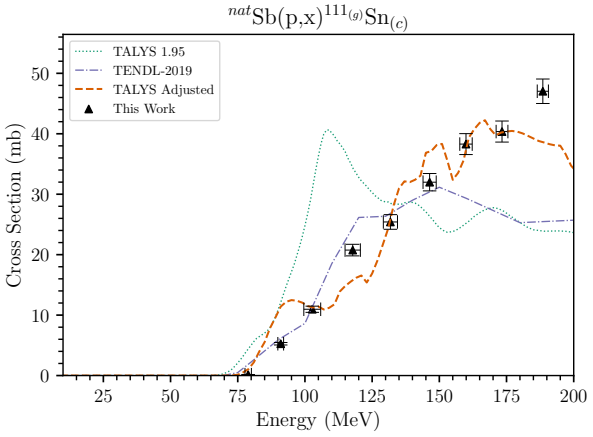

Figure 4.29: Experimental and theoretical measurements for ^{111}Sn

.

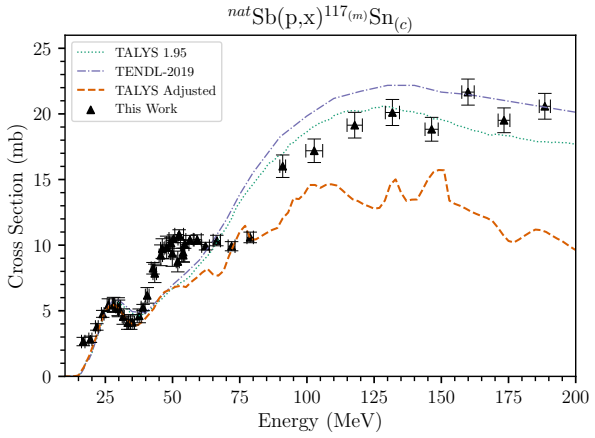

Figure 4.29: Experimental and theoretical measurements for ^{117m}Sn.

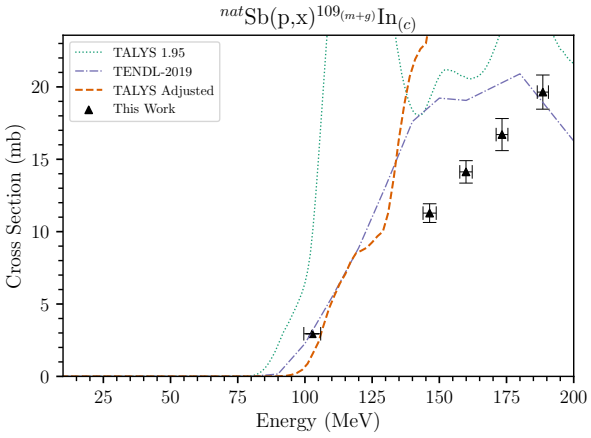

Figure 4.30: Experimental and theoretical measurements for^{109}In.

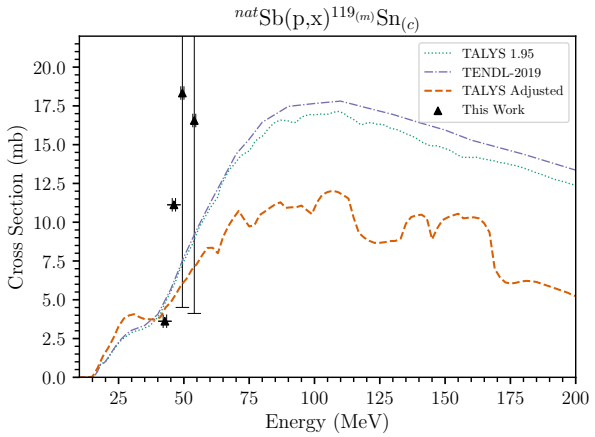

Figure 4.30: Experimental and theoretical measurements for ^{119m}Sn.

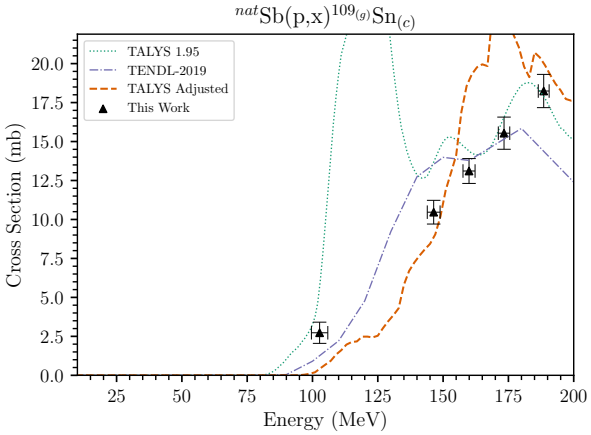

Figure 4.31: Experimental and theoretical measurements for^{109}Sn.

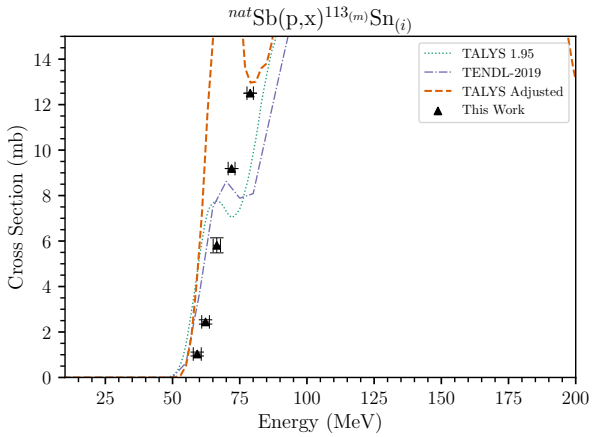

Figure 4.31: Experimental and theoretical measurements for ^{113m}Sn.

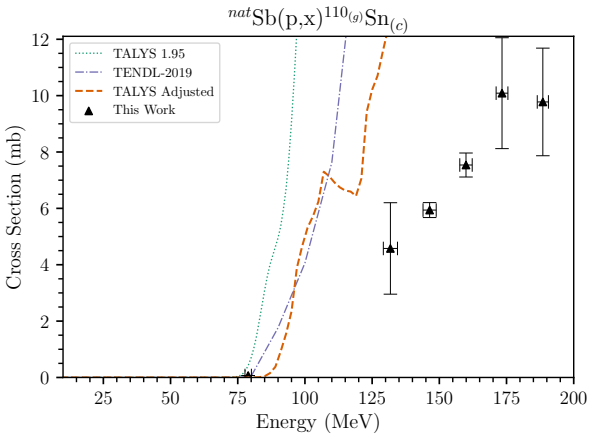

Figure 4.32: Experimental and theoretical measurements for^{110}Sn.

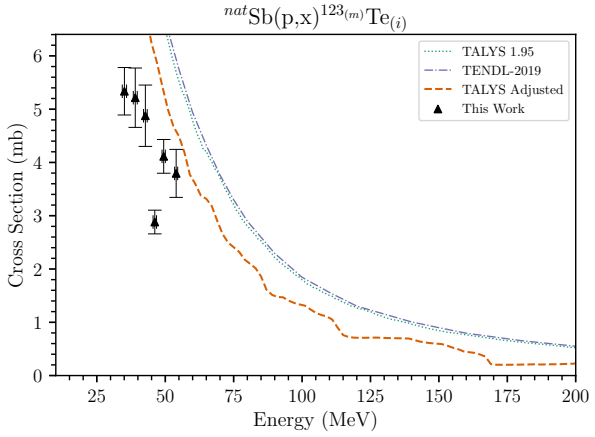

Figure 4.32: Experimental and theoretical measurements for ^{123m}Te

.

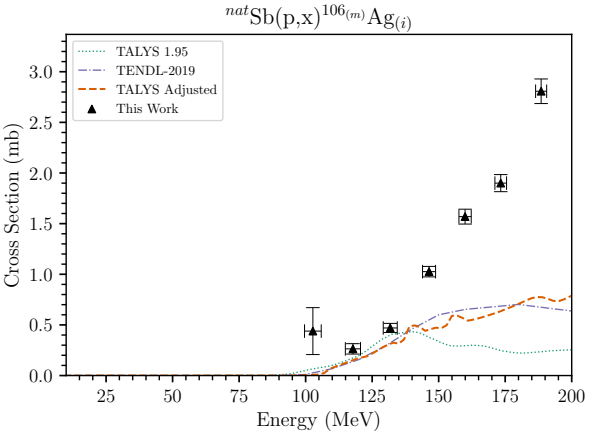

Figure 4.33: Experimental and theoretical measurements for ^{106m}Ag

.

Table 4.6: Default and optimized parameters for validation cross sections with improvement ratio.

	TALYS 1.95 Default	Optimized Parameters	Improvement Ratio
Cumulative σ	1070.88	86.41	12.39
Maximum σ	1073.90	89.17	12.04

Again, however, several validation cross sections had a decrease in fit with the optimized parameters. The optimized parameters involved adjustments to optical model parameters, which affect both the real and imaginary optical model potentials. Table 4.7 provides the optimized adjustments.

Table 4.7: Optimal parameter adjustments for validation cross sections

TALYS Parameter	Best Fit (Independent)	Best Fit (Validation)
`rvadjust`	1	2.5
`rwadjust`	1	0.5
`avadjust`	1	1.5
`awadjust`	1	1.5

4.9 Comparison to overall predicted TENDL nonelastic scattering cross section

As a check, the parameter adjustments performed in this analysis were compared against the total nonelastic scattering channel in TENDL–2019. The values agree with the TENDL–2019 results, likely the result of strictly using global parameter adjustments (Figure 4.34).

Table 4.8: Optimized TALYS Parameter Adjustments

TALYS Parameter	Value
`ldmodel`	2
`strength`	5
`equidistant`	y
`rspincut`	0.4
`spincutmodel`	2
`colldamp`	n
`w1adjust`	n 2.5
`w2adjust`	n 0.6
`preeqspin`	1
`preeqmode`	1
`mpreeqmode`	2
`m2constant`	2

4.10 Conclusions and Takeaways from Reaction Modeling

The reaction model fits were dominated by the largest independent reaction channels, specifically ^{nat}Sb(p,xn) channels for residual Te products. The optimized parameters are provided in Table 4.8

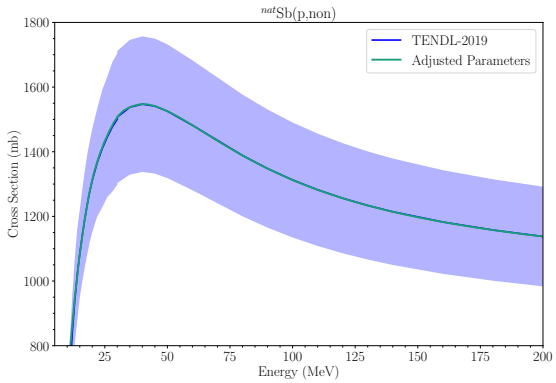

Figure 4.34: Total Nonelastic scattering cross section with TALYS adjustments compared to TENDL–2019.

The overall fit for these channels was dramatically improved, even in isomer-to-ground-state ratios. However, this research raises several concerns. The fit in the pre-equilibrium region is still imperfect, as illustrated both by other independent cross sections as well as by the validation cross sections.

Analyzing the remaining independent cross sections indicated a need for adjustment to the residual nucleon-nucleon interaction in the pre-equilibrium region, but these values were adjusted to such a significant degree that it was deemed not physically defensible. These adjustments concurrently flattened the compound peaks in the Te channels, producing worse fits for Te channels.

The validation channels, 9 of which were cumulative and 3 independent, had improved fit overall but, again, the largest reaction channels dominated this optimization. A review of the validation channels alone suggested changes to the form factor values in the optical potential model. This impacts both the real and imaginary components of the model, which suggests changing the physical volume of the nucleus for this specific reaction.

This research proposes that secondary neutron production plays a significant role in stacked target measurements at high incident proton energy. Future experimental work can elucidate this by including neutron monitor foils at the back of the stack when incident charged particle current is stopped. Further information can be gathered via experimental work using prompt gamma irradiation of a single foil and observation of neutron scattering with an array of neutron detectors.

Chapter 5

Business Model

The measurements and reaction modeling work presented are valuable research for the scientific community. Still the viability of production for these medical radionuclides is essential for preclinical and clinical testing of potential medical treatments. The US Department of Energy provides over 35 radionuclides for application, with dozens more under development. These isotopes can be licensed for commercial production. Among this list, ^{117m}Sn has already demonstrated significant potential for the treatment of osteoarthritis. Exubrion Therapeutics has commercialized Synovium OA®, a ^{117m}Sn colloid for the treatment of canine osteoarthritis[57]. The parent company, Serene LLC, is conducting preclinical trials for treating rheumatoid and osteoarthritis in humans. In addition, Serene is utilizing ^{117m}Sn in preclinical trials for small mass tumors in the bile duct (Cholangiocarcinoma), Phase 2 trials for treating bone metastases in collaboration with the National Cancer Institute, and Phase 1 clinical trials for carotid artery stenosis (atherosclerosis).

This chapter will explore the potential for commercial production of this radionuclide. The market size and business startup considerations were driven by case studies from establishing a facility at UC Berkeley and insights from Dr Richard Friefelder, who has been instrumental in establishing facilities at The University of Pennsylvania and The University of Chicago [58].

5.1 Market Size

As of 2012, arthritis was estimated to afflict 22.7% of the US adult population (52.5 million) in 2012 and is projected to increase to 25.9%, or 78.4 million adults, by 2040 [59]. Osteoarthritis is among the most expensive diseases treated in the US. As of 2013, arthritis-related medical costs per year accounted for $139.8 billion, which, when accounting for lost income, exceeded $300 billion. [60]. As a progressive disease, palliative care is required. This disease has shown a positive correlation to secondary issues, including depression, anxiety, stress, physical limitation, and social function. [61]. There is not only a large market for novel treatments of this disease but also a societal obligation to do so.

^{117m}Sn has also shown promise for palliative care of bone metastases. This is a frequent complication of metastatic cancer, and up to 80% of afflicted patients experience pain. With growing cancer rates, this accounts for an estimated 350,000 deaths in the US per year[62]. Treatment can be applied in a single dose, the lowest of which among various existing theranostic treatments was 3 Gy, or via dose fractionation, with the highest dose being 60 Gy over 30 treatments[62]. Since ^{117m}Sn it is still in pre-clinical or clinical trials for human use, the treatment dose for treatment can only be speculated on. This is discussed in section 5.2.

Another potential application is in the treatment of Cholangiocarcinoma, or cancer in the bile duct. While it is a relatively rare disease afflicting only 1.2-2.4 per 100,000 members of the US population, the incidence is increasing. It is a particularly aggressive form of cancer, and life expectancy upon diagnosis has a 5-year survival rate of only 10%[63]. In a study of 1,298 patients, the average survival time was only 5.3 months, with treatment costs averaging $7,743 per month as of 2019[64]. Previous work by He *et al.*[65] indicated success in treating via brachytherapy with a biliary duct radioactive stent using ^{103}Pd.

Serene LLC has filed patents using ^{117m}Sn-colloid stent [66] as well as a method for chemical separation[57] of electroplating [67]

5.2 Cyclotron Facility Startup Considerations

A large portion of radionuclides are produced in nuclear reactors. New reactor construction has stalled in the United States, and the aging reactor fleet is being decommissioned. Simultaneously, there is increased demand for these isotopes. Production via a cyclotron or linear accelerator (LINAC) is emerging as the best solution. Along with the demand outpacing the supply, there are advantages to using accelerators to produce these radionuclides. Facility supervision is more manageable, and the working environment is safer. Furthermore, accelerators present a far smaller risk of nuclear proliferation than nuclear reactors. They also benefit from lower operation, maintenance, and decommissioning costs. Finally, accelerator-produced radionuclides produce 90% less waste than reactor production [68].

However, setting up a cyclotron-based isotope production facility is not without significantly challenging considerations including target fabrication and irradiation, establishing facilities for chemical separation and labeling of radiopharmaceuticals. These are the first three steps shown in Figure 5.1.

The complex interplay among these considerations requires the combined expertise and input of various individuals to recognize and address the facility's needs throughout the design and construction process and beyond. The success of establishing a commercial facility requires cooperation among experts in architecture, radiochemistry, nuclear medicine, physics, radiation safety, regulatory requirements, marketing, and administration. This group can determine the programmatic goals, the location and type of space, regulatory compliance needs, and the profit potential.

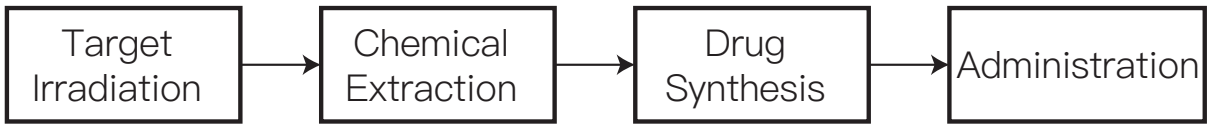

Figure 5.1: Simplified Isotope Production Pipeline [68].

Programmatic Goals

A facility does not need to focus strictly on the production of a single isotope, like ^{117m}Sn; several valuable radionuclides can be produced via proton bombardment with planning and precautions to prevent cross-contamination. The simplest way to implement the production of multiple radionuclides is to leverage their basic physical characteristics, the most fundamental of which is the isotope half-life. Short-lived isotopes that decay to stable progeny will decay to background levels within a few days. Depending on target separation chemistry, waste stream, and the radiolabeling to produce the final radiopharmaceutical, a single hot cell or clean room can be used for the production and processing of multiple radionuclides with minimal downtime between processing by simply allowing the radionuclide to decay over multiple $t_{1/2}$.

A fundamental example of multiple radionuclide production, while maintaining Current Good Manufacturing Practice (cGMP) section 5.2, is ^{18}F and ^{68}Ga, commercially used PET imaging radionuclides. ^{18}F, with $t_{1/2} = 109.8$ m, can be produced via ^{18}O(p,n) reactions with 16 MeV protons on a water target[28]. ^{68}Ga, with a halt-life of 68 m, can be produced via the ^{68}Zn(p,n) reaction with 14 MeV incident protons[69].

These radionuclides are widely used commercial isotopes, but their short $t_{1/2}$ require the facility to be located in close proximity to the patient imaging facility. This could limit the profitability of production based on population density and the availability of space for a facility. Of course, this issue can be mitigated by focusing development on isotopes with longer$t_{1/2}$, enabling shipment and storage options. This includes radionuclides in pre-clinical trials. Another example to consider is the co-produced, dually diagnostic and therapeutic radionuclides $^{133/135}$La, produced via ^{nat}Ba(p,x). High yield with minimal contaminants can be achieved at incident proton energies of 22 MeV [70].

An important aspect of establishing programmatic goals is flexibility of the facility while isotope needs change over time. The maximum potential yield for radiopure ^{nat}Sb(p,x)^{117m}Sn is maximized at around 45 MeV as seen in experimental results from these experiments. Figure 5.2. Beyond incident particles at that energy, the competing contaminant ^{119m}Sn, with a $t_{1/2}$ of 293.1 (7) d, will be present in chemical separation of Sn.

The ^{nat}Sb(p,x)^{119m}Te production is highly impacted by co-produced contaminants, Best™ Cyclotron Systems, further discussed in section 5.2, provides a list of potential radionuclides

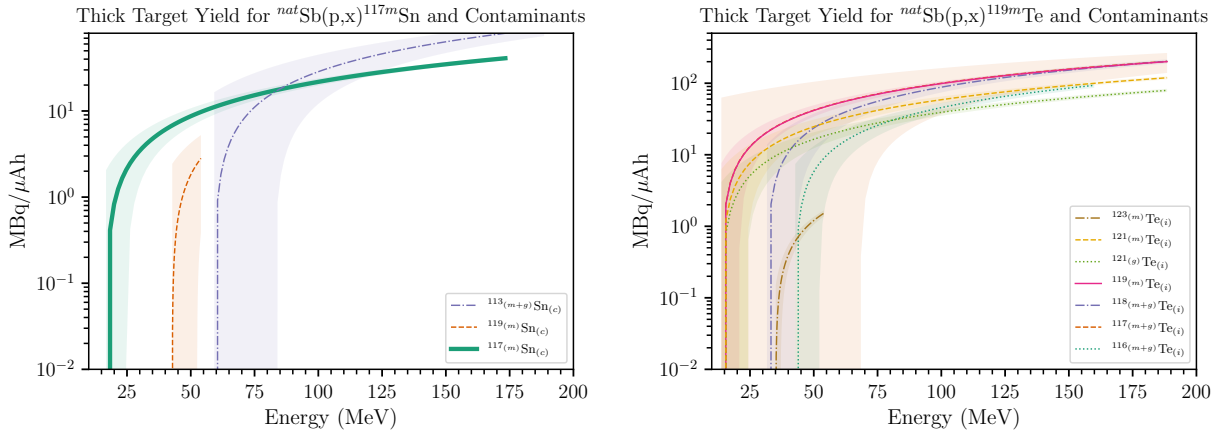

(a) (b)

Figure 5.2: Yield curves for the isotopes of interest with competing potential contaminant channels.

under development or in commercial production in Table 5.1.

Table 5.1: Potential Isotopes for Production at incident energies up to 70 MeV [71].

Isotope	$t_{1/2}$	Status
^{52}Fe	8.3 h	R&D
^{122}Xe	20.1 h	R&D
^{28}Mg	21 h	R&D
^{128}Ba	2.43 d	R&D
^{67}Cu	2.58 d	Potentially Commercial
^{97}Ru	2.79 d	R&D
^{117m}Sn	13.6 d	Potentially Commercial
^{82}Sr	25.4 d	Commercial
^{225}Ac	10 d	Commercial

Facility Design

The Database of Cyclotrons for Radionuclide Production, available through the International Atomic Energy Agency (IAEA), tracks cyclotron facilities in member countries worldwide. As of 2024, there are over 1500 cyclotron facilities in operation worldwide for medical radiopharmaceutical production. The database provides facility location, cyclotron

manufacturer and model, and proton energy. There are over 240 cyclotrons in the United States alone, but access to high-energy facilities, as defined in Table 5.2, is limited.

Table 5.2: Medical Cyclotron Energies and Applications[68, 72]

Cyclotron Size	Energy Range (MeV)	Application
Small medical cyclotron	< 20	Short-lived radionuclides for PET
Medium-energy cyclotron	20–35	Production of SPECT and some PET radionuclides
High-energy cyclotron	> 35	Production of radionuclides for therapy

While low-energy cyclotrons have the benefit of minimizing contaminant isotopes, require less operational energy, have far more simplified cooling systems, and require smaller targets, they limit the isotopes that can be produced and may require enriched targets, increasing costs. As energies increase, these benefits and drawbacks swap. Contaminant products can potentially increase as more reaction channels open, and the incident energy requires increased cooling. However, the greater number of products can be a net benefit depending on the radionuclide of interest, as certain products require a specific incident particle reaction energy for production.

There are few high-energy cyclotrons or particle accelerator facilities for commercial production of radionuclides. In fact, even worldwide, there are limited high-energy cyclotron facilities for commercial isotope production, as seen in Table 5.3.

Table 5.3: High-Energy Cyclotron and LINAC Facilities for Radionuclide Production[73].

Organization	Location	E_p for Isotope Production (MeV)	Beam Current (μA)
Institute for Nuclear Research, RAS	Troitsk-Moscow,Russia	160	120
Los Alamos National Laboratory (LANL)	Los Alamos, NM USA	100	200
Brookhaven National Laboratory (BNL)	Upton, New York USA	200	120
Canada's Particle Accelerator Centre TRIUMF	Vancouver, Canada	110, 500	80
iThemba Laboratory for Accelerator Based Sciences (LABS)	Faure, South Africa	66	250
ARRONAX (Accelerator for Research in Radiochemistry and Oncology at Nantes Atlantique)	Nantes,France	70	2 x 150
Curium	Indianapolis,IN USA	70	2 x 100

^{117m}Sn production yield via ^{nat}Sb(p,x) is optimized around 45- 50 MeV, requiring a high energy cyclotron. Two well-known cyclotron system producers are IBA Radiopharmacy Solutions, Inc. (IBA) and Best® Cyclotron Systems(Best). IBA provides the Cyclone® 70

Proton (IBA Cyclone 70), with a variable energy range from 30-70 MeV with a maximum current of 750 µA and the flexibility of two beam lines [74]. Similarly, Best provides the Best® 70p Cyclotron (Best 70p Cyclotron), with a variable energy from 35-70 MeV, a maximum current of 700 µA. The design can be configured to raise current to 1000 µA and up to 6 beam lines. [71]

While the cyclotron itself is a significant investment, the infrastructure considerations are a larger cost. IBA provides consulting through IntegraLab® (IntegraLab) for facility design and installation of necessary equipment, ensuring regulatory compliance. Best provides guidance as well through TeamBest® (TeamBest).

Consultation with cyclotron designers and design input with a highly experienced architectural firm throughout the design process is essential. Since the design of a cyclotron facility is a fairly niche field, case studies recommend hiring an architectural firm specializing in the design of pharmacology or virology laboratories with high bio-safety concerns. Compliance with regulatory standards ensuring workplace safety and high-quality radiopharmaceutical products are crucial considerations in each step of design and construction. This includes considerations for shielding, ventilation systems, drainage, floor loading (as an assembled K-70 cyclotron magnet weighs an estimated 220 tons), power, HVAC, and many other requirements to meet building codes, safety codes, certifications, and Nuclear Regulatory Commission (NRC) regulations. Local governments and municipalities may impose additional requirements that would increase the total facility cost.

Site requirements start with estimating space requirements. This includes determining whether the facility will be constructed in a "Legacy Space"- a location that has been previously used as a facility—or a "Green Space"—essentially a blank canvas. Cost and geographic location also play a role in determining this, but a green space has the benefit of more design flexibility, whereas a legacy space may introduce size constraints. Conversely, a legacy space may have existing construction that can be repurposed, while a green space introduces the costs of building from the ground up. Again, though, this could serve as a benefit if the legacy space requires significant demolition and redesign.

In an extremely high-level overview, facility design incorporates the cyclotron vault (including the installation process for the main magnet), target vaults, control room, power supply room, and service rooms. In addition, active work areas–including hot cells, local radionuclide transportation paths, proper material storage spaces, and clean rooms for radiochemistry and laboratory equipment all need to be designed to ensure safe and effective workflow for employees and a final product that meets regulatory standards. For a sense of scale, sample vault schematics from Best are provided in Figures 5.3a and 5.3b.

After the construction of facility components, installation and commissioning of the cyclotron can take several months to nearly a year. Along with every other step in design and construction requires careful planning and time management, incorporating parallel tasks of assembly, mechanical, electrical, and piping installation, testing, individual system commissioning, and optimization for the range of operation. With so many variables, it is not reasonable to estimate the total cost of a facility. In comparison, however, the setup of a K-18 cyclotron from IBA in a legacy space had an estimated cost of \$10-\$20k / m^2. [58], and

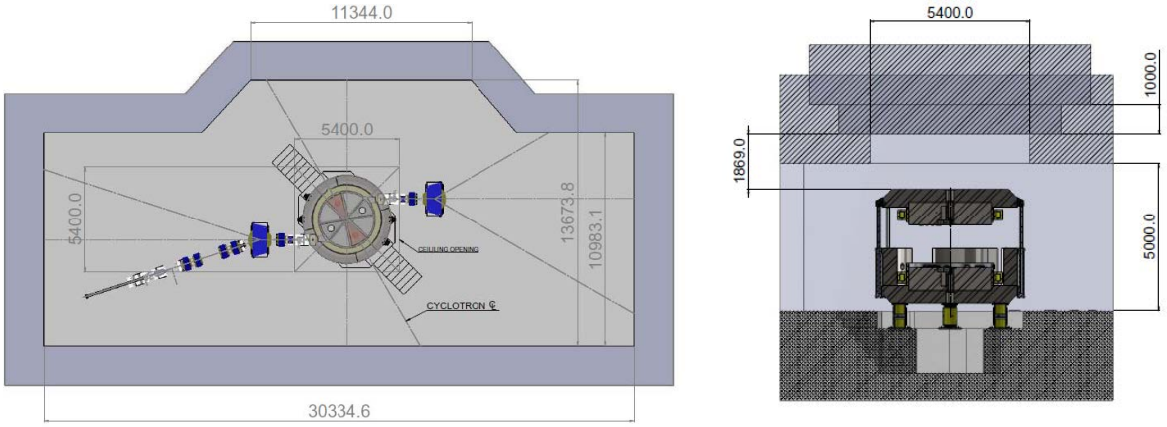

(a) (b)

Figure 5.3: Cyclotron vault design for a Best 70p Cyclotron with two beamlines [71].

Table 5.4: Minimum floor space for a K-70 Best Cyclotron, excluding hot cell/clean room space [71]

Room	Description	Minimum Area (m)
Cyclotron Vault	Shielded vault sized for Best 70p Cyclotron and beam lines	30 x 13.5
Target vaults	Shielded vaults sized for target stations	TBD
Control Console	Room for cyclotron control	4 x 5
Power Supply Room (non-active area)	Equipment room for cyclotron programmable logic controller, power supplies, electronic equipment	10 x 10
Service room	Housing for DI water	4 x 5
Active work area and storage	Workspace around cyclotron vault	6 x 3
Maintenance, spare parts inventory room	Workspace, storage	TBD

roughly half the cost for setup in a green space.

The minimum space for the required setup of a cyclotron facility, excluding processing and radiolabeling facilities, is provided in Table 5.4.

Regulatory Hurdles

Facility Requirements for Radioactive work and Radiation-Producing Machines

The specific design needs, which are only briefly covered in the above section, are required to be in compliance for the facility to obtain governmental approval to install and operate a cyclotron. These requirements may vary significantly between different states and potentially even among different cities. Regulators may, in addition to fully vetting design plans, require an assessment to explore potential effects or impacts to the environment and nearby

communities.

Even after obtaining the proper licences to construct the facility and obtaining a cyclotron and other regulated materials, the facility will be monitored to ensure ongoing compliance. Inspectors will routinely examine the facility to assess safety standards are in place and expect an in-house radiation safety officer or group to monitor everyday operations.

In the United States, under Title 10, Part 19, of the Code of Federal Regulations(10 CFR Part 19), staff are required to undergo sufficient and ongoing training relevant to their positions. A work environment involving the use and handling of radioactive materials and radiation-producing machines, health monitoring of the staff for exposure, and strict protocols ensure that an employee does not receive more than the maximum permissible dose based on the locality. 10 CFR Part 20, "Standards for Protection Against Radiation", caps annual dose limits for radiation workers at 5 rem whole body dose within a year, with further limitations enforced for pregnant workers. Certain licensees may also be required to maintain a radiation dose history for employees within the Radiation Exposure Information and Reporting System database, where under Freedom of Information Act requests, an individual can access these records. Despite the complexity of regulations, clear and open communication with the NRC fosters a shared trust in which regulators' oversight is neither a burden nor intrusive and encourages a safe working environment.

IND vs cGMP: Considerations for FDA Facility Rating

The regulatory oversight from the Food and Drug Administration (FDA) has not been addressed so far. A business involved in the research, synthesis, and administration of pharmaceuticals must adhere to additional guidelines and regulations. With respect to new pharmaceutical development, manufacturing, and trials,, the FDA distinguishes between an Investigational New Drug (IND) and Current Good Manufacturing Practices (cGMP) under 501(a)(2)(B) of the Federal Food, Drug, and Cosmetic Act. IND can be exempt from 21 CFR, part 211 and 21 CFR 210.2(c). IND is the initial step in developing new and novel drugs governing the pre-clinical trials in humans prior to formal FDA approval. An IND facility is required to provide details of the pharmaceutical's chemical composition, the manufacturing facility—including the manufacturing process—prior studies in animals, reporting on toxicology and adverse effects, and a proposed pipeline for clinical trials.

cGMP is, in a way, more stringent. Again, the manufacturing process quality control (QC) process is thoroughly vetted to ensure that the pharmaceuticals are produced consistently at high quality. cGMP enforces more rigid rules on facility design and maintenance, training, and record-keeping. It is structured to mitigate any and all risks of potential cross-contamination and to maintain high QC during the manufacturing process.

The broader cGMP guidelines cover the entire manufacturing process for both IND-approved pharmaceuticals and FDA-approved pharmaceuticals, while IND classification focuses on the safety of participants and enforcing scientific rigor in pre-clinical and clinical trial results and reporting. Returning to basic design considerations, it is important to consider whether a cyclotron is developed for IND or cGMP and what the implications will

be for the business. It is not impossible to straddle the line between both types of facilities, where a separation of areas within the facility can provide for IND and experimental that is not constrained by cGMP. This requires very strict engineering and administrative controls to maintain the standards for cGMP.

Estimation of Potential Revenue

A large-scale production facility capable of producing a variety of radionuclides is strategically positioned to adjust to market demand. Proper planning and scheduling of radionuclide production and labeling of radiopharmaceuticals will reduce costs, as hot cells and clean rooms do not have to be designated for individual radionuclide processing. As governed by the statistical probability of decay of radionuclides, short-lived isotopes can be processed with minimal risk of downtime and cross-contamination. For simplification, this section will look only at the production of ^{117m}Sn.

Currently, the only commercially approved product is Synovetin OA ®, used for treatment of joint pain in canines. A single injection is priced at $2200 and palliative effects last for between 6 months and 1 year [75]. The dose for each joint ranges between 1-2 mCi. For metastatic bone palliation in humans, a study by Srivastava *et al.*[76] performed a trial treatment on patients with pain from bone metastases, with an average dose of 10-20 mCi for the average 70 kg patient, with 80 percent of participants indicating a reduction in pain. In preclinical trials for treatment of OA in humans via RSV, the average dose is 6 mCi per knee. In a presentation in 2018, Dr. Nigel Stevenson provided an estimate of ^{117m}Sn demand pending FDA approval of radiopharmaceuticals in development at Serene LLC[77].

- Canine OA - Synovetin OA®: 250Ci/yr (US)
- Human RSV for OA, RA: 2000 Ci/yr (US/Canada)
- Palliative care for bone metastases: 1,200 Ci/yr (5% of market) (US/CA/EU)

Radiopharmaceuticals not quite as far along in development include the treatment of plaque formation in the carotid artery and for the treatment of Alzheimer's Disease, by reducing amyloid plaques, considered a major contributor to inflammation and neurodegeneracy[78].

- Cardiovascular plaque: 360 Ci/yr (US)
- Alzheimer's Disease: 5,000 Ci/yr (10% of market) (US)

This suggests a market size of 9000+ Ci /yr. Cornering even 10% of this market and assuming that net profit is only 1%-2% after licensing, operational, and production costs, and using the cost of dose from Synovium as a guide, net profit is provided in Table 5.5. Given that this can be produced rapidly at high SA, it provides significant beam time for additional radionuclide production and R&D opportunities.

Table 5.5: Estimated Potential Profit for ^{117m}Sn.

Market Size	9000 Ci/y
Market Share (10%)	900 Ci/y
Cost per Synovium Dose (0.002Ci)	$2,200
Cost per Curie - Radiopharmaceutical	$1,100,000
Net Profit per Curie, assuming 1-2 %	$11,000-$22,000
Net profit per Year	$990,000-$1,980,000

Competition in the Market

^{117m}Sn is only one of many radionuclides with theranostic potential. The theranostic market has differing valuations, but studies agree on an upward trend. ^{117m}Sn production is currently dominated by the Department of Energy Isotope program in collaboration with BNL, and and Exubrion Therapeutics with its parent company, Serene, LLC. Among business competition, there are also competing methods for production. Suggested alternate production methods include reactor-induced production via ^{116}Sn(n,γ)^{117m}Sn and ^{117}Sn(n,n'γ)^{117m}Sn and accelerator production via ^{116}Cd(α,3n)^{117m}Sn. The former reactor-produced competition has been addressed earlier, as reactors are shuttered in the United States as radionuclide needs increase. Production using ^{116}Cd requires a cyclotron capable of high energy α acceleration, as this reaction has a threshold reaction energy of 20.6454(5) MeV, peaking around 35 MeV. Additionally, the three aforementioned production pathways require enriched targets.

Cornering the market as a large regional supplier is a tool for determining product price, which can allow for further expansion. However, with a commercial off-the-shelf cyclotron available, new market entries are always a concern. Accurately predicting the market trends of new radiopharmaceuticals as they are approved and strategizing production for large-scale production roll-out would be crucial for retaining market share. Investing in research in emerging market trends and fostering strong relationships with research universities and regulatory agencies can provide an upper hand in the industry.

Chapter 6

Conclusions

The results presented in this dissertation add to a growing body of work from the Trilaboratory Effort in Nuclear Data to provide experimental data via stacked target activation measurements to guide reaction models for proton-induced reactions up to 200 MeV. The focus of this work involves proton-induced reactions on ^{nat}Sb for the production of ^{117m}Sn and ^{119m}Te, a generator for ^{119}Sb, which are both Auger-emitting radionuclides of interest for a variety of radiopharmaceutical applications.

In addition to measuring the cross sections for ^{117m}Sn and ^{119m}Te, 14 independent and 10 cumulative cross sections for ^{nat}Sb(p,x) reactions are provided; this includes measurements of ^{113}Sn, ^{119}Sn, ^{116}Te, ^{117}Te, ^{118}Te, ^{121}Te, and ^{123m}Te contaminants that impact viability of these radionuclides for *in vivo* use. Additionally, 54 (p,x) cross section measurements on ^{nat}Nb,^{nat}Cu, and ^{nat}Ti are provided in the appendices.

The residual product cross section measurements on ^{nat}Sb provided an opportunity to explore the underlying nuclear physics from experimental results in comparison to current nuclear reaction models. Experimental data was compared to charged particle reaction modeling in TALYS 1.95. Major takeaways from this research include adjustments to reaction modeling and the observation of secondary neutron production in stacked target measurements.

One particularly important finding based on the measurement of neighboring isomer and ground states of ^{119}Te and ^{121}Te was a need to significantly curtail spin distributions in near-stability Te isotopes. The results of this experimental dataset align with the results of Rodrigo *et al.*[14]. These results have implications for not only proton-induced radionuclide production but may also have broader applications to the nuclear data community since adjustment of the spin cut-off parameter could impact the modeling of quasi-continuum nuclear structure and astrophysical nucleosynthesis via the s-process and r-processes.

This work also demonstrated the need for alterations in the pre-equilibrium particle emission. This includes changes in the excitation energy-dependence of pre-equilibrium emission and the magnitude of individual nucleon-nucleon exciton scattering matrix elements. It also showed that the logarithmic, non-equidistant binning of particle spectra and transmission coefficients employed in default TALYS 1.95 calculations creates an unrealistic offset in the

threshold energy for high-energy reactions.

In addition, optical model parameter adjustments were studied. While the form factor of the optical model was briefly reviewed and showed only modest improvements in fit to experimental data, significant improvements resulted from adjustments to the imaginary volume term of the optical potential. Such adjustments to the imaginary optical model potential have been suggested for decades. To quote Marmier and Sheldon, *"Only σ_{tot} permits an unambiguous comparison between theory and experiment"*[47].

The iterative adjustments among level density, pre-equilibrium, and optical model parameters were driven for the most part by the largest magnitude independent reaction channels, specifically the (p,xn) channels leading to the production of the neutron-deficient Te isotopes. Following the approach of Fox *et al.*, the cumulative channels were used to validate, but not to guide, parameter adjustments.

In contrast to the improvements seen in the Te channels as a result of the parameter adjustments, there was often a marked *decrease* in the goodness-of-fit for neutron deficient Sb nuclei via (p,pxnx) reactions. Furthermore, there was a glaring discontinuity in the production of ^{120}Sb and ^{118}Sb between the LANL and BNL data sets, and a measurable amount of ^{124}Sb was seen, which could only be produced by neutron capture on ^{124}Sb. Taken together, these observations strongly suggest the presence of a large secondary neutron flux leading to (n,γ) and (n,xn) reactions on the targets. This finding isn't that surprising given that the BNL target stacks were subject to the highest incident proton energies, had thick copper degraders, and has a large neutron-moderating water channel surrounding the target box. Measurements of the secondary neutron and proton production for high incident proton energies over a range of angles and energies would not only improve reaction modeling but would also help minimize the co-production of unwanted contaminant nuclides.

While stacked target measurements are an economical way of measuring multiple reaction channels across a wide energy range, the large secondary particle flux, together with the inability to quickly count the targets following irradiation, limits the utility of the technique. Future work using prompt in-beam gamma data on a single target can address these complications and provide insight into the production of residual products with either extremely short half-lives or long half-lives, including stable isotopes.

In summation, utilizing a wider range of experimental techniques will provide a deeper understanding of charged particle reactions and can inform the reliable production of clean theranostic radionuclides for the treatment of human illness.

Appendix A

Stacked Target Foil Characterization

Table A.1: Stack design for the LBNL 2020 55 MeV Run

Target Layer	Areal Density (mg/cm^2)	Areal density uncertainty (%)
SS Profile Monitor 2	100.20	0.07
Cu-SN1	22.28	0.22
Sb-SN1	15.04	0.64
Polyester Back-SN1	5.83	1.95
Nb-SN1	22.27	0.27
Ti-SN1	11.03	0.75
Al Degrader E1	68.31	0.07
Al Degrader E2	68.25	0.07
Cu-SN2	22.10	0.23
Sb-SN2	15.61	0.32
Polyester Back-SN2	5.83	1.95
Nb-SN2	22.39	0.38
Ti-SN2	11.26	0.44
Al Degrader E3	68.35	0.07
Al Degrader E4	68.29	0.07
Cu-SN3	22.18	0.22
Sb-SN3	15.19	0.53
Polyester Back-SN3	5.83	1.95
Nb-SN3	22.61	0.66
Ti-SN3	11.06	0.51
Al Degrader E5	68.24	0.07
Al Degrader E6	68.22	0.07

Table A.1 Continued from previous page

Target Layer	Areal Density (mg/cm^2)	Areal density uncertainty (%)
Cu-SN4	22.35	0.22
Sb-SN4	16.81	0.49
Polyester Back-SN4	5.83	1.95
Nb-SN4	22.41	0.25
Ti-SN4	11.12	0.86
Al Degrader E7	68.19	0.07
Al Degrader E8	68.16	0.07
Cu-SN5	22.32	0.45
Sb-SN5	15.95	0.51
Polyester Back-SN5	5.83	1.95
Nb-SN5	22.40	0.36
Ti-SN5	11.22	0.43
Al Degrader E9	68.24	0.07
Al Degrader E10	68.22	0.07
Cu-SN6	22.45	0.24
Sb-SN6	17.89	0.32
Polyester Back-SN6	5.83	1.95
Nb-SN6	22.25	0.22
Ti-SN6	10.99	0.47
Al Degrader D1	174.44	0.05
Cu-SN7	22.57	0.26
Sb-SN7	15.63	0.37
Polyester Back-SN7	5.83	1.95
Nb-SN7	22.41	0.23
Ti-SN7	10.74	0.54
Al Degrader D2	174.88	0.06
Cu-SN8	22.42	0.01
Sb-SN8	16.70	0.49
Polyester Back-SN8	5.83	1.95
Nb-SN8	22.50	0.26
Ti-SN8	10.79	1.27
Al Degrader D3	175.05	0.08
Cu-SN9	22.41	0.00
Sb-SN9	17.67	0.29
Polyester Back-SN9	5.83	1.95
Nb-SN9	22.27	0.00
Ti-SN9	11.02	5.02
Al Degrader C1	261.48	0.07

Table A.1 Continued from previous page

Target Layer	Areal Density (mg/cm^2)	Areal density uncertainty (%)
Cu-SN10	22.48	0.23
Sb-SN10	15.24	0.38
Polyester Back-SN10	5.83	1.95
Nb-SN10	22.44	0.22
Ti-SN10	10.79	0.50
SS Profile Monitor 2	100.87	0.07

Table A.2: Stack design for the LBNL 2020 35 MeV Run

Target Layer	Areal Density (mg/cm^2)	Areal density uncertainty (%)
SS Profile Monitor 4	101.25	0.07
Cu-SN11	22.40	0.22
Sb-SN11	17.50	0.33
Polyester Back-SN11	5.83	1.95
Ti-SN11	10.93	0.48
Al Degrader E8	68.16	0.07
Cu-SN12	22.42	0.27
Sb-SN12	17.57	0.55
Polyester Back-SN12	5.83	1.95
Ti-SN12	11.06	0.88
Al Degrader E9	68.18	0.07
Cu-SN13	22.15	0.26
Sb-SN13	17.68	0.55
Polyester Back-SN13	5.83	1.95
Ti-SN13	10.93	0.89
Al Degrader E1	68.31	0.07
Cu-SN14	22.11	0.26
Sb-SN14	16.11	0.51
Polyester Back-SN14	5.83	1.95
Ti-SN14	11.07	0.74
Al Degrader E2	68.25	0.07
Cu-SN15	22.22	0.24
Sb-SN15	16.11	0.31
Polyester Back-SN15	5.83	1.95
Ti-SN15	10.88	0.54

Table A.2 Continued from previous page

Target Layer	Areal Density (mg/cm^2)	Areal density uncertainty (%)
Al Degrader E3	68.35	0.07
Cu-SN16	22.44	0.00
Sb-SN16	16.53	0.30
Polyester Back-SN16	5.83	1.95
Ti-SN16	10.86	0.75
Al Degrader E4	68.29	0.07
Cu-SN17	22.27	0.23
Sb-SN17	16.08	0.36
Polyester Back-SN17	5.83	1.95
Ti-SN17	11.07	0.00
Al Degrader E5	68.24	0.07
Cu-SN18	22.40	0.35
Sb-SN18	17.83	0.28
Polyester Back-SN18	5.83	1.95
Ti-SN18	10.87	0.45
Al Degrader E6	68.22	0.07
Cu-SN19	22.51	0.24
Sb-SN19	16.55	0.49
Polyester Back-SN19	5.83	1.95
Ti-SN19	11.10	0.87
Al Degrader E7	68.19	0.07
Cu-SN20	22.37	0.00
Sb-SN20	15.74	0.32
Polyester Back-SN20	5.83	1.95
Ti-SN20	11.13	0.44
SS Profile Monitor 5	100.57	0.07

Table A.3: Stack design for the LBNL 2022 55 MeV Run

Target Layer	Areal Density (mg/cm^2)	Areal density uncertainty (%)
SS Profile Monitor 1	100.20	0.07
Cu-SN01	22.06	0.05
Sb-SN01	16.52	0.10
Polyester Back-SN01	5.83	1.95
Ti-SN01	11.09	0.00

Table A.3 Continued from previous page

Target Layer	Areal Density (mg/cm^2)	Areal density uncertainty (%)
Al Degrader B1	415.02	0.07
Cu-SN02	21.92	0.06
Sb-SN02	16.19	0.00
Polyester Back-SN02	5.83	1.95
Ti-SN02	11.19	0.00
Al Degrader C1	261.48	0.07
Cu-SN03	22.04	0.00
Sb-SN03	17.43	0.06
Polyester Back-SN03	5.83	1.95
Ti-SN03	11.19	0.00
Al Degrader C2	261.65	0.07
Cu-SN04	21.72	0.06
Sb-SN04	16.56	0.05
Polyester Back-SN04	5.83	1.95
Ti-SN04	11.12	0.05
Al Degrader C3	261.64	0.07
Cu-SN05	21.90	0.05
Sb-SN05	17.19	0.05
Polyester Back-SN05	5.83	1.95
Ti-SN05	11.06	0.05
Al Degrader C4	261.71	0.07
Cu-SN06	22.00	0.05
Sb-SN06	15.98	0.05
Polyester Back-SN06	5.83	1.95
Ti-SN06	11.08	0.05
SS Profile Monitor 3	100.48	0.07

Table A.4: Stack design for the LANL 100 MeV Run

Target Layer	Areal Density (mg/cm^2)	Areal density uncertainty (%)
SS Profile Monitor 1	101.78	1.18
Cu-SN01	22.07	0.26
Sb-SN01	14.35	0.35
Polyester Back-SN01	5.83	1.95
Nb-SN01	22.52	0.00

Table A.4 Continued from previous page

Target Layer	Areal Density (mg/cm^2)	Areal density uncertainty (%)
Ti-SN01	10.88	0.48
Al Degrader D1	1709.20	0.00
Cu-SN02	22.12	0.01
Sb-SN02	17.33	0.29
Polyester Back-SN02	5.83	1.95
Nb-SN02	22.13	0.23
Ti-SN02	10.79	0.46
Al Degrader D2	863.27	0.04
Cu-SN03	22.07	0.22
Sb-SN03	17.68	0.00
Polyester Back-SN03	5.83	1.95
Nb-SN03	22.30	0.00
Ti-SN03	10.89	0.45
Al Degrader D3	624.52	0.11
Cu-SN04	22.01	0.24
Sb-SN04	17.14	0.30
Polyester Back-SN04	5.83	1.95
Nb-SN04	22.28	0.26
Ti-SN04	10.99	0.46
Al Degrader D4	428.52	0.08
Cu-SN05	22.03	0.00
Sb-SN05	18.15	0.27
Polyester Back-SN05	5.83	1.95
Nb-SN05	22.24	0.23
Ti-SN05	11.04	0.44
Al Degrader D5	280.15	0.12
Cu-SN06	22.08	0.26
Sb-SN06	18.04	0.28
Polyester Back-SN06	5.83	1.95
Nb-SN06	22.55	0.26
Ti-SN06	10.99	0.00
Al Degrader D6	226.22	0.43
Cu-SN07	21.98	0.36
Sb-SN07	15.08	0.38
Polyester Back-SN07	5.83	1.95
Nb-SN07	22.42	0.26
Ti-SN07	11.02	0.45
Al Degrader D7	139.16	0.19

Table A.4 Continued from previous page

Target Layer	Areal Density (mg/cm^2)	Areal density uncertainty (%)
Cu-SN08	22.06	0.00
Sb-SN08	15.86	0.52
Polyester Back-SN08	5.83	1.95
Nb-SN08	22.29	0.00
Ti-SN08	11.07	0.00
Al Degrader D8	140.17	0.86
Cu-SN09	21.96	0.00
Sb-SN09	18.06	0.32
Polyester Back-SN09	5.83	1.95
Nb-SN09	22.35	0.36
Ti-SN09	11.45	0.43
Al Degrader D9	140.31	0.18
Cu-SN10	21.22	0.24
Sb-SN10	15.99	0.32
Polyester Back-SN10	5.83	1.95
Nb-SN10	22.14	0.45
Ti-SN10	10.99	0.45
SS Profile Monitor 2	101.52	1.18

Table A.5: Stack design for the BNL 200 MeV Run

Target Layer	Areal Density (mg/cm^2)	Areal density uncertainty (%)
SS Profile Monitor 1	96.80	0.08
Cu-SN01	22.15	0.26
Sb-SN01	16.12	0.31
Polyester Back-SN01	5.83	1.95
Nb-SN01	22.42	0.38
Al Degrader D1	4668.98	0.40
Cu-SN02	22.25	0.26
Sb-SN02	17.14	0.34
Polyester Back-SN02	5.83	1.95
Nb-SN02	22.72	0.00
Al Degrader D2	3892.53	0.46
Cu-SN03	22.27	0.23
Sb-SN03	15.98	0.00

Table A.5 Continued from previous page

Target Layer	Areal Density (mg/cm^2)	Areal density uncertainty (%)
Polyester Back-SN03	5.83	1.95
Nb-SN03	22.49	0.37
Al Degrader D3	3716.27	1.09
Cu-SN04	22.17	0.26
Sb-SN04	16.75	0.34
Polyester Back-SN04	5.83	1.95
Nb-SN04	22.52	0.22
Al Degrader D4	3754.24	0.43
Cu-SN05	22.17	0.26
Sb-SN05	18.12	0.32
Polyester Back-SN05	5.83	1.95
Nb-SN05	22.54	0.35
Al Degrader D5	3340.26	0.75
Cu-SN06	22.18	0.26
Sb-SN06	15.34	0.33
Polyester Back-SN06	5.83	1.95
Nb-SN06	22.42	0.22
Al Degrader D6	3285.91	0.43
Cu-SN07	22.16	0.37
Sb-SN07	17.06	0.29
Polyester Back-SN07	5.83	1.95
Nb-SN07	22.52	0.22
SS Profile Monitor 2	96.80	0.08

Appendix B

Monitor Reaction Correlation Matrices

Table B.1: $\int \sigma(E)\frac{d\phi}{dE}dE$ Correlation Matrix

Product	^{48}V	^{46}Sc	^{62}Zn	^{63}Zn	^{65}Zn	^{56}Co	^{58}Co
^{48}V	1	0.3	0	0	0	0	0
^{46}Sc	0.3	1	0	0	0	0	0
^{62}Zn	0	0	1	0.3	0.3	0.3	0.3
^{63}Zn	0	0	0.3	1	0.3	0.3	0.3
^{65}Zn	0	0	0.3	0.3	1	0.3	0.3
^{56}Co	0	0	0.3	0.3	0.3	1	0.3
^{58}Co	0	0	0.3	0.3	0.3	0.3	1

Table B.2: Δt_{irr} Correlation Matrix

Product	^{48}V	^{46}Sc	^{62}Zn	^{63}Zn	^{65}Zn	^{56}Co	^{58}Co
^{48}V	1	1	1	1	1	1	1
^{46}Sc	1	1	1	1	1	1	1
^{62}Zn	1	1	1	1	1	1	1
^{63}Zn	1	1	1	1	1	1	1
^{65}Zn	1	1	1	1	1	1	1
^{56}Co	1	1	1	1	1	1	1
^{58}Co	1	1	1	1	1	1	1

Table B.3: λ Correlation Matrix

Product	^{48}V	^{46}Sc	^{62}Zn	^{63}Zn	^{65}Zn	^{56}Co	^{58}Co
^{48}V	1	0	0	0	0	0	0
^{46}Sc	0	1	0	0	0	0	0
^{62}Zn	0	0	1	0	0	0	0
^{63}Zn	0	0	0	1	0	0	0
^{65}Zn	0	0	0	0	1	0	0
^{56}Co	0	0	0	0	0	1	0
^{58}Co	0	0	0	0	0	0	1

Table B.4: $\rho_N \Delta r$ Correlation Matrix

Product	^{48}V	^{46}Sc	^{62}Zn	^{63}Zn	^{65}Zn	^{56}Co	^{58}Co
^{48}V	1	1	0	0	0	0	0
^{46}Sc	1	1	0	0	0	0	0
^{62}Zn	0	0	1	1	1	1	1
^{63}Zn	0	0	1	1	1	1	1
^{65}Zn	0	0	1	1	1	1	1
^{56}Co	0	0	1	1	1	1	1
^{58}Co	0	0	1	1	1	1	1

Table B.5: R Correlation Matrix

Product	^{48}V	^{46}Sc	^{62}Zn	^{63}Zn	^{65}Zn	^{56}Co	^{58}Co
^{48}V	1	0.3	0.3	0.3	0.3	0.3	0.3
^{46}Sc	0.3	1	0.3	0.3	0.3	0.3	0.3
^{62}Zn	0.3	0.3	1	0.3	0.3	0.3	0.3
^{63}Zn	0.3	0.3	0.3	1	0.3	0.3	0.3
^{65}Zn	0.3	0.3	0.3	0.3	1	0.3	0.3
^{56}Co	0.3	0.3	0.3	0.3	0.3	1	0.3
^{58}Co	0.3	0.3	0.3	0.3	0.3	0.3	1

Appendix C

Threshold Energy for Sb(p,x) Channels

Table C.1: Reaction Threshold energy for independent Sb(p,x) cross sections [79].

Product	Reaction	Reaction Threshold (MeV)
^{89m}Nb	^{121}Sb(p,11p22n)^{89m}Nb	261.59
	^{121}Sb(p,α9p20n)^{89m}Nb	233.06
	^{121}Sb(p,2α7p18n)^{89m}Nb	204.53
	^{121}Sb(p,3α5p16n)^{89m}Nb	176.00
	^{121}Sb(p,4α3p14n)^{89m}Nb	147.47
	^{121}Sb(p,5α1p12n)^{89m}Nb	118.94
	^{123}Sb(p,11p24n)^{89m}Nb	277.46
	^{123}Sb(p,α9p22n)^{89m}Nb	248.93
	^{123}Sb(p,2α7p20n)^{89m}Nb	220.40
	^{123}Sb(p,3α5p18n)^{89m}Nb	191.87
	^{123}Sb(p,4α3p16n)^{89m}Nb	163.34
	^{123}Sb(p,5α1p14n)^{89m}Nb	134.82
^{102m}Rh	^{121}Sb(p,7p13n)^{102m}Rh	152.87
	^{121}Sb(p,α5p11n)^{102m}Rh	124.34
	^{121}Sb(p,2α3p9n)^{102m}Rh	95.811
	^{121}Sb(p,3α1p7n)^{102m}Rh	67.281
	^{123}Sb(p,7p15n)^{102m}Rh	168.74
	^{123}Sb(p,α5p13n)^{102m}Rh	140.22
	^{123}Sb(p,2α3p11n)^{102m}Rh	111.69
	^{123}Sb(p,3α1p9n)^{102m}Rh	83.167

Product	Reaction	Reaction Threshold (MeV)
^{106m}Ag	^{121}Sb(p,5p11n)^{106m}Ag	121.68
	^{121}Sb(p,α3p9n)^{106m}Ag	93.154
	^{121}Sb(p,2α1p7n)^{106m}Ag	64.625
	^{123}Sb(p,5p13n)^{106m}Ag	137.56
	^{123}Sb(p,α3p11n)^{106m}Ag	109.04
	^{123}Sb(p,2α1p9n)^{106m}Ag	80.511
^{110m}Ag	^{121}Sb(p,5p7n)^{110m}Ag	88.641
	^{121}Sb(p,α3p5n)^{110m}Ag	60.111
	^{121}Sb(p,2α1p3n)^{110m}Ag	31.582
	^{123}Sb(p,5p9n)^{110m}Ag	104.52
	^{123}Sb(p,α3p7n)^{110m}Ag	75.998
	^{123}Sb(p,2α1p5n)^{110m}Ag	47.472
^{113m}Sn	^{121}Sb(p,2p7n)^{113m}Sn	65.675
	^{121}Sb(p,α5n)^{113m}Sn	37.145
	^{123}Sb(p,2p9n)^{113m}Sn	81.561
	^{123}Sb(p,α7n)^{113m}Sn	53.035
^{114m}In	^{121}Sb(p,3p5n)^{114m}In	56.618
	^{121}Sb(p,α1p3n)^{114m}In	28.089
	^{123}Sb(p,3p7n)^{114m}In	72.505
	^{123}Sb(p,α1p5n)^{114m}In	43.980
^{116m}Sb	^{121}Sb(p,p5n)^{116m}Sb	43.876
	^{123}Sb(p,p7n)^{116m}Sb	59.765
^{116}Te	^{121}Sb(p,6n)^{116}Te	45.850
	^{123}Sb(p,8n)^{116}Te	61.738
^{117}Te	^{121}Sb(p,5n)^{117}Te	37.882
	^{123}Sb(p,7n)^{117}Te	53.772
^{118m}Sb	^{121}Sb(p,p3n)^{118m}Sb	26.282
	^{123}Sb(p,p5n)^{118m}Sb	42.174
^{118}Te	^{121}Sb(p,4n)^{118}Te	27.127
	^{123}Sb(p,6n)^{118}Te	43.018
^{119}Te	^{121}Sb(p,3n)^{119}Te	19.501
	^{123}Sb(p,5n)^{119}Te	35.393
^{119m}Te	^{121}Sb(p,3n)^{119m}Te	19.764
	^{123}Sb(p,5n)^{119m}Te	35.656
^{120m}Sb	^{121}Sb(p,pn)^{120m}Sb	9.3300
	^{123}Sb(p,p3n)^{120m}Sb	25.223
^{121}Te	^{121}Sb(p,n)^{121}Te	1.8570
	^{123}Sb(p,3n)^{121}Te	17.751

Product	Reaction	Reaction Threshold (MeV)
^{121m}Te	^{121}Sb(p,n)^{121m}Te	2.1490
	^{123}Sb(p,3n)^{121m}Te	18.043
^{122}Sb	^{123}Sb(p,pn)^{122}Sb	9.0330
^{123m}Te	^{123}Sb(p,n)^{123m}Te	1.0910

Appendix D

Decay Data for Sb(p,x) Products

Table D.1: Decay data for cross sections measured on Sb foils

Isotope	Half Life	Energy (keV)	I_γ (%)
^{89m}Nb[80]	1.100 (33) h	588	95.5700 (47785)%[3]
^{91m}Nb[81]	60.86 (22) d	603.5	1.30 (13)%
		1082.6	1.09 (11)%
		1204.67	2.0 (3)%
		1790.6	36.3 (12)%
		1984.6	62.6 (15)%
^{106m}Ag[82]	8.28 (2) d	221.701	6.6 (3)%[3]
		228.633	2.1 (1)%[3]
		328.463	1.14 (5)%
		406.182	13.4 (4)%
		429.646	13.2 (4)%
		450.976	28.2 (7)%
		601.17	1.61 (9)%
		680.42	1.54 (8)%[3]
		717.34	28.9 (8)%
		748.36	20.6 (6)%
		793.17	5.9 (3)%[3]
		804.28	12.4 (5)%
		808.36	4.0 (4)%
		824.69	15.3 (4)%
		847.03	2.8 (6)%
		847.27	1.6 (5)%

Table D.1 Continued from previous page

Isotope	Half Life	Energy (keV)	I_γ (%)
		1019.72	1.04 (16)%
		1045.83	29.6 (10)%
		1128.02	11.8 (5)%
		1199.39	11.2 (5)%
		1222.88	7.0 (4)%
		1394.35	1.49 (18)%
		1527.65	16.3 (13)%
		1572.35	6.6 (5)%
		1722.76	1.40 (18)%
		1839.05	2.0 (3)%
^{110m}Ag[83]	249.76 (4) d	620.3553	2.73 (8)%
		657.76	95.6100 (47805)%[3]
		677.6217	10.70 (5)%
		687.0091	6.53 (3)%
		706.676	16.69 (7)%
		744.2755	4.77 (3)%
		818.0244	7.43 (4)%
		884.6781	75.0 (11)%
		937.485	35.0 (3)%
		1384.2931	25.1 (5)%
		1475.7792	4.08 (5)%
		1505.028	13.33 (15)%
		1562.294	1.22 (3)%
^{109}In[84]	4.167 (18) h	288.1	1.51 (11)%
		426.3	4.05 (12)%
		623.8	5.64 (23)%
		1148.5	4.67 (15)%
		1419	1.25 (5)%
		1622.3	2.08 (8)%
^{110}In[83]	4.9 (1) h	120.154	1.41 (4)%
		584.21	6.49 (23)%
		641.68	26.0 (8)%
		707.4	29.5 (11)%
		708.12	1.64 (17)%
		759.87	3.15 (12)%
		844.667	3.24 (12)%
		997.16	10.5 (3)%
		1117.36	4.23 (13)%

Table D.1 Continued from previous page

Isotope	Half Life	Energy (keV)	I_γ (%)
^{110m}In[83]	69.102 (498) m	2129.4	2.15 (3)%
		2211.33	1.74 (3)%
^{111}In[85]	2.8047 (4) d	171.28	90.7 (9)%
		245.35	94.1 (10)%
^{114m}In[86]	49.51 (1) d	190.27	15.56 (15)%
		558.43	4.4 (6)%
		725.24	4.4 (6)%
^{113}Sn[87]	115.09 (3) d	255.134	2.11 (8)%
		391.698	64.97 (17)%
^{117m}Sn[3]	13.60 (4) d	156.02	2.113 (12)%
		158.56	86.40 (432)%[3]
^{119m}Sn[9]	293 (1) d	23.875	16.5 (2)%
^{115}Sb[88]	32.1 (3) m	489.3	1.3 (3)%
		497.31	97.900 (4895)%[3]
^{116m}Sb[36]	1.01 (1) h	99.802	100 (4)%
		135.511	28.5 (12)%
		436.666	3.58 (16)%
		542.867	48.1 (200)%
		844.001	11.2 (5)%
		972.573	100 (4)%
		1072.373	25.5 (11)%
		1293.557	100 (4)%
^{118m}Sb[89]	5.00 (2) h	253.678	99 (6)%
		984	1.5 (5)%
		1050.69	97 (5)%[3]
		1091.51	3.6 (3)%
		1229.65	100 (5)%[3]
^{120m}Sb[90]	5.76 (2) d	197.3	87.0 (11)%
		1023.3	99.4 (3)%
		1171.7	100 (0)%
^{122}Sb[91]	2.7238 (2) d	564.24	70.6700 (35335)%[3]
		692.65	3.85 (13)%
^{116}Te[36]	2.49 (4) h	93.7	33.1 (21)%
		103	1.98 (14)%
		628.7	3.21 (15)%[3]
		931.84	24.8 (19)% [1]
		2225	14.6 (13)% [1]
^{117}Te[3]	61.99 (198) m	719.7	64.700 (3235)%[3]

Table D.1 Continued from previous page

Isotope	Half Life	Energy (keV)	I_γ (%)
		886.7	1.49 (20)%
		923.9	6.2 (7)%
		996.7	3.9 (4)%
		1090.7	6.9 (7)%
		1716.4	15.9 (17)%
		2300	11.2 (12)%
^{118}Te[89]	6.00 (2) d	1229.33	2.5 (3)% [2]
^{119}Te[9]	16.05 (5) h	644.01	84.100 (4205)%[3]
		699.85	10.1 (5)%[3]
		1413.19	1.09 (8)%
		1749.65	4.0 (3)%
^{119m}Te[9]	4.70 (4) d	153.59	66 (3)%[3]
		164.34	1.30 (5)%
		270.53	28.0 (4)%
		912.6	6.24 (8)%
		942.21	5.08 (6)%
		976.37	2.71 (7)%
		979.29	3.01 (7)%
		1013.2	1.7 (3)%
		1048.44	3.19 (5)%
		1081.35	1.59 (3)%
		1095.75	2.23 (3)%
		1136.75	7.65 (7)%
		1212.73	66.100 (3305)%[3]
		1366.39	1.064 (20)%
		2089.57	4.68 (6)%
^{121}Te[92]	19.17 (4) d	470.472	1.41 (4)%
		573.139	80.4 (22)%
^{121m}Te[92]	164.2 (8) d	212.189	81.500 (4075)%[3]
		1102.149	2.5 (3)%
^{123m}Te[38]	119.2 (3) d	159	84.3 (42)%[3]

[1]These are decay gammas from the progeny isotope, ^{116}Sb
[2]These are decay gammas from the progeny isotope, ^{118}Sb
[3]When no listed uncertainty is provided, a 5% uncertainty is assumed

Appendix E

TALYS: Nuclear Level Density Parameter Adjustments

Table E.1: TALYS Level Density Parameters Explored

TALYS Parameter	Description	Range	Default	Explored [1]	Chosen
`ldmodel`	Model for level densities	1: Constant temperature + Fermi gas model 2: Back-shifted Fermi gas model 3: Generalized superfluid model 4: Microscopic level densities (Skyrme force) from Goriely's tables 5: Microscopic level densities (Skyrme force) from Hilaire's combinatorial tables 6: Microscopic level densities (temperature dependent HF, Gogny force) from Hilaire's combinatorial tables	1	1-6	2
`spincutmodel`	Model for spin cut-off parameter	1,2	1	1-2	2
`rspincut`	Adjustable constant for spin cut-off parameter	$0 < x \leq 10$	1	0.01-10	0.4

[1] These values were explored in different bin sizes to determine effects on results

[2] Six additional level density parameters were explored, including `ldmodelracap`, `colenhance`, `colldamp`, `parity`, `pglobal`, and `cglobal`.

Appendix F

TALYS: Pre-Equilibrium Parameter Adjustments

Table F.1: TALYS Pre-Equilibrium Parameters Explored

TALYS Parameter	Description	Range	Default	Explored[1]	Chosen
`preeqmode`	Model for pre-eq reactions	1: Exciton model: Analytical transition rates 2: Exciton model: Numerical transition rates 3: Exciton model: Numerical transition rates with optical model for collision probability. 4: Multi-step direct/compound model	2	1-4	1
`m2constant`	Overall constant for the matrix element in exciton model	$0.1 \leq x \leq 100$	1	0.1-10.0	2
`m2limit`	Constant to scale asymptotic value of matrix element	$0.1 \leq x \leq 100$	1	0.1-10.0	0.8
`m2shift`	Constant to scale energy shift of the matrix element	$0.1 \leq x \leq 100$	1	0.1-10.0	1.8
`rpinu`	Proton-neutron ratio in two-component exciton model	$0.1 \leq x \leq 100$	1	0.1-50.0	1.5
`rnupi`	Neutron-proton ratio in two-component exciton model	$0.1 \leq x \leq 100$	1	0.1-50.0	1.5

[1]These values were explored in different bin sizes to determine effects on results

[2]Eight additional pre-equilibrium parameters were explored – `cknock`, `cstrip`, and `cbreak` for both proton and alpha particles, and `mpreeqmode`, `preeqspin`, `rgamma`, `rpipi`, and `rnunu`. Ultimately, there was little improvement in the reaction model fit to justify changing these parameters from their default value.

Appendix G

TALYS: Optical Model Parameter Adjustments

Table G.1: TALYS Optical Model Parameters Explored

TALYS Parameter	Description	Range	Default	Explored [1]	Chosen
`w1adjust` (n)	w1 term for neutrons	$0.1 \leq x \leq 10$	1	0.1-5.0	2.5
`w2adjust` (n)	w2 term for neutrons	$0.1 \leq x \leq 10$	1	0.1-5.0	0.6

[1]These values were explored in different bin sizes to determine effects on results

[2]Thirteen additional optical model parameters were explored for protons and neutrons: `avadjust`, `avdadjust`, `avdadjust`, `avsoadjust`, `awadjust`,`awdadjust`,`awsoadjust`, `rvadjust`, `rvdadjust`, `rvsoadjust`, `rwadjust`, `rwdadjust`, and `rwsoadjust`. Four additional parameters were explored: `w1adjust` and `w2adjust` for adjusting the proton imaginary optical potential model, and `w3adjust` and `w4adjust` for neutrons to adjust the imaginary optical potential model above 180 MeV.

Appendix H

Decay Data for Monitor Foil Products

Table H.1: Decay data for cross sections measured on Cu foils

Isotope	Half Life	Energy (keV)	I_γ (%)
^{51}Cr[93]	27.7010 (11) d	320.0824	9.91 (1)%
^{52}Mn[94]	5.591 (3) d	744.233	90.0 (12)%
		848.18	3.32 (4)%
		935.544	94.5 (13)%
		1246.278	4.21 (7)%
		1434.092	100.0 (14)%
^{54}Mn[95]	312.05 (4) d	834.848	99.976 (1)%
^{56}Mn[96]	2.5789 (1) h	1810.726	26.9 (4)%
		2113.092	14.2 (3)%
		2523.06	1.018 (20)%
^{59}Fe[97]	44.495 (9) d	142.651	1.02 (4)%
		192.343	3.08 (12)%
		1099.245	56.5 (18)%
		1291.59	43.2 (14)%
^{55}Co[98]	17.53 (3) h	91.9	1.16 (9)%
		411.5	1.07 (8)%
		477.2	20.2 (17)%
		803.7	1.87 (15)%
		931.1	75.00 (375)%[1]
		1316.6	7.1 (3)%
		1370	2.9 (3)%
		1408.5	16.9 (8)%[1]

Table H.1 Continued from previous page

Isotope	Half Life	Energy (keV)	I_γ (%)
^{56}Co[96]	77.233 (27) d	846.77	99.939 (4996)%[1]
		977.372	1.421 (6)%
		1037.843	14.05 (4)%
		1175.101	2.252 (6)%
		1238.288	66.46 (12)%
		1360.212	4.283 (12)%
		1771.357	15.41 (6)%
		2015.215	3.016 (12)%
		2034.791	7.77 (3)%
		2598.5	16.97 (4)%
^{57}Co[99]	271.74 (6) d	14.4129	9.16 (15)%
		122.06065	85.60 (17)%
		136.47356	10.68 (8)%
^{58}Co[100]	70.86 (6) d	810.7593	99.45 (497)%[1]
		863	0.686 (10)%
		1674.725	0.517 (10)%
^{60}Co[101]	5.27113 (38) y	1173.228	99.85 (3)%
		1332.492	99.9826 (6)%
^{61}Co[102]	1.649 (5) h	917.5	3.6 (3)%
^{56}Ni[96]	6.08 (1) d	158.38	98.8 (10)%
		269.5	36.5 (8)%
		480.44	36.5 (8)%
		749.95	49.5 (12)%
		1561.8	14.0 (6)%
^{57}Ni[99]	35.60 (6) h	127.164	16.7 (5)%
		1377.63	81.7 (24)%
		1757.55	5.75 (20)%
		1919.52	12.3 (4)%
^{61}Cu[102]	3.333 (5) h	282.956	12.20 (61)%[1]
		373.05	2.1 (4)%
		588.605	1.17 (21)%
		656.008	10.8 (20)%
		908.631	1.1 (2)%
		1185.234	3.7 (7)%
^{64}Cu[103]	12.701 (2) h	1345.77	0.472 (4)%
^{60}Cu[101]	23.7 (4) m	467.3	3.52 (18)%[1]
		497.9	1.67 (9)%[1]
		826.4	21.7 (11)%[1]

Table H.1 Continued from previous page

Isotope	Half Life	Energy (keV)	I_γ (%)
		952.4	2.73 (18)%
		1035.2	3.70 (18)%[1]
		1110.5	1.06 (18)%
		1293.7	1.85 (18)%
^{62}Zn[104]	9.26 (2) h	40.85	25.5 (24)%
		243.36	2.52 (23)%
		246.95	1.90 (18)%
		260.43	1.35 (13)%
		394.03	2.24 (17)%
		548.35	15.3 (14)%
		596.56	26.0 (13)%[1]
^{63}Zn[23]	38.47 (5) m	669.62	8.20 (41)%[1]
		962.06	6.5 (4)%
^{65}Zn[105]	243.93 (9) d	1115.539	50.04 (10)%

[1]When no listed uncertainty is provided, a 5% uncertainty is assumed

Table H.2: Decay data for cross sections measured on Nb foils

Isotope	Half Life	Energy (keV)	I_γ (%)
^{69}Ge[106]	39.0504 (1008) h	1106.77	36.0 (18)%[2]
		1336.6	4.5 (6)%
^{71}As[103]	65.2992 (696) h	174.954	82.4 (20)%
		1095.49	4.10 (12)%
^{72}As[107]	25.9992 (1008) h	1050.75	1.00 (3)%
		1464	1.13 (3)%
^{76}As[108]	26.2392 (912) h	1212.92	1.44 (11)%
		1216.08	3.42 (24)%
		1228.52	1.22 (10)%
^{77}Br[109]	57.0360 (48) h	87.59	1.40 (4)%
		238.98	23.1 (11)%[2]
		439.47	1.56 (5)%
^{82}Br[110]	35.2824 (72) h	698.374	28.3 (4)%
		776.517	83.4 (12)%
		1007.59	1.276 (21)%
		1044.002	28.3 (4)%
		1317.473	26.8 (4)%
		1474.88	16.60 (23)%
^{76}Kr[108]	14.8 (1) h	252	6.2 (8)%
^{79}Kr[111]	1.4600 (42) d	261.29	12.7 (6)%[2]
		306.47	2.60 (13)%[2]
		397.54	9.3 (4)%
^{83}Rb[112]	86.2 (1) d	520.3991	45 (3)%
		529.5945	29.3 (21)%
		552.5512	16.0 (11)%
^{84}Rb[113]	32.82 (7) d	881.6041	68.9 (34)%[2]
^{86}Rb[114]	18.631 (18) d	1077	8.640 (432)%[2]
^{83}Sr[112]	32.4096 (312) h	381.17	1.79 (22)%
		381.53	14.0 (11)%
		418.37	4.2 (3)%
		423.63	1.44 (11)%
		762.65	26.7 (22)%
		778.44	1.76 (14)%
		1147.33	1.14 (8)%
		1159.97	1.36 (11)%
		1562.51	1.60 (12)%

Table H.2 Continued from previous page

Isotope	Half Life	Energy (keV)	I_γ (%)
^{85m}Sr[115]	67.632 (42) m	151.194	12.8 (4)%
^{85m}Y[115]	4.86 (13) h	231.7	22.8 (22)%
		504.4	1.51 (13)%
		535.6	3.5 (3)%
		568.4	1.67 (14)%
		787.9	1.57 (13)%
		1123.2	1.78 (15)%
		1220.5	1.98 (17)%
		1404.6	3.1 (3)%
		2123.8	5.0 (5)%
^{86}Y[114]	14.74 (2) h	187.87	1.26 (4)%
		190.8	1.01 (3)%
		443.13	16.9 (5)%
		580.57	4.78 (14)%
		608.29	2.01 (15)%
		627.72	32.6 (10)%
		644.82	2.2 (3)%
		645.87	9.2 (11)%
		703.33	15.4 (4)%
		709.9	2.62 (8)%
		740.81	1.36 (5)%
		767.63	2.4 (3)%
		777.37	22.4 (6)%
		835.67	4.4 (6)%
		955.35	1.04 (4)%
		1024.04	3.79 (17)%
		1076.63	82.0 (41)%[2]
		1153.05	30.5 (9)%
		1163.03	1.18 (4)%
		1253.11	1.53 (5)%
		1349.15	2.95 (9)%
		1801.7	1.65 (5)%
		1854.38	17.2 (5)%
		1920.72	20.8 (7)%
		2567.97	2.25 (11)%[2]
		2610.11	1.24 (7)%
^{87}Y[116]	3.325 (125) d	388.5276	82.2 (41)%[2]
		484.805	89.8 (9)%

Table H.2 Continued from previous page

Isotope	Half Life	Energy (keV)	I_γ (%)
^{88}Y[117]	106.626 (21) d	898.042	93.7 (3)%
		1836.063	99.2 (3)%
^{90m}Y[21]	3.19 (6) h	479.51	90.74 (5)%
^{84}Y[113]	39.5 (8) m	703.6	5.8 (6)%
		793.1	98.3 (49)%[2]
		974.3	78 (4)%[2]
		2309.5	1.18 (20)%
^{86m}Y[114]	48 (1) m	208.1	93.80 (469)%[2]
^{91}Y[81]	58.51 (6) d	1204.8	0.26 (4)%
^{87m}Y[116]	13.37 (3) h	380.79	78.05 (390)%[2]
^{86}Zr[114]	16.5 (1) h	29.1	21.6 (15)%
		242.8	95.840 (4792)%[2]
		612	5.8 (3)%[2]
^{87}Zr[116]	1.68 (1) h	1227	2.80 (4)%
^{88}Zr[117]	83.4 (3) d	392.87	97.29 (486)%[2]
^{89}Nb[80]	2.03 (7) h	920.5	1.4 (3)%
		1127	2.1 (5)%
		1259	1.2 (3)%
		1511.4	1.9 (4)%
		1627.2	3.50 (18)%[2]
		2572.3	2.7 (6)%
		2960.1	1.8 (4)%
^{89m}Nb[80]	1.100 (33) h	588	95.57 (478)%[2]
^{90}Nb[21]	14.60 (5) h	132.716	4.13 (4)%
		141.178	66.8 (7)%
		371.307	1.80 (7)%
		890.64	1.80 (4)%
		1129.224	92.7 (5)%
		1270.396	1.296 (25)%
		1611.76	2.38 (7)%
		1913.194	1.280 (17)%
		2186.242	17.96 (17)%
		2318.959	82.0 (3)%
^{91m}Nb[81]	60.86 (22) d	50.1	6.5 (7)%
		1082.6	1.09 (11)%
		1204.67	2.0 (3)%
		1790.6	36.3 (12)%
		1984.6	62.6 (15)%

Table H.2 Continued from previous page

Isotope	Half Life	Energy (keV)	I_γ (%)
^{90}Mo[21]	5.67 (5) h	122.37	64 (3)%[2]
		162.93	6.0 (6)%
		203.13	6.4 (6)%
		257.34	78 (4)%[2]
		323.2	6.3 (6)%
		445.37	6.0 (7)%
		472.2	1.42 (16)%
		941.5	5.5 (7)%
		990.2	1.02 (11)%
		1271.3	4.1 (4)%
		1387.4	1.86 (24)%
		1454.6	1.9 (5)%
^{93m}Mo[118]	6.85 (7) h	263.049	57.4 (11)%
		684.693	99.9 (8)%
		1477.138	99.1 (11)%

[2]When no listed uncertainty is provided, a 5% uncertainty is assumed

Table H.3: Decay data for cross sections measured on Ti foils

Isotope	Half Life	Energy (keV)	I_γ (%)
^{42}K[119]	12.36 (12) h	1524.6	18.08 (90)%[3]
^{43}K[120]	22.3 (1) h	220.632	4.80 (6)%
		372.76	86.8 (43)%[3]
		396.861	11.85 (8)%
		593.39	11.26 (8)%
		617.49	79.2 (6)%
		1021.698	1.96 (3)%
^{47}Ca[121]	4.536 (3) d	1297.09	67.0 (34)%[3]
^{46}Sc[122]	83.79 (4) d	889.277	99.984 (1)%
		1120.545	99.987 (1)%
^{48}Sc[123]	43.6704 (912) h	175.361	7.48 (10)%
		1037.522	97.6 (7)%
		1212.88	2.38 (4)%
^{47}Sc[121]	80.3808 (144) h	159.381	68.3 (4)%
^{44}Ti[124]	60.0 (11) y	67.8679	93 (2)%
		78.3234	96.4 (17)%
^{48}V[123]	15.9735 (25) d	944.13	7.870 (7)%
		983.525	99.98 (4)%
		1312.106	98.2 (3)%
		2240.396	2.333 (13)%

[3]When no listed uncertainty is provided, a 5% uncertainty is assumed

Appendix I

Monitor Foil Product Cross Section Plots

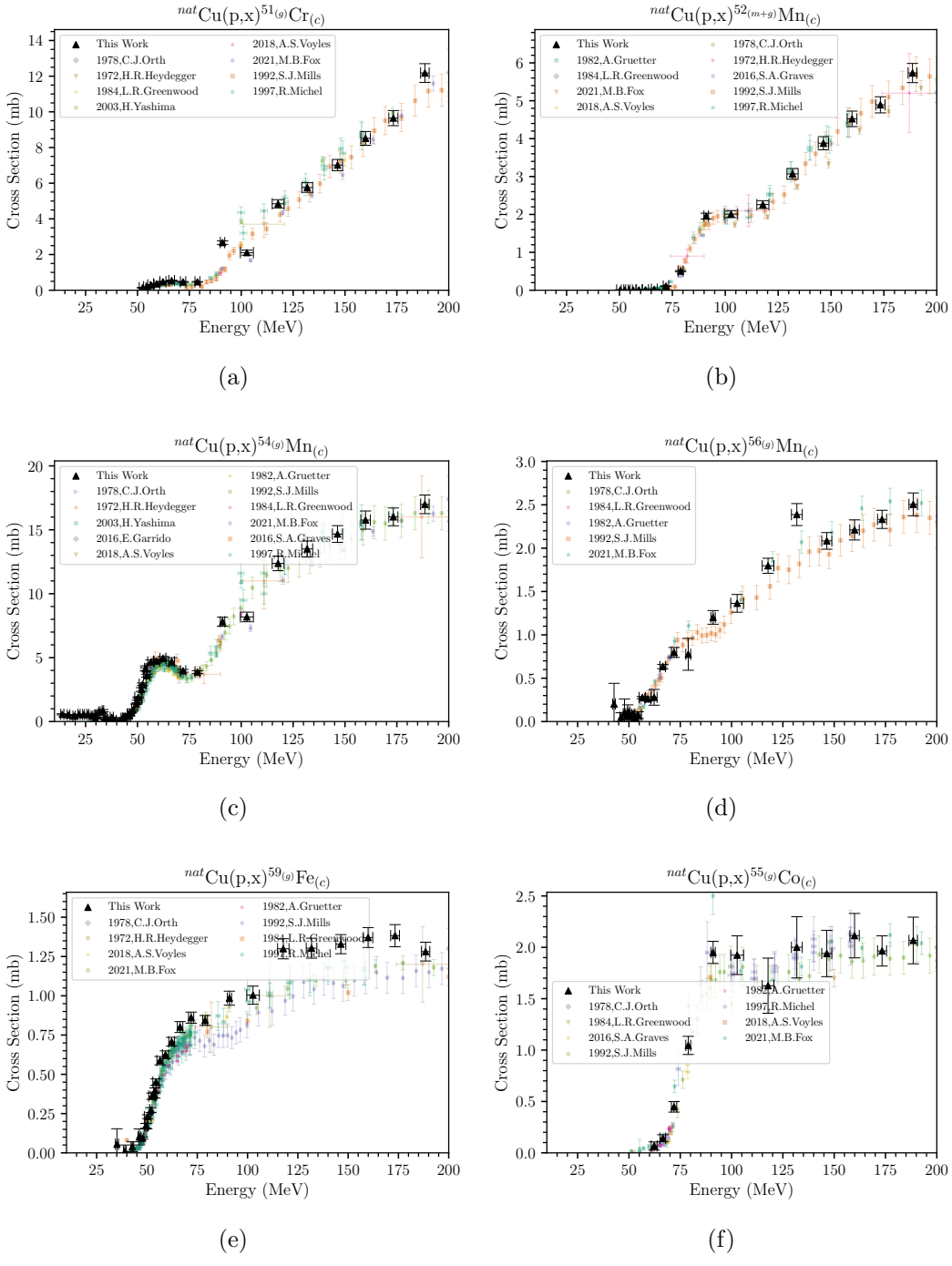

Figure I.1: Proton-induced reactions on ^{nat}Cu foils [125, 126, 127, 128, 129, 13, 130, 17, 131, 132, 133, 134, 135, 136, 137, 138, 139, 140, 141, 142, 143, 144, 145, 146, 147, 148, 149, 11, 150, 151, 152, 153, 154]

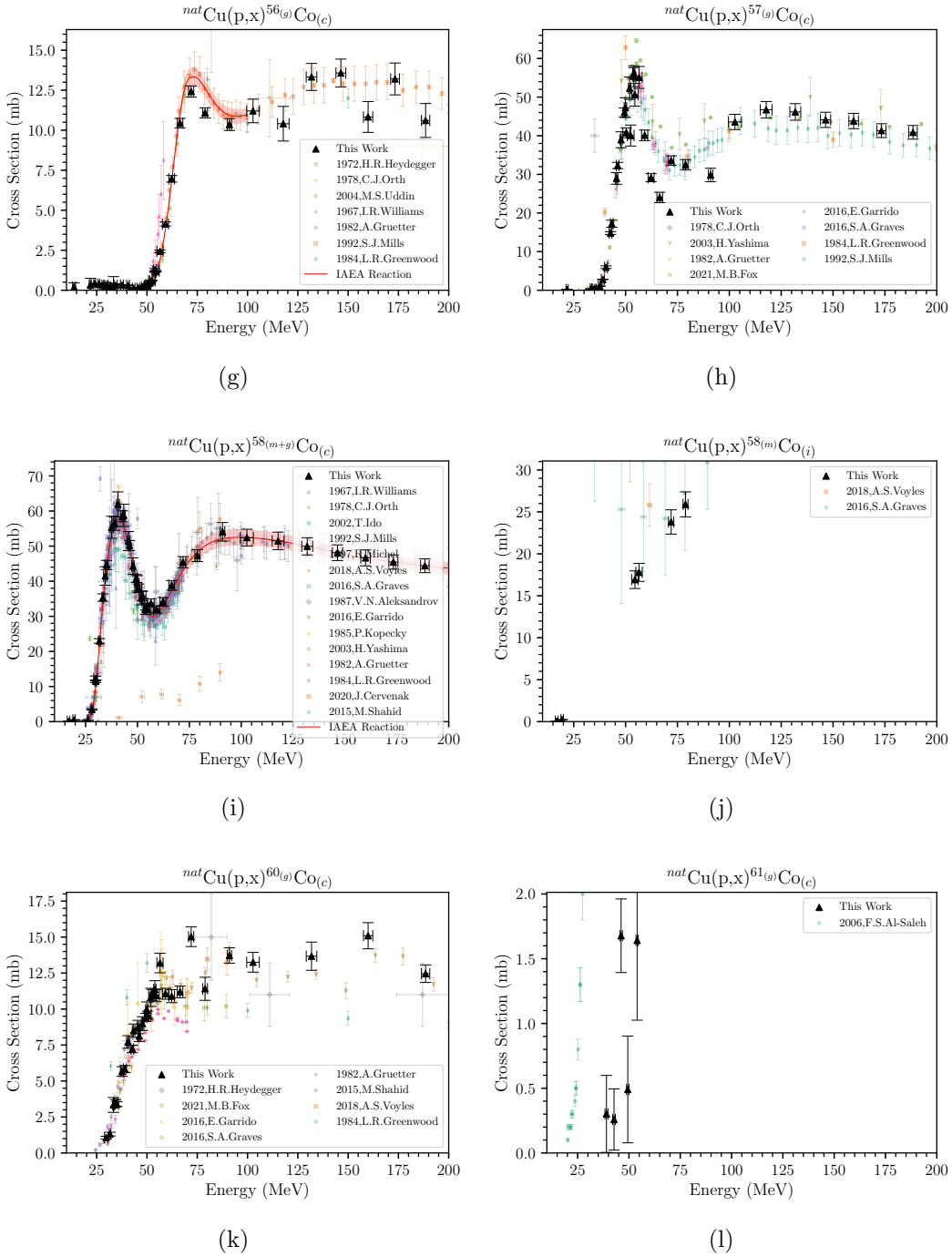

Figure I.1: Proton-induced reactions on $^{\text{nat}}$Cu foils [125, 126, 127, 128, 129, 13, 130, 17, 131, 132, 133, 134, 135, 136, 137, 138, 139, 140, 141, 142, 143, 144, 145, 146, 147, 148, 149, 11, 150, 151, 152, 153, 154]

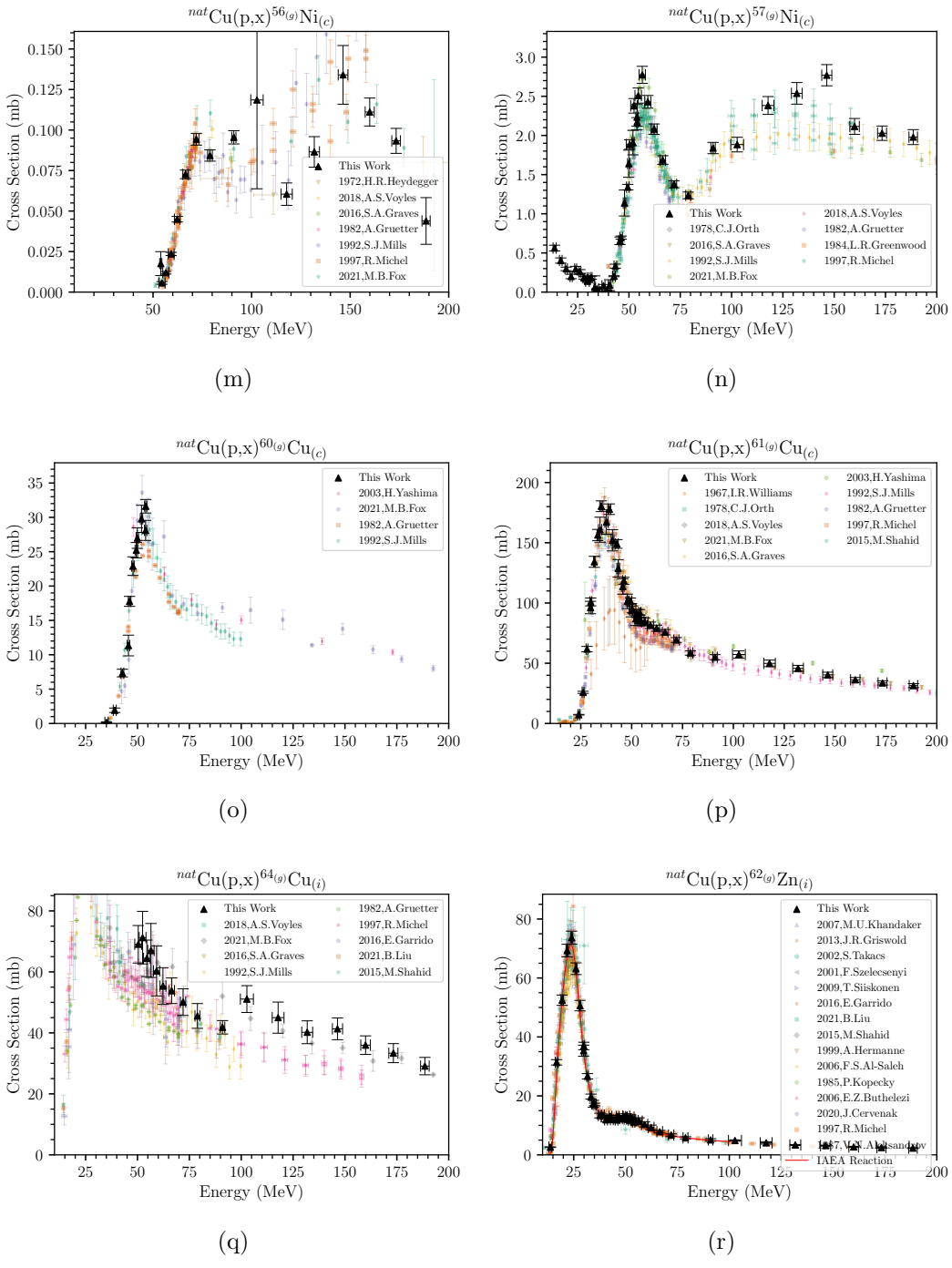

Figure I.1: Proton-induced reactions on ^{nat}Cu foils [125, 126, 127, 128, 129, 13, 130, 17, 131, 132, 133, 134, 135, 136, 137, 138, 139, 140, 141, 142, 143, 144, 145, 146, 147, 148, 149, 11, 150, 151, 152, 153, 154]

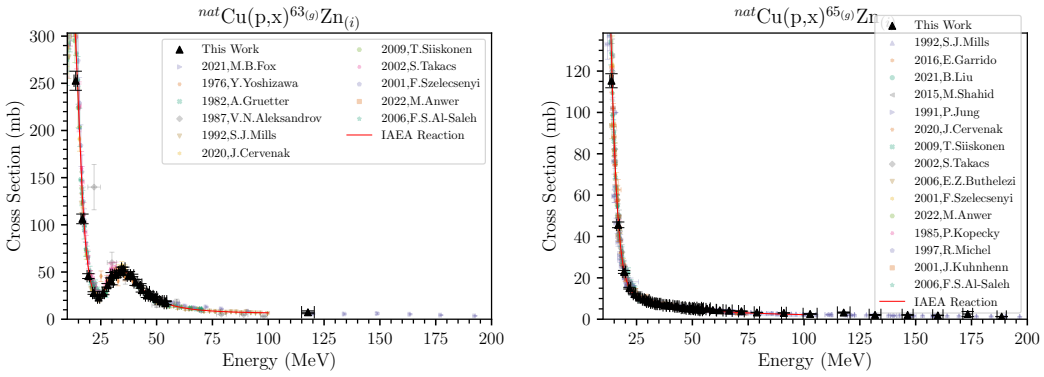

(a) (b)

Figure I.2: Proton-induced reactions on ^{nat}Cu foils [125, 126, 127, 128, 129, 13, 130, 17, 131, 132, 133, 134, 135, 136, 137, 138, 139, 140, 141, 142, 143, 144, 145, 146, 147, 148, 149, 11, 150, 151, 152, 153, 154]

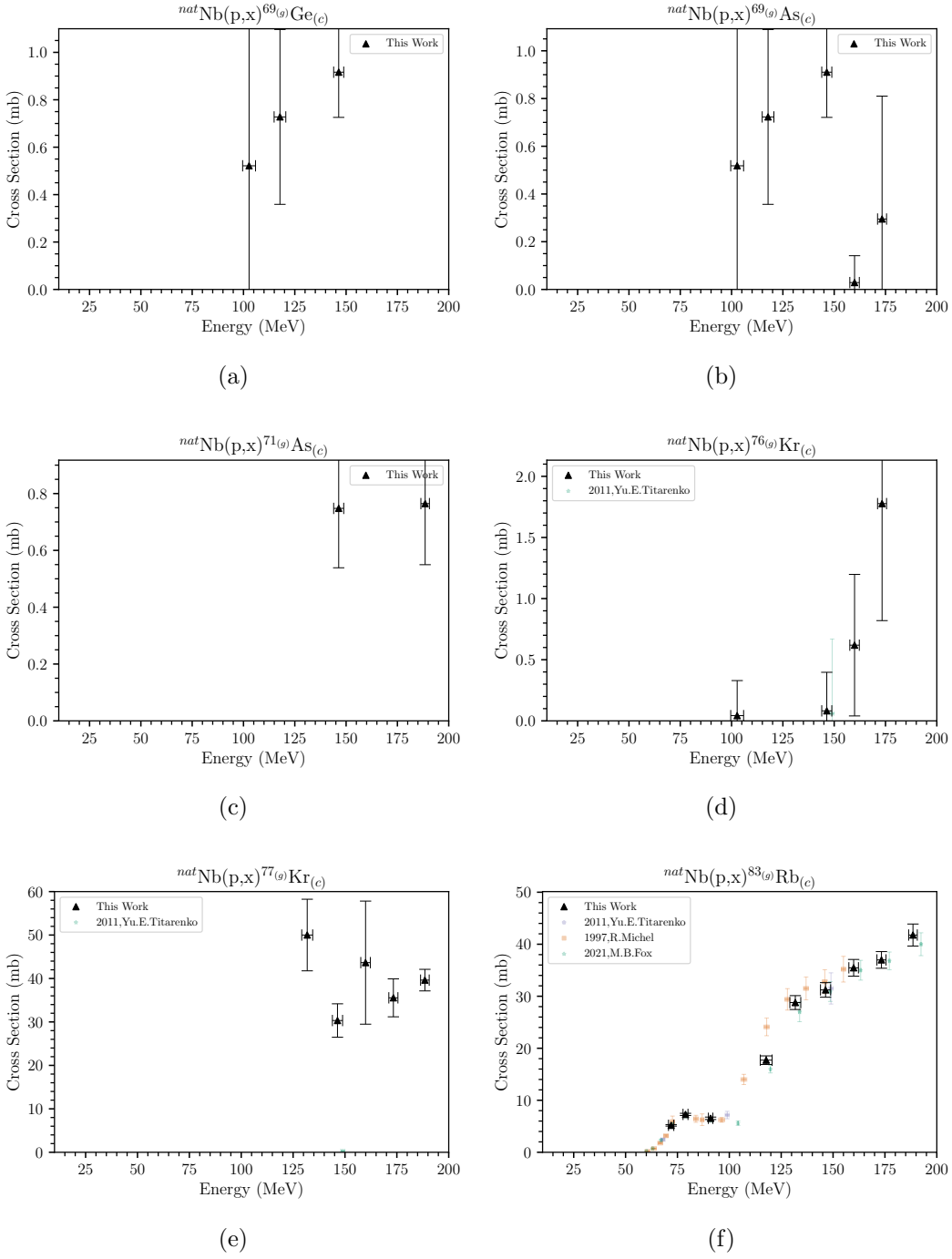

Figure I.3: Proton-induced reactions on ^{nat}Nb foils [155, 156, 157, 158, 159, 160, 161, 12, 162, 163, 164, 141, 165, 166, 167, 168, 169, 11]

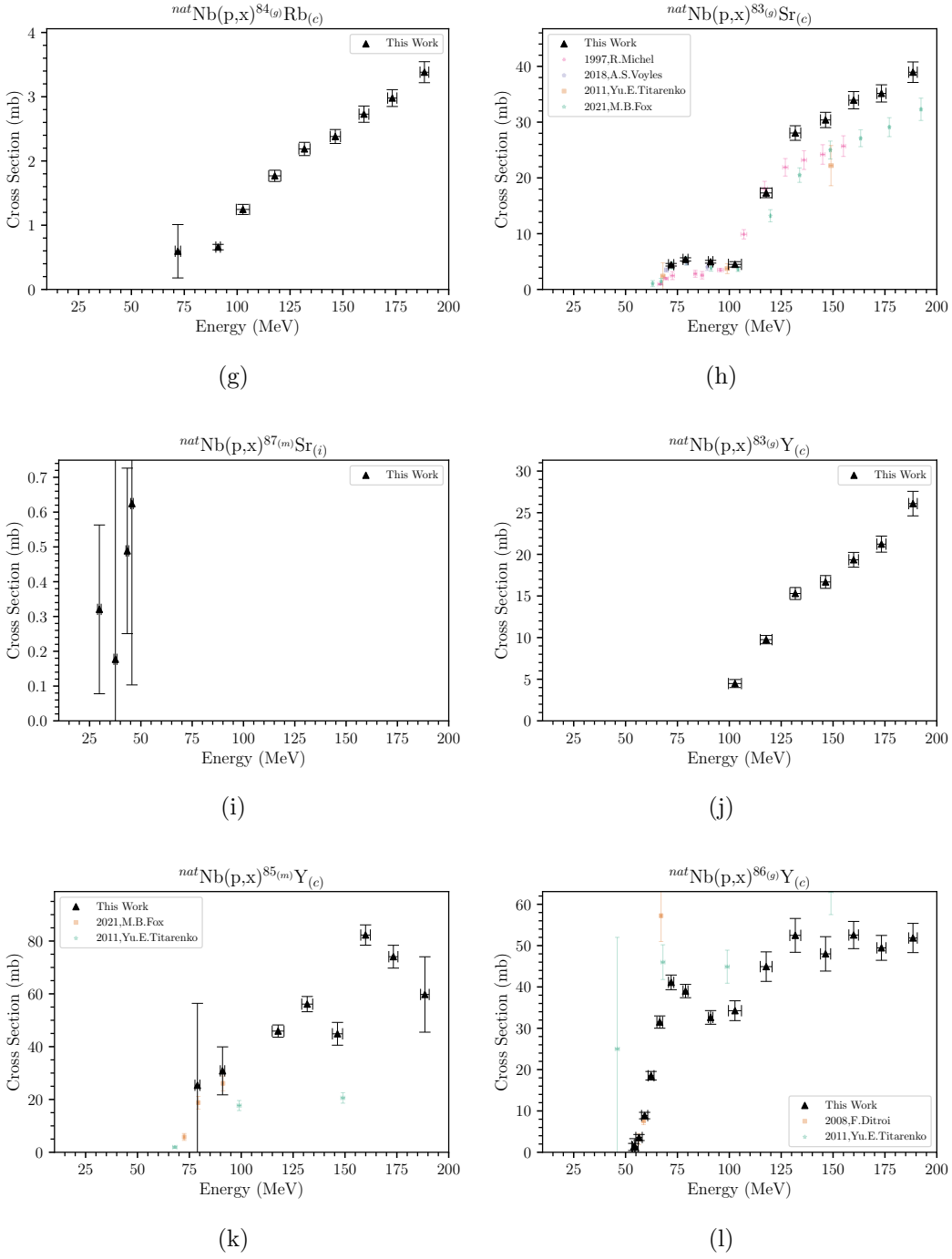

Figure I.3: Proton-induced reactions on ^{nat}Nb foils [155, 156, 157, 158, 159, 160, 161, 12, 162, 163, 164, 141, 165, 166, 167, 168, 169, 11]

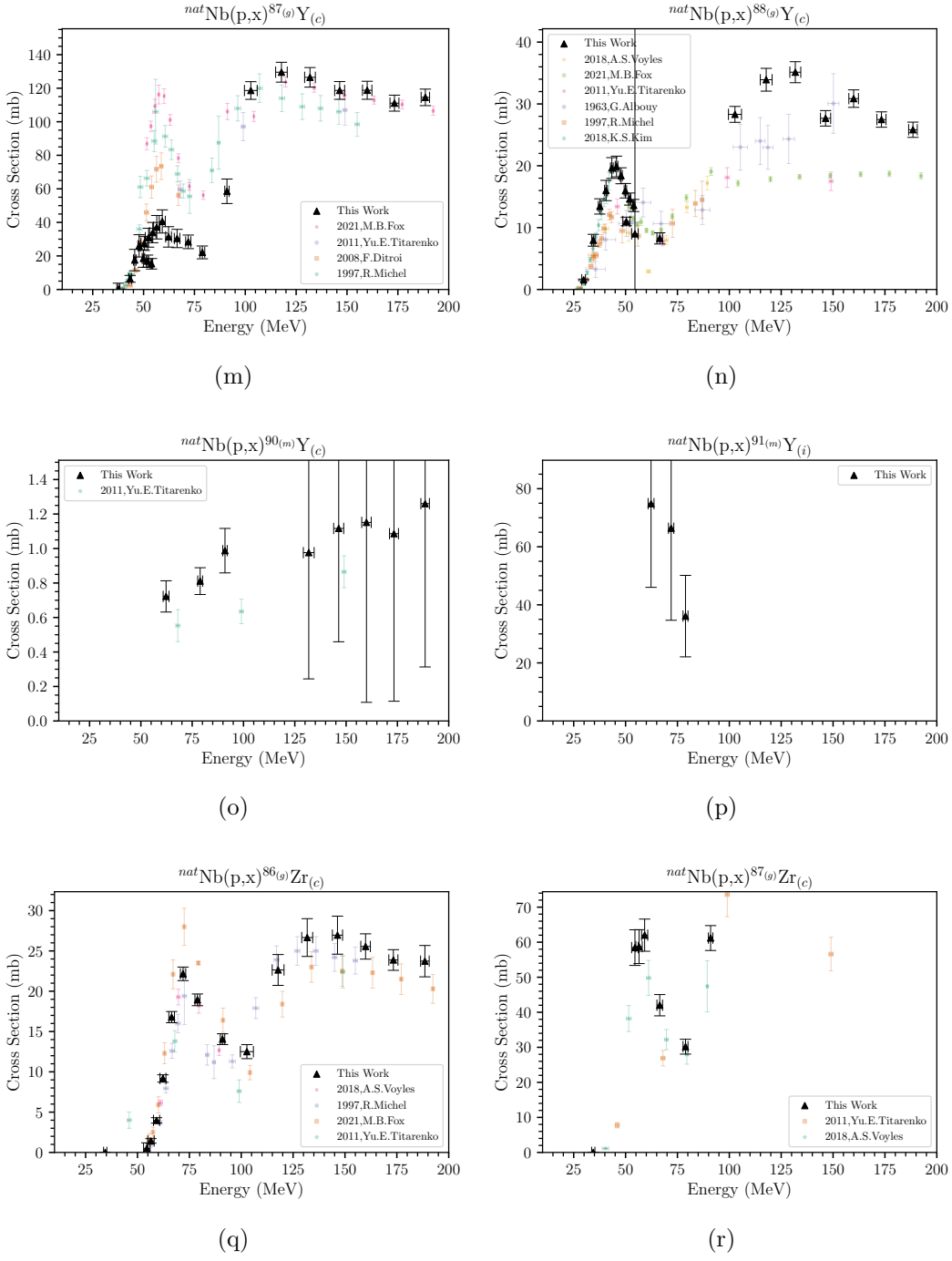

Figure I.3: Proton-induced reactions on ^{nat}Nb foils [155, 156, 157, 158, 159, 160, 161, 12, 162, 163, 164, 141, 165, 166, 167, 168, 169, 11]

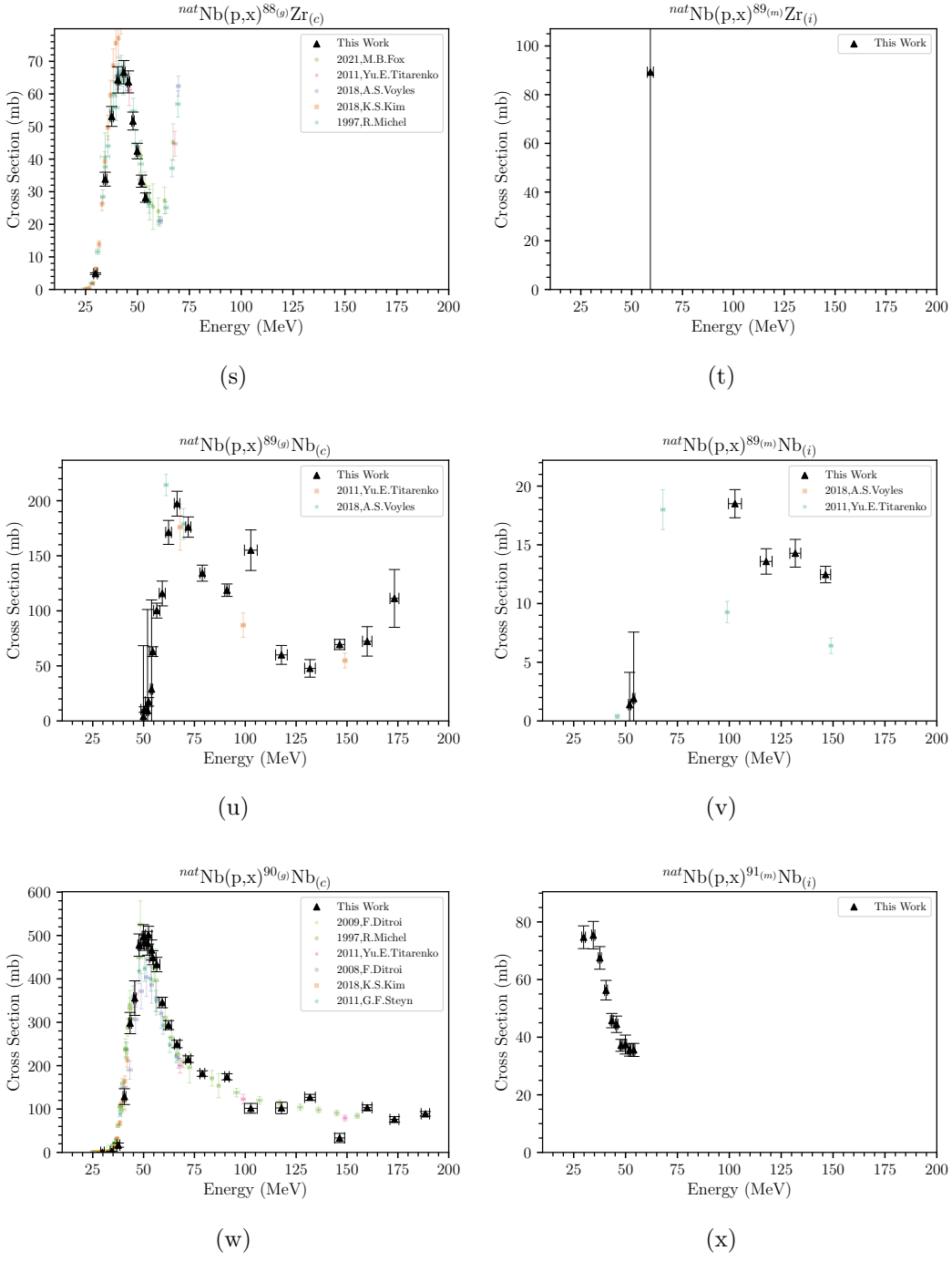

Figure I.3: Proton-induced reactions on ^{nat}Nb foils [155, 156, 157, 158, 159, 160, 161, 12, 162, 163, 164, 141, 165, 166, 167, 168, 169, 11]

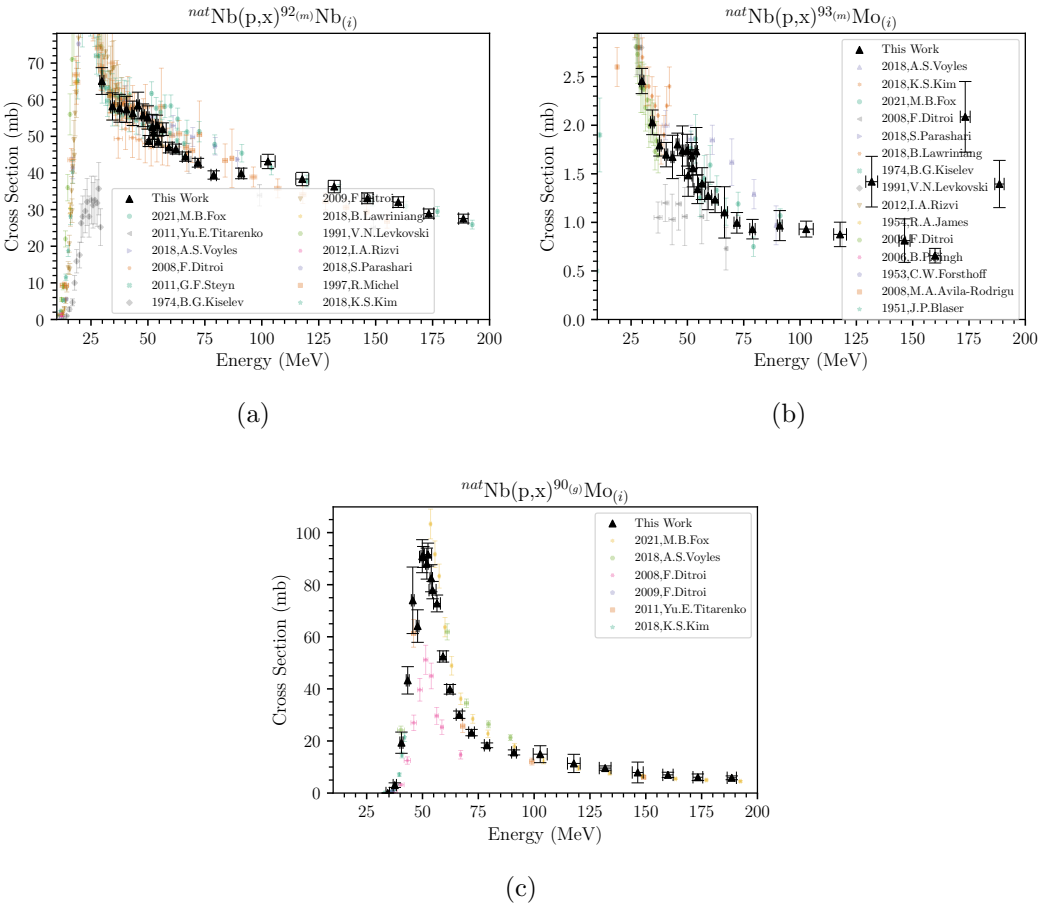

Figure I.4: Proton-induced reactions on ^{nat}Nb foils [155, 156, 157, 158, 159, 160, 161, 12, 162, 163, 164, 141, 165, 166, 167, 168, 169, 11]

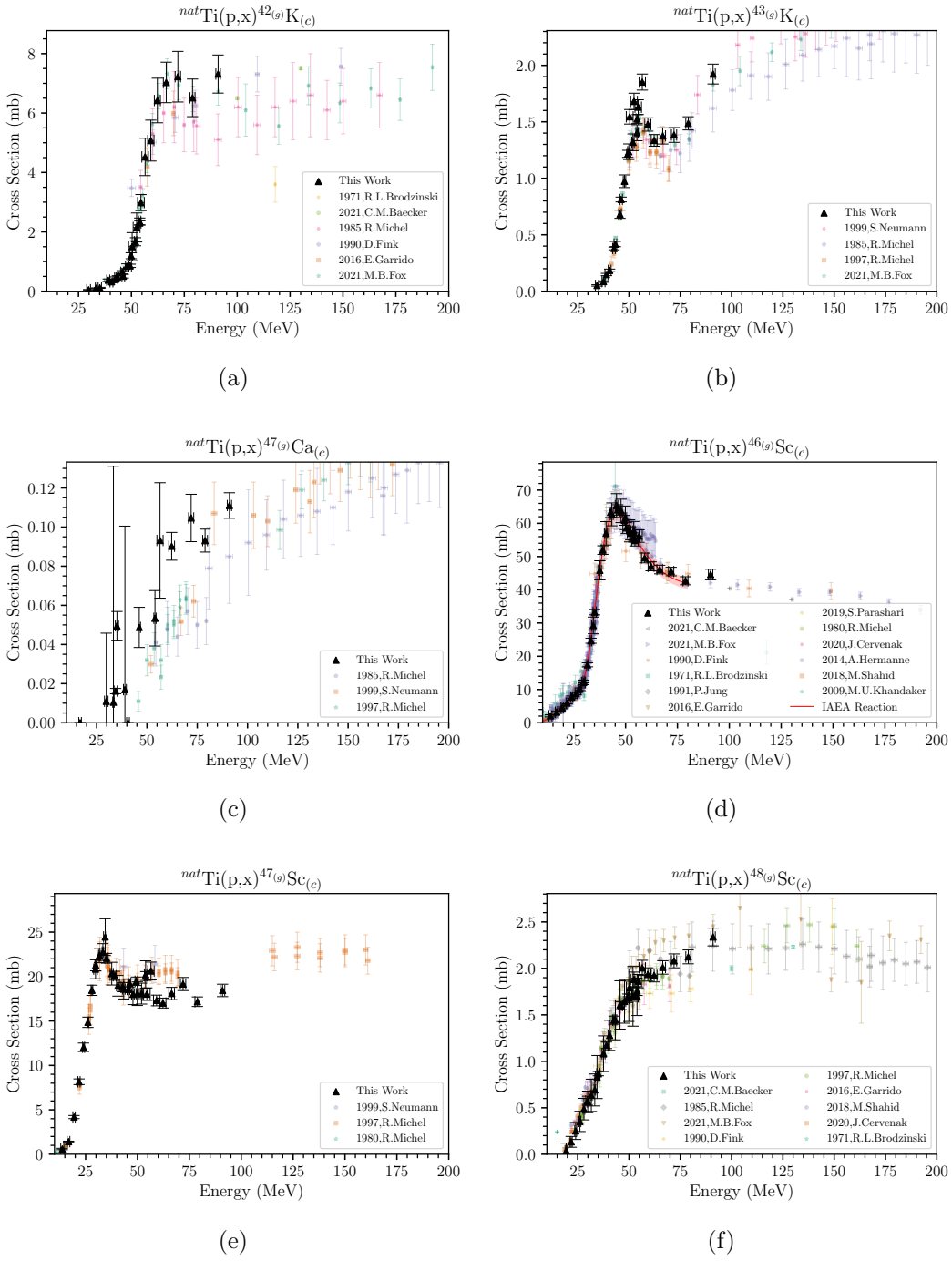

Figure I.5: Proton-induced reactions on ^{nat}Ti foils [127, 170, 171, 172, 173, 174, 129, 175, 176, 13, 130, 177, 178, 179, 180, 140, 141, 181, 182, 183, 184, 185, 147, 148, 186, 187]

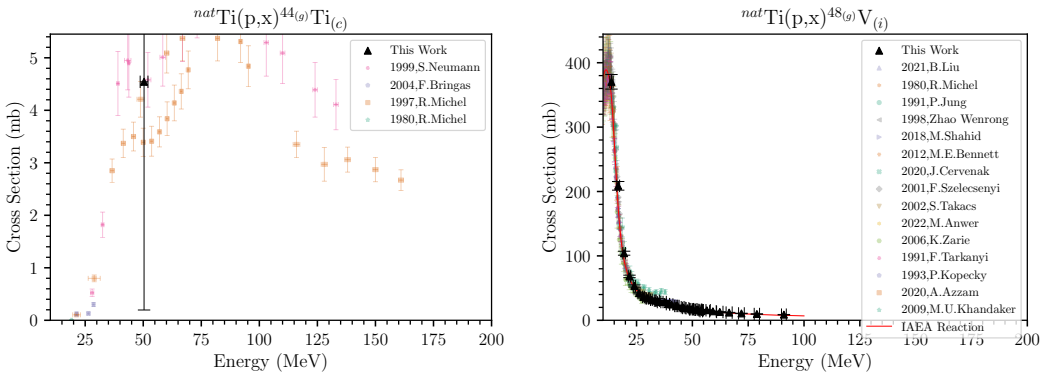

(g) (h)

Figure I.5: Proton-induced reactions on ^{nat}Ti foils [127, 170, 171, 172, 173, 174, 129, 175, 176, 13, 130, 177, 178, 179, 180, 140, 141, 181, 182, 183, 184, 185, 147, 148, 186, 187]

Appendix J

Monitor Foil Product Cross Section Data

Table J.1: Independent and cumulative cross sections measured on Cu foils

E_p (MeV)	188.565 (2069)	173.381 (2183)	159.984 (2301)	146.453 (2441)	131.868 (2621)	117.847 (2835)	102.805 (3123)
Location	BNL	BNL	BNL	BNL	BNL	BNL	BNL
$^{51g}Cr_{(c)}$	12.176 (524)	9.648 (423)	8.512 (386)	7.016 (315)	5.757 (270)	4.844 (231)	2.107 (143)
$^{52g}Mn_{(c)}$	5.731 (253)	4.892 (213)	4.522 (204)	3.880 (174)	3.070 (143)	2.259 (104)	2.009 (92)
$^{54g}Mn_{(c)}$	16.992 (730)	16.010 (695)	15.761 (713)	14.670 (656)	13.502 (629)	12.373 (571)	8.183 (375)
$^{56g}Mn_{(c)}$	2.505 (132)	2.332 (105)	2.210 (116)	2.084 (96)	2.387 (127)	1.797 (87)	1.363 (102)
$^{59g}Fe_{(c)}$	1.281 (60)	1.383 (71)	1.371 (63)	1.329 (61)	1.303 (64)	1.299 (64)	1.004 (58)
$^{55g}Co_{(c)}$	2.067 (227)	1.965 (147)	2.114 (216)	1.940 (225)	2.000 (298)	1.627 (268)	1.924 (188)
$^{56g}Co_{(c)}$	10.607 (1060)	13.204 (995)	10.828 (964)	13.573 (870)	13.328 (843)	10.406 (1082)	11.203 (736)
$^{57g}Co_{(c)}$	40.874 (1767)	41.312 (1788)	43.806 (1980)	44.107 (1970)	46.156 (2141)	46.709 (2145)	43.561 (1975)
$^{58(m+g)}Co_{(i)}$	44.406 (1965)	45.471 (2019)	46.641 (2263)	48.117 (2229)	49.939 (2456)	51.494 (2496)	52.421 (2392)
$^{60g}Co_{(c)}$	12.456 (610)		15.094 (909)		13.672 (981)		13.251 (687)
$^{56g}Ni_{(c)}$	0.044 (14)	0.093 (8)	0.111 (9)	0.134 (18)	0.087 (9)	0.060 (7)	0.119 (55)
$^{57g}Ni_{(c)}$	1.979 (95)	2.029 (92)	2.115 (101)	2.769 (135)	2.537 (138)	2.382 (114)	1.883 (94)
$^{61g}Cu_{(c)}$	31.417 (1669)	33.644 (1741)	36.240 (1921)	40.324 (2222)	45.750 (2488)	49.891 (2737)	57.243 (3051)
$^{64g}Cu_{(i)}$	29.107 (2855)	33.353 (3119)	35.973 (3041)	41.329 (3572)	40.203 (3749)	44.997 (5112)	51.084 (4402)
$^{62g}Zn_{(i)}$	2.285 (141)	2.466 (237)	2.687 (152)	3.130 (166)	3.352 (156)	4.062 (401)	4.853 (234)
$^{63g}Zn_{(i)}$						7.367 (1513)	
$^{65g}Zn_{(i)}$	1.278 (62)	2.510 (1239)	1.849 (132)	2.056 (126)	2.078 (200)	3.215 (281)	2.539 (128)
E_p (MeV)	91.109 (1073)	79.096 (1192)	72.193 (1277)	66.702 (1356)	62.532 (1425)	59.456 (1481)	56.748 (1536)
Location	LANL	LANL	LANL	LANL	LANL	LANL	LANL
$^{51g}Cr_{(c)}$	2.670 (99)	0.469 (18)	0.466 (20)	0.538 (25)	0.477 (16)	0.360 (17)	0.298 (18)
$^{52g}Mn_{(c)}$	1.957 (75)	0.504 (16)	0.109 (5)	0.025 (1)	0.011 (0)	0.009 (0)	0.004 (0)
$^{54g}Mn_{(c)}$	7.811 (351)	3.873 (108)	3.968 (110)	4.682 (317)	4.940 (146)	4.732 (143)	4.663 (156)
$^{56g}Mn_{(c)}$	1.201 (79)	0.775 (184)	0.797 (57)	0.634 (24)	0.279 (91)	0.261 (24)	0.276 (13)
$^{59g}Fe_{(c)}$	0.985 (45)	0.843 (31)	0.861 (35)	0.801 (35)	0.707 (28)	0.625 (25)	0.587 (26)
$^{55g}Co_{(c)}$	1.950 (108)	1.046 (88)	0.448 (51)	0.142 (34)	0.067 (40)		
$^{56g}Co_{(c)}$	10.355 (372)	11.083 (318)	12.417 (353)	10.440 (298)	6.963 (204)	4.141 (127)	2.432 (83)
$^{57g}Co_{(c)}$	29.837 (1751)	32.518 (1303)	33.576 (1219)	24.025 (1340)	29.134 (1044)	40.100 (1375)	55.081 (2834)
$^{58(m+g)}Co_{(i)}$	54.080 (2642)	47.310 (1697)	45.402 (1616)	38.811 (1392)	34.130 (1223)	31.978 (1060)	33.747 (1200)
$^{58m}Co_{(i)}$		25.894 (1498)	23.799 (1448)				17.790 (1072)
$^{60g}Co_{(c)}$	13.723 (531)	11.409 (801)	15.023 (683)	11.192 (404)	10.894 (452)	11.064 (379)	13.200 (682)
$^{56g}Ni_{(c)}$	0.095 (4)	0.084 (4)	0.094 (4)	0.073 (3)	0.045 (2)	0.024 (1)	0.012 (1)
$^{57g}Ni_{(c)}$	1.839 (72)	1.234 (43)	1.376 (45)	1.686 (55)	2.080 (66)	2.429 (81)	2.773 (109)
$^{61g}Cu_{(c)}$	55.012 (2085)	58.515 (1816)	69.274 (2004)	75.766 (2231)	79.087 (2523)	81.505 (2683)	84.330 (3322)
$^{64g}Cu_{(i)}$	41.835 (2204)	45.552 (4056)	50.082 (4362)	53.811 (4202)	55.344 (6032)	60.325 (8204)	67.021 (8849)
$^{62g}Zn_{(i)}$	5.064 (416)	5.773 (367)	6.723 (404)	7.857 (436)	9.281 (821)	10.315 (860)	0.283 (349)
$^{65g}Zn_{(i)}$	3.034 (113)	3.253 (93)	3.877 (110)	4.132 (116)	4.311 (127)	4.447 (136)	5.143 (170)

Table J.1 Continued from previous page

E_p (MeV)	54.784 (1578)	54.082 (562)	54.078 (562)	52.751 (1624)	52.110 (578)	50.641 (1673)	50.075 (594)
Location	LANL	LBNL	LBNL2022	LANL	LBNL	LANL	LBNL
$^{51g}Cr_{(c)}$	0.195 (21)			0.139 (23)			
$^{52g}Mn_{(c)}$	0.004 (3)			0.003 (3)		0.006 (5)	
$^{54g}Mn_{(c)}$	3.594 (108)	4.148 (205)	4.101 (104)	2.919 (100)	2.510 (141)	1.885 (55)	1.561 (100)
$^{56g}Mn_{(c)}$	0.075 (39)		0.006 (18)	0.045 (3)	0.084 (9)		0.110 (15)
$^{59g}Fe_{(c)}$	0.451 (20)	0.368 (19)	0.397 (17)	0.361 (20)	0.273 (16)	0.231 (12)	0.171 (17)
$^{56g}Co_{(c)}$	1.196 (38)	1.278 (75)	1.155 (36)	0.605 (21)	0.564 (59)	0.279 (9)	0.348 (57)
$^{57g}Co_{(c)}$	50.584 (2942)	55.403 (2695)	56.224 (1401)	40.046 (2715)	52.294 (2899)	40.745 (1282)	47.271 (2553)
$^{58(m+g)}Co_{(i)}$	32.202 (1042)	32.096 (1579)	32.706 (929)	35.805 (1318)	35.240 (1966)	38.000 (1214)	39.383 (2195)
$^{58m}Co_{(i)}$	16.918 (1050)						
$^{60g}Co_{(c)}$	10.934 (423)	11.369 (601)	11.078 (301)	10.976 (388)	10.811 (630)	9.580 (276)	9.955 (539)
$^{61g}Co_{(c)}$			1.642 (616)				
$^{56g}Ni_{(c)}$	0.006 (1)	0.018 (7)					
$^{57g}Ni_{(c)}$	2.509 (97)	2.234 (161)	2.173 (54)	2.378 (93)	1.908 (156)	1.884 (61)	1.639 (173)
$^{60g}Cu_{(c)}$		28.099 (1460)	31.616 (985)		29.782 (1975)		26.980 (1496)
$^{61g}Cu_{(c)}$	85.454 (2682)	85.732 (4507)	92.169 (2308)	91.266 (3232)	86.807 (5479)	94.684 (2841)	94.023 (5499)
$^{64g}Cu_{(i)}$	64.435 (5994)			71.239 (8624)		69.059 (6147)	
$^{62g}Zn_{(i)}$	11.612 (659)	11.139 (649)	11.951 (301)	12.826 (733)	11.784 (746)	13.218 (744)	12.174 (709)
$^{63g}Zn_{(i)}$		17.102 (1685)	19.011 (543)		19.065 (1340)		21.468 (1306)
$^{65g}Zn_{(i)}$	4.897 (150)	4.435 (217)	4.721 (129)	5.402 (185)	4.747 (288)	5.478 (156)	4.958 (269)
E_p (MeV)	49.529 (600)	47.985 (613)	46.287 (632)	45.814 (635)	43.564 (660)	42.848 (670)	40.769 (695)
Location	LBNL2022	LBNL	LBNL2022	LBNL	LBNL	LBNL2022	LBNL
$^{54g}Mn_{(c)}$	1.382 (38)	0.897 (73)	0.456 (28)	0.592 (33)	0.286 (30)	0.245 (36)	
$^{56g}Mn_{(c)}$	0.059 (133)	0.091 (170)	0.051 (51)			0.203 (238)	
$^{59g}Fe_{(c)}$	0.172 (15)	0.094 (7)	0.101 (51)			0.039 (31)	
$^{56g}Co_{(c)}$	0.241 (50)	0.209 (50)	0.013 (28)	0.122 (41)	0.118 (55)		0.314 (19)
$^{57g}Co_{(c)}$	46.041 (1149)	38.956 (2062)	32.294 (810)	28.953 (1522)	17.217 (906)	14.787 (358)	5.967 (338)
$^{58(m+g)}Co_{(i)}$	40.751 (1110)	44.313 (2340)	50.180 (1436)	51.456 (2711)	58.766 (3159)	58.502 (1582)	61.892 (3572)
$^{60g}Co_{(c)}$	9.421 (284)	8.991 (476)	8.131 (382)	8.753 (465)	8.499 (462)	7.225 (259)	7.711 (437)
$^{61g}Co_{(c)}$	0.491 (412)		1.678 (284)			0.259 (237)	
$^{57g}Ni_{(c)}$	1.340 (35)	1.137 (166)	0.696 (19)	0.655 (49)	0.331 (25)	0.203 (6)	0.088 (70)
$^{60g}Cu_{(c)}$	25.213 (1122)	22.900 (1352)	17.771 (724)	11.347 (1506)		7.335 (554)	
$^{61g}Cu_{(c)}$	101.653 (2516)	101.286 (6044)	118.457 (2900)	113.724 (6381)	128.737 (7274)	149.029 (3593)	152.081 (8830)
$^{62g}Zn_{(i)}$	12.935 (323)	12.276 (774)	12.969 (319)	11.843 (757)	11.954 (650)	13.055 (323)	11.890 (711)
$^{63g}Zn_{(i)}$	23.405 (656)	24.531 (1576)	28.663 (829)	25.119 (2150)	30.830 (2046)	36.576 (1115)	39.026 (3189)
$^{65g}Zn_{(i)}$	5.234 (145)	5.142 (492)	5.687 (174)	5.456 (286)	6.117 (558)	6.166 (155)	6.443 (365)

Table J.1 Continued from previous page

E_p (MeV)	39.187 (719)	37.832 (736)	35.231 (781)	34.693 (788)	33.525 (378)	31.846 (394)	30.093 (411)
Location	LBNL2022	LBNL	LBNL2022	LBNL	LBNL	LBNL	LBNL
$^{54g}Mn_{(c)}$	0.089 (34)	0.328 (19)	0.155 (35)	0.318 (24)	0.849 (88)	0.746 (97)	0.541 (34)
$^{59g}Fe_{(c)}$	0.010 (40)		0.055 (98)				
$^{56g}Co_{(c)}$		0.321 (23)		0.308 (97)	0.123 (730)	0.207 (119)	0.248 (205)
$^{57g}Co_{(c)}$	2.801 (73)	1.053 (61)	0.237 (13)	0.209 (22)	0.338 (20)		
$^{58(m+g)}Co_{(i)}$	56.397 (1889)	55.375 (3153)	44.623 (1297)	41.497 (2639)	35.334 (1052)	22.972 (662)	11.489 (362)
$^{60g}Co_{(c)}$	5.838 (243)	5.660 (334)	3.391 (172)	3.481 (226)	3.336 (516)	1.310 (128)	
$^{61g}Co_{(c)}$	0.302 (297)						
$^{57g}Ni_{(c)}$	0.017 (3)	0.081 (16)	0.001 (4)	0.040 (4)	0.059 (148)	0.184 (19)	0.182 (23)
$^{60g}Cu_{(c)}$	1.921 (325)		0.151 (79)				
$^{61g}Cu_{(c)}$	177.856 (4401)	167.189 (10133)	180.322 (4461)	160.846 (10397)	156.454 (4649)	134.188 (4571)	100.895 (3264)
$^{62g}Zn_{(i)}$	13.478 (345)	13.333 (789)	17.101 (430)	17.320 (1174)	19.753 (858)	26.656 (897)	36.926 (1272)
$^{63g}Zn_{(i)}$	46.394 (1315)	46.098 (4377)	53.731 (1478)	50.810 (4378)	49.598 (2131)	47.175 (3140)	46.930 (2499)
$^{65g}Zn_{(i)}$	6.640 (185)	6.680 (381)	7.366 (185)	7.350 (454)	7.615 (205)	8.008 (251)	8.464 (257)

E_p (MeV)	30.053 (881)	28.257 (431)	26.340 (456)	24.305 (485)	22.124 (522)	19.764 (570)	17.136 (637)
Location	LBNL	LBNL	LBNL	LBNL	LBNL	LBNL	LBNL
$^{54g}Mn_{(c)}$	0.223 (30)	0.430 (55)	0.552 (92)	0.544 (18)	0.557 (23)	0.417 (59)	0.518 (36)
$^{56g}Co_{(c)}$	0.298 (20)	0.311 (151)	0.379 (20)	0.412 (21)	0.326 (419)		
$^{57g}Co_{(c)}$					0.175 (13)		
$^{58(m+g)}Co_{(i)}$	12.293 (687)	3.475 (170)	0.416 (19)			0.504 (17)	0.073 (118)
$^{58m}Co_{(i)}$						0.236 (15)	0.039 (5)
$^{60g}Co_{(c)}$	1.067 (90)						
$^{57g}Ni_{(c)}$	0.138 (13)	0.182 (15)	0.259 (28)	0.294 (35)	0.199 (28)	0.296 (23)	0.403 (33)
$^{61g}Cu_{(c)}$	96.242 (5175)	61.721 (2222)	25.829 (872)	7.257 (280)			
$^{62g}Zn_{(i)}$	35.329 (1879)	50.624 (1783)	63.150 (1979)	73.694 (2193)	69.292 (2143)	52.470 (1749)	31.384 (915)
$^{63g}Zn_{(i)}$	39.969 (3457)	35.938 (1966)	27.742 (1758)	22.907 (634)	27.752 (1372)	45.681 (2565)	106.330 (5116)
$^{65g}Zn_{(i)}$	9.178 (496)	9.537 (393)	10.447 (314)	12.161 (355)	15.015 (407)	22.872 (726)	45.642 (1372)

E_p (MeV)	14.166 (733)
Location	LBNL
$^{54g}Mn_{(c)}$	0.563 (46)
$^{56g}Co_{(c)}$	0.203 (260)
$^{57g}Ni_{(c)}$	0.562 (37)
$^{62g}Zn_{(i)}$	2.613 (109)
$^{63g}Zn_{(i)}$	252.707 (10115)
$^{65g}Zn_{(i)}$	115.325 (3398)

Table J.2: Independent and cumulative cross sections measured on Nb foils

E_p (MeV)	188.398 (2070)	173.201 (2185)	159.798 (2303)	146.254 (2443)	131.650 (2625)	117.620 (2838)	102.548 (3129)
Location	BNL	BNL	BNL	BNL	BNL	BNL	BNL
$^{69g}Ge_{(c)}$				0.916 (191)		0.728 (369)	0.522 (1345)
$^{69g}As_{(c)}$		0.295 (515)	0.029 (113)	0.910 (189)		0.723 (366)	0.518 (1336)
$^{71g}As_{(c)}$	0.765 (215)			0.748 (209)			
$^{76g}Kr_{(c)}$		1.777 (957)	0.619 (579)	0.082 (315)			0.043 (287)
$^{77g}Kr_{(c)}$	39.623 (2484)	35.548 (4368)	43.649 (14167)	30.326 (3847)	50.002 (8241)		
$^{83g}Rb_{(c)}$	41.768 (2117)	36.983 (1602)	35.466 (1608)	31.213 (1401)	28.782 (1335)	17.708 (825)	
$^{84g}Rb_{(c)}$	3.382 (163)	2.979 (131)	2.729 (127)	2.381 (109)	2.187 (103)	1.768 (87)	1.245 (79)
$^{83g}Sr_{(c)}$	38.955 (1839)	35.150 (1545)	33.935 (1543)	30.390 (1370)	28.045 (1305)	17.301 (844)	4.498 (483)
$^{83g}Y_{(c)}$	26.093 (1473)	21.226 (967)	19.342 (887)	16.682 (767)	15.295 (719)	9.756 (499)	4.481 (481)
$^{85m}Y_{(c)}$	59.764 (14278)	74.070 (4321)	82.275 (3838)	44.869 (4317)	56.111 (2885)	45.894 (2326)	
$^{86g}Y_{(c)}$	51.845 (3536)	49.457 (3006)	52.562 (3291)	48.003 (4162)	52.478 (4092)	44.919 (3569)	34.253 (2397)
$^{87g}Y_{(c)}$	114.533 (4924)	111.090 (4768)	118.770 (5367)	118.669 (5283)	126.478 (5845)	129.542 (5923)	118.630 (5262)
$^{88g}Y_{(c)}$	25.827 (1232)	27.478 (1241)	30.862 (1412)	27.677 (1249)	35.133 (1698)	33.915 (1843)	28.313 (1286)
$^{90m}Y_{(c)}$	1.260 (947)	1.086 (972)	1.151 (1043)	1.116 (657)	0.976 (732)		
$^{86g}Zr_{(c)}$	23.730 (1943)	23.874 (1282)	25.552 (1570)	26.955 (2357)	26.658 (2342)	22.639 (1913)	12.505 (869)
$^{89g}Nb_{(c)}$		111.269 (26242)	72.280 (13378)	69.442 (4633)	47.754 (7972)	59.978 (8573)	155.077 (18436)
$^{89m}Nb_{(i)}$				12.468 (701)	14.282 (1180)	13.585 (1084)	18.505 (1201)
$^{90g}Nb_{(c)}$	88.989 (5248)	76.238 (6339)	103.274 (6328)	33.364 (10613)	127.018 (6779)	102.540 (13245)	101.691 (11314)
$^{92m}Nb_{(i)}$	27.545 (1213)	28.912 (1259)	32.040 (1459)	33.088 (1481)	36.285 (1701)	38.344 (1819)	43.144 (1954)
$^{90g}Mo_{(i)}$	5.858 (729)	6.077 (1260)	6.986 (1008)	7.907 (3990)	9.596 (826)	11.377 (3503)	14.923 (3247)
$^{93m}Mo_{(i)}$	1.395 (243)	2.087 (364)	0.657 (75)	0.812 (224)	1.419 (261)	0.876 (126)	0.931 (82)
E_p (MeV)	90.831 (1075)	78.772 (1195)	71.845 (1282)	66.336 (1362)	62.141 (1432)	59.049 (1489)	56.347 (1544)
Location	LANL	LANL	LANL	LANL	LANL	LANL	LANL
$^{83g}Rb_{(c)}$	6.534 (232)	7.284 (209)	5.181 (148)				
$^{84g}Rb_{(c)}$	0.659 (43)		0.595 (416)				
$^{83g}Sr_{(c)}$	4.965 (245)	5.385 (292)	4.429 (230)				
$^{85m}Y_{(c)}$	30.837 (9084)	25.372 (31032)					
$^{86g}Y_{(c)}$	32.626 (1654)	39.007 (1608)	41.109 (1772)	31.505 (1489)	18.516 (1040)	8.882 (783)	3.572 (729)
$^{87g}Y_{(c)}$	58.550 (7308)	22.105 (3819)	28.402 (4062)	30.401 (5449)	31.361 (6091)	40.561 (6917)	37.125 (7002)
$^{88g}Y_{(c)}$				8.257 (902)			
$^{90m}Y_{(c)}$	0.988 (129)	0.811 (78)			0.722 (91)		
$^{91m}Y_{(i)}$		36.114 (14029)	66.376 (31691)		74.839 (28815)		
$^{86g}Zr_{(c)}$	14.052 (669)	18.932 (727)	22.155 (843)	16.787 (695)	9.176 (457)	3.972 (337)	1.429 (284)
$^{87g}Zr_{(c)}$	61.184 (3553)	30.184 (2122)		42.018 (3037)		62.007 (4590)	58.732 (4833)
$^{89g}Nb_{(c)}$	118.742 (5676)	134.227 (7289)	176.075 (9234)	197.315 (11282)	171.241 (10872)	115.765 (11250)	100.221 (6761)
$^{90g}Nb_{(c)}$	174.377 (7090)	181.855 (6328)	214.904 (7662)	249.963 (8620)	293.461 (10339)	345.637 (12086)	433.082 (16639)
$^{92m}Nb_{(i)}$	39.874 (1449)	39.446 (1133)	42.792 (1197)	44.457 (1270)	46.527 (1365)	46.941 (1456)	51.946 (1737)
$^{90g}Mo_{(i)}$	15.606 (971)	18.337 (921)	23.221 (1222)	30.089 (1415)	39.842 (1851)	52.442 (2157)	72.802 (3232)

Table J.2 Continued from previous page

E_p (MeV)	90.831 (1075)	78.772 (1195)	71.845 (1282)	66.336 (1362)	62.141 (1432)	59.049 (1489)	56.347 (1544)
Location	LANL	LANL	LANL	LANL	LANL	LANL	LANL
$^{93m}Mo_{(i)}$	0.967 (155)	0.930 (100)	0.995 (106)	1.103 (264)	1.235 (134)	1.272 (142)	1.399 (164)
E_p (MeV)	54.367 (1587)	53.674 (565)	52.308 (1634)	51.687 (581)	50.203 (1682)	49.644 (597)	47.529 (616)
Location	LANL	LBNL	LANL	LBNL	LANL	LBNL	LBNL
$^{86g}Y_{(c)}$	1.436 (1858)	1.288 (855)					
$^{87g}Y_{(c)}$	33.919 (6043)	15.324 (3125)	30.870 (5622)	16.886 (3618)	27.485 (4211)	18.504 (5264)	26.009 (6635)
$^{88g}Y_{(c)}$	8.989 (80592)	13.582 (983)		14.622 (977)	11.001 (696)	15.967 (1169)	18.388 (1292)
$^{86g}Zr_{(c)}$	0.510 (682)						
$^{87g}Zr_{(c)}$	58.456 (5086)						
$^{88g}Zr_{(c)}$		28.189 (1420)		33.230 (1862)		42.472 (2379)	51.683 (2749)
$^{89g}Nb_{(c)}$	62.992 (4380)	28.864 (81061)	17.321 (3860)	9.404 (91802)	10.335 (2527)	4.116 (64264)	
$^{89m}Nb_{(i)}$		1.907 (5661)		1.388 (2750)			
$^{90g}Nb_{(c)}$	448.839 (16171)	466.560 (23201)	500.805 (20483)	482.096 (27454)	483.387 (17703)	497.253 (27726)	477.863 (25762)
$^{91m}Nb_{(i)}$		35.581 (2267)		35.570 (2141)		37.447 (3287)	37.170 (2075)
$^{92m}Nb_{(i)}$	48.532 (1502)	53.042 (2741)	51.044 (1807)	52.555 (3441)	48.712 (1502)	55.135 (3181)	55.743 (3105)
$^{90g}Mo_{(i)}$	77.921 (3334)	82.478 (5196)	91.558 (4407)	88.101 (5957)	90.654 (4022)	90.947 (6338)	64.118 (6244)
$^{93m}Mo_{(i)}$	1.342 (149)	1.732 (245)	1.557 (191)	1.688 (135)	1.484 (216)	1.743 (164)	1.738 (255)
E_p (MeV)	45.348 (639)	43.065 (665)	40.261 (701)	37.284 (744)	34.100 (797)	29.412 (895)	
Location	LBNL	LBNL	LBNL	LBNL	LBNL	LBNL	
$^{87m}Sr_{(i)}$	0.624 (521)	0.489 (238)		0.177 (2441)		0.320 (243)	
$^{87g}Y_{(c)}$	17.549 (6383)	6.346 (2051)		0.197 (3561)			
$^{88g}Y_{(c)}$	19.886 (1673)	19.639 (1678)	16.003 (1641)	13.429 (1233)	7.960 (961)	1.560 (126)	
$^{86g}Zr_{(c)}$					0.000 (0)		
$^{87g}Zr_{(c)}$					0.010 (2)		
$^{88g}Zr_{(c)}$	63.690 (3374)	66.665 (3574)	64.315 (4033)	53.089 (3048)	33.845 (2133)	4.858 (255)	
$^{90g}Nb_{(c)}$	355.743 (39821)	298.210 (24553)	128.645 (18195)	16.891 (4801)	1.924 (523)	0.415 (135)	
$^{91m}Nb_{(i)}$	44.477 (2851)	45.750 (2483)	56.311 (3399)	67.516 (3922)	75.412 (4770)	74.687 (3947)	
$^{92m}Nb_{(i)}$	58.414 (3640)	56.281 (3332)	57.354 (3556)	57.659 (3798)	58.158 (3718)	65.097 (3651)	
$^{90g}Mo_{(i)}$	74.009 (12772)	43.278 (5252)	19.343 (4073)	3.042 (881)	0.012 (74)		
$^{93m}Mo_{(i)}$	1.803 (116)	1.674 (223)	1.697 (126)	1.792 (109)	2.030 (127)	2.455 (130)	

Table J.3: Independent and cumulative cross sections measured on Ti foils

E_p (MeV)	90.742 (1075)	78.674 (1196)	71.739 (1282)	66.223 (1363)	62.023 (1433)	58.925 (1490)	56.219 (1546)
Location	LANL	LANL	LANL	LANL	LANL	LANL	LANL
$^{42g}K_{(c)}$	7.314 (642)	6.512 (633)	7.225 (853)	7.031 (682)	6.423 (751)	5.073 (689)	4.522 (629)
$^{43g}K_{(c)}$	1.923 (88)	1.486 (58)	1.384 (66)	1.375 (72)	1.336 (52)	1.476 (59)	1.852 (71)
$^{47g}Ca_{(c)}$	0.111 (7)	0.093 (6)	0.105 (12)		0.090 (7)		0.093 (30)
$^{46(m+g)}Sc_{(i)}$	44.588 (1590)	42.715 (1210)	45.494 (1281)	46.096 (1297)	47.056 (1354)	49.575 (1470)	56.170 (1881)
$^{47g}Sc_{(c)}$	18.440 (699)	17.171 (539)	19.159 (738)	18.095 (690)	17.019 (559)	17.308 (600)	20.626 (1001)
$^{48g}Sc_{(c)}$	2.338 (96)	2.124 (75)	2.081 (75)	2.010 (72)	1.925 (70)	1.935 (72)	2.006 (82)
$^{48g}V_{(i)}$	8.723 (329)	9.734 (303)	10.633 (313)	11.932 (363)	12.931 (411)	13.928 (424)	15.632 (513)
E_p (MeV)	54.235 (1589)	53.696 (562)	53.545 (563)	52.171 (1636)	51.553 (580)	50.065 (1684)	49.506 (595)
Location	LANL	LBNL2022	LBNL	LANL	LBNL	LANL	LBNL
$^{42g}K_{(c)}$	2.986 (271)	2.301 (71)	2.351 (115)	2.148 (488)	1.668 (135)	1.502 (472)	1.196 (101)
$^{43g}K_{(c)}$	1.630 (65)	1.525 (38)	1.403 (70)	1.681 (73)	1.319 (74)	1.544 (64)	1.235 (69)
$^{47g}Ca_{(c)}$		0.053 (14)					
$^{46(m+g)}Sc_{(i)}$	54.806 (1629)	55.740 (1401)	57.718 (2840)	57.015 (1950)	57.730 (3319)	58.595 (1681)	61.650 (3556)
$^{47g}Sc_{(c)}$	18.022 (705)	20.058 (500)	20.226 (1544)		18.079 (1177)		18.070 (1328)
$^{48g}Sc_{(c)}$	1.863 (72)	1.755 (47)	1.694 (202)	1.881 (80)	1.700 (321)	1.793 (69)	1.711 (282)
$^{44g}Ti_{(c)}$						4.543 (4347)	
$^{48g}V_{(i)}$	15.544 (466)	14.151 (382)	15.981 (973)	16.434 (575)	16.285 (1266)	17.193 (605)	17.298 (1307)
E_p (MeV)	49.126 (600)	47.387 (615)	45.852 (633)	45.201 (638)	42.914 (664)	42.395 (672)	40.103 (699)
Location	LBNL2022	LBNL	LBNL2022	LBNL	LBNL	LBNL2022	LBNL
$^{42g}K_{(c)}$	0.857 (55)	0.845 (77)	0.507 (62)	0.639 (55)	0.474 (49)	0.444 (39)	0.320 (35)
$^{43g}K_{(c)}$	1.217 (31)	0.974 (56)	0.812 (21)	0.682 (36)	0.418 (23)	0.379 (12)	0.185 (12)
$^{47g}Ca_{(c)}$			0.049 (10)				0.000 (0)
$^{46(m+g)}Sc_{(i)}$	60.908 (1490)	63.746 (3522)	64.040 (1563)	65.360 (3576)	62.700 (3447)	63.299 (1552)	56.994 (3521)
$^{47g}Sc_{(c)}$	19.473 (476)	17.998 (1154)	19.239 (470)	18.557 (1181)	18.588 (1111)	18.806 (519)	18.958 (1163)
$^{48g}Sc_{(c)}$	1.678 (46)	1.645 (234)	1.599 (43)	1.607 (260)	1.445 (214)	1.443 (44)	1.280 (162)
$^{48g}V_{(i)}$	16.954 (421)	18.736 (1332)	19.126 (472)	20.373 (1395)	22.228 (1474)	22.267 (543)	24.526 (2341)
E_p (MeV)	38.696 (722)	37.116 (743)	34.708 (786)	33.919 (797)	32.975 (373)	31.271 (388)	29.494 (406)
Location	LBNL2022	LBNL	LBNL2022	LBNL	LBNL	LBNL	LBNL
$^{42g}K_{(c)}$	0.372 (40)		0.115 (17)		0.104 (11)		
$^{43g}K_{(c)}$	0.148 (10)	0.086 (7)		0.051 (6)			
$^{47g}Ca_{(c)}$	0.017 (84)		0.050 (7)	0.016 (1)	0.011 (121)		
$^{46(m+g)}Sc_{(i)}$	51.954 (1294)	45.856 (2870)	33.292 (831)	29.275 (2510)	24.679 (759)	17.426 (590)	12.418 (421)
$^{47g}Sc_{(c)}$	20.089 (501)	20.327 (1276)	22.057 (549)	24.452 (2052)	22.757 (947)	22.378 (802)	21.276 (632)
$^{48g}Sc_{(c)}$	1.173 (35)	1.082 (192)	0.867 (23)	0.831 (232)	0.692 (172)	0.635 (174)	0.563 (116)
$^{48g}V_{(i)}$	25.124 (629)	28.341 (2418)	28.323 (724)	30.346 (3331)	30.472 (1330)	31.786 (1372)	33.941 (1329)

Table J.3 Continued from previous page

E_p (MeV)	29.211 (895)	27.644 (428)	25.692 (452)	23.608 (483)	21.379 (522)	18.925 (574)	16.212 (647)
Location	LBNL	LBNL	LBNL	LBNL	LBNL	LBNL	LBNL
$^{42g}K_{(c)}$	0.050 (5)						
$^{47g}Ca_{(c)}$	0.011 (35)						0.000 (0)
$^{46(m+g)}Sc_{(i)}$	12.103 (647)	10.093 (398)	8.758 (338)	7.731 (316)	5.946 (264)	4.487 (257)	3.175 (284)
$^{47g}Sc_{(c)}$	20.834 (1082)	18.455 (577)	14.853 (581)	12.041 (477)	8.163 (318)	4.184 (176)	1.415 (61)
$^{48g}Sc_{(c)}$	0.576 (48)	0.486 (116)	0.353 (109)	0.251 (92)	0.133 (58)	0.039 (81)	
$^{48g}V_{(i)}$	34.373 (1947)	36.307 (1479)	42.181 (1271)	53.281 (1671)	68.140 (1919)	104.171 (3093)	208.809 (6713)

E_p (MeV)	13.104 (764)
Location	LBNL
$^{46(m+g)}Sc_{(i)}$	2.088 (331)
$^{47g}Sc_{(c)}$	0.592 (77)
$^{48g}V_{(i)}$	370.353 (11319)

Bibliography

[1] Jerry Obaldo and Barbara Hertz. "The Early Years of Nuclear Medicine: A Retelling." eng. In: *Asia Oceania Journal of Nuclear Medicine and Biology* 9.2 (July 2021). DOI: 10.22038/aojnmb.2021.55514.1385. URL: https://doi.org/10.22038/aojnmb.2021.55514.1385 (visited on 03/11/2024).

[2] Sneha S. Kelkar and Theresa M. Reineke. "Theranostics: Combining Imaging and Therapy." en. In: *Bioconjugate Chemistry* 22.10 (Oct. 2011), pp. 1879–1903. ISSN: 1043-1802, 1520-4812. DOI: 10.1021/bc200151q. URL: https://pubs.acs.org/doi/10.1021/bc200151q (visited on 03/11/2024).

[3] Jean Blachot. "Nuclear Data Sheets for A = 117." en. In: *Nuclear Data Sheets* 95.3 (Mar. 2002), pp. 679–836. ISSN: 00903752. DOI: 10.1006/ndsh.2002.0007. URL: https://linkinghub.elsevier.com/retrieve/pii/S0090375202900074 (visited on 01/08/2024).

[4] M.J. Berger et al. *ESTAR, PSTAR, and ASTAR: Computer Programs for Calculating Stopping-Power and Range Tables for Electrons, Protons, and Helium Ions (version 1.2.3)*. Gaithersburg, MD, 2005. URL: http://physics.nist.gov/Star (visited on 03/11/2024).

[5] E. Browne and J.K. Tuli. "Nuclear Data Sheets for A = 99." en. In: *Nuclear Data Sheets* 145 (Nov. 2017), pp. 25–340. ISSN: 00903752. DOI: 10.1016/j.nds.2017.09.002. URL: https://linkinghub.elsevier.com/retrieve/pii/S0090375217300674 (visited on 03/11/2024).

[6] P. V. Harper et al. "Technetium 99m as a Scanning Agent." en. In: *Radiology* 85.1 (July 1965), pp. 101–109. ISSN: 0033-8419, 1527-1315. DOI: 10.1148/85.1.101. URL: http://pubs.rsna.org/doi/10.1148/85.1.101 (visited on 04/30/2024).

[7] Alessandra Boschi, Licia Uccelli, and Petra Martini. "A Picture of Modern Tc-99m Radiopharmaceuticals: Production, Chemistry, and Applications in Molecular Imaging." en. In: *Applied Sciences* 9.12 (June 2019), p. 2526. ISSN: 2076-3417. DOI: 10.3390/app9122526. URL: https://www.mdpi.com/2076-3417/9/12/2526 (visited on 04/30/2024).

[8] G. T. Krishnamurthy et al. "Tin-117m(4+)DTPA: pharmacokinetics and imaging characteristics in patients with metastatic bone pain." eng. In: *Journal of Nuclear Medicine: Official Publication, Society of Nuclear Medicine* 38.2 (Feb. 1997), pp. 230–237. ISSN: 0161-5505.

[9] D.M. Symochko, E. Browne, and J.K. Tuli. "Nuclear Data Sheets for A = 119." en. In: *Nuclear Data Sheets* 110.11 (Nov. 2009), pp. 2945–3105. ISSN: 00903752. DOI: 10.1016/j.nds.2009.10.003. URL: https://linkinghub.elsevier.com/retrieve/pii/S0090375209000908 (visited on 11/06/2023).

[10] Lee A Bernstein et al. "Our Future Nuclear Data Needs." In: *Annu. Rev. Nucl. Part. Sci* 69 (2019), pp. 109–136. DOI: 10.1146/annurev-nucl-101918. URL: https://doi.org/10.1146/annurev-nucl-101918-.

[11] Andrew S. Voyles et al. "Excitation functions for (p,x) reactions of niobium in the energy range of Ep = 40–90 MeV." In: *Nuclear Instruments and Methods in Physics Research, Section B: Beam Interactions with Materials and Atoms* 429 (Aug. 2018), pp. 53–74. ISSN: 0168583X. DOI: 10.1016/j.nimb.2018.05.028.

[12] Morgan B. Fox et al. "Investigating high-energy proton-induced reactions on spherical nuclei: Implications for the preequilibrium exciton model." en. In: *Physical Review C* 103.3 (Mar. 2021), p. 034601. ISSN: 2469-9985, 2469-9993. DOI: 10.1103/PhysRevC.103.034601. URL: https://link.aps.org/doi/10.1103/PhysRevC.103.034601 (visited on 09/15/2023).

[13] Morgan B. Fox et al. "Measurement and modeling of proton-induced reactions on arsenic from 35 to 200 MeV." en. In: *Physical Review C* 104.6 (Dec. 2021), p. 064615. ISSN: 2469-9985, 2469-9993. DOI: 10.1103/PhysRevC.104.064615. URL: https://link.aps.org/doi/10.1103/PhysRevC.104.064615 (visited on 09/15/2023).

[14] A. Rodrigo et al. "Compilation of isomeric ratios of light particle induced nuclear reactions." en. In: *Atomic Data and Nuclear Data Tables* 153 (Sept. 2023), p. 101583. ISSN: 0092640X. DOI: 10.1016/j.adt.2023.101583. URL: https://linkinghub.elsevier.com/retrieve/pii/S0092640X23000116 (visited on 12/14/2023).

[15] J. W. Engle et al. "Recommended Nuclear Data for the Production of Selected Therapeutic Radionuclides." In: *Nuclear Data Sheets* 155 (Jan. 2019), pp. 56–74. ISSN: 00903752. DOI: 10.1016/j.nds.2019.01.003.

[16] M. Kireeff Covo et al. "The 88-Inch Cyclotron: A one-stop facility for electronics radiation and detector testing." en. In: *Measurement* 127 (Oct. 2018), pp. 580–587. ISSN: 02632241. DOI: 10.1016/j.measurement.2017.10.018. URL: https://linkinghub.elsevier.com/retrieve/pii/S0263224117306401 (visited on 09/25/2023).

[17] Stephen A. Graves et al. "Nuclear excitation functions of proton-induced reactions (Ep= 35–90 MeV) from Fe, Cu, and Al." en. In: *Nuclear Instruments and Methods in Physics Research Section B: Beam Interactions with Materials and Atoms* 386 (Nov. 2016), pp. 44–53. ISSN: 0168583X. DOI: 10.1016/j.nimb.2016.09.018. URL: https://linkinghub.elsevier.com/retrieve/pii/S0168583X16303998 (visited on 07/25/2023).

[18] Jonathan T. Morrell et al. "Measurement of 139La(p,x) cross sections from 35–60 MeV by stacked-target activation." In: *European Physical Journal A* 56.1 (Jan. 2020). ISSN: 1434601X. DOI: 10.1140/epja/s10050-019-00010-0.

[19] Andrew S. Voyles et al. "Proton-induced reactions on Fe, Cu, and Ti from threshold to 55 MeV." en. In: *The European Physical Journal A* 57.3 (Mar. 2021), p. 94. ISSN: 1434-6001, 1434-601X. DOI: 10.1140/epja/s10050-021-00401-2. URL: https://link.springer.com/10.1140/epja/s10050-021-00401-2 (visited on 09/25/2023).

[20] A. Hermanne et al. "Reference Cross Sections for Charged-particle Monitor Reactions." en. In: *Nuclear Data Sheets*. Special Issue on Nuclear Reaction Data 148 (Feb. 2018), pp. 338–382. ISSN: 0090-3752. DOI: 10.1016/j.nds.2018.02.009. URL: https://www.sciencedirect.com/science/article/pii/S0090375218300280 (visited on 07/18/2023).

[21] S.K. Basu and E.A. Mccutchan. "Nuclear Data Sheets for A = 90." en. In: *Nuclear Data Sheets* 165 (Mar. 2020), pp. 1–329. ISSN: 00903752. DOI: 10.1016/j.nds.2020.04.001. URL: https://linkinghub.elsevier.com/retrieve/pii/S0090375220300090 (visited on 01/08/2024).

[22] E. M. O'Brien et al. "Novel design and diagnostics improvements for increased production capacity and improved reliability at the Los Alamos Isotope Production Facility." en. In: *Nuclear Instruments and Methods in Physics Research Section A: Accelerators, Spectrometers, Detectors and Associated Equipment* 956 (Mar. 2020), p. 163316. ISSN: 0168-9002. DOI: 10.1016/j.nima.2019.163316. URL: https://www.sciencedirect.com/science/article/pii/S0168900219315578 (visited on 07/18/2023).

[23] Bai Erjun and Huo Junde. "Nuclear Data Sheets for A = 63." en. In: *Nuclear Data Sheets* 92.1 (Jan. 2001), pp. 147–252. ISSN: 00903752. DOI: 10.1006/ndsh.2001.0002. URL: https://linkinghub.elsevier.com/retrieve/pii/S009037520190002X (visited on 01/08/2024).

[24] Jonathan T. Morrell. *Curie*. http://pypi.org/project/curie. Nov. 2023. URL: http://pypi.org/project/curie.

[25] T. Vidmar et al. "A semi-empirical model of the efficiency curve for extended sources in gamma-ray spectrometry." en. In: *Nuclear Instruments and Methods in Physics Research Section A: Accelerators, Spectrometers, Detectors and Associated Equipment* 470.3 (Sept. 2001), pp. 533–547. ISSN: 01689002. DOI: 10.1016/S0168-9002(01)00799-9. URL: https://linkinghub.elsevier.com/retrieve/pii/S0168900201007999 (visited on 12/20/2023).

[26] Stephen Seltzer. *XCOM-Photon Cross Sections Database, NIST Standard Reference Database 8*. en. 1987. DOI: 10.18434/T48G6X. URL: http://www.nist.gov/pml/data/xcom/index.cfm (visited on 01/16/2024).

[27] James F. Ziegler, M.D. Ziegler, and J.P. Biersack. "SRIM – The stopping and range of ions in matter (2010)." en. In: *Nuclear Instruments and Methods in Physics Research Section B: Beam Interactions with Materials and Atoms* 268.11-12 (June 2010), pp. 1818–1823. ISSN: 0168583X. DOI: 10.1016/j.nimb.2010.02.091. URL: https://linkinghub.elsevier.com/retrieve/pii/S0168583X10001862 (visited on 01/01/2024).

[28] Peter J Huber. "The Behavior of Maximum Likelihood Estimates under Nonstandard Conditions." In: vol. 1. University of California Press, Berkeley, 1967, pp. 221–223.

[29] Stanislav V. Ermolaev et al. "Cross sections and production yields of ^{117m} Sn and other radionuclides generated in natural and enriched antimony with protons up to 145 MeV." en. In: *Radiochimica Acta* 108.5 (Apr. 2020), pp. 327–351. ISSN: 2193-3405, 0033-8230. DOI: 10.1515/ract-2019-3158. URL: https://www.degruyter.com/document/doi/10.1515/ract-2019-3158/html (visited on 11/07/2023).

[30] M.A. Mosby et al. "Cross sections for proton-induced reactions on natSb up to 68 MeV." en. In: *Nuclear Instruments and Methods in Physics Research Section B: Beam Interactions with Materials and Atoms* 412 (Dec. 2017), pp. 34–40. ISSN: 0168583X. DOI: 10.1016/j.nimb.2017.08.038. URL: https://linkinghub.elsevier.com/retrieve/pii/S0168583X17308339 (visited on 11/07/2023).

[31] S. Takács et al. "Cross sections of proton induced reactions on natSb." en. In: *Nuclear Instruments and Methods in Physics Research Section B: Beam Interactions with Materials and Atoms* 297 (Feb. 2013), pp. 44–57. ISSN: 0168583X. DOI: 10.1016/j.nimb.2012.12.010. URL: https://linkinghub.elsevier.com/retrieve/pii/S0168583X12007549 (visited on 11/07/2023).

[32] Jong Hwa Yi and David A. Miller. "Cross sections of natSb(p,x) reactions for 30–46 MeV protons." en. In: *International Journal of Radiation Applications and Instrumentation. Part A. Applied Radiation and Isotopes* 43.9 (Sept. 1992), pp. 1103–1106. ISSN: 08832889. DOI: 10.1016/0883-2889(92)90051-F. URL: https://linkinghub.elsevier.com/retrieve/pii/088328899290051F (visited on 11/07/2023).

[33] Manuel C. Lagunas-Solar et al. "Cyclotron production of PET radionuclides: 118Sb (3.5 min; β+ 75%; EC 25%) from high-energy protons on natural Sb targets." en. In: *International Journal of Radiation Applications and Instrumentation. Part A. Applied Radiation and Isotopes* 41.6 (Jan. 1990), pp. 521–529. ISSN: 08832889. DOI: 10.1016/0883-2889(90)90033-D. URL: https://linkinghub.elsevier.com/retrieve/pii/088328899090033D (visited on 11/07/2023).

[34] D. A. Miller, S. Sun, and J. H. Yi. "Preparation of a118Te/118Sb radionuclide generator." en. In: *Journal of Radioanalytical and Nuclear Chemistry Articles* 160.2 (July 1992), pp. 467–476. ISSN: 0236-5731, 1588-2780. DOI: 10.1007/BF02037122. URL: http://link.springer.com/10.1007/BF02037122 (visited on 03/27/2024).

[35] Alaa Elbinawi et al. "Proton induced nuclear reactions on natural antimony up to 17 MeV." en. In: *Radiochimica Acta* 104.4 (Apr. 2016), pp. 221–226. ISSN: 0033-8230, 2193-3405. DOI: 10.1515/ract-2015-2483. URL: https://www.degruyter.com/document/doi/10.1515/ract-2015-2483/html (visited on 11/09/2023).

[36] Jean Blachot. "Nuclear Data Sheets for A = 113." en. In: *Nuclear Data Sheets* 111.6 (June 2010), pp. 1471–1618. ISSN: 00903752. DOI: 10.1016/j.nds.2010.05.001. URL: https://linkinghub.elsevier.com/retrieve/pii/S0090375210000529 (visited on 01/29/2024).

[37] Jean Blachot. "Nuclear Data Sheets for117Sb." en. In: *Nuclear Data Sheets* 84.2 (June 1998), pp. 277–305. ISSN: 00903752. DOI: 10.1006/ndsh.1998.0011. URL: https://linkinghub.elsevier.com/retrieve/pii/S0090375298900114 (visited on 11/06/2023).

[38] Jun Chen. "Nuclear Data Sheets for A=123." en. In: *Nuclear Data Sheets* 174 (May 2021), pp. 1–463. ISSN: 00903752. DOI: 10.1016/j.nds.2021.05.001. URL: https://linkinghub.elsevier.com/retrieve/pii/S0090375221000260 (visited on 01/04/2024).

[39] Morgan B Fox. *TREND As, Nb, Cu, Ti Gamma Spectroscopy*. Mar. 2021. DOI: 10.5281/ZENODO.4648949. URL: https://zenodo.org/record/4648949 (visited on 01/04/2024).

[40] L. Bernstein et al. "Probing reaction dynamics with the 196Pt(n,xnγ) reactions for x˜15." en. In: *Physical Review C* 57.6 (June 1998), R2799–R2803. ISSN: 0556-2813, 1089-490X. DOI: 10.1103/PhysRevC.57.R2799. URL: https://link.aps.org/doi/10.1103/PhysRevC.57.R2799 (visited on 04/25/2024).

[41] M. Herman et al. "EMPIRE: Nuclear Reaction Model Code System for Data Evaluation." en. In: *Nuclear Data Sheets* 108.12 (Dec. 2007), pp. 2655–2715. ISSN: 00903752. DOI: 10.1016/j.nds.2007.11.003. URL: https://linkinghub.elsevier.com/retrieve/pii/S0090375207000981 (visited on 09/15/2023).

[42] Toshihiko Kawano et al. "Monte Carlo Simulation for Particle and γ-Ray Emissions in Statistical Hauser-Feshbach Model." en. In: *Journal of Nuclear Science and Technology* 47.5 (May 2010), pp. 462–469. ISSN: 0022-3131, 1881-1248. DOI: 10.1080/18811248.2010.9711637. URL: http://www.tandfonline.com/doi/abs/10.1080/18811248.2010.9711637 (visited on 09/18/2023).

[43] M. Blann. "New precompound decay model." en. In: *Physical Review C* 54.3 (Sept. 1996), pp. 1341–1349. ISSN: 0556-2813, 1089-490X. DOI: 10.1103/PhysRevC.54.1341. URL: https://link.aps.org/doi/10.1103/PhysRevC.54.1341 (visited on 09/18/2023).

[44] Aryan J Koning, S Hilaire, and S Goriely. *TALYS-1.95 - A Nuclear Reaction Program*. 2019. URL: https://tendl.web.psi.ch/tendl_2019/talys.html (visited on 09/18/2023).

[45] Niels Bohr. "Neutron Capture and Nuclear Constitution." en. In: *Nature* 137.3461 (Feb. 1936), pp. 344–348. ISSN: 0028-0836, 1476-4687. DOI: 10.1038/137344a0. URL: https://www.nature.com/articles/137344a0 (visited on 06/06/2024).

[46] Tsing-Lien Chang et al. "The isotopic abundance of antimony." en. In: *International Journal of Mass Spectrometry and Ion Processes* 123.1 (Jan. 1993), pp. 77–82. ISSN: 01681176. DOI: 10.1016/0168-1176(93)87056-X. URL: https://linkinghub.elsevier.com/retrieve/pii/016811769387056X (visited on 05/01/2024).

[47] Pierre Marmier and Eric Sheldon. *Physics of nuclei and particles. 2*. eng. 2. print. Vol. 2. New York: Acad. Pr, 1971. ISBN: 978-0-12-473102-8.

[48] Kenneth S. Krane and David Halliday. *Introductory nuclear physics*. New York: Wiley, 1987. ISBN: 978-0-471-80553-3.

[49] Hideki YUKAWA. *On the Interaction of Elementary Particles. I*. en. 1935. DOI: 10.11429/ppmsj1919.17.0_48. URL: https://doi.org/10.11429/ppmsj1919.17.0_48 (visited on 04/29/2024).

[50] A.J. Koning and J.P. Delaroche. "Local and global nucleon optical models from 1 keV to 200 MeV." en. In: *Nuclear Physics A* 713.3-4 (Jan. 2003), pp. 231–310. ISSN: 03759474. DOI: 10.1016/S0375-9474(02)01321-0. URL: https://linkinghub.elsevier.com/retrieve/pii/S0375947402013210 (visited on 01/25/2024).

[51] Pierre Marmier and Eric Sheldon. *Physics of nuclei and particles. 1*. eng. 2. print. Vol. 1. New York: Acad. Pr, 1971. ISBN: 978-0-12-473101-1.

[52] A.J. Koning et al. "TENDL: Complete Nuclear Data Library for Innovative Nuclear Science and Technology." en. In: *Nuclear Data Sheets* 155 (Jan. 2019), pp. 1–55. ISSN: 00903752. DOI: 10.1016/j.nds.2019.01.002. URL: https://linkinghub.elsevier.com/retrieve/pii/S009037521930002X (visited on 09/18/2023).

[53] Walter Hauser and Herman Feshbach. "The Inelastic Scattering of Neutrons." en. In: *Physical Review* 87.2 (July 1952), pp. 366–373. ISSN: 0031-899X. DOI: 10.1103/PhysRev.87.366. URL: https://link.aps.org/doi/10.1103/PhysRev.87.366 (visited on 04/27/2024).

[54] F Dietrich. *Simple Derivation of the Hauser-Feshbach and Weisskopf-Ewing Formulae, with Application to Surrogate Reactions*. Tech. rep. UCRL-TR-201718, 15013687. Jan. 2004, UCRL–TR–201718, 15013687. DOI: 10.2172/15013687. URL: https://www.osti.gov/servlets/purl/15013687/ (visited on 05/02/2024).

[55] A. J. Koning and M. C. Duijvestijn. "A global pre-equilibrium analysis from 7 to 200 MeV based on the optical model potential." In: *Nuclear Physics A* 744 (Nov. 2004), pp. 15–76. ISSN: 03759474. DOI: 10.1016/j.nuclphysa.2004.08.013.

[56] C.K. Cline and M. Blann. "The pre-equilibrium statistical model: Description of the nuclear equilibration process and parameterization of the model." en. In: *Nuclear Physics A* 172.2 (Sept. 1971), pp. 225–259. ISSN: 03759474. DOI: 10.1016/0375-9474(71)90713-5. URL: https://linkinghub.elsevier.com/retrieve/pii/0375947471907135 (visited on 05/05/2024).

[57] Nigel R Stevenson, Gilbert R. Gonzales, and Jaime Simón. "NOVEL TIN - 117M COLLOID FORMULATION WITH THE ABILITY TO DISTINGUISH IT FROM EXISTING TIN - 117M COLLOID FORMULATIONS." US 2022/0305150 A1.

[58] Richard Freifelder. *Setting up a cyclotron radiopharmacy: Navigating the challenges through two case studies*. Webinar, Feb. 2024. (Visited on 02/27/2024).

[59] Jennifer M. Hootman et al. "Updated Projected Prevalence of Self-Reported Doctor-Diagnosed Arthritis and Arthritis-Attributable Activity Limitation Among US Adults, 2015–2040." en. In: *Arthritis & Rheumatology* 68.7 (July 2016), pp. 1582–1587. ISSN: 2326-5191, 2326-5205. DOI: 10.1002/art.39692. URL: https://acrjournals.onlinelibrary.wiley.com/doi/10.1002/art.39692 (visited on 02/12/2024).

[60] Louise B. Murphy et al. "Medical Expenditures and Earnings Losses Among ¡span style="font-variant:small-caps;"¿US¡/span¿ Adults With Arthritis in 2013." en. In: *Arthritis Care & Research* 70.6 (June 2018), pp. 869–876. ISSN: 2151-464X, 2151-4658. DOI: 10.1002/acr.23425. URL: https://acrjournals.onlinelibrary.wiley.com/doi/10.1002/acr.23425 (visited on 04/29/2024).

[61] Kiran Mahendru et al. "Need for Palliative Care in Patient with Rheumatoid Arthritis: A Cross-sectional Observational Study." eng. In: *Indian Journal of Palliative Care* 27.2 (2021), pp. 275–280. ISSN: 0973-1075. DOI: 10.25259/IJPC_395_20.

[62] Marko Popovic et al. "Review of international patterns of practice for the treatment of painful bone metastases with palliative radiotherapy from 1993 to 2013." en. In: *Radiotherapy and Oncology* 111.1 (Apr. 2014), pp. 11–17. ISSN: 01678140. DOI: 10.1016/j.radonc.2014.01.015. URL: https://linkinghub.elsevier.com/retrieve/pii/S0167814014000310 (visited on 05/06/2024).

[63] Nicolas Patel and Bikramjit Benipal. "Incidence of Cholangiocarcinoma in the USA from 2001 to 2015: A US Cancer Statistics Analysis of 50 States." eng. In: *Cureus* 11.1 (Jan. 2019), e3962. ISSN: 2168-8184. DOI: 10.7759/cureus.3962.

[64] Christina X. Chamberlain et al. "Burden of illness for patients with cholangiocarcinoma in the United States: a retrospective claims analysis." In: *Journal of Gastrointestinal Oncology* 12.2 (Apr. 2021), pp. 658–668. ISSN: 20786891, 2219679X. DOI: 10.21037/jgo-20-544. URL: https://jgo.amegroups.com/article/view/50919/html (visited on 05/06/2024).

[65] Gui-jin He et al. "Induction of biliary cholangiocarcinoma cell apoptosis by 103Pd cholangial radioactive stent gamma-rays." eng. In: *Chinese Medical Journal* 121.11 (June 2008), pp. 1020–1024. ISSN: 0366-6999.

[66] Gilbert R. Gonzales. "Method of treating cholangiocarcinoma and \newline apparatus." US9492573B2. Nov. 2016. URL: https://patentimages.storage.googleapis.com/a0/3d/25/f57f3bfba5ec84/US9492573.pdf (visited on 05/05/2024).

[67] Suresh C. Shrivastava et al. "METHOD OF ELECTROPLATING A CONVERSION ELECTRON EMITTING SOURCE ON IMPLANT." US 2012/0109287 A1.

[68] Yiwei Wang et al. "Production Review of Accelerator-Based Medical Isotopes." eng. In: *Molecules (Basel, Switzerland)* 27.16 (Aug. 2022), p. 5294. ISSN: 1420-3049. DOI: 10.3390/molecules27165294.

[69] Zarif Ashhar et al. "Cyclotron Production of Gallium-68 Radiopharmaceuticals Using the 68Zn(p,n)68Ga Reaction and Their Regulatory Aspects." en. In: *Pharmaceutics* 15.1 (Dec. 2022), p. 70. ISSN: 1999-4923. DOI: 10.3390/pharmaceutics15010070. URL: https://www.mdpi.com/1999-4923/15/1/70 (visited on 04/30/2024).

[70] Bryce J. B. Nelson et al. "High yield cyclotron production of a novel 133/135La theranostic pair for nuclear medicine." en. In: *Scientific Reports* 10.1 (Dec. 2020), p. 22203. ISSN: 2045-2322. DOI: 10.1038/s41598-020-79198-x. URL: https://www.nature.com/articles/s41598-020-79198-x (visited on 05/05/2024).

[71] *Best\textsuperscript{\textregistered Cyclotron Systems Information Package for B70P.* Information Package. #7-8765 Ash St., Vancouver, BC V6P 6T3 Canada: Best Cyclotron Systems, Inc., 2019, p. 34. URL: http://www.bestcyclotron.com/about.html (visited on 05/05/2024).

[72] Mateusz Adam Synowiecki, Lars Rutger Perk, and J. Frank W. Nijsen. "Production of novel diagnostic radionuclides in small medical cyclotrons." en. In: *EJNMMI Radiopharmacy and Chemistry* 3.1 (Dec. 2018), p. 3. ISSN: 2365-421X. DOI: 10.1186/s41181-018-0038-z. URL: https://ejnmmipharmchem.springeropen.com/articles/10.1186/s41181-018-0038-z (visited on 05/05/2024).

[73] B L Zhuikov and S V Ermolaev. "Radioisotope research and development at the Linear Accelerator of the Institute for Nuclear Research of RAS." In: *Physics-Uspekhi* 64.12 (Dec. 2021), pp. 1311–1322. ISSN: 1063-7869, 1468-4780. DOI: 10.3367/UFNe.2021.07.039010. URL: https://iopscience.iop.org/article/10.3367/UFNe.2021.07.039010 (visited on 05/05/2024).

[74] *IBA Brochure for Cyclone 70*. Brochure. Chemin du Cyclotron, 3 — 1348 Louvain-la-Neuve, Belgium: IBA RadioPharma Solutions, Mar. 2019, p. 7. (Visited on 05/05/2024).

[75] Karanvir S. Aulakh et al. "Prospective Clinical Evaluation of Intra-Articular Injection of Tin-117m (117mSn) Radiosynoviorthesis Agent for Management of Naturally Occurring Elbow Osteoarthritis in Dogs: A Pilot Study." eng. In: *Veterinary Medicine (Auckland, N.Z.)* 12 (2021), pp. 117–128. ISSN: 2230-2034. DOI: 10.2147/VMRR.S295309.

[76] S. C. Srivastava et al. "Treatment of metastatic bone pain with tin-117m Stannic diethylenetriaminepentaacetic acid: a phase I/II clinical study." eng. In: *Clinical Cancer Research: An Official Journal of the American Association for Cancer Research* 4.1 (Jan. 1998), pp. 61–68. ISSN: 1078-0432.

[77] Nigel R Stevenson. *Applications of Sn-117m and the Potential World Supply and Demand*. Busan, Sept. 2018. URL: http://serene-llc.com/wp-content/uploads/2018/10/Stevenson-Applications-of-Sn-117m.pdf (visited on 05/06/2024).

[78] Elio Scarpini, Philip Schelterns, and Howard Feldman. "Treatment of Alzheimer's disease; current status and new perspectives." en. In: *The Lancet Neurology* 2.9 (Sept. 2003), pp. 539–547. ISSN: 14744422. DOI: 10.1016/S1474-4422(03)00502-7. URL: https://linkinghub.elsevier.com/retrieve/pii/S1474442203005027 (visited on 05/07/2024).

[79] W.J. Huang et al. "The AME 2020 atomic mass evaluation (I). Evaluation of input data, and adjustment procedures*." In: *Chinese Physics C* 45.3 (Mar. 2021), p. 030002. ISSN: 1674-1137, 2058-6132. DOI: 10.1088/1674-1137/abddb0. URL: https://iopscience.iop.org/article/10.1088/1674-1137/abddb0 (visited on 10/30/2023).

[80] Balraj Singh. "Nuclear Data Sheets for A = 89." en. In: *Nuclear Data Sheets* 114.1 (Jan. 2013), pp. 1–208. ISSN: 00903752. DOI: 10.1016/j.nds.2013.01.001. URL: https://linkinghub.elsevier.com/retrieve/pii/S0090375213000021 (visited on 11/06/2023).

[81] Coral M. Baglin. "Nuclear Data Sheets for A = 91." en. In: *Nuclear Data Sheets* 114.10 (Oct. 2013), pp. 1293–1495. ISSN: 00903752. DOI: 10.1016/j.nds.2013.10.002. URL: https://linkinghub.elsevier.com/retrieve/pii/S0090375213000665 (visited on 11/06/2023).

[82] D. De Frenne and A. Negret. "Nuclear Data Sheets for A = 106." en. In: *Nuclear Data Sheets* 109.4 (Apr. 2008), pp. 943–1102. ISSN: 00903752. DOI: 10.1016/j.nds.2008.03.002. URL: https://linkinghub.elsevier.com/retrieve/pii/S0090375208000203 (visited on 11/06/2023).

[83] G. Gürdal and F.G. Kondev. "Nuclear Data Sheets for A = 110." en. In: *Nuclear Data Sheets* 113.5 (May 2012), pp. 1315–1561. ISSN: 00903752. DOI: 10.1016/j.nds.2012.05.002. URL: https://linkinghub.elsevier.com/retrieve/pii/S0090375212000415 (visited on 11/06/2023).

[84] S. Kumar, J. Chen, and F.G. Kondev. "Nuclear Data Sheets for A = 109." en. In: *Nuclear Data Sheets* 137 (Nov. 2016), pp. 1–286. ISSN: 00903752. DOI: 10.1016/j.nds.2016.09.001. URL: https://linkinghub.elsevier.com/retrieve/pii/S0090375216300321 (visited on 11/06/2023).

[85] Jean Blachot. "Nuclear Data Sheets for A = 111." en. In: *Nuclear Data Sheets* 110.6 (June 2009), pp. 1239–1407. ISSN: 00903752. DOI: 10.1016/j.nds.2009.04.002. URL: https://linkinghub.elsevier.com/retrieve/pii/S0090375209000374 (visited on 11/06/2023).

[86] Jean Blachot. "Nuclear Data Sheets for A = 114." en. In: *Nuclear Data Sheets* 113.2 (Feb. 2012), pp. 515–714. ISSN: 00903752. DOI: 10.1016/j.nds.2012.02.002. URL: https://linkinghub.elsevier.com/retrieve/pii/S0090375212000129 (visited on 11/06/2023).

[87] Jean Blachot. "Nuclear Data Sheets for A = 116." en. In: *Nuclear Data Sheets* 111.3 (Mar. 2010), pp. 717–895. ISSN: 00903752. DOI: 10.1016/j.nds.2010.03.002. URL: https://linkinghub.elsevier.com/retrieve/pii/S0090375210000281 (visited on 01/29/2024).

[88] Jean Blachot. "Nuclear Data Sheets for A = 115." en. In: *Nuclear Data Sheets* 113.10 (Oct. 2012), pp. 2391–2535. ISSN: 00903752. DOI: 10.1016/j.nds.2012.10.002. URL: https://linkinghub.elsevier.com/retrieve/pii/S0090375212000683 (visited on 11/06/2023).

[89] K. Kitao. "Nuclear Data Sheets Update for A = 118." en. In: *Nuclear Data Sheets* 75.1 (May 1995), pp. 99–198. ISSN: 00903752. DOI: 10.1006/ndsh.1995.1022. URL: https://linkinghub.elsevier.com/retrieve/pii/S0090375285710228 (visited on 11/06/2023).

[90] K. Kitao, Y. Tendow, and A. Hashizume. "Nuclear Data Sheets fo A = 120." en. In: *Nuclear Data Sheets* 96.2 (June 2002), pp. 241–390. ISSN: 00903752. DOI: 10.1006/ndsh.2002.0012. URL: https://linkinghub.elsevier.com/retrieve/pii/S0090375202900128 (visited on 11/06/2023).

[91] T. Tamura. "Nuclear Data Sheets for A = 122." en. In: *Nuclear Data Sheets* 108.3 (Mar. 2007), pp. 455–632. ISSN: 00903752. DOI: 10.1016/j.nds.2007.02.001. URL: https://linkinghub.elsevier.com/retrieve/pii/S0090375207000208 (visited on 11/06/2023).

[92] S. Ohya. "Nuclear Data Sheets for A = 121." en. In: *Nuclear Data Sheets* 111.6 (June 2010), pp. 1619–1806. ISSN: 00903752. DOI: 10.1016/j.nds.2010.05.002. URL: https://linkinghub.elsevier.com/retrieve/pii/S009037521000061X (visited on 11/06/2023).

[93] Jimin Wang and Xiaolong Huang. "Nuclear Data Sheets for A = 51." en. In: *Nuclear Data Sheets* 144 (Sept. 2017), pp. 1–296. ISSN: 00903752. DOI: 10.1016/j.nds.2017.08.002. URL: https://linkinghub.elsevier.com/retrieve/pii/S0090375217300546 (visited on 01/08/2024).

[94] Yang Dong and Huo Junde. "Nuclear Data Sheets for A = 52." en. In: *Nuclear Data Sheets* 128 (Sept. 2015), pp. 185–314. ISSN: 00903752. DOI: 10.1016/j.nds.2015.08.003. URL: https://linkinghub.elsevier.com/retrieve/pii/S0090375215000368 (visited on 01/08/2024).

[95] Yang Dong and Huo Junde. "Nuclear Data Sheets for A = 54." en. In: *Nuclear Data Sheets* 121 (Sept. 2014), pp. 1–142. ISSN: 00903752. DOI: 10.1016/j.nds.2014.09.001. URL: https://linkinghub.elsevier.com/retrieve/pii/S0090375214006553 (visited on 01/08/2024).

[96] Huo Junde, Huo Su, and Yang Dong. "Nuclear Data Sheets for A = 56." en. In: *Nuclear Data Sheets* 112.6 (June 2011), pp. 1513–1645. ISSN: 00903752. DOI: 10.1016/j.nds.2011.04.004. URL: https://linkinghub.elsevier.com/retrieve/pii/S0090375211000457 (visited on 01/08/2024).

[97] M. Shamsuzzoha Basunia. "Nuclear Data Sheets for A=59." en. In: *Nuclear Data Sheets* 151 (July 2018), pp. 1–333. ISSN: 00903752. DOI: 10.1016/j.nds.2018.08.001. URL: https://linkinghub.elsevier.com/retrieve/pii/S0090375218300590 (visited on 01/08/2024).

[98] Huo Junde. "Nuclear Data Sheets for A = 55." en. In: *Nuclear Data Sheets* 109.4 (Apr. 2008), pp. 787–942. ISSN: 00903752. DOI: 10.1016/j.nds.2008.03.001. URL: https://linkinghub.elsevier.com/retrieve/pii/S0090375208000197 (visited on 01/08/2024).

[99] M.R. Bhat. "Nuclear Data Sheets for A = 57." en. In: *Nuclear Data Sheets* 85.3 (Nov. 1998), pp. 415–536. ISSN: 00903752. DOI: 10.1006/ndsh.1998.0021. URL: https://linkinghub.elsevier.com/retrieve/pii/S0090375298900217 (visited on 01/08/2024).

[100] Caroline D. Nesaraja, Scott D. Geraedts, and Balraj Singh. "Nuclear Data Sheets for A = 58." en. In: *Nuclear Data Sheets* 111.4 (Apr. 2010), pp. 897–1092. ISSN: 00903752. DOI: 10.1016/j.nds.2010.03.003. URL: https://linkinghub.elsevier.com/retrieve/pii/S0090375210000359 (visited on 01/08/2024).

[101] E. Browne and J.K. Tuli. "Nuclear Data Sheets for A = 60." en. In: *Nuclear Data Sheets* 114.12 (Dec. 2013), pp. 1849–2022. ISSN: 00903752. DOI: 10.1016/j.nds.2013.11.002. URL: https://linkinghub.elsevier.com/retrieve/pii/S0090375213000823 (visited on 01/08/2024).

[102] Kazimierz Zuber and Balraj Singh. "Nuclear Data Sheets for A = 61." en. In: *Nuclear Data Sheets* 125 (Mar. 2015), pp. 1–200. ISSN: 00903752. DOI: 10.1016/j.nds.2015.02.001. URL: https://linkinghub.elsevier.com/retrieve/pii/S0090375215000022 (visited on 01/08/2024).

[103] Balraj Singh and Jun Chen. "Nuclear Data Sheets for A=64." en. In: *Nuclear Data Sheets* 178 (Dec. 2021), pp. 41–537. ISSN: 00903752. DOI: 10.1016/j.nds.2021.11.002. URL: https://linkinghub.elsevier.com/retrieve/pii/S0090375221000624 (visited on 01/08/2024).

[104] Alan L. Nichols, Balraj Singh, and Jagdish K. Tuli. "Nuclear Data Sheets for A = 62." en. In: *Nuclear Data Sheets* 113.4 (Apr. 2012), pp. 973–1114. ISSN: 00903752. DOI: 10.1016/j.nds.2012.04.002. URL: https://linkinghub.elsevier.com/retrieve/pii/S0090375212000312 (visited on 01/08/2024).

[105] E. Browne and J.K. Tuli. "Nuclear Data Sheets for A = 65." en. In: *Nuclear Data Sheets* 111.9 (Sept. 2010), pp. 2425–2553. ISSN: 00903752. DOI: 10.1016/j.nds.2010.09.002. URL: https://linkinghub.elsevier.com/retrieve/pii/S0090375210000864 (visited on 01/08/2024).

[106] C.D. Nesaraja. "Nuclear Data Sheets for A = 69." en. In: *Nuclear Data Sheets* 115 (Jan. 2014), pp. 1–134. ISSN: 00903752. DOI: 10.1016/j.nds.2013.12.001. URL: https://linkinghub.elsevier.com/retrieve/pii/S0090375213000938 (visited on 01/08/2024).

[107] D. Abriola and A.A. Sonzogni. "Nuclear Data Sheets for A = 72." en. In: *Nuclear Data Sheets* 111.1 (Jan. 2010), pp. 1–140. ISSN: 00903752. DOI: 10.1016/j.nds.2009.12.001. URL: https://linkinghub.elsevier.com/retrieve/pii/S0090375209001136 (visited on 01/08/2024).

[108] Balraj Singh. "Nuclear Data Sheets Update for A = 76." en. In: *Nuclear Data Sheets* 74.1 (Jan. 1995), pp. 63–164. ISSN: 00903752. DOI: 10.1006/ndsh.1995.1005. URL: https://linkinghub.elsevier.com/retrieve/pii/S0090375285710058 (visited on 01/08/2024).

[109] Balraj Singh and Ninel Nica. "Nuclear Data Sheets for A = 77." en. In: *Nuclear Data Sheets* 113.5 (May 2012), pp. 1115–1314. ISSN: 00903752. DOI: 10.1016/j.nds.2012.05.001. URL: https://linkinghub.elsevier.com/retrieve/pii/S0090375212000403 (visited on 01/08/2024).

[110] J.K. Tuli and E. Browne. "Nuclear Data Sheets for A=82." en. In: *Nuclear Data Sheets* 157 (Mar. 2019), pp. 260–494. ISSN: 00903752. DOI: 10.1016/j.nds.2019.04.002. URL: https://linkinghub.elsevier.com/retrieve/pii/S0090375219300274 (visited on 01/08/2024).

[111] Balraj Singh. "Nuclear Data Sheets for A = 79." en. In: *Nuclear Data Sheets* 135 (July 2016), pp. 193–382. ISSN: 00903752. DOI: 10.1016/j.nds.2016.06.002. URL: https://linkinghub.elsevier.com/retrieve/pii/S0090375216300138 (visited on 01/08/2024).

[112] E.A. McCutchan. "Nuclear Data Sheets for A = 83." en. In: *Nuclear Data Sheets* 125 (Mar. 2015), pp. 201–394. ISSN: 00903752. DOI: 10.1016/j.nds.2015.02.002. URL: https://linkinghub.elsevier.com/retrieve/pii/S0090375215000034 (visited on 01/08/2024).

[113] Daniel Abriola et al. "Nuclear Data Sheets for A = 84." en. In: *Nuclear Data Sheets* 110.11 (Nov. 2009), pp. 2815–2944. ISSN: 00903752. DOI: 10.1016/j.nds.2009.10.002. URL: https://linkinghub.elsevier.com/retrieve/pii/S0090375209000891 (visited on 01/08/2024).

[114] Alexandru Negret and Balraj Singh. "Nuclear Data Sheets for A = 86." en. In: *Nuclear Data Sheets* 124 (Feb. 2015), pp. 1–156. ISSN: 00903752. DOI: 10.1016/j.nds.2014.12.045. URL: https://linkinghub.elsevier.com/retrieve/pii/S0090375214007455 (visited on 01/08/2024).

[115] Balraj Singh and Jun Chen. "Nuclear Data Sheets for A = 85." en. In: *Nuclear Data Sheets* 116 (Feb. 2014), pp. 1–162. ISSN: 00903752. DOI: 10.1016/j.nds.2014.01.001. URL: https://linkinghub.elsevier.com/retrieve/pii/S0090375214000106 (visited on 01/08/2024).

[116] T.D. Johnson and W.D. Kulp. "Nuclear Data Sheets for A = 87." en. In: *Nuclear Data Sheets* 129 (Nov. 2015), pp. 1–190. ISSN: 00903752. DOI: 10.1016/j.nds.2015.09.001. URL: https://linkinghub.elsevier.com/retrieve/pii/S0090375215000460 (visited on 01/08/2024).

[117] E.A. McCutchan and A.A. Sonzogni. "Nuclear Data Sheets for A = 88." en. In: *Nuclear Data Sheets* 115 (Jan. 2014), pp. 135–304. ISSN: 00903752. DOI: 10.1016/j.nds.2013.12.002. URL: https://linkinghub.elsevier.com/retrieve/pii/S009037521300094X (visited on 01/08/2024).

[118] Coral M. Baglin. "Nuclear Data Sheets for A = 93." en. In: *Nuclear Data Sheets* 112.5 (May 2011), pp. 1163–1389. ISSN: 00903752. DOI: 10.1016/j.nds.2011.04.001. URL: https://linkinghub.elsevier.com/retrieve/pii/S0090375211000299 (visited on 01/09/2024).

[119] Jun Chen and Balraj Singh. "Nuclear Data Sheets for A = 42." en. In: *Nuclear Data Sheets* 135 (July 2016), pp. 1–192. ISSN: 00903752. DOI: 10.1016/j.nds.2016.06.001. URL: https://linkinghub.elsevier.com/retrieve/pii/S0090375216300126 (visited on 01/08/2024).

[120] Balraj Singh and Jun Chen. "Nuclear Data Sheets for A = 43." en. In: *Nuclear Data Sheets* 126 (May 2015), pp. 1–150. ISSN: 00903752. DOI: 10.1016/j.nds.2015.05.001. URL: https://linkinghub.elsevier.com/retrieve/pii/S0090375215000125 (visited on 01/08/2024).

[121] T.W. Burrows. "Nuclear Data Sheets for A = 47." en. In: *Nuclear Data Sheets* 108.5 (May 2007), pp. 923–1056. ISSN: 00903752. DOI: 10.1016/j.nds.2007.04.002. URL: https://linkinghub.elsevier.com/retrieve/pii/S0090375207000403 (visited on 01/08/2024).

[122] S.-C. Wu. "Nuclear Data Sheets for A = 46." en. In: *Nuclear Data Sheets* 91.1 (Sept. 2000), pp. 1–116. ISSN: 00903752. DOI: 10.1006/ndsh.2000.0014. URL: https://linkinghub.elsevier.com/retrieve/pii/S0090375200900140 (visited on 01/08/2024).

[123] Jun Chen. "Nuclear Data Sheets for A=48." en. In: *Nuclear Data Sheets* 179 (Jan. 2022), pp. 1–382. ISSN: 00903752. DOI: 10.1016/j.nds.2021.12.001. URL: https://linkinghub.elsevier.com/retrieve/pii/S0090375221000697 (visited on 01/08/2024).

[124] Jun Chen and Balraj Singh. "Nuclear Structure and Decay Data for A=44 Isobars." en. In: *Nuclear Data Sheets* 190 (Aug. 2023), pp. 1–318. ISSN: 00903752. DOI: 10.1016/j.nds.2023.06.001. URL: https://linkinghub.elsevier.com/retrieve/pii/S009037522300042X (visited on 01/08/2024).

[125] F. S. Al-Saleh, A. A. Al-Harbi, and A. Azzam. "Excitation functions of proton induced nuclear reactions on natural copper using a medium-sized cyclotron." en. In: *Radiochimica Acta* 94.8 (Aug. 2006), pp. 391–396. ISSN: 2193-3405, 0033-8230. DOI: 10.1524/ract.2006.94.8.391. URL: https://www.degruyter.com/document/doi/10.1524/ract.2006.94.8.391/html (visited on 03/29/2024).

[126] V. N. Aleksandrov, M. P. Semenova, and V. G. Semenov. "Production cross section of radionuclides in (p, x) reactions at copper and nickel nuclei." en. In: *Soviet Atomic Energy* 62.6 (June 1987), pp. 478–481. ISSN: 0038-531X, 1573-8205. DOI: 10.1007/BF01124118. URL: http://link.springer.com/10.1007/BF01124118 (visited on 03/29/2024).

[127] Mahwish Anwer et al. "Ion beam activation of ^{nat} Cu, ^{nat} Ti, ^{nat} Ni and measurement of product formation cross sections at low energy (¡10 MeV)." en. In: *Radiochimica Acta* 110.10 (Oct. 2022), pp. 799–808. ISSN: 0033-8230, 2193-3405. DOI: 10.1515/ract-2021-1132. URL: https://www.degruyter.com/document/doi/10.1515/ract-2021-1132/html (visited on 03/29/2024).

[128] E.Z. Buthelezi, F.M. Nortier, and I.W. Schroeder. "Excitation functions for the production of 82Sr by proton bombardment of natRb at energies up to 100MeV." en. In: *Applied Radiation and Isotopes* 64.8 (Aug. 2006), pp. 915–924. ISSN: 09698043. DOI: 10.1016/j.apradiso.2006.03.009. URL: https://linkinghub.elsevier.com/retrieve/pii/S0969804306001710 (visited on 03/29/2024).

[129] Jaroslav Červenák and Ondřej Lebeda. "New cross-section data for proton-induced reactions on natTi and natCu with special regard to the beam monitoring." en. In: *Nuclear Instruments and Methods in Physics Research Section B: Beam Interactions with Materials and Atoms* 480 (Oct. 2020), pp. 78–97. ISSN: 0168583X. DOI: 10.1016/j.nimb.2020.08.006. URL: https://linkinghub.elsevier.com/retrieve/pii/S0168583X20303682 (visited on 03/29/2024).

[130] E. Garrido et al. "New excitation functions for proton induced reactions on natural titanium, nickel and copper up to 70 MeV." en. In: *Nuclear Instruments and Methods in Physics Research Section B: Beam Interactions with Materials and Atoms* 383 (Sept. 2016), pp. 191–212. ISSN: 0168583X. DOI: 10.1016/j.nimb.2016.07.011. URL: https://linkinghub.elsevier.com/retrieve/pii/S0168583X16303068 (visited on 03/29/2024).

[131] J. R. Griswold et al. "Production of Th 229 for medical applications: Excitation functions of low-energy protons on Th 232 targets." en. In: *Physical Review C* 98.4 (Oct. 2018), p. 044607. ISSN: 2469-9985, 2469-9993. DOI: 10.1103/PhysRevC.98.044607. URL: https://link.aps.org/doi/10.1103/PhysRevC.98.044607 (visited on 03/29/2024).

[132] I.B. Häller and G. Rudstam. "Relative yields of the isomeric pairs 69gZn–69mZn and 52gMn–52mMn in some spallation reactions induced by 20–153 MeV protons." en. In: *Journal of Inorganic and Nuclear Chemistry* 19.1-2 (Sept. 1961), pp. 1–8. ISSN: 00221902. DOI: 10.1016/0022-1902(61)80038-9. URL: https://linkinghub.elsevier.com/retrieve/pii/0022190261800389 (visited on 03/29/2024).

[133] A. Hermanne et al. "New cross section data on68Zn(p, 2n)67Ga andnatZn(p,xn)67Ga nuclear reactions for the development of a reference data base." en. In: *Journal of Radioanalytical and Nuclear Chemistry* 240.2 (May 1999), pp. 623–630. ISSN: 0236-5731, 1588-2780. DOI: 10.1007/BF02349423. URL: http://link.springer.com/10.1007/BF02349423 (visited on 03/29/2024).

[134] H. R. Heydegger, C. K. Garrett, and A. Van Ginneken. "Thin-Target Cross Sections for Some Cr, Mn, Fe, Co, Ni, and Zn Nuclides Produced in Copper by 82- to 416-MeV Protons." en. In: *Physical Review C* 6.4 (Oct. 1972), pp. 1235–1240. ISSN: 0556-2813. DOI: 10.1103/PhysRevC.6.1235. URL: https://link.aps.org/doi/10.1103/PhysRevC.6.1235 (visited on 03/29/2024).

[135] Tatsuo Ido et al. "Excitation functions of proton induced nuclear reactions on natRb from 30 to 70 MeV. Implication for the production of 82Sr and other medically important Rb and Sr radioisotopes." en. In: *Nuclear Instruments and Methods in Physics Research Section B: Beam Interactions with Materials and Atoms* 194.4 (Oct. 2002), pp. 369–388. ISSN: 0168583X. DOI: 10.1016/S0168-583X(02)00958-8. URL: https://linkinghub.elsevier.com/retrieve/pii/S0168583X02009588 (visited on 03/29/2024).

[136] Tatsuo Ido et al. "Re-measurement of the Excitation Function of the ^{85}Rb(p, 4n) ^{82}Sr Nuclear Reaction Near the Threshold: Relevance to the Production of a ^{82}Sr(^{82}Rb) Generator System with a Medium Energy Cyclotron." en. In: *Journal of Nuclear Science and Technology* 39.sup2 (Aug. 2002), pp. 1310–1313. ISSN: 0022-3131, 1881-1248. DOI: 10.1080/00223131.2002.10875345. URL: http://www.tandfonline.com/doi/full/10.1080/00223131.2002.10875345 (visited on 03/29/2024).

[137] C. U. Jost et al. "Measurement of cross sections for the [sup 232]Th(P,4n)[sup 229]Pa reaction at low proton energies." In: Ft. Worth, TX, USA, 2013, pp. 520–524. DOI: 10.1063/1.4802383. URL: https://pubs.aip.org/aip/acp/article/1525/1/520-524/848594 (visited on 03/29/2024).

[138] M.U. Khandaker et al. "Measurement of cross-sections for the (p,xn) reactions in natural molybdenum." en. In: *Nuclear Instruments and Methods in Physics Research Section B: Beam Interactions with Materials and Atoms* 262.2 (Sept. 2007), pp. 171–181. ISSN: 0168583X. DOI: 10.1016/j.nimb.2007.05.028. URL: https://linkinghub.elsevier.com/retrieve/pii/S0168583X07011524 (visited on 03/29/2024).

[139] Mayeen Uddin Kh. "Measurements of the Proton-Induced Reaction Cross-Sections of natMo(p,xn) 94m,94g,93m,93gTc." en. In: *Journal of the Korean Physical Society* 50.95 (May 2007), p. 1518. ISSN: 0374-4884. DOI: 10.3938/jkps.50.1518. URL: http://www.kps.or.kr/jkps/abstract_view.asp?articleuid=4950569D-87AC-4BBD-A0A0-3FC8817DE7FB (visited on 03/29/2024).

[140] B. Liu et al. "Excitation functions of proton induced reactions on titanium and copper." en. In: *Applied Radiation and Isotopes* 173 (July 2021), p. 109713. ISSN: 09698043. DOI: 10.1016/j.apradiso.2021.109713. URL: https://linkinghub.elsevier.com/retrieve/pii/S0969804321001202 (visited on 03/29/2024).

[141] R. Michel et al. "Cross sections for the production of residual nuclides by low- and medium-energy protons from the target elements C, N, O, Mg, Al, Si, Ca, Ti, V, Mn, Fe, Co, Ni, Cu, Sr, Y, Zr, Nb, Ba and Au." en. In: *Nuclear Instruments and Methods in*

Physics Research Section B: Beam Interactions with Materials and Atoms 129.2 (July 1997), pp. 153–193. ISSN: 0168583X. DOI: 10.1016/S0168-583X(97)00213-9. URL: https://linkinghub.elsevier.com/retrieve/pii/S0168583X97002139 (visited on 03/29/2024).

[142] S.J. Mills, G.F. Steyn, and F.M. Nortier. "Experimental and theoretical excitation functions of radionuclides produced in proton bombardment of copper up to 200 MeV." en. In: *International Journal of Radiation Applications and Instrumentation. Part A. Applied Radiation and Isotopes* 43.8 (Aug. 1992), pp. 1019–1030. ISSN: 08832889. DOI: 10.1016/0883-2889(92)90221-Y. URL: https://linkinghub.elsevier.com/retrieve/pii/088328899290221Y (visited on 03/29/2024).

[143] H. Noma et al. "Cross sections of the 63Cu(p, 3n)61Zn and the 63Cu(p, p3n)60Cu reactions." en. In: *Journal of Inorganic and Nuclear Chemistry* 39.11 (1977), pp. 1923–1927. ISSN: 00221902. DOI: 10.1016/0022-1902(77)80518-6. URL: https://linkinghub.elsevier.com/retrieve/pii/0022190277805186 (visited on 03/29/2024).

[144] C. J. Orth et al. "Pion-induced spallation of copper across the (3,3) resonance." en. In: *Physical Review C* 18.3 (Sept. 1978), pp. 1426–1435. ISSN: 0556-2813. DOI: 10.1103/PhysRevC.18.1426. URL: https://link.aps.org/doi/10.1103/PhysRevC.18.1426 (visited on 03/29/2024).

[145] Muhammad Shahid et al. "Measurement of excitation functions in proton induced reactions on natural copper from their threshold to 43MeV." en. In: *Nuclear Instruments and Methods in Physics Research Section B: Beam Interactions with Materials and Atoms* 342 (Jan. 2015), pp. 305–313. ISSN: 0168583X. DOI: 10.1016/j.nimb.2014.10.019. URL: https://linkinghub.elsevier.com/retrieve/pii/S0168583X1400857X (visited on 03/29/2024).

[146] T. Siiskonen et al. "Excitation functions of proton-induced reactions in natCu in the energy range 7–17MeV." en. In: *Applied Radiation and Isotopes* 67.11 (Nov. 2009), pp. 2037–2039. ISSN: 09698043. DOI: 10.1016/j.apradiso.2008.11.005. URL: https://linkinghub.elsevier.com/retrieve/pii/S0969804308005125 (visited on 03/29/2024).

[147] F Szelecsényi et al. "Excitation function for the nuclear process: Evaluation and new measurements for practical applications." en. In: *Nuclear Instruments and Methods in Physics Research Section B: Beam Interactions with Materials and Atoms* 174.1-2 (Mar. 2001), pp. 47–64. ISSN: 0168583X. DOI: 10.1016/S0168-583X(00)00516-4. URL: https://linkinghub.elsevier.com/retrieve/pii/S0168583X00005164 (visited on 03/29/2024).

[148] S. Takács et al. "New cross-sections and intercomparison of proton monitor reactions on Ti, Ni and Cu." en. In: *Nuclear Instruments and Methods in Physics Research Section B: Beam Interactions with Materials and Atoms* 188.1-4 (Apr. 2002), pp. 106–111. ISSN: 0168583X. DOI: 10.1016/S0168-583X(01)01032-1. URL: https://linkinghub.elsevier.com/retrieve/pii/S0168583X01010321 (visited on 03/29/2024).

[149] M.S Uddin et al. "Experimental studies on the proton-induced activation reactions of molybdenum in the energy range 22–67MeV." en. In: *Applied Radiation and Isotopes* 60.6 (June 2004), pp. 911–920. ISSN: 09698043. DOI: 10.1016/j.apradiso.2004.02.004. URL: https://linkinghub.elsevier.com/retrieve/pii/S0969804304000454 (visited on 03/29/2024).

[150] I. R. Williams and C. B. Fulmer. "Excitation Functions for Radioactive Isotopes Produced by Protons below 60 MeV on Al, Fe, and Cu." en. In: *Physical Review* 162.4 (Oct. 1967), pp. 1055–1061. ISSN: 0031-899X. DOI: 10.1103/PhysRev.162.1055. URL: https://link.aps.org/doi/10.1103/PhysRev.162.1055 (visited on 03/29/2024).

[151] H. Yashima et al. "Measurement and calculation of radioactivities of spallation products by high-energy heavy ions." en. In: *Radiochimica Acta* 91.12 (Dec. 2003), pp. 689–696. ISSN: 2193-3405, 0033-8230. DOI: 10.1524/ract.91.12.689.23423. URL: https://www.degruyter.com/document/doi/10.1524/ract.91.12.689.23423/html (visited on 03/29/2024).

[152] Hiroshi Yashima et al. "Projectile Dependency of Radioactivities of Spallation Products Induced in Copper." en. In: *Journal of Nuclear Science and Technology* 39.sup2 (Aug. 2002), pp. 1179–1182. ISSN: 0022-3131, 1881-1248. DOI: 10.1080/00223131.2002.10875312. URL: http://www.tandfonline.com/doi/full/10.1080/00223131.2002.10875312 (visited on 03/29/2024).

[153] H. Yashima et al. "Projectile dependence of radioactive spallation products induced in copper by high-energy heavy ions." en. In: *Physical Review C* 66.4 (Oct. 2002), p. 044607. ISSN: 0556-2813, 1089-490X. DOI: 10.1103/PhysRevC.66.044607. URL: https://link.aps.org/doi/10.1103/PhysRevC.66.044607 (visited on 03/29/2024).

[154] Y. Yoshizawa et al. "Isotope separator on-line at INS FM cyclotron." en. In: *Nuclear Instruments and Methods* 134.1 (Apr. 1976), pp. 93–100. ISSN: 0029554X. DOI: 10.1016/0029-554X(76)90128-2. URL: https://linkinghub.elsevier.com/retrieve/pii/0029554X76901282 (visited on 03/29/2024).

[155] G. Albouy et al. "Réactions (p, 3p3n) entre 30 et 150 MeV." In: *Journal de Physique et le Radium* 24.1 (1963), pp. 67–68. ISSN: 0368-3842. DOI: 10.1051/jphysrad:0196300240106700. URL: http://www.edpsciences.org/10.1051/jphysrad:0196300240106700 (visited on 03/29/2024).

[156] J. P. Blaser et al. "Anregungsfunktionen und wirkungsquerschnitte der (p,n)-Reaktion (II)." In: *Helvetica Physica Acta* 24 (1951), p. 441.

[157] A. A. Cowley et al. "Multistep direct mechanism in the (p → , 3 He) inclusive reaction on 59 Co and 93 Nb at an incident energy of 100 MeV." en. In: *Physical Review C* 62.6 (Nov. 2000), p. 064605. ISSN: 0556-2813, 1089-490X. DOI: 10.1103/PhysRevC.62.064605. URL: https://link.aps.org/doi/10.1103/PhysRevC.62.064605 (visited on 03/29/2024).

[158] A. A. Cowley et al. "Multistep direct mechanism in the (p → , He 3) inclusive reaction on Co 59 and Nb 93 at incident energies between 100 and 160 MeV." en. In: *Physical Review C* 75.5 (May 2007), p. 054617. ISSN: 0556-2813, 1089-490X. DOI: 10.1103/PhysRevC.75.054617. URL: https://link.aps.org/doi/10.1103/PhysRevC.75.054617 (visited on 03/29/2024).

[159] F. Ditrói et al. "Investigation of proton induced reactions on niobium at low and medium energies." en. In: *Nuclear Instruments and Methods in Physics Research Section B: Beam Interactions with Materials and Atoms* 267.19 (Oct. 2009), pp. 3364–3374. ISSN: 0168583X. DOI: 10.1016/j.nimb.2009.07.010. URL: https://linkinghub.elsevier.com/retrieve/pii/S0168583X09008337 (visited on 03/29/2024).

[160] F. Ditrói et al. "Study of proton induced reactions on niobium targets up to 70MeV." en. In: *Nuclear Instruments and Methods in Physics Research Section B: Beam Interactions with Materials and Atoms* 266.24 (Dec. 2008), pp. 5087–5100. ISSN: 0168583X. DOI: 10.1016/j.nimb.2008.09.023. URL: https://linkinghub.elsevier.com/retrieve/pii/S0168583X08010458 (visited on 03/29/2024).

[161] C. W. Forsthoff, R. H. Goeckermann, and R. A. Naumann. "Formation and Decay of Mo 9 3 m." en. In: *Physical Review* 90.5 (June 1953), pp. 1004–1005. ISSN: 0031-899X. DOI: 10.1103/PhysRev.90.1004. URL: https://link.aps.org/doi/10.1103/PhysRev.90.1004 (visited on 03/29/2024).

[162] Kwangsoo Kim et al. "Excitation functions of 93Nb(p,x) reactions from threshold to 42.5 MeV." en. In: *Journal of Radioanalytical and Nuclear Chemistry* 317.2 (Aug. 2018), pp. 1021–1031. ISSN: 0236-5731, 1588-2780. DOI: 10.1007/s10967-018-5949-3. URL: http://link.springer.com/10.1007/s10967-018-5949-3 (visited on 03/29/2024).

[163] B. G. Kiselev and N. R. Faizrakhmanova. "Reaction cross sections of (p,n), (p,pn) and (p,alpha+n) on 93-Nb." In: 1974, p. 356.

[164] B. Lawriniang et al. "Measurement of cross-sections for the 93Nb(p,n)93mMo and 93Nb(p,pn)92mNb reactions up to ∼20 MeV energy." en. In: *Nuclear Physics A* 973 (May 2018), pp. 79–88. ISSN: 03759474. DOI: 10.1016/j.nuclphysa.2018.02.008. URL: https://linkinghub.elsevier.com/retrieve/pii/S0375947418300423 (visited on 03/29/2024).

[165] Siddharth Parashari et al. "Excitation functions of the p + Nb-93 reaction in the energy range 10–22 MeV." en. In: *Nuclear Physics A* 978 (Oct. 2018), pp. 160–172. ISSN: 03759474. DOI: 10.1016/j.nuclphysa.2018.08.002. URL: https://linkinghub.elsevier.com/retrieve/pii/S0375947418301386 (visited on 03/29/2024).

[166] I. A. Rizvi et al. "Energy dependence of pre-equilibrium emission for the (p,xn) reactions in niobium." en. In: *Indian Journal of Physics* 86.10 (Oct. 2012), pp. 913–918. ISSN: 0973-1458, 0974-9845. DOI: 10.1007/s12648-012-0134-y. URL: http://link.springer.com/10.1007/s12648-012-0134-y (visited on 03/29/2024).

[167] B.P. Singh et al. "A study of pre-equilibrium emission in some proton- and alpha-induced reactions." en. In: *Nuclear Instruments and Methods in Physics Research Section A: Accelerators, Spectrometers, Detectors and Associated Equipment* 562.2 (June 2006), pp. 717–720. ISSN: 01689002. DOI: 10.1016/j.nima.2006.02.030. URL: https://linkinghub.elsevier.com/retrieve/pii/S0168900206002658 (visited on 03/29/2024).

[168] G. F. Steyn et al. "Excitation Functions of Proton Induced Reactions on 89Y and 93Nb with Emphasis on the Production of Selected Radio-Zirconiums." en. In: *Journal of the Korean Physical Society* 59.2(3) (Aug. 2011), pp. 1991–1994. ISSN: 0374-4884. DOI: 10.3938/jkps.59.1991. URL: http://www.jkps.or.kr/journal/DOIx.php?id=10.3938/jkps.59.1991 (visited on 03/29/2024).

[169] Yu. E. Titarenko et al. "Measurement and simulation of the cross sections for nuclide production in ^{93}Nb and ^{nat}Ni targets irradiated with 0.04- to 2.6-GeV protons." In: *Physics of Atomic Nuclei* 74 (2011), p. 537. DOI: 10.1134/S106377881104017X. URL: http://dx.doi.org/10.1134/S106377881104017X.

[170] A. Azzam et al. "Excitation functions for proton-induced reactions on Te and natTi targets: Measurements and model calculations special relevant to the 128Te(p,n)128I reaction." en. In: *Nuclear Physics A* 999 (July 2020), p. 121790. ISSN: 03759474. DOI: 10.1016/j.nuclphysa.2020.121790. URL: https://linkinghub.elsevier.com/retrieve/pii/S0375947420301007 (visited on 03/29/2024).

[171] Claus Maximilian Bäcker et al. "Towards using secondary gamma-rays from proton-induced radioactivation of titanium implants for off-line field verification." en. In: *Nuclear Instruments and Methods in Physics Research Section B: Beam Interactions with Materials and Atoms* 492 (Apr. 2021), pp. 56–63. ISSN: 0168583X. DOI: 10.1016/j.nimb.2021.02.006. URL: https://linkinghub.elsevier.com/retrieve/pii/S0168583X21000653 (visited on 03/29/2024).

[172] Megan E. Bennett et al. "Measurement of the natLu(p,x)175Hf excitation function." en. In: *Nuclear Instruments and Methods in Physics Research Section B: Beam Interactions with Materials and Atoms* 276 (Apr. 2012), pp. 62–65. ISSN: 0168583X. DOI: 10.1016/j.nimb.2012.01.039. URL: https://linkinghub.elsevier.com/retrieve/pii/S0168583X12000626 (visited on 03/29/2024).

[173] F. Bringas. "Measurement of Proton-Induced Reaction Cross Sections in Ti, Ni and Zr near the Threshold." en. In: *AIP Conference Proceedings*. Vol. 769. ISSN: 0094243X. Santa Fe, New Mexico (USA): AIP, 2005, pp. 1374–1377. DOI: 10.1063/1.1945260. URL: https://pubs.aip.org/aip/acp/article/769/1/1374-1377/946277 (visited on 03/29/2024).

[174] R. L. Brodzinski et al. "High-Energy Proton Spallation of Titanium." en. In: *Physical Review C* 4.4 (Oct. 1971), pp. 1250–1257. ISSN: 0556-2813. DOI: 10.1103/PhysRevC.4.1250. URL: https://link.aps.org/doi/10.1103/PhysRevC.4.1250 (visited on 03/29/2024).

[175] David Fink, Stephan Vogt, and Michael Hotchkis. "Cross-sections for 36Cl from Ti at Ep=35–150 MeV: Applications to in-situ exposure dating." en. In: *Nuclear Instruments and Methods in Physics Research Section B: Beam Interactions with Materials and Atoms* 172.1-4 (Oct. 2000), pp. 861–866. ISSN: 0168583X. DOI: 10.1016/S0168-583X(00)00200-7. URL: https://linkinghub.elsevier.com/retrieve/pii/S0168583X00002007 (visited on 03/29/2024).

[176] D. Fink et al. "Production of 41Ca and K, Sc and V short-lived isotopes by the irradiation of Ti with 35 to 150 MeV protons: applications to solar cosmic ray studies." en. In: *Nuclear Instruments and Methods in Physics Research Section B: Beam Interactions with Materials and Atoms* 52.3-4 (Dec. 1990), pp. 601–607. ISSN: 0168583X. DOI: 10.1016/0168-583X(90)90483-B. URL: https://linkinghub.elsevier.com/retrieve/pii/0168583X9090483B (visited on 03/29/2024).

[177] A. Hermanne et al. "Excitation functions for production of 46 Sc by deuteron and proton beams in nat Ti: A basis for additional monitor reactions." en. In: *Nuclear Instruments and Methods in Physics Research Section B: Beam Interactions with Materials and Atoms* 338 (Nov. 2014), pp. 31–41. ISSN: 0168583X. DOI: 10.1016/j.nimb.2014.07.026. URL: https://linkinghub.elsevier.com/retrieve/pii/S0168583X14006776 (visited on 03/29/2024).

[178] K. Kettern. "Nuclear Reaction Cross-Section Measurements via Characterization of Soft Radiation Emitting Products." en. In: *AIP Conference Proceedings*. Vol. 769. ISSN: 0094243X. Santa Fe, New Mexico (USA): AIP, 2005, pp. 758–761. DOI: 10.1063/1.1945117. URL: https://pubs.aip.org/aip/acp/article/769/1/758-761/1014018 (visited on 03/29/2024).

[179] M.U. Khandaker et al. "Investigations of the natTi(p,x)43,44m,44g,46,47,48Sc,48V nuclear processes up to 40 MeV." en. In: *Applied Radiation and Isotopes* 67.7-8 (July 2009), pp. 1348–1354. ISSN: 09698043. DOI: 10.1016/j.apradiso.2009.02.030. URL: https://linkinghub.elsevier.com/retrieve/pii/S096980430900150X (visited on 03/29/2024).

[180] P. Kopecky et al. "Excitation functions of (p, xn) reactions on natTi: Monitoring of bombarding proton beams." en. In: *Applied Radiation and Isotopes* 44.4 (Apr. 1993), pp. 687–692. ISSN: 09698043. DOI: 10.1016/0969-8043(93)90133-U. URL: https://linkinghub.elsevier.com/retrieve/pii/096980439390133U (visited on 03/29/2024).

[181] R. Michel and G. Brinkmann. "On the depth-dependent production of radionuclides (44≤A≤59) by solar protons in extraterrestrial matter." en. In: *Journal of Radioanalytical Chemistry* 59.2 (Sept. 1980), pp. 467–510. ISSN: 0134-0719, 1588-2780. DOI: 10.1007/BF02517298. URL: http://link.springer.com/10.1007/BF02517298 (visited on 03/29/2024).

[182] R. Michel, F. Peiffer, and R. Stück. "Measurement and hybrid model analysis of integral excitation functions for proton-induced reactions on vanadium, manganese and cobalt up to 200 MeV." en. In: *Nuclear Physics A* 441.4 (Aug. 1985), pp. 617–639. ISSN: 03759474. DOI: 10.1016/0375-9474(85)90441-5. URL: https://linkinghub.elsevier.com/retrieve/pii/0375947485904415 (visited on 03/29/2024).

[183] Siddharth Parashari et al. "Excitation function of the nat-Ti(p,x)48V, 47, 46, 44mSc reactions within the energy range of 10-22 MeV." en. In: *Nuclear Physics A* 987 (July 2019), pp. 128–143. ISSN: 03759474. DOI: 10.1016/j.nuclphysa.2019.04.009. URL: https://linkinghub.elsevier.com/retrieve/pii/S0375947419300806 (visited on 03/29/2024).

[184] Syed M. Qaim et al. "Excitation functions of nuclear reactions leading to the soft-radiation emitting radionuclides ^{45} Ca, ^{49} V and ^{204} Tl in beam collimator materials used in proton therapy." en. In: *Radiochimica Acta* 98.8 (Aug. 2010), pp. 447–457. ISSN: 0033-8230. DOI: 10.1524/ract.2010.1740. URL: https://www.degruyter.com/document/doi/10.1524/ract.2010.1740/html (visited on 03/29/2024).

[185] Muhammad Shahid et al. "Measurement of excitation functions of residual radionuclides from natTi(p,x) reactions up to 44 MeV." en. In: *Journal of Radioanalytical and Nuclear Chemistry* 318.3 (Dec. 2018), pp. 2049–2057. ISSN: 0236-5731, 1588-2780. DOI: 10.1007/s10967-018-6315-1. URL: http://link.springer.com/10.1007/s10967-018-6315-1 (visited on 03/29/2024).

[186] F. Tárkányi, F. Szelecsényi, and P. Kopecky. "Excitation functions of proton induced nuclear reactions on natural nickel for monitoring beam energy and intensity." en. In: *International Journal of Radiation Applications and Instrumentation. Part A. Applied Radiation and Isotopes* 42.6 (Jan. 1991), pp. 513–517. ISSN: 08832889. DOI: 10.1016/0883-2889(91)90154-S. URL: https://linkinghub.elsevier.com/retrieve/pii/088328899190154S (visited on 03/29/2024).

[187] K. Zarie, N. Al-Hammad, and A. Azzam. "Experimental study of excitation functions of some proton induced reactions on ^{nat} Ti for beam monitoring purposes." en. In: *Radiochimica Acta* 94.12 (Dec. 2006), pp. 795–799. ISSN: 2193-3405, 0033-8230. DOI: 10.1524/ract.2006.94.12.795. URL: https://www.degruyter.com/document/doi/10.1524/ract.2006.94.12.795/html (visited on 03/29/2024).